

Development of a Capillary-Assisted Low-pressure Evaporator for Sorption Heat Transformers and Thermal Storage Systems

by

Gholamreza Bamorovat Abadi

B. Sc., Iran University of Science and Technology, 2012

Thesis Submitted in Partial Fulfillment of the
Requirements for the Degree of
Doctor of Philosophy

in the
School of Mechatronic Systems Engineering
Faculty of Applied Sciences

© Gholamreza Bamorovat Abadi 2022

Simon Fraser University

Summer 2022

Copyright in this work is held by the author. Please ensure that any reproduction or re-use is done in accordance with the relevant national copyright legislation.

Declaration of Committee

Name: Gholamreza Bamorovat Abadi
Degree: Doctor of Philosophy
Title: Development of a Capillary-Assisted Low-pressure Evaporator for Sorption Heat Transformers and Thermal Storage Systems

Examining Committee:

Chair: Helen Bailey
Lecturer, Mechatronic Systems Engineering

Majid Bahrami
Supervisor
Professor, Mechatronic Systems Engineering

Gordon McTaggart-Cowan
Committee Member
Associate Professor, Sustainable Energy Engineering

Colin Copeland
Committee Member
Associate Professor, Sustainable Energy Engineering

Sami Khan
Examiner
Assistant Professor, Sustainable Energy Engineering

Andrea Frazzica
External Examiner
Permanent Researcher
Institute for Advanced Energy Technologies
(CNR-ITAE)

Abstract

Vapor compression refrigeration is the dominant technology used in air conditioning systems in almost all industrial, automotive, and residential applications. Vapor compression refrigeration is reliable, efficient, and low-cost; however, it consumes a significant amount of electrical energy, which is generated mostly by burning fossil fuels. It also uses refrigerants such as hydrofluorocarbons or hydrochlorofluorocarbons that have a high Ozone Depletion Potential and Global Warming Potential. These all contribute greatly to global warming. One promising technology is the waste heat-driven sorption heat transformers that run on low-grade waste-heat sources with temperatures of less than 90 degrees Celsius. Sorption heat transformers use alternative environmentally friendly refrigerants, such as water that have no environmental impact and no Global Warming Potential. However, sorption heat transformers have not penetrated the market as they are bulky and inefficient due to their low heat removal capacity, low coefficient of performance, and low operating pressure. This PhD program aims to address the first challenge, i.e., a low heat removal capacity, which is due to poor heat and mass transfer of the existing evaporator designs and leads to high weight and volume. A fundamental study is performed to assess, model, and optimize the performance of Capillary-Assisted Low-pressure Evaporator (CALPE) with water as a refrigerant. Capillary rise and heat transfer models are developed and experimentally validated by especially designed testbeds. A new modular design is proposed that maximizes the heat removal capacity of CALPE. This is done by establishing an in-depth understanding of the capillary mechanism in a capillary-assisted low-pressure evaporator, leading to a fin design with a maximum heat transfer area. Additionally, fundamental characterization of the capillary phenomenon is performed to design optimal fin geometries. An analytical model is developed that includes pertinent geometrical and operational parameters and thermophysical properties and accurately predicts the heat removal capacity of a CALPE. A novel CALPE is designed and fabricated using 3D-printing to provide a proof-of-concept demonstration for an optimal CALPE. Finally, experimental validation of the analytical models to predict the novel CALPE sample using custom-built test beds is given. The methodology of this PhD research project can be applied to various sorption heat transformers applications.

Keywords: Sorption; evaporator; capillary; low-pressure; heat transformer; heat transfer

Dedication

To my dear parents for their love, support, and encouragement. To my friends who have always been there during difficult and trying times.

Acknowledgements

I would like to express my deepest gratitude to the people without whom this dissertation would not have been possible. I would like to thank my senior supervisor at Simon Fraser University, SFU, Dr. Majid Bahrami, for his patient guidance, support, encouragement, and advice he has provided throughout my PhD. It has been a pleasure and a privilege working with Dr. Bahrami and learning from him. I am also thankful to my supervisory committee members, Dr. Gordon McTaggart-Cowan, and Dr. Colin Copeland, associate professors at Sustainable Energy Engineering, SFU, for their discussions and comments on my research project. I am grateful to Dr. Sami Khan, and Dr. Andrea Frazzica for their time reading this thesis and feedback. Also, I am grateful to Dr. Helen Bailey, School of Mechatronic Systems Engineering, for being the defense committee chair.

I would like to thank my friends and colleagues at Laboratory for Alternative Energy Conversion (LAEC) at Simon Fraser University for their support and contributions. Especially, I thank Dr. Claire McCague who supported this research project, and for her technical support and expert guidance. Furthermore, I'd like to thank Mr. G. Mustafa Sajid and Mr. James Shoults at SFU machine shop for their help with manufacturing samples. Finally, I thank my friend and colleague, Ali Rahnama, for endless late-night discussions on thin film evaporation heat transfer mechanism.

I would like to offer my gratitude to co-op students who helped this research. Completing this work would have been difficult if not for the support and friendship provided by the members of the School of Mechatronic Systems Engineering in Surrey, and Faculty of Applied Science in Burnaby. I am indebted to them for their help. Finally, I would like to express thanks to the Natural Sciences and Engineering Research Council of Canada (NSERC) for funding my Ph.D. research.

Table of Contents

Declaration of Committee	ii
Abstract	iii
Dedication	iv
Acknowledgements	v
Table of Contents	vi
List of Tables	ix
List of Figures	x
Nomenclature	xvi
Executive Summary	xviii
Research objectives and methodology	xix
Research roadmap and contributions	xx
Scholarly contributions	xxiii
Chapter 1. Introduction	1
1.1. State of the art	4
1.1.1. Vapor compression refrigeration systems	4
1.1.2. Sorption heat transformers	5
1.2. Low-pressure evaporation	7
1.2.1. Falling film evaporator	8
1.2.2. Capillary-assisted evaporation	9
1.3. Objective	13
1.4. Thesis structure	14
Chapter 1: Introduction	14
Chapter 2: A general form of capillary rise equation in micro-grooves	15
Chapter 3: Effect of surface roughness and Experimental validation of capillary height	15
Chapter 4: Heat transfer mechanisms of CALPE and governing equations	16
Chapter 5: Experimental validation of heat transfer models	16
Chapter 6: Future work and recommendations	16
Appendix I: Capillary rise equation for different cross sections	16
Appendix II: Non-dimensional capillary rise equation for different cross-sections	17
Appendix III: Force balance in a capillary groove	17
Appendix IV: Fin resistance	17
Appendix V: Uncertainty analysis	17
Appendix VI: Data analysis	17
Appendix VII: Genetic algorithm optimization	17
Appendix VIII: Momentum conservation model	18
Appendix IX: Results for thin film evaporation in an extended meniscus	18
Appendix X: Experimental setup and equipment list	18
Chapter 2. A general form of capillary rise equation in micro-grooves	19
2.1. Introduction	20

2.2.	The capillary rise equation for various cross-sections.....	22
2.3.	The unified non-dimensional capillary rise equation.....	27
2.4.	Results and discussion.....	28
2.5.	Conclusion to the chapter.....	37
Chapter 3. The effect of surface roughness on capillary rise in micro-grooves		39
3.1.	Introduction.....	40
3.2.	Model development and the effect of surface roughness.....	42
3.3.	Experimental study.....	47
3.4.	Sample preparation.....	50
3.5.	Uncertainty analysis.....	54
3.6.	Results and discussion.....	54
3.7.	Hydrophilicity and hydrophobicity.....	62
3.8.	Profilometer and sandblasting.....	63
3.9.	Conclusion to the chapter.....	68
Chapter 4. Heat transfer mechanisms of CALPE and governing equations		69
4.1.	Fundamental definitions.....	71
4.2.	Assumptions.....	74
4.3.	Natural convection in liquid pool.....	74
4.4.	Two-dimensional conductive heat transfer in the bulk region.....	76
4.4.1.	Analytical solution to the two-dimensional conductive heat transfer.....	79
4.5.	Multi-objective genetic algorithm optimization.....	83
4.6.	Thin film evaporation.....	84
4.7.	Comparison of natural convection, thin film evaporation, and bulk conductive heat transfer in CALPE.....	98
4.8.	Bulk material conductive thermal resistance model.....	99
4.9.	Conclusion to the chapter.....	114
Chapter 5. Experimental validation of heat removal capacity of CALPE		115
5.1.	3D-printed CALPE.....	116
5.2.	Experimental setup.....	119
5.3.	Uncertainty analysis.....	121
5.4.	Data reduction.....	121
5.5.	Experimental results and comparison.....	124
5.6.	Conclusion to the chapter.....	128
Chapter 6. Summary, conclusions, and future work		129
6.1.	Summary and general conclusions.....	129
6.2.	Specific conclusions.....	130
6.3.	Future work.....	132
References		134
Appendix A. Capillary rise equation for different cross sections		142

Appendix B. Non-dimensional capillary rise equation for different cross-sections	149
Appendix C. Force balance in a capillary groove	153
Appendix D. Fin resistance	154
Appendix E. Uncertainty analysis	157
Appendix F. Data analysis	158
Appendix G. Genetic algorithm optimization	161
Appendix H. Momentum conservation model	164
Appendix I. Results for thin film evaporation in an extended meniscus.....	171
Appendix J. P&ID and equipment list	175
Appendix K. CALPE experiment transient data	176

List of Tables

Table 1.	Advantages and disadvantages of sorption heat transformer vs vapor compression refrigeration.....	6
Table 2.	Summary of published studies on capillary-assisted low-pressure evaporators (CALPE) – all with water as refrigerant and copper tubes...	12
Table 3.	Capillary rise equation for various cross-sections.....	26
Table 4.	A summary of surface roughness values for each sample, measured by the SJ-400 profilometer. Contact angles were measured using a sessile drop method.....	55
Table 5.	Thermo-physical properties of water at 283 K	80
Table 6.	Geometry specifications of the CALPEs manufactured for this study ...	117

List of Figures

Figure 1.	Percentage of houses in British Columbia with air conditioning or heat pump units. The air conditioning usage has increased by more than 400 % in a span of two decades [6].....	2
Figure 2.	Percentage of houses in developing countries with air conditioning units. The air conditioning usage has increased by more than 200 % in a span of less than two decades [7].....	2
Figure 3.	Energy break-down of a typical fuel cell-driven bus. About half of the energy produced by a fuel cell is wasted to the ambient in a fuel cell bus [11].	3
Figure 4.	Integration of sorption heat transformers in a PEM fuel cell bus. The waste heat of a fuel cell can be used to power a sorption cooling device [11].....	3
Figure 5.	A schematic of a vapor refrigeration compression. A vapor compression refrigeration works between two temperature points whereas sorption heat transformers works between three temperatures.....	5
Figure 6.	A schematic of a sorption heat transformer. A sorption heat transformer works between three temperature points whereas vapor compression refrigeration works between two temperatures.	6
Figure 7.	Saturation pressure versus saturation temperature of water as a refrigerant. At low-pressure conditions, a small increase in pressure increases the saturation temperature greatly.....	8
Figure 8.	An overview of a falling film evaporator. Additional pumping power is required to spray the refrigerant on the evaporation surface.	9
Figure 9.	An overview of a capillary-assisted evaporator and its thermal resistance network – w , L , and H are the width, length, and height of the evaporator, respectively. h is the capillary height. W and D are the fin cross-section width and depth. R_1 , R_2 , and R_3 are the single-phase, conduction, and evaporation thermal resistances, respectively.	11
Figure 10.	An overview of heat transfer mechanisms in a CALPE. The thin film evaporation, though having the highest heat flux (\sim MW/m ²), takes place on less than 1% of fins' area.	13
Figure 11.	A summary of heat removal capacity of CALPEs available in the literature. The shaded area from darker to lighter denotes the: off-the-shelf tubes, coated off-the-shelf tubes, and 3D-printed CALPEs. The cost values are expected to significantly reduce when the designed CALPE is mass produced.....	14
Figure 12.	A schematic of a drop of a liquid on a flat surface showing three forces of surface tension leading to Young's equation under static equilibrium.....	23
Figure 13.	Force balance and inclination angle in a rectangular micro-groove	24
Figure 14.	Top and front view of a rectangular micro-groove.....	25
Figure 15.	The effect of groove width and height on the capillary rise in a rectangular cross-section for $\alpha=90^\circ$	28
Figure 16.	A comparison between the capillary rise in a rectangular and triangular cross-section groove, $D = 1$ mm, and $\alpha=90^\circ$	29

Figure 17.	A comparison between the capillary rise in a rectangular and curved cross-section groove, $D = 1 \text{ mm}$, and $\alpha=90^\circ$	29
Figure 18.	A comparison between active heat transfer area of a rectangular cross-section compared with a triangular design, showing up to 83% increase in wetted area ($D = 1 \text{ mm}$, and $\alpha=90^\circ$)	30
Figure 19.	A comparison between two fin spacing values, showing the increase in active heat transfer area of a smaller fin spacing. A 75% decrease in fin spacing leads to a 300% increase in the wetted area ($D = 1 \text{ mm}$, and $\alpha=90^\circ$)	31
Figure 20.	The effect of contact angle on the capillary rise in a rectangular cross-section with $D = 1 \text{ mm}$ and $\alpha=90^\circ$	32
Figure 21.	The effect of inclination angle on the capillary rise in a rectangular cross-section with $D=1 \text{ mm}$	32
Figure 22.	The effect of surface tension of different media on the capillary rise in a rectangular cross-section with $D=1 \text{ mm}$	33
Figure 23.	A comparison of capillary rise (Eq. 9) with data extracted from [47]	34
Figure 24.	A comparison of capillary rise (Eq. 9) with data extracted from [50]	34
Figure 25.	The unified non-dimensional form of capillary rise as a function of characteristic length scale and contact angle. Data from (\circ [47], Δ [50], \square [54], \diamond [52], \times [53])	36
Figure 26.	Top and front view of capillary rise, h , in a rough micro-groove with width of W and depth of D . Our previous model [84] is extended to include the effects of surface roughness. Dash line shows the mean surface line. α denotes an inclination angle of the capillary channel.	43
Figure 27.	A schematic of a droplet on a flat surface showing three forces of surface tension leading to Young's equation under static equilibrium on a rough surface.	44
Figure 28.	The actual surface roughness profile length vs the ideal smooth surface length. R_{Lo} is the percentage increase in the profile length.	47
Figure 29.	A schematic of the contact angle measurement using the sessile drop method. The contact angle is formed between the liquid-solid-vapor interface.	49
Figure 30.	Micro-grooves made by stereolithography (SLA1.03) were used for the capillary rise measurement. The inset shows a micro-groove thickness of $500 \mu\text{m}$ and a micro-groove width of $400 \mu\text{m}$. Micro-groove depth is 1 mm . Table 4 lists the sample details.	49
Figure 31.	SLA (stereolithography) micro-grooves with various thicknesses and spacing fabricated to measure the capillary height. The micro-groove width range is between 100 to $500 \mu\text{m}$. Micro-groove depth is 1 mm and their thickness ranges between 200 to $500 \mu\text{m}$. Table 4 lists the sample details.	51
Figure 32.	Two cross-sectional micro-groove geometries considered, rectangular (SLA1.03R) and triangular (SLA1.03T) cross-sections, made with stereolithography (SLA). The triangular cross-section has a higher capillary height as compared to the rectangular one. Table 4 lists the sample details.	52

Figure 33.	Two micro-grooves considered, rectangular (SS12.01R) and triangular (SS12.01T) cross-sections made with direct metal laser sintering (DMLS). The triangular cross-section has a higher capillary height as compared to the rectangular one, see the results. Table 4 lists the sample details.53
Figure 34.	The contact angle measurement using the sessile drop method. Images show the static contact angle formed for water on aluminum, stainless-steel, 3D-printed polymer, 3D-printed stainless-steel, and natural graphite sheet surfaces. Table 4 lists the sample details.....56
Figure 35.	A comparison of experimental contact angles, measured in this study, with the present model, Eq. 25. Error bars show the uncertainty of the experimental data, approximately 10%.....57
Figure 36.	A capillary meniscus is formed between two adjacent micro-grooves due to the disjoining pressure. Top: SLA1.03, Bottom: SS12.01. A 1% solution of water and food coloring is used for better image contrast in the polymer sample. Table 4 lists the sample details.59
Figure 37.	A comparison between the capillary height of SLA1.03 micro-grooves with different micro-groove geometry. Top: rectangular, bottom: triangular micro-grooves. Dashed lines are an average height. Table 4 lists the sample details.60
Figure 38.	A comparison between capillary height in micro-grooves vs the micro-grooves' width. Two cross-sections are considered, rectangular and triangular, and experimental results are compared against the present model, Eq. 20.61
Figure 39.	The unifying non-dimensional form of capillary height, Eq. 26, as a function of the characteristic length scale, contact angle, and surface roughness, as compared to our experimental data.....62
Figure 40.	Contact angle definition for different wetting properties. Contact angle below 90 degrees: hydrophilic/wetting, almost no contact angle: superhydrophilic/perfectly wetting, contact angle over 90 degrees: hydrophobic/non-wetting, an almost 180 degrees contact angle: superhydrophobic/perfectly non-wetting.63
Figure 41.	Surface roughness measurement using Mitutoyo SJ-400 profilometer. ...65
Figure 42.	Smooth and rough metallic surfaces used for roughness and contact angle measurement. Top left: sandblasted rough aluminum, Top right: smooth aluminum, Bottom left: sandblasted rough stainless steel, Bottom right: smooth stainless steel. The inset takes a closer look at the surface of each sheet.66
Figure 43.	3D-printed grooved samples used for roughness and contact angle measurement. Top: 3D-printed stainless steel, Bottom: 3D-printed SLA polymer. The opposite side of each sample was used for roughness and contact angle measurement.67
Figure 44.	Schematic of a rectangular groove on a finned wall. θ is contact angle, σ surface tension, κ meniscus curvature, P_l and P_v the liquid and vapor pressure, respectively. W , D , and h are groove width, depth, and height respectively.72

Figure 45.	Schematic of thin film evaporation site in a rectangular groove. The thin film evaporation heat transfer is orders of magnitude larger than the conductive heat transfer.....	73
Figure 46.	Schematic of a finned wall partially submerged in a liquid pool. Natural convection occurs between the wall and the liquid pool due to the temperature difference of $T_w - T_{sat}$	75
Figure 47.	Schematic of two-dimensional conductive heat transfer solution domain in CALPE meniscus with top: dimensional, and bottom: non-dimensional parameters.....	78
Figure 48.	Temperature distribution, sides, and bottom heat flux for two-dimensional conductive heat transfer in a capillary meniscus, $T_{sat}=9\text{ }^\circ\text{C}$ and $T_{wal}=10\text{ }^\circ\text{C}$. a) fin height 0.5 mm, fin spacing 0.4 mm, b) fin height 0.7 mm, fin spacing 0.11 mm, c) fin height 1.2 mm, fin spacing 0.224 mm, d) fin height 2 mm, fin spacing 1 mm.	82
Figure 49.	A schematic of a rectangular groove, temperature boundary conditions, and thin film evaporation location.....	84
Figure 50.	Detailed view of the extended meniscus in a rectangular groove and its division into I: non-evaporating, II: thin film evaporation, and III: bulk region.....	85
Figure 51.	A control volume selected in the thin film region showing the forces, film thickness and the evaporation mass flux – rectangular groove.....	86
Figure 52.	Schematic of the selected control volume in the thin film region; boundary conditions.....	87
Figure 53.	A schematic of a triangular groove, temperature boundary conditions, and thin film evaporation location.....	89
Figure 54.	Detailed view of the extended meniscus in a triangular groove and its division into I: non-evaporating, II: thin film evaporation, and III: bulk region.....	89
Figure 55.	A control volume selected in the thin film region showing the forces, film thickness and the evaporation mass flux – triangular groove.....	90
Figure 56.	Average velocity in x direction versus the x position in an extended meniscus; comparison between rectangular and triangular groove.....	92
Figure 57.	Evaporation mass flux versus the x position in an extended meniscus; comparison between rectangular and triangular groove.....	93
Figure 58.	Evaporation heat flux versus the x position in an extended meniscus; comparison between rectangular and triangular groove.....	94
Figure 59.	Heat transfer rate for a 10 by 15 cm finned wall with 1000 fins versus superheat degree; comparison between rectangular and triangular grooves.....	95
Figure 60.	Heat removal capacity for a 10 by 15 cm finned wall with 1000 fins versus superheat degree; comparison between rectangular and triangular grooves.....	96
Figure 61.	Heat removal capacity in terms of wetted area for a 10 by 15 cm finned wall with 1000 fins versus superheat degree; comparison between rectangular and triangular grooves.....	97

Figure 62.	Comparison of natural convection, two-dimensional conductive heat transfer, and thin film evaporation for a 10 by 15 cm finned wall with 1000 fins for a superheat degree of 1 K; comparison between rectangular and triangular grooves98
Figure 63.	Thermal resistance of CALPE include the external convection, the internal convection, and the conductive bulk material thermal resistances..... 100
Figure 64.	A schematic of CALPE showing the heat transfer fluid, bulk material, and fin side, along with the heat flow direction and important temperatures 101
Figure 65.	CALPE heat transfer solution flowchart; an analytical model follows the solution flowchart until there is a balance between heat transfers of CALPE 102
Figure 66.	Various cross sections considered in modeling of effect of fin geometry on bulk material conduction thermal resistance..... 103
Figure 67.	Various cross sections considered in modeling of effect of fin geometry on bulk material conduction thermal resistance; overlaid view 103
Figure 68.	Geometrical parameters of a rectangular and a triangular cross-section considered in solving the bulk material conduction thermal resistance . 105
Figure 69.	Half the symmetrical geometry of a rectangular cross-section considered in solving the bulk material conduction thermal resistance 106
Figure 70.	The temperature distribution for a rectangular cross-section fin with D and w of 1 mm, and t_f and t_b of 0.1 mm. Bottom wall temperature is 15 °C.. 108
Figure 71.	The temperature distribution for a curved cross-section fin with D and w of 1 mm, and t_f and t_b of 0.1 mm. Bottom wall temperature is 15 °C. 109
Figure 72.	The temperature distribution for a circular cross-section fin with D and w of 1 mm, and t_f and t_b of 0.1 mm. Bottom wall temperature is 15 °C. 110
Figure 73.	The temperature distribution for a hyperellipse cross-section fin with D and w of 1 mm, and t_f and t_b of 0.1 mm. Bottom wall temperature is 15 °C.. 111
Figure 74.	The temperature distribution for a triangular cross-section fin with D and w of 1 mm, and t_f and t_b of 0.1 mm. Bottom wall temperature is 15 °C. 112
Figure 75.	Comparison of the volumetric thermal resistance, R^* , for various cross-sections considered 113
Figure 76.	A set of novel CALPEs fabricated with stainless steel 3D-printing to maximize capillary height and heat removal capacity. 117
Figure 77.	Front view and microscopic top view of an example 3D-printed CALPE compared with a Canadian quarter. Fin spacing and thickness: 100 μ m, height: 6 cm, length: 10 cm. Detailed geometries are presented in Table 6. Tests were performed with a 5-25 °C heat transfer fluid (HTF) inlet temperature..... 118
Figure 78.	Microscopic top view of multiple 3D-printed CALPE with fin spacing and thickness of 100, 200, and 500 μ m. CALPE height: 6 cm, length: 10 cm. Detailed geometries are presented in..... 119
Figure 79.	Top, a schematic diagram of the test bed purpose-built for heat removal capacity testing of CALPEs. Bottom, an image of the test setup showing the evaporator chamber, condenser (vapor collector), thermal bath, and data collection device. 123

Figure 80.	Experimental results for the heat removal capacity of the 3D-printed CALPE vs the pressure difference between the evaporator and vapor collector chamber.....	125
Figure 81.	Experimental heat removal capacity of the 3D-printed CALPE vs the pressure difference between the evaporator and vapor collector chamber; comparison between rectangular and triangular grooves	126
Figure 82.	Comparison of experimental CALPEs – comparison between this study and state-of-the-art CALPEs, showing up to 60% improvement in heat removal capacity.....	126
Figure 83.	Comparison of experimental CALPEs – comparison between pressure drop of CALPE in this study and those made previously, showing up to 20% reduction	127

Nomenclature

A	area (m ²)
c_p	heat capacity at constant pressure (J/kg.K)
D	depth (m), diameter (m)
d	diameter (m)
f	friction factor
F	force (N)
FPI	fins per inch
g	gravitational acceleration (m/s ²)
Gr	Grashof number
h	heat transfer coefficient (W/(m ² ·K)), capillary height (m)
H	height (m)
h_{fg}	heat of vaporization (kJ/kg)
HTF	heat transfer fluid
k	thermal conductivity (W/(m·K))
ICE	internal combustion engine
L	length (m)
m	mass (kg)
\dot{m}	mass flow rate (kg/s)
p	pressure (Pa)
Pr	Prandtl number
\dot{q}	heat transfer rate (W)
\dot{Q}	total heat transfer rate (W)
r	radius (m)
R	heat transfer thermal resistance (K/W)
Re	Reynolds number
T	temperature (°C)
t	time (s)
ΔT_{LMTD}	logarithmic mean temperature difference (°C)
U	overall heat transfer coefficient (W/(m ² ·K))
W,w	width (m)

x	Cartesian coordinate (m)
y	Cartesian coordinate (m)
α	angle (degrees)
β	coefficient of thermal expansion (1/K)
δ	film thickness (m)
σ	surface tension (N/m)
θ	contact angle (degrees)
κ	meniscus curvature (1/m)
μ	dynamic viscosity (N.s/m ²)
ν	kinematic viscosity (m ² /s)
ρ	density (kg/m ³)
ϕ	non-dimensional temperature
ε	non-dimensional coordinate
η	non-dimensional coordinate

Subscripts

evap	evaporator
avg	average
i	inside surface/in
o	outside surface/out
sv	solid-vapor
sl	solid-liquid
lv	liquid-vapor
c	capillary

Executive Summary

Vapor compression refrigeration is the dominant technology used in air conditioning and refrigeration systems in almost all industrial, automotive, and residential applications. It is estimated that around 15% of global electricity is used by air conditioning and refrigeration units, most of which use vapor compression refrigeration technology. In vehicles, air conditioning adds up to 20% extra load on the engine, resulting in significant increase in fuel consumption. Vapor compression refrigeration is reliable, efficient, and low-cost; however, it is mechanically driven and consumes a significant amount of electrical energy (to activate the compressor), which is generated mostly by burning fossil fuels. It also uses refrigerants such as hydrofluorocarbons or hydrochlorofluorocarbons that have a high Ozone Depletion Potential and Global Warming Potential. These all contribute greatly to global warming, which, in turn, increase the demand for air conditioning units globally. One promising technology is the sorption heat transformer system that can run on low-grade (or waste) heat sources, i.e., temperatures less than 90°C, instead of electrically driven compressors, to produce cooling effect. Moreover, sorption systems use alternative environmentally friendly refrigerants, such as water that have no environmental impact, which makes them sustainable and a great alternative for vapor compression refrigeration systems.

However, sorption systems have not penetrated the market as they are bulky and inefficient due to their:

- i) low heat removal capacity, due to low performance of off-the-shelf heat and mass exchangers commonly used in existing sorption systems,
- ii) low coefficient of performance; partly due to high thermal inertia of the currently used off-the-shelf heat and mass exchangers, and
- iii) low operating pressure (2-4 kPa), which poses challenges for optimal design of heat exchangers, especially low-pressure evaporators. It also brings about sealing issues and increases the existing sorption systems' cost and maintenance.

This study aims to address the first challenge, which is due to poor heat transfer of the existing evaporator designs that leads to high weight, volume, and ultimately cost.

To this end, new evaporators should be specifically designed and optimized for sorption systems to increase their heat transfer performance with minimum weight and volume. Although flooded evaporators are commonly used, they are neither compact nor efficient under low-pressure conditions. An alternative solution is to use a capillary-assisted low-pressure evaporator (CALPE). They do not need a refrigerant pump and are desirable in terms of power consumption, cost, and reliability. The fin spacing in such evaporators is small enough to enable the capillary effect, i.e., to pull the refrigerant from a pool to evaporation regions.

In a CALPE, the following three heat transfer resistances exist that should be minimized to increase its heat removal capacity:

- i) the internal convective heat transfer resistance of the single-phase heat transfer fluid inside the heat exchanger conduit,
- ii) the external resistance in the liquid pool, where evaporation occurs, and
- iii) the bulk material resistance of the heat exchanger.

In the existing off-the-shelf tube designs, the largest resistance is the internal resistance, which may be reduced by developing an efficient internal micro-/mini-channel design with a small conduit/tube diameter. The external resistance is the heat transfer resistance of the fin side and can be decreased by designing an optimized fin structure that maximizes the heat transfer area where evaporation occurs, while minimizing the volume of the bulk of the pool of liquid refrigerant (water). The material resistance is due to the thickness and the thermal conductivity of the material and can be lowered by using thinner walls made from materials with higher thermal conductivity.

Research objectives and methodology

In this PhD program, a fundamental study is performed to assess, model, and optimize the performance of CALPEs with water as a refrigerant. The methodology of this PhD research project can be applied to various sorption system applications. Capillary rise and heat transfer models are developed and experimentally validated using custom-made testbeds. A new modular design is proposed that maximizes the heat removal

capacity of CALPEs. This is done by establishing an in-depth understanding of the capillary mechanism in a capillary-assisted low-pressure evaporator, leading to an optimal fin design with a maximum heat transfer area. The developed CALPE is installed in a lab-scale waste heat-driven sorption system testbed, currently available in our laboratory, the Laboratory for Alternative Energy Conversion (LAEC), to serve as a proof-of-concept demonstration. The following milestones are achieved during this research:

- In-depth understanding and characterization of capillary phenomenon to design optimal fin geometries,
- Development of an analytical model that includes all pertinent geometrical and operational parameters as well as thermophysical properties that can accurately predict the heat removal capacity of a CALPE,
- Experimental validation of the analytical models to predict the novel CALPE's performance,
- Design and fabrication of a novel CALPE using 3D-printing to provide a proof-of-concept demonstration.

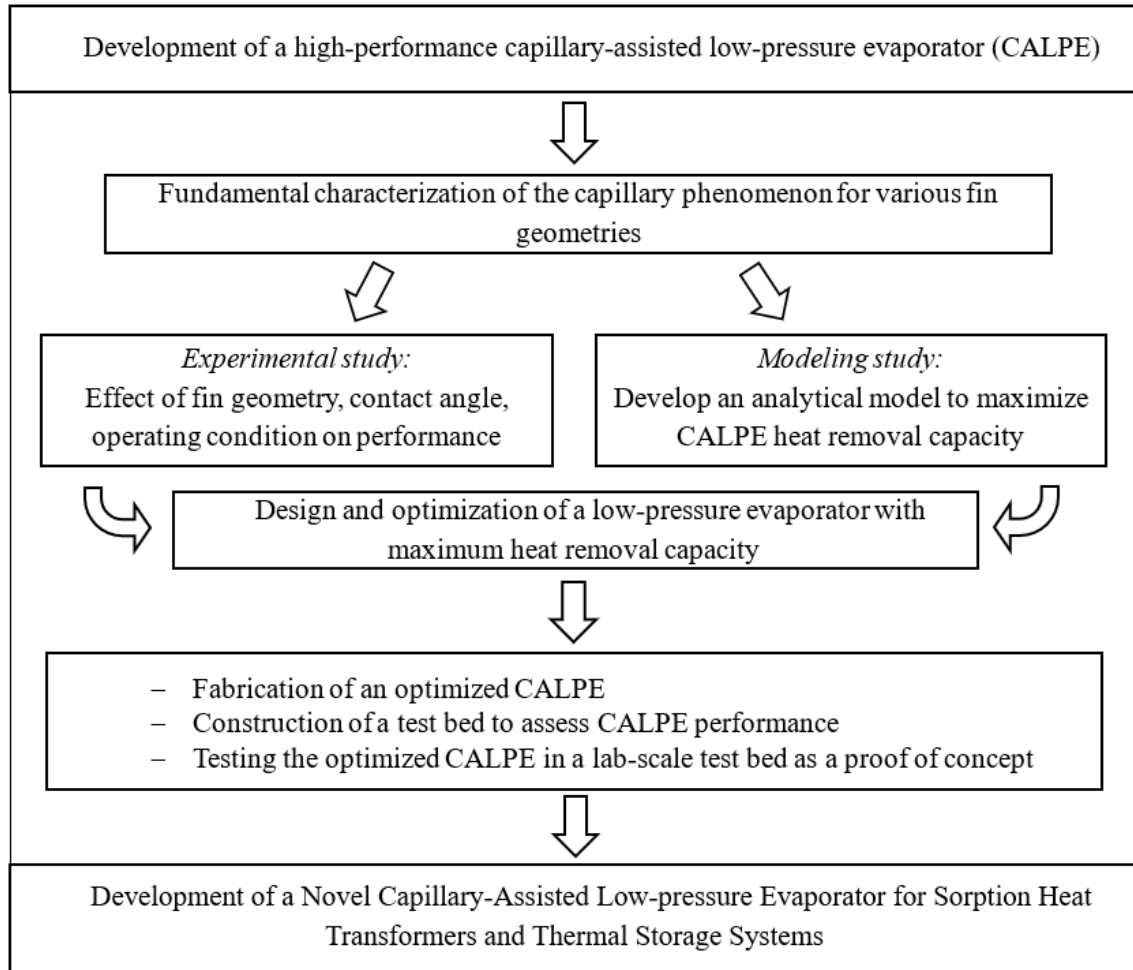
Research roadmap and contributions

A roadmap for accomplishing the research milestones is shown in the following figure. The contributions of this PhD program can be summarized as:

1. **Fundamental characterization of the capillary mechanism to determine optimal fin geometries:** A new analytical model is developed to determine the effect of surface roughness, surface tension, viscosity, contact angle, and fin geometries (height, spacing, depth, and angle with respect to gravity) to maximize the capillary action. An efficient fin design for the CALPE provides the highest height of the liquid refrigerant between the fins which is prerequisite for increasing the largest heat transfer area.
2. **Experimental validation of capillary rise models:** Capillary height in various fin geometries and built from several materials are measured

and compared with the proposed analytical model. Contact angle of the samples are measured and used in the analytical model to predict the capillary height.

3. **Optimization of fin geometry with respect to heat transfer.** A new model is developed to minimize the heat transfer resistance between the evaporation site and the bottom of the fin for various fin geometries. This model is used to determine the optimal geometry of a CALPE fin with respect to its heat transfer performance and in terms of heat removal capacity.
4. **Experimental study of CALPE and comparison of geometries.** 3D-printed CALPEs and an experimental testbed are custom-built to determine the effects of operating conditions (e.g., evaporation temperature) as well as geometrical parameters (e.g., fin geometry, cross-sectional area, etc.) on CALPE's performance.



The scope and roadmap of the present research project.

Scholarly contributions

- G. B. Abadi and Majid Bahrami, "The effect of surface roughness on capillary rise in micro-grooves", Nature Scientific Reports
- C. Chhokar, G. B. Abadi, M. Bahrami, "A new analytical model for the conduction shape factor of annulus sectors", International Journal of Heat and Mass Transfer, 196, 123304, 2022
- G. B. Abadi and Majid Bahrami, "A general form of capillary rise equation in micro-grooves", Nature Scientific Reports, (2020), 10, 19709
- G. B. Abadi and Majid Bahrami, "Combined Evaporator and Condenser for Sorption Cooling Systems: A Steady-state Performance Analysis", Energy, Volume 209
- C. Chhokar, G. B. Abadi, N. McDaniel, C. Botting, Majid Bahrami, "Naturally-Cooled Heat Sinks for Next-Generation Battery Chargers", ASME InterPACK 2022
- C. Chhokar, G. B. Abadi, Majid Bahrami, "A Simple Analytical Design Tool for the Conduction Shape Factor of Conventionally Mounted Heat Spreaders and Sinks", ASME InterPACK 2022
- G. B. Abadi, M. Bahrami, "Performance analysis of a combined evaporator condenser for sorption cycles" The Fifth International Symposium on Innovative Materials and Processes in Energy Systems, IMPRES2019 20th - 23rd October 2019, Kanazawa, Japan
- G. B. Abadi, M. Bahrami, "Capillary assisted low pressure combined evaporator and condenser" 5th IEA Experts Meetings, University of Ottawa, May 1-3, 2019
- M. Bollwein, H. Bahrehmand, G. B. Abadi, and M. Bahrami, "Integration of sorption cooling systems in PEM fuel cell buses", 5th IEA Experts Meetings, University of Ottawa
- G. B. Abadi and Majid Bahrami, "A 3D-printed capillary-assisted low-pressure evaporator, CALPE, for sorption systems cooling and heat pumps", TU Berlin August 22nd to 25th ISHPC 2021

Chapter 1.

Introduction

The air conditioning and refrigeration industry is dominated by vapor compression refrigeration technology that is mechanically and/or electrically driven, which is produced mainly from burning fossil fuels. Approximately 15% of the electricity produced globally is used by air conditioning units [1–3]. A significant portion of the global greenhouse gas emission is directly linked to this energy consumption and air conditioning units. Although newly invented hydrofluorocarbons as refrigerants are ozone-friendly, they have a high global warming potential. Utilizing water as a refrigerant addresses one aspect of ongoing climate crisis. Water is environmentally friendly and has no toxicity. It is an ideal substitute for systems using low-grade heat with a temperature below 100°C. Such heat sources are available through solar panels, geothermal, and industrial waste-heat [4]. Space cooling is growing rapidly as a source of energy expenditure. The demand for space cooling is increasing exponentially as the temperature of our planet continues to rise and summers are hotter than before. Since most of the space cooling is done through vapor compression refrigeration, this adds a significant amount of electricity usage, and further adds greenhouse gas emissions [5]. In British Columbia, the percentage of houses with some form of air conditioning or heat pump has increased more than 400 % during the past two decades, as shown in Figure 1 [6]. Globally, it is seen that in developing countries, there is a significant increase in houses with air conditioning. In the last 15 years, number of homes with air conditioning have tripled in the developing world. This trend is expected to continue with global warming and the continuing need for space cooling [7]. This fact is demonstrated in Figure 2.

In internal combustion vehicles, air conditioning increases the fuel consumption by up to 20% because of the extra load on the engine while up to 70% of total fuel energy is wasted to the ambient [8,9]. This waste heat can be used to run sorption heat transformers to produce cooling, increasing the overall vehicle efficiency. The waste heat potential is significant when considering there are more than 35 million motor vehicles registered in Canada. In 2020, the gross sale of motor vehicle fuel, gasoline, amounted to 38.6 billion liters [10]. Although the electric vehicles are on the rise, the gas consuming vehicles stay dominant. In an internal combustion engine or fuel cell powered vehicle, a portion of the

waste heat can be used to run a sorption cooling. Figure 3 provides a schematic of the energy break-down of a typical fuel cell-powered bus. Figure 4 shows the integration of a sorption cooling system in a fuel cell bus and the potential of utilizing its waste heat [11].

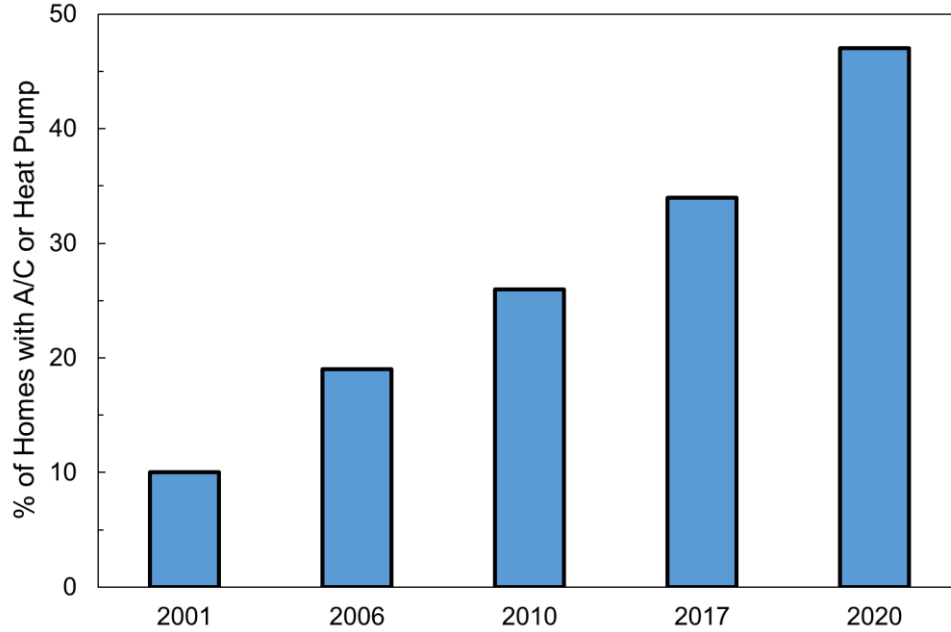


Figure 1. Percentage of houses in British Columbia with air conditioning or heat pump units. The air conditioning usage has increased by more than 400 % in a span of two decades [6].

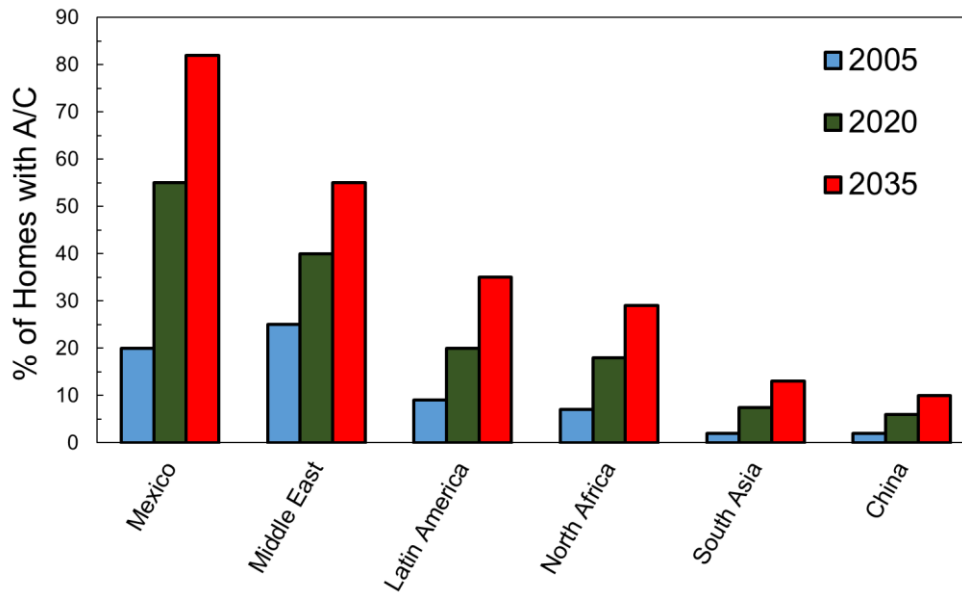


Figure 2. Percentage of houses in developing countries with air conditioning units. The air conditioning usage has increased by more than 200 % in a span of less than two decades [7].

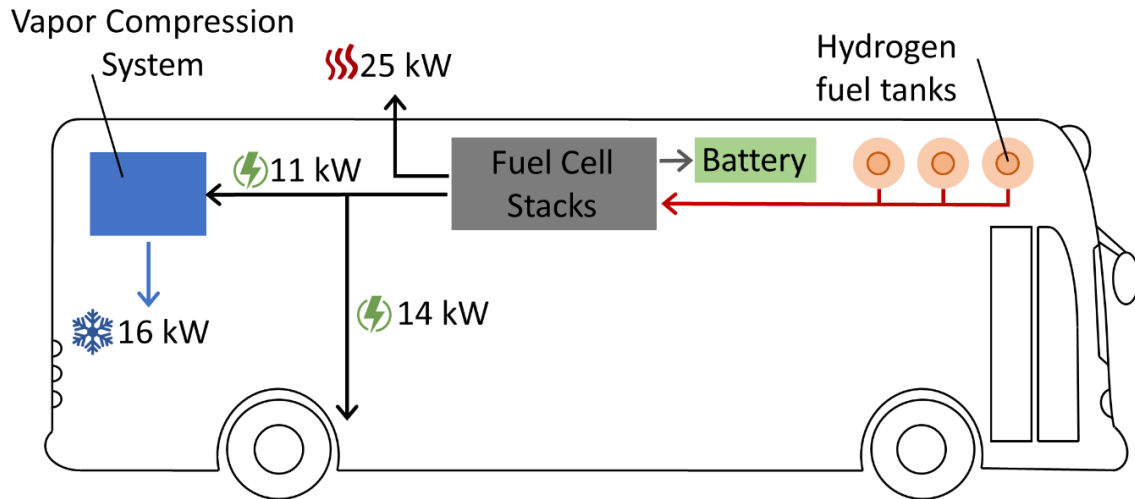


Figure 3. Energy break-down of a typical fuel cell-driven bus. About half of the energy produced by a fuel cell is wasted to the ambient in a fuel cell bus [11].

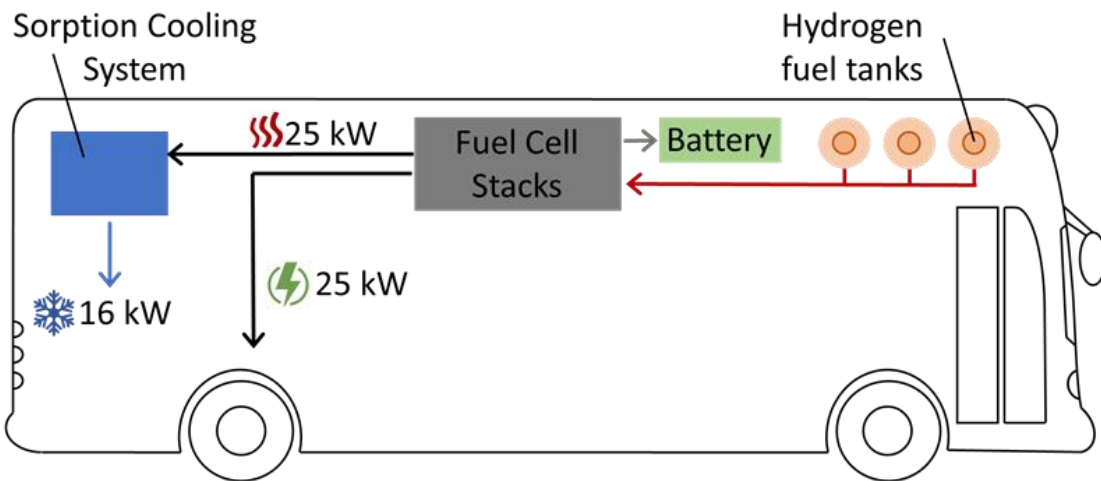


Figure 4. Integration of sorption heat transformers in a PEM fuel cell bus. The waste heat of a fuel cell can be used to power a sorption cooling device [11].

Sorption cooling system is an alternative technology that can utilize low-grade waste heat (sources with temperatures lower than 100 °C), that is readily available from internal combustion engines, fuel cells, solar thermal panels, and geothermal sources, to produce cooling power. A sorption heat transformer is comprised of a sorption bed, an evaporator, and a condenser, assembled inside sealed chambers [12]. Sorption heat transformers have no harmful materials, no moving parts, and need negligible electrical power compared to vapor compression refrigeration. It also eliminates the need for hydrofluorocarbons and provides a platform, as water can be used as the refrigerant,

further addressing climate change and promoting the phase-out of hydrofluorocarbons [13].

However, the commercialization of sorption heat transformers faces major challenges, including: i) a low operating pressure, as the saturation pressure for water at 5-20 °C is between 0.87 to 2.34 kPa [14], leading to major sealing and associated maintenance and cost issues; ii) a low heat removal capacity due to poor heat (and/or mass) transfer; iii) the low performance of the currently available low-pressure evaporators; and iv) a low coefficient of performance compared to that of vapor compression refrigeration. These, in turn, make the current sorption heat transformers bulky and heavy, and expensive. To address these issues, heat/mass exchangers need to be specifically designed and optimized for sorption heat transformers. A potential solution to address these issues is to use a capillary-assisted low-pressure evaporator (CALPE), to reduce weight, complexity, and cost. More importantly, adequate vapor generation in CALPE is crucial to achieve maximum capacity of the sorption process in sorber beds.

1.1. State of the art

Although vapor compression refrigeration technology is the dominant technology in the industry, residential, and automotive sectors, the alternative methods are more environmentally friendly. An alternative cooling technology, sorption cooling, is discussed below and compared to vapor compression refrigeration.

1.1.1. Vapor compression refrigeration systems

Figure 5 depicts a schematic for a vapor compression refrigeration, vapor compression refrigeration. This 4-component cycle has a compressor, an evaporator, an expansion valve, and a condenser. A liquid refrigerant is used as a heat transfer medium. Refrigerant in vapor state enters the compressor and is compressed to a higher-pressure level. High-pressure superheated vapor enters the condenser and undergoes phase-change. The heat addition happens in the evaporator. Subcooled liquid refrigerant then exits the condenser, passes through the expansion valve, and loses its pressure in a sudden adiabatic event. Part of the refrigerant is vaporized in this process. The mixture of

vapor and liquid enters the evaporator where the heat addition to the cycle happens. The vapor exits the evaporator, and the cycle completes.

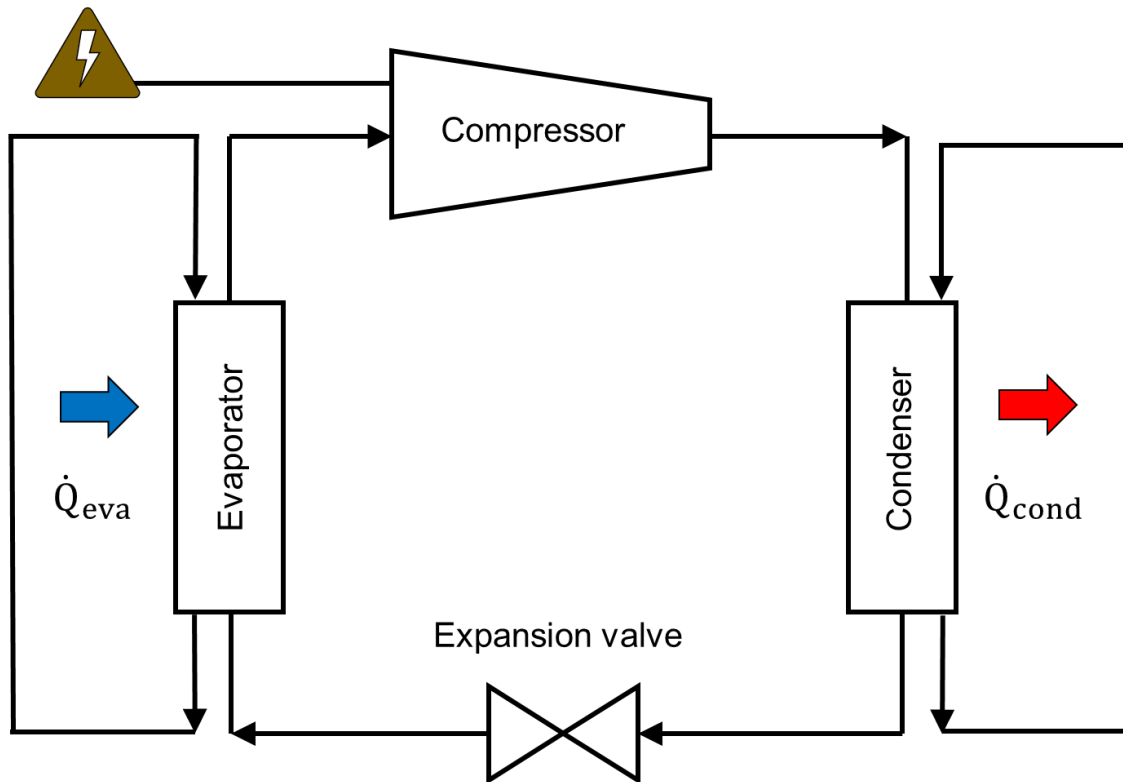


Figure 5. A schematic of a vapor refrigeration compression. A vapor compression refrigeration works between two temperature points whereas sorption heat transformers works between three temperatures.

1.1.2. Sorption heat transformers

Figure 6 demonstrates a typical sorption cooling system. In sorption cooling, the refrigerant, water in the present study, is adsorbed onto a solid adsorbent material such as silica gel or zeolite in an exothermic process. The refrigerant is desorbed when heated. Sorption cooling cycles have four main components: a sorber bed, a condenser, an expansion valve, and an evaporator. The cycle shown here works intermittently between adsorption and desorption processes [12]. Having two sorber beds makes it possible to run a continuous cycle by properly timing one bed to adsorb the refrigerant while the other one is desorbing. Table 1 compares the advantages and disadvantages of vapor

compression refrigeration vs sorption heat transformer technologies [13]. An adsorption refrigeration cycle eliminates the need for hydrofluorocarbons and provides a platform on which water can be used as refrigerant, further addressing the climate change, and promoting phase-out of hydrofluorocarbons.

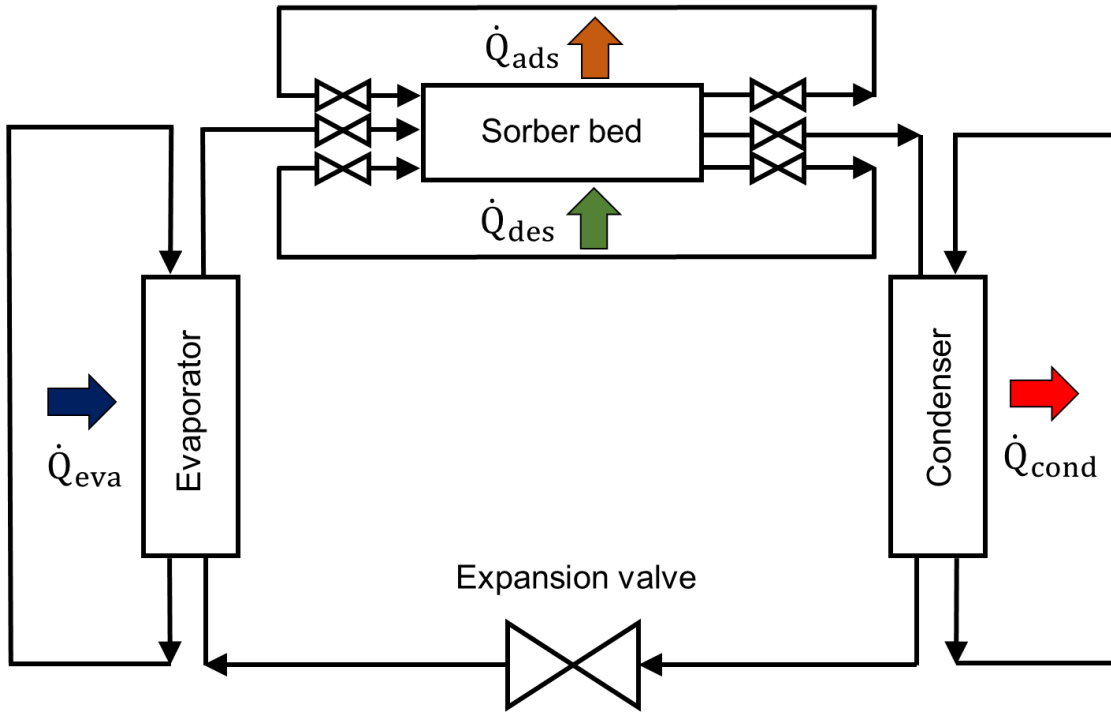


Figure 6. A schematic of a sorption heat transformer. A sorption heat transformer works between three temperature points whereas vapor compression refrigeration works between two temperatures.

Table 1. Advantages and disadvantages of sorption heat transformer vs vapor compression refrigeration

Technology	Advantages	Disadvantages
Vapor compression refrigeration	High specific cooling power High coefficient of performance	Electricity consumption Environmental impact Needs high quality energy (high exergy)
Sorption heat transformer	No electricity consumption No hydrofluorocarbon refrigerant No moving parts No vibration Can use low quality energy	High vacuum (low-pressure refrigerant) Low specific cooling capacity Low coefficient of performance Larger in size

In vapor compression refrigeration, coefficient of performance is defined as the ratio of cooling power to the input power for cooling, and the ratio of heating power (cooling

power plus input power) to the input power for heating applications. For sorption heat transformers, coefficient of performance is defined as the ratio of evaporator power to desorption power for cooling applications. The main advantage for sorption systems is the quality of input energy, i.e., low exergy waste heat, as opposed to high exergy mechanical or electrical input energy needed for vapor compression refrigeration.

1.2. Low-pressure evaporation

Flooded evaporators perform by submerging an evaporator in a pool of water. However, the performance of a flooded evaporator is severely reduced when working under low pressure conditions. Figure 7 shows the saturation pressure versus saturation temperature of water as a refrigerant. At low pressure conditions, a small increase in pressure increases the saturation temperature greatly. For example, as shown in Figure 7, the saturation temperature of water jumps from 0 to 20 °C when the pressure increases for only a couple of kPa. Therefore, when a liquid water column exists, as in a flooded evaporator, the hydrostatic pressure is significant. A flooded evaporator at 1.0 kPa, for example, experiences this additional hydrostatic pressure with increase in the saturation temperature across the column of liquid water. This variation in saturation temperature adversely affects the evaporator and reduces its performance. Therefore, low-pressure evaporators should be specifically designed for vacuum applications with optimized heat transfer.

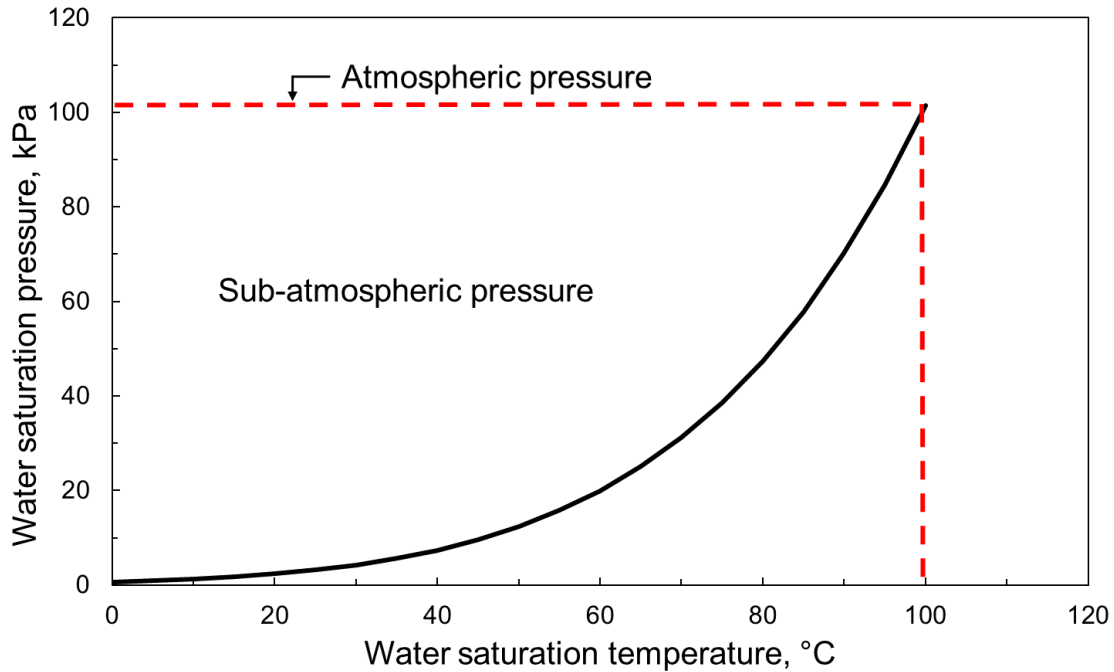


Figure 7. Saturation pressure versus saturation temperature of water as a refrigerant. At low-pressure conditions, a small increase in pressure increases the saturation temperature greatly.

1.2.1. Falling film evaporator

Low-pressure evaporation in a sorption heat transformer is possible through two enhancement technologies: falling film evaporation and capillary-assisted evaporation. Recent studies have classified, studied, experimented, and provided mathematical models for falling film evaporation [15–18]. Figure 8 shows the schematic of a typical falling film evaporation system. This type of evaporator is a heat exchanger in which the cold heat transfer fluid is sprayed on the surface of a hot tube that can have an enhanced surface or be as simple as a plain tube. Enhanced tubes are tubes with fins or patterns on their other surface to produce high surface area as compared to a plain tube. Although falling film evaporators have large heat transfer coefficients, they come with challenges. The uniformity of refrigerant distribution on the surface of the evaporator should be guaranteed. Moreover, the additional power needed pumping and circulator the refrigerant adds to the overall power consumption. Also, the spraying equipment adds complexity to the system. These challenges make this design undesirable for many applications, including sorption cooling on board a moving vehicle.

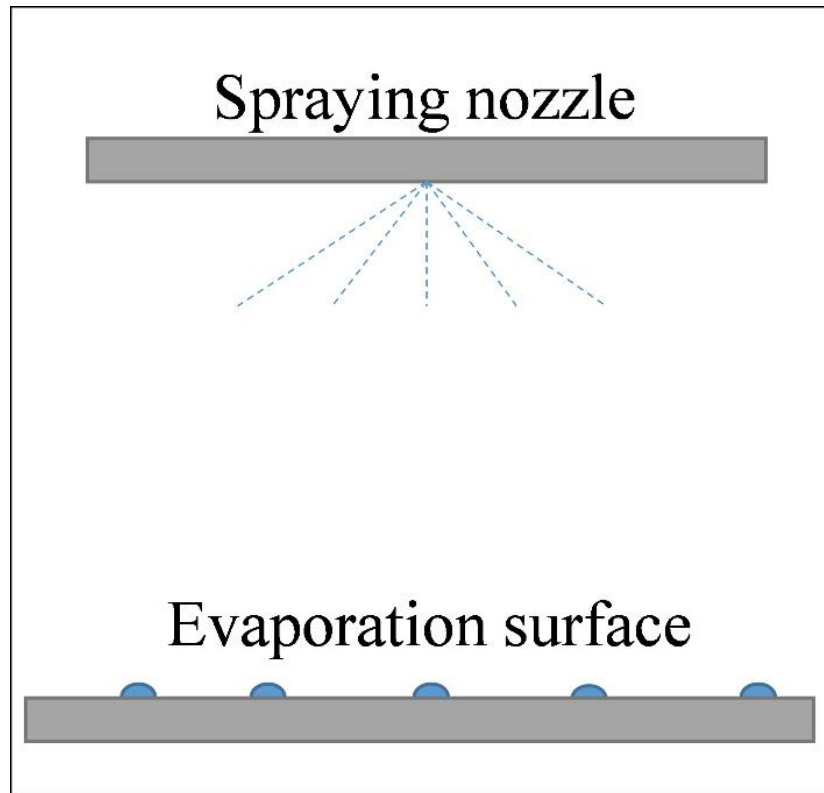


Figure 8. An overview of a falling film evaporator. Additional pumping power is required to spray the refrigerant on the evaporation surface.

1.2.2. Capillary-assisted evaporation

A capillary-assisted evaporator removes the need for a pumping system. Figure 9 demonstrates the basic concept of a capillary evaporator. As shown in Figure 9, the fins on the outer surface of a wall pull the refrigerant up due to their surface energy. The evaporation happens along this upward movement. The heat transfer fluid flows inside the internal channels. This design removes the need for a pump with parasitic energy consumption as in falling film evaporators. Figure 9 also shows the thermal resistance network of a CALPE. For reference, the internal convection thermal resistance of a CALPE made of off-the-shelf tubes accounts for up to 91% of total thermal resistance, while the conduction and fin side convection resistances make up 5 and 4% of its total resistance, respectively [12]. However, this major bottleneck shifts to the bulk and external resistance when micro-channels are used for the heat transfer fluid side.

A CALPE takes advantage of the capillary effect. There are several experimental, numerical, and analytical studies published in the literature on the topic and summarized

in Table 2. Sabir et al. [19] presented their experimental results on the effect of a porous layer on the thermal performance of their water evaporators. They were able to achieve boiling heat transfer coefficients of up to $5 \text{ kW/m}^2 \text{ }^\circ\text{C}$. They proposed an analytical model and reported it was in good agreement with their model and experimental findings in Ref. [20]. Xia et al. [21,22] considered a series of enhanced heat transfer tubes featuring circumferential rectangular micro-grooves for experimental investigation. The refrigerant height inside the liquid pool, evaporation pressure, and degree of superheat were deemed influential. They concluded that the evaporation heat transfer coefficient, and evaporation pressure has a positive correlation, while the relation between heat transfer coefficient and superheat degree and refrigerant height is negative. They also provided an analytical model in a later study [22]. The idea of using capillary forces originates in designing heat pipes and is focused on micro-scale designs, however, recent attempts have been done to utilize this technology for macro-scale evaporators, especially in adsorption cooling devices. Recently, the use of CALPEs for larger scale evaporators in adsorption cooling have been reported in [4,23–28]. Thimmaiah et al. [24] studied the performance of a CALPE for a sorption heat transformer using water as the refrigerant and reported that the capillary-assisted tubes provide 1.6–2.2 times higher heat transfer coefficient compared to a plain tube with the same diameter. Similar data was published in [23].

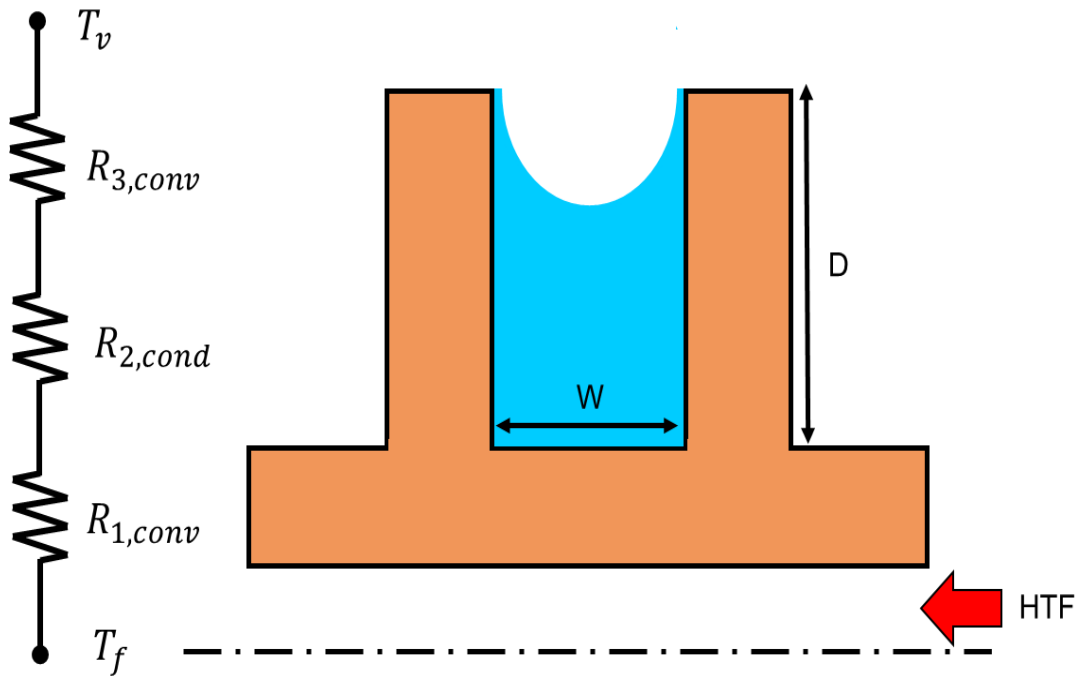
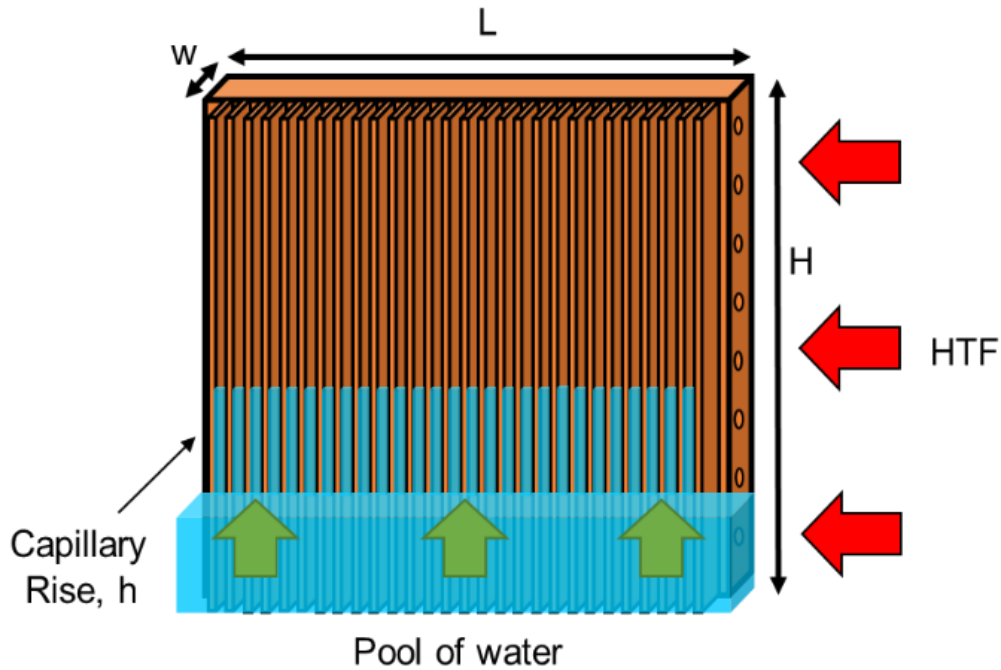


Figure 9. An overview of a capillary-assisted evaporator and its thermal resistance network – w , L , and H are the width, length, and height of the evaporator, respectively. h is the capillary height. W and D are the fin cross-section width and depth. R_1 , R_2 , and R_3 are the single-phase, conduction, and evaporation thermal resistances, respectively.

Table 2. Summary of published studies on capillary-assisted low-pressure evaporators (CALPE) – all with water as refrigerant and copper tubes

Reference	Power (W)	P (kPa)	Coating	UA (W/K)	Notes
Thimmaiah et al. [24]	400	<1	coated /uncoated	46	Tested five different enhanced tubes and compared with plain tubes.
Lanzerath et al. [25]	600	1-2	coated /uncoated	56	Tested coated and uncoated plain and finned tubes.
Xia et al. [22]	450	~ 1	uncoated	63	Compared falling film to capillary assisted evaporators.
Sabir et al. [19]	1600	1.5	coated	-	Examined the effect of porous coating on capillary evaporation. Area not given but HTC of up to 5kW/m ² reported.
Schnabel et al. [27]	1200	1-2	uncoated	~100	Evaporation capacity of different tubes and flooding modes reported. UA value for LMTD of 3 K.

Figure 10 takes a closer look at one fin of a CALPE. Three main heat transfer mechanisms are identified for a CALPE. The main heat transfer mechanism of CALPE, thin film evaporation, has a high heat flux (~MW/m²), but only takes place on a small area of the fin (~ μm). The liquid thickness inside the meniscus is thicker and prevents thin film evaporation. It is evident that increasing the area on which thin film evaporation happens will result in an increase in the overall heat removal capacity if the internal resistance is not limiting the heat transfer. Therefore, a compact and high-performance CALPE should aim to increase the external heat transfer area by an optimization scheme based on geometry parameters.

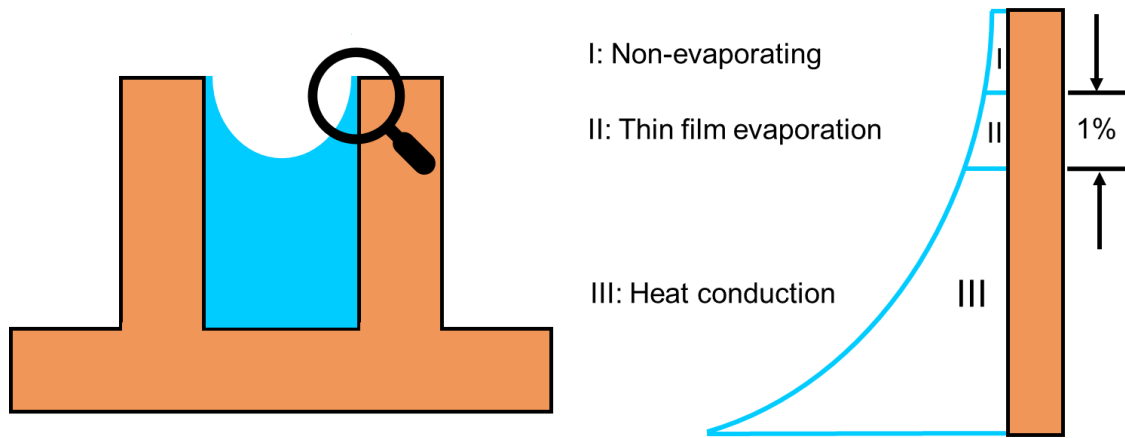


Figure 10. An overview of heat transfer mechanisms in a CALPE. The thin film evaporation, though having the highest heat flux ($\sim \text{MW}/\text{m}^2$), takes place on less than 1% of fins' area.

1.3. Objective

Figure 11 provides an overview and a comparison of experimental CALPEs, at the same operating conditions, published in the literature. It is evident from this review that there exists a gap in the literature regarding the design of CALPE. Currently, adsorption chillers cost $\sim \$900$ per kWh. First and foremost, off-the shelf evaporator tubes are not specifically designed and optimized for sorption heat transformers, therefore. They exhibit poor thermal performance under low-pressure conditions. Second, the effect of fin geometry is not explored on a fundamental level, i.e., it is not clear what geometry is the most optimal when it comes to CALPE fin design. The heat removal capacity of the off-the-shelf tubes, even when coated, is rather low. 3D-printing, a promising solution, is costly, and corrosion is present in all metallic evaporators.

The objective of this PhD study is to provide a methodology with which it is possible to design and optimize capillary-assisted low-pressure evaporators for sorption systems. This method is then applied to develop a CALPE with optimal thermal performance which can pave the way for widespread adoption of sorption heat transformers in A/C applications. The methodology of this PhD thesis can also be applied to other sorption applications, such as heat pumps, heat transformers, heat storage, dehumidification, desalination, and gas separation. This PhD program aims to address this gap by studying CALPEs on a fundamental level, and by modeling, designing, and building a novel CALPE as a proof-of-concept to be integrated in sorption heat transformers. To this end, a novel

analytical model that unifies the capillary rise equations for various fin geometries is proposed, validated, and used to design a new heat exchanger. Further modeling provides insight into the heat transfer of CALPE. This novel CALPE is custom-built and 3D-printed from stainless steel to increase its heat removal capacity and tackle the corrosion.

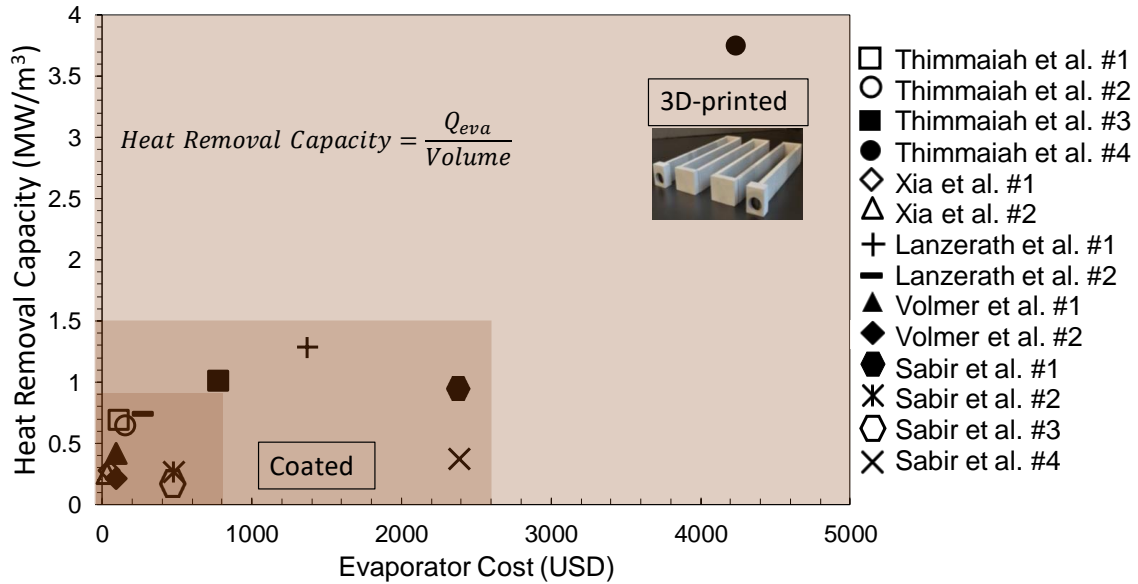


Figure 11. A summary of heat removal capacity of CALPEs available in the literature. The shaded area from darker to lighter denotes the: off-the-shelf tubes, coated off-the-shelf tubes, and 3D-printed CALPEs. The cost values are expected to significantly reduce when the designed CALPE is mass produced.

1.4. Thesis structure

This PhD dissertation is comprised of five chapters and six appendices organized as follows:

Chapter 1: Introduction

This chapter introduces and outlines the motivation for the research and reviews two cooling technologies for air conditioning, A/C, and refrigeration. It was discussed that vapor compression refrigeration is currently the dominant technology used by the industry due to its high performance, compactness, and low cost. However, it was also discussed that vapor compression refrigeration systems have significant greenhouse gas emissions. An alternative, sorption heat transformers, was discussed and its potential due to its

environmentally friendliness by utilization of waste heat was demonstrated. This chapter also introduces in brief two methods of achieving high-performance low-pressure evaporation. It was shown that falling film evaporators, while having high performance, add complexity and extra pumping work to the system. Alternatively, capillary-assisted evaporators do not need an additional pumping system for the refrigerant. This chapter also reviews the literature and summarizes developed technologies in capillary-assisted low-pressure evaporators.

Chapter 2: A general form of capillary rise equation in micro-grooves

This chapter discusses a closed form unified model to find the best geometry among available fin designs that maximizes the active heat transfer area per wall surface area, volume, and weight. This model fundamentally characterizes the capillary phenomenon. This is not only beneficial for designing CALPEs, but also any micro-groove can be defined by this approach. Although the capillary action is well studied, all the available equations for the capillary rise are case-specific and depend on the geometry of the groove, surface properties, and the transport liquid. This unified non-dimensional model for capillary rise can accurately predict the capillary rise for any given groove geometry and condition and only depends on two parameters: contact angle and characteristic length scale, defined as the ratio of the liquid-vapor to the solid-liquid interface.

Chapter 3: Effect of surface roughness and Experimental validation of capillary height

In this chapter, the model proposed in chapter 2 is extended to include the effect of surface roughness. A new characteristic length scale is proposed that includes salient geometrical parameters, such as micro-grooves height, width, and surface roughness. Furthermore, it is shown that by using the proposed characteristic length scale, it can be determined whether the capillary action would occur in each micro-groove and liquid. The model is also compared against experimental data collected at the Laboratory for Alternative Energy Conversion. The model captures the experimental results with less than 10% relative difference.

Chapter 4: Heat transfer mechanisms of CALPE and governing equations

This chapter discusses the effect fin geometry on heat transfer. Different heat transfer mechanisms of CALPE, natural convection, two-dimensional conductive heat transfer, and thin film evaporation, are explained in detail and the governing equations are presented. Comparison is made between the mechanisms of heat transfer for rectangular and triangular grooves. A new model is developed to minimize the heat transfer resistance between the evaporation site and the bottom of the fin for various fin geometries. This model is used to determine the optimal geometry of a CALPE fin with respect to its heat transfer performance and in terms of heat removal capacity.

Chapter 5: Experimental validation of heat transfer models

Chapter 5 presents an experimental study of CALPE and comparison of geometries. 3D-printed CALPEs and an experimental testbed is custom-built to determine the effects of operating conditions (e.g., evaporation temperature) as well as geometrical parameters (e.g., fin geometry, and cross-sectional area) on CALPE's performance.

Chapter 6: Future work and recommendations

This chapter outlines the future work that can be performed based on the findings of this thesis. General recommendations are given to continue this work, or to use the thesis in practical applications.

Appendix I: Capillary rise equation for different cross sections

In this appendix, detailed equations of capillary height for each geometry are derived and shown. For each geometry, the characteristic length scale and the capillary height equation can be determined.

Appendix II: Non-dimensional capillary rise equation for different cross-sections

This appendix extends the capillary height equations to non-dimensional unified closed form model for capillary rise and shows how all geometries can be defined by Eq. (6).

Appendix III: Force balance in a capillary groove

Appendix III provides a force balance diagram and shows the relationship between forces affecting the liquid meniscus in a capillary groove.

Appendix IV: Fin resistance

In this appendix, equations to calculate the fin resistance, internal convective heat transfer resistance, external convective heat transfer resistance, and conductive heat transfer resistance are derived.

Appendix V: Uncertainty analysis

Appendix V discusses the uncertainty of experiments and derives equations for each source of uncertainty in the experiments.

Appendix VI: Data analysis

This appendix discusses the data reduction and analysis procedure and shows how measured data such as temperature, pressure and flow rate are turned into performance metrics, such as heat removal capacity.

Appendix VII: Genetic algorithm optimization

Appendix VII provides a short summary of a genetic algorithm optimization scheme. Such optimization methods were taken to find the best geometry and configuration of CALPE's fins, maximizing the heat transfer rate. Results are given in a table of best possible candidate for geometrical parameters.

Appendix VIII: Momentum conservation model

A detailed approach in solving the thin film heat transfer model through a momentum conservation method is presented. An order of magnitude analysis is performed to simplify the governing equations. Non-dimensional parameters are introduced and used to non-dimensionalize the governing equations. An integral method is used to solve the equations of heat transfer and fluid flow.

Appendix IX: Results for thin film evaporation in an extended meniscus

This appendix presents more detailed results of thin film evaporation in an extended meniscus. Plots of meniscus profile, curvature, mass flux, and heat flux are given versus the meniscus position.

Appendix X: Experimental setup and equipment list

This appendix presents a more detailed experimental diagram of CALPE heat transfer measurement along with a list of equipment used.

Chapter 2.

A general form of capillary rise equation in micro-grooves

As discussed in the last chapter, one of the main technical challenges curtailing the commercialization of sorption heat transformers is low heat removal capacity, leading to a bulky design. A compact and efficient CALPE addresses this issue by, i) having a large active heat transfer area (wet area) on the fin side; and ii) a low-thermal-resistance microchannel design on the heat transfer fluid side. This chapter discusses the first challenge. The goal is to find the best geometry among available fin designs that maximizes the active heat transfer area per wall surface area, volume, and weight. Therefore, there is a need to fundamentally characterize the capillary phenomenon. This is not only beneficial for designing CALPEs, but also any micro-groove can be defined by this approach.

Micro-grooves are a crucial feature in many applications, such as microelectro-mechanical systems (MEMS), drug delivery, heat pipes, sorption systems, and microfluidic devices. Micro-grooves utilize capillary action to deliver a liquid, with no need for an extra pumping device, which makes them unique and desirable for numerous systems. Although the capillary action is well studied, all the available equations for the capillary rise are case-specific and depend on the geometry of the groove, surface properties, and the transport liquid. In this study, a unified non-dimensional model for capillary rise is proposed that can accurately predict the capillary rise for any given groove geometry and condition and only depends on two parameters: contact angle and characteristic length scale, defined as the ratio of the liquid-vapor to the solid-liquid interface. The proposed model is compared against data from the literature and can capture the experimental results with less than 10% relative difference. The effect of the grooves' height, width, and contact angle is investigated and reported. This study can be used for a unified approach in designing heat pipes, capillary-assisted evaporators for sorption systems, drug delivery micro-fluidic devices, etc.

2.1. Introduction

The self-driving flow of a liquid in a capillary micro-groove is an important feat of engineering with a wide range of applications, from space applications due to microgravity to power electronics and heat pipes, to sorption technology and capillary-assisted evaporators.

One main application of capillary action in micro-grooves is in heat pipes. These two-phase heat transfer devices are a crucial part of any modern power electronic device. In fact, the capillary rise is one of the important factors in designing heat pipes. Hopkins et al. [29] experimented with flat miniature heat pipes to determine the maximum heat flow rate and heat flux for different operating temperatures. They concluded that heat pipes with deep and narrow capillary grooves produce the best results while most of their data showed that the heat flux bottleneck of the evaporator was the capillarity limitation. Ma and Peterson [30] performed a series of experiments to determine the heat transport in triangular grooves, similar to those used in heat pipes, purely based on the capillary rise limit. They reported the maximum capillary heat transport capacity and pure capillary limit of methanol flowing in triangular grooves. Another example of capillary limit in heat pipes is [31]. They concluded that a heat pipe's performance is greatly dominated by the capillary limit. They established a mathematical model of the capillary limit for a micro heat pipe with trapezium-grooved substrate.

Vapor chambers or flat heat pipes are of particular interest and are used extensively in electronic devices due to their reliability, simplicity, passive operational mode, and effective heat transport capacity [32]. They remove the need for active liquid-cooling while providing a high-performance heat removal capability. Weibel and Garimella [32] note that the high performance of heat pipes and vapor chambers depends on the capillary pressure generated by the wick material so that it can overcome the viscous and inertial pressure drops along the vapor and liquid flow paths.

A general understanding of flow in open micro-grooves and its limitation is available in the literature for different geometries. Zhang et al. [24] explored the mechanism of open channel capillary flow experimentally and numerically, with applications such as the refueling stations of the International Space Station (ISS). They calculated the critical flow rate and the height of fluid level using the Newton method.

Similarly, Haake et al. [33] investigated the liquid flow through open capillary grooves experimentally and numerically. They also concluded that there exists a capillary flow limit. Other notable works on capillary-driven flow in open grooves can be found in [34–40]. More recently, attention has been given to surface properties and its effect on capillary rise. Kim et al. [41] experimented on hydrophilic surfaces to observe the capillary rise dynamics within channels and concluded that the capillary rise is initially governed by the bulk rise.

In sorption cooling and heat pump technology, the main obstacle preventing commercialization is size and weight. Capillary-assisted low-pressure evaporators (CALPEs) are used in closed-cycle sorption systems, including heat pumps, heat transformers, desalination, and thermal energy storage systems [42]. A CALPE eliminates the need for a circulating pump in the low-pressure evaporator, taking advantage of the capillary phenomenon. After experimenting with a series of enhanced heat transfer tubes featuring circumferential rectangular micro-grooves, liquid height due to capillarity, evaporation pressure, and the degree of superheat were deemed the most important factors in heat transfer performance [22,42].

From this introduction, two points are concluded: i) the capillary action in micro-grooves have a wide range of application. In most of these applications, the capillary rise or the ability of the groove or a wicking material to transport the liquid is the design bottleneck; and ii) all the experimental, analytical, or numerical studies dealing with this topic are case-specific and can be applied to only a specific geometry or transport liquid and cannot be generalized. The objective of this paper is to provide an analytical solution to the capillary rise in micro-grooves by using a fundamental approach and to propose a unified equation. There is a desire to develop an analytical model that can predict the capillary rise in any groove with a given cross-section, since it removes extra calculation steps and unifies the capillary equation regardless of the cross-sectional area. It is understandable that there is a need for exploring the fundamentals of capillarity, capillary rise equations, and the important parameters affecting it to reach a unified approach. In this study, the capillary rise in micro-grooves with selected cross-sections (rectangular, cylindrical, curved, trapezoidal, triangular, and hyperellipse) is studied analytically, the relative importance of different parameters (contact angle, groove width, depth, etc.) is investigated, and then a novel, general, and non-dimensional equation is proposed.

2.2. The capillary rise equation for various cross-sections

Here, we start with a rectangular cross-section groove, list the assumptions, provide the governing equations, and make a conclusion on the capillary rise equation. Similar steps can be taken for other cross-sections. The results for all the studied cross-sections are summarised in Table 3 and the detailed step-by-step procedure is given in Appendix I. The assumptions are as follows:

- Surfaces are smooth and roughness is not considered,
- The open grooves' width is small enough for the capillary action to occur, but is not too small (length scale >10 nm), therefore nanoscale effects are negligible [43]
- Partial capillarity is not studied, and it is assumed that the full area of the grooves is filled with a liquid (e.g. water),
- The micro-groove is placed vertically (or with a slanted angle) so that the bottom end always touches a big fluid reservoir,
- The physical properties of all materials are constant,
- The vapor-liquid interface is homogenous, and
- Heat transfer is negligible since the capillary action is a fast, almost instantaneous process.

Considering these assumptions, and looking at Figure 12, the Young's equation can be written as follows [44–46]:

$$\sigma_{sv} = \sigma_{sl} + \sigma_{lv} \cos \theta \quad (1)$$

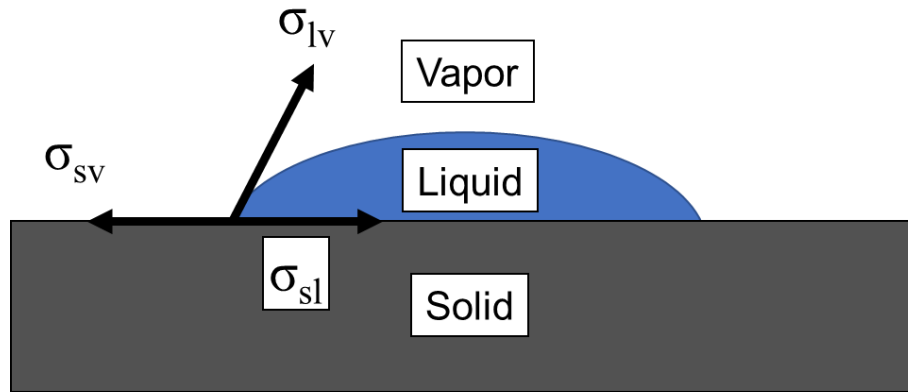


Figure 12. A schematic of a drop of a liquid on a flat surface showing three forces of surface tension leading to Young's equation under static equilibrium

Here, σ and θ are surface tension and contact angle, respectively. When a micro-groove with a rectangular cross-section is placed in a liquid as shown in Figure 13, the change in interface area of the liquid-vapor and solid-liquid are respectively:

$$dA_{lv} = Wdy \tag{2}$$

$$dA_{sl} = (2D+W)dy \tag{3}$$

Where, D is the groove depth and W is the groove width. Here, to further generalize the equations, a slanted column is considered that is tilted with the angle α . Therefore, in general form, the micro-groove is not vertical unless $\alpha=90$, as seen in Figure 13. Figure 14 shows more details of front and top view of the micro-groove, the surface tension vectors, and the direction of gravity.

Looking at Figure 14, the Helmholtz free energy between three interfaces can be written as [47], [48]:

$$dE = \sigma_{sv}dA_{sv} + \sigma_{sl}dA_{sl} + \sigma_{lv}dA_{lv} \tag{4}$$

The capillary force is given as “ $-dE/dy$ ”. It follows that:

$$F_c = -dE/dy = \sigma_w [(2D+W)\cos\theta - W] \quad (5)$$

The capillary force balances the gravity force that is exerted on the weight of the water column, resulting in the following capillary rise equation for a rectangular cross-section groove [47]:

$$h_{rec} = \frac{\sigma[(2D+W)\cos\theta - W]}{\rho g D W \sin\alpha} \quad (6)$$

Appendix I provides a detailed and step-by-step approach of how Eq. 6 is concluded. It also explores other cross-sectional areas and how the capillary rise equation resulted for them.

Following the same approach, the capillary rise equation can be derived for any cross-section. Table 3 lists the capillary rise equation for six cross-sections of rectangular [47], cylindrical [49], curved (modified form of [49]), trapezoidal, triangular, and general form of hyperellipse. The effect of groove's width, height, wetting perimeter (defined later), contact angle, and surface tension can be studied using Eq. 6.

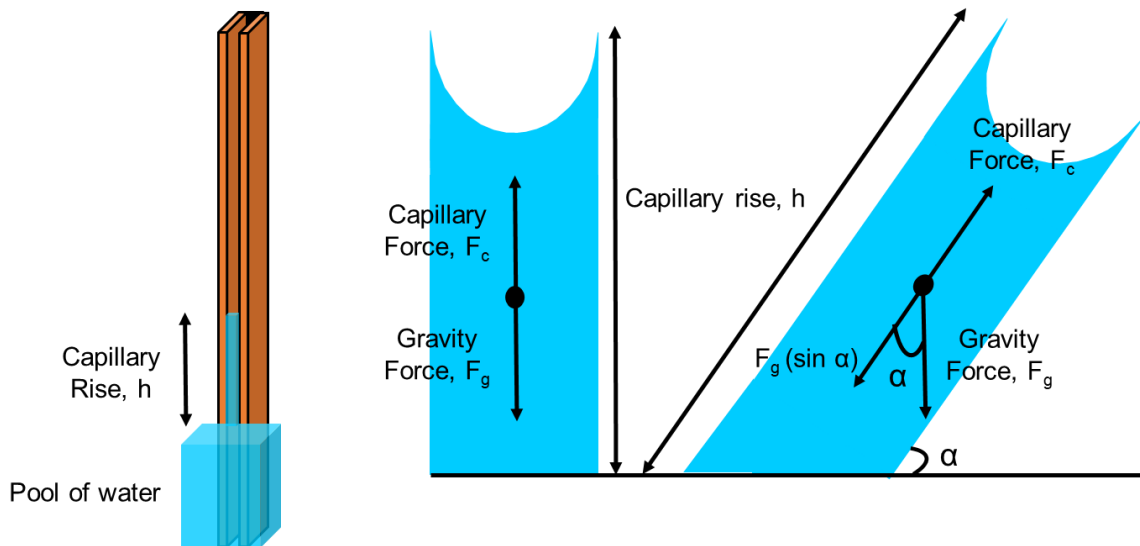


Figure 13. Force balance and inclination angle in a rectangular micro-groove

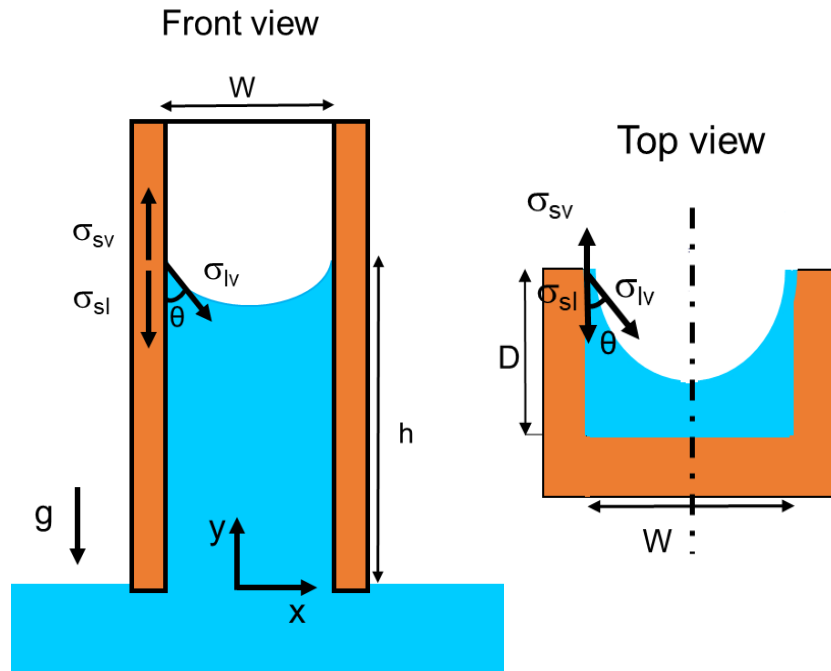
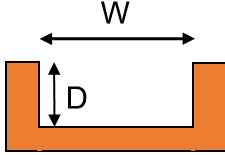
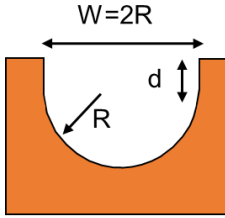
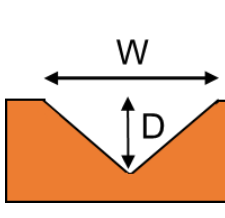
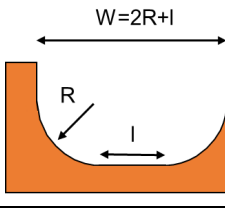
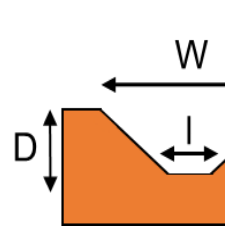
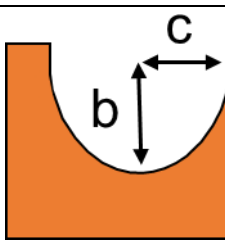


Figure 14. Top and front view of a rectangular micro-groove

Table 3. Capillary rise equation for various cross-sections

Capillary rise equation	Groove cross-section	Non-dimensional equation	Ref.
$h_{rec} = \frac{\sigma[(2D + W)\cos\theta - W]}{\rho g DW \text{Sin}\alpha}$ $P_w = 2D+W$ $A_c = D \times W$		$h_{rec}^* = \frac{\cos\theta}{\frac{W}{P_w}}$	[47]
$h_{cyl} = \frac{\sigma[(\pi R + 2d)\cos\theta - 2R]}{\rho g [2dR + \pi R^2/2] \text{Sin}\alpha}$ $P_w = \pi R + 2d$ $A_c = 2dR + \pi R^2/2$		$h_{cyl}^* = \frac{\cos\theta}{\frac{W}{P_w}}$	[49]
$h_{tri} = \frac{\sigma[2\cos\theta\sqrt{D^2 + \frac{W^2}{4}} - W]}{\rho g WD/2 \text{Sin}\alpha}$ $P_w = 2\sqrt{D^2 + \frac{W^2}{4}}$ $A_c = W \times D/2$		$h_{tri}^* = \frac{\cos\theta}{\frac{W}{P_w}}$	[50]
$h_{curv} = \frac{\sigma[(\pi R + 2d + l)\cos\theta - 2R - l]}{\rho g [2dR + dl + Rl + \pi R^2/2] \text{Sin}\alpha}$ $P_w = \pi R + 2d + l$ $A_c = 2dR + l(d + R) + \pi R^2/2$		$h_{curv}^* = \frac{\cos\theta}{\frac{W}{P_w}}$	[49]
$h_{trap} = \frac{\sigma[(l + 2\sqrt{D^2 + \frac{(W-l)^2}{4}})\cos\theta - W]}{\rho g (l + W)D/2 \text{Sin}\alpha}$ $P_w = l + 2\sqrt{D^2 + \frac{(W-l)^2}{4}}$ $A_c = (l + W) \times D/2$		$h_{trap}^* = \frac{\cos\theta}{\frac{W}{P_w}}$	-
$h_{ellip} = \frac{\sigma[(2bE(\sqrt{1 - \varepsilon^2}))\cos\theta - 2b\varepsilon]}{\rho g [\pi\varepsilon b^2/2] \text{Sin}\alpha}$ $P_w = 2bE(\sqrt{1 - \varepsilon^2})$ $A_c = \pi\varepsilon b^2/2$		$h_{ellip}^* = \frac{\cos\theta}{\frac{W}{P_w}}$	[51]

2.3. The unified non-dimensional capillary rise equation

An analytical model that can predict the capillary rise in any cross-section groove is highly desired since it removes extra steps and unifies all the equations in Appendix I. Eq. 6 can be non-dimensionalized by rearranging and introducing two parameters: P_w is the wetting perimeter and denotes the wetted length of the cross-section (excluding the liquid-vapor interface; in other words, the wetting perimeter is the solid-liquid interface length), and A_c is the cross-sectional area. For a rectangular cross-section, P_w and A_c are given as:

$$P_w = 2D + W \quad (7)$$

$$A_c = DW \quad (8)$$

For a rectangular cross-section, the non-dimensional capillary rise is:

$$h^* = \frac{\rho g h \sin \alpha}{\sigma} * \frac{A_c}{P_w} = \cos \theta - \frac{W}{P_w} \quad (9)$$

Where $\mathcal{L} = \frac{W}{P_w}$ is a characteristic length scale and is the ratio of the liquid-vapor interface to the wetting perimeter. Appendix II demonstrates the step-by-step procedure to non-dimensionalize Eq. 6 and conclude Eq. 9. Looking at the capillary rise equations in the Appendix I and using P_w , it is concluded that in fact all the Eqs. A.9, 18, 27, 36, 45, and 54 can be written similarly to Eq. 9. This fact is given in Table 3 where all the non-dimensional capillary rise equations are listed along with the cross-sectional area and wetting perimeter for each cross-section.

2.4. Results and discussion

The effect of the groove's width, height, wetting perimeter, contact angle, and surface tension can be all studied using Eq. 6. Although, most of the upcoming plots are for a rectangular groove, a similar approach and conclusions can be made for various cross-sections. Before plotting the non-dimensional parameters, the dimensional capillary rise is plotted for different cross-sections. Figure 15 shows the effect of depth and width on capillary height of a rectangular groove. It is concluded that the change in width of the groove has a greater effect on capillary height than the change in depth. Figure 16 presents a comparison between the capillary rise in a rectangular and triangular groove. It is seen that the capillary rise in a triangular groove is considerably higher than that in a rectangular cross-section. This fact is explained by the fact that a triangular groove contains half of the liquid as compared to a rectangular one, therefore, the capillary force is able to take the body of water higher. This fact can be used to increase the active (wetted) surface area on the fin side of a CALPE. Figure 17 compares the capillary rise in a rectangular groove with a curved groove.

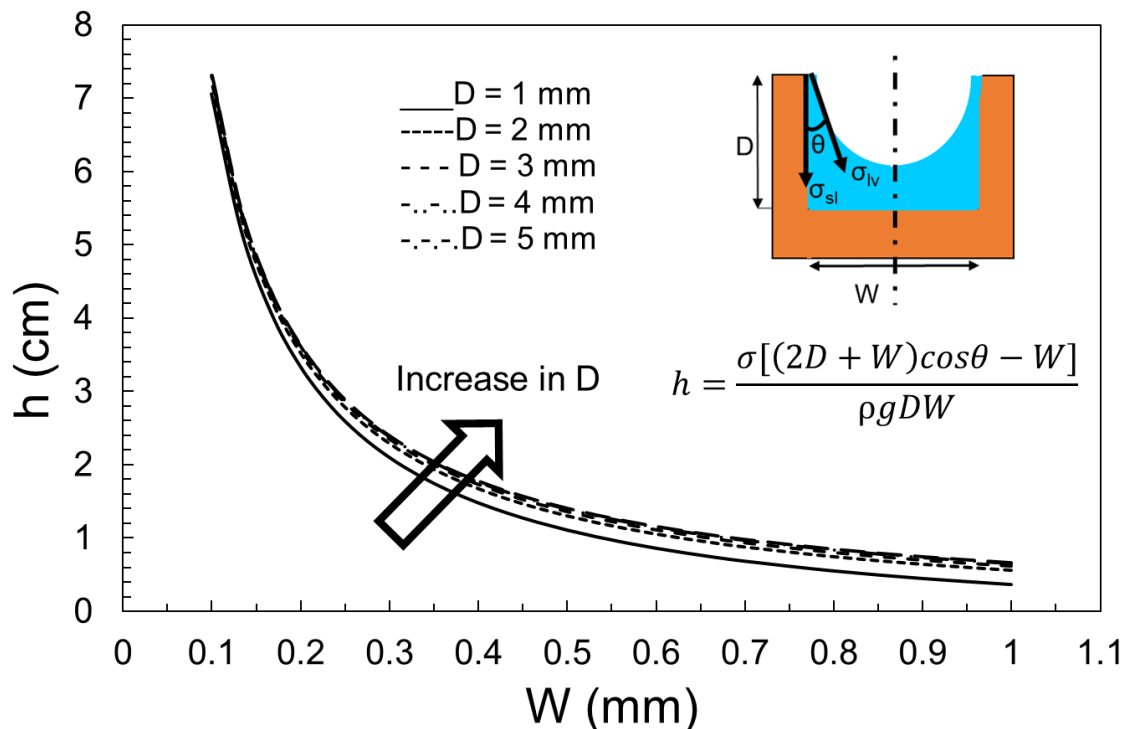


Figure 15. The effect of groove width and height on the capillary rise in a rectangular cross-section for $\alpha=90^\circ$

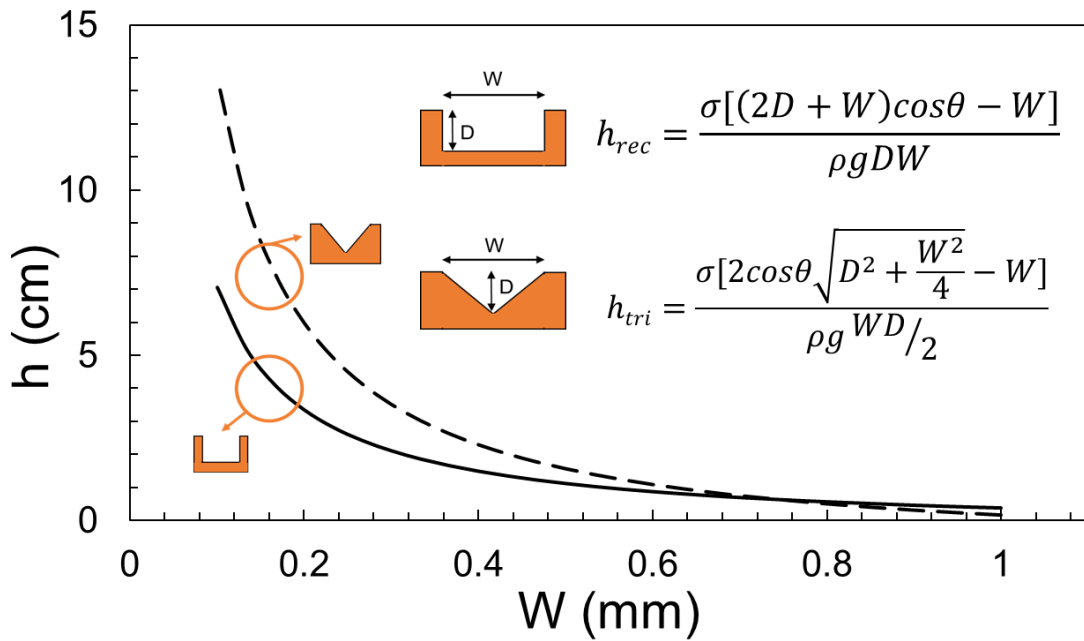


Figure 16. A comparison between the capillary rise in a rectangular and triangular cross-section groove, $D = 1 \text{ mm}$, and $\alpha = 90^\circ$

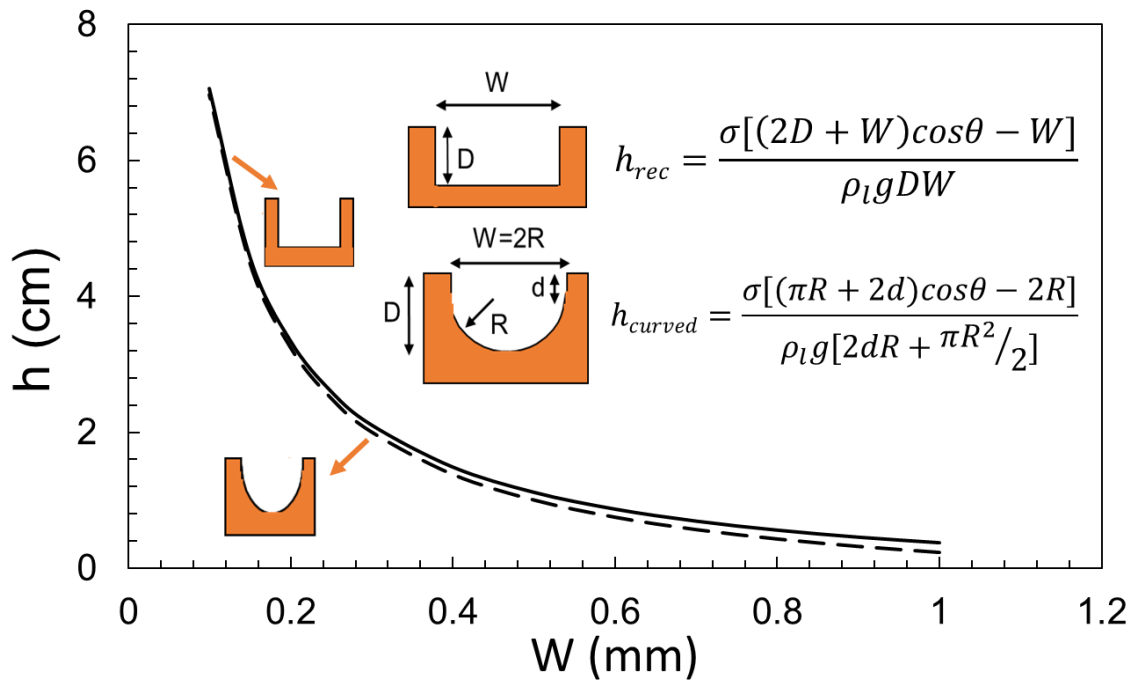


Figure 17. A comparison between the capillary rise in a rectangular and curved cross-section groove, $D = 1 \text{ mm}$, and $\alpha = 90^\circ$

As shown in Figure 18, by designing a triangular cross-section fin, up to 83% increase in wetted area of the fins can be achieved. On the other hand, reducing the fin spacing leads to a higher capillary rise (refer to Figure 16). Figure 19 shows that a 75% decrease in fin spacing leads to a 300% increase in the wetted area of a rectangular fin.

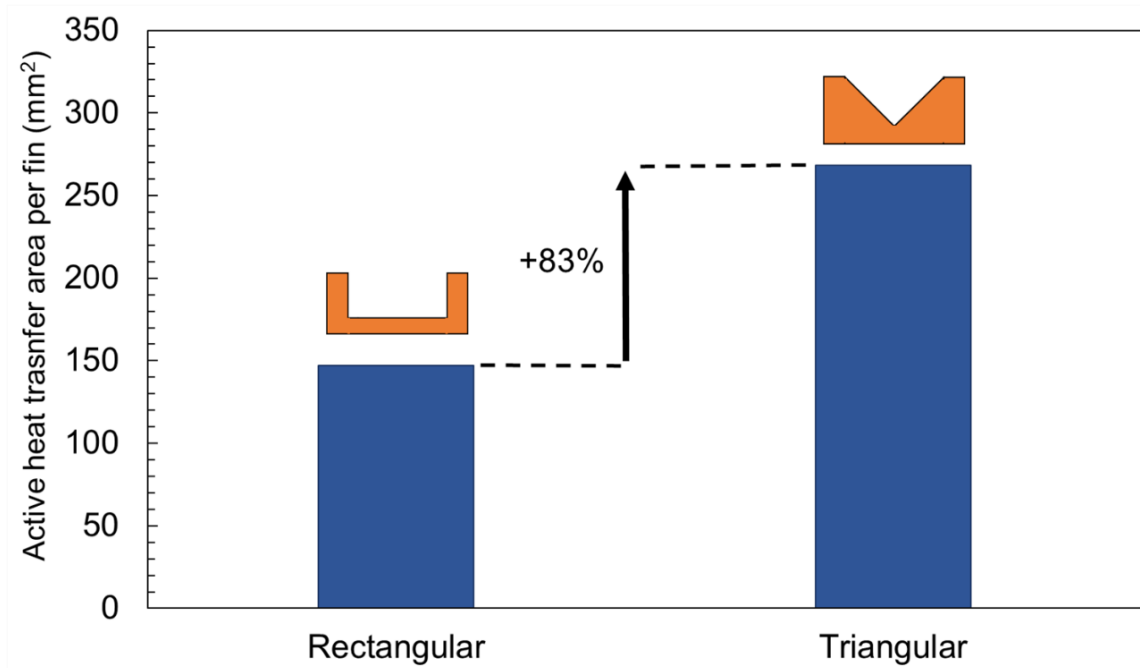


Figure 18. A comparison between active heat transfer area of a rectangular cross-section compared with a triangular design, showing up to 83% increase in wetted area ($D = 1 \text{ mm}$, and $\alpha=90^\circ$)

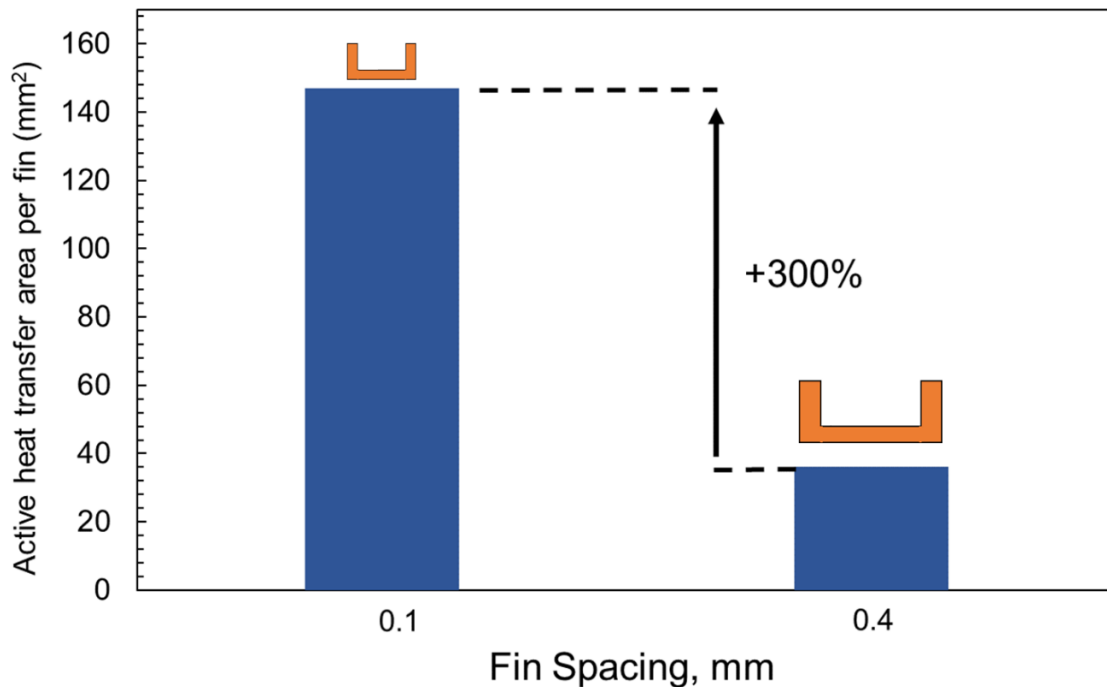


Figure 19. A comparison between two fin spacing values, showing the increase in active heat transfer area of a smaller fin spacing. A 75% decrease in fin spacing leads to a 300% increase in the wetted area ($D = 1 \text{ mm}$, and $\alpha=90^\circ$)

The contact angle has a great effect on the overall capillarity in micro-grooves. Figure 20 plots the effect of contact angle on capillary height in a rectangular groove. It is concluded that the more hydrophilic the surface, the higher the capillary rise would be. Although Figure 15 was plotted for an inclination angle of 90° , it is possible to investigate the effect of α . Figure 21 plots the capillary height as the inclination angle drops from 90 to 40 degrees. It is worth mentioning that for α smaller than 90° , h is the capillary length, the length of rise of the liquid along the groove, rather than the overall height of the liquid column (refer to Figure 14 for clarification). It is concluded that for smaller inclination angles, the liquid travels further to reach the same water height level as a vertical groove (since the pressure of the pool of water and that of the top of the capillary height should equalize). Figure 22 compares the capillary rise between different media. If methanol, ethanol, or isopropyl alcohol were used instead of water, the capillary height decreases for small groove spacing, specifically less than 500 microns. However, if ammonia were used instead of water, the capillary height increases, specifically for groove spacing larger than 200 microns.

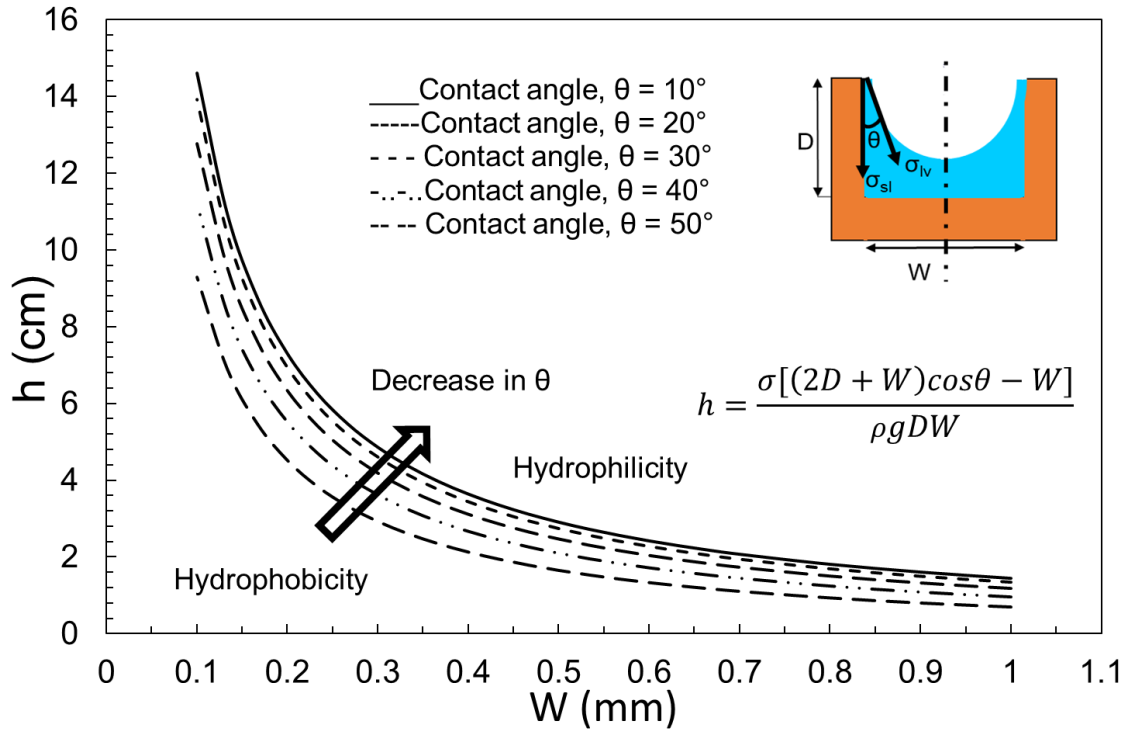


Figure 20. The effect of contact angle on the capillary rise in a rectangular cross-section with $D = 1 \text{ mm}$ and $\alpha = 90^\circ$

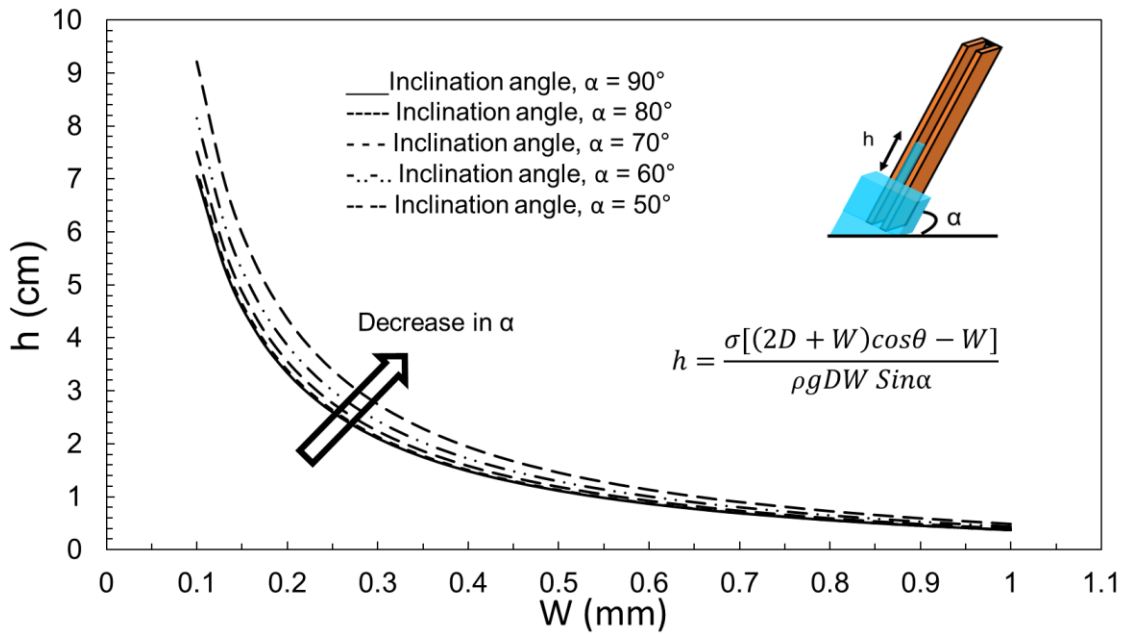


Figure 21. The effect of inclination angle on the capillary rise in a rectangular cross-section with $D = 1 \text{ mm}$

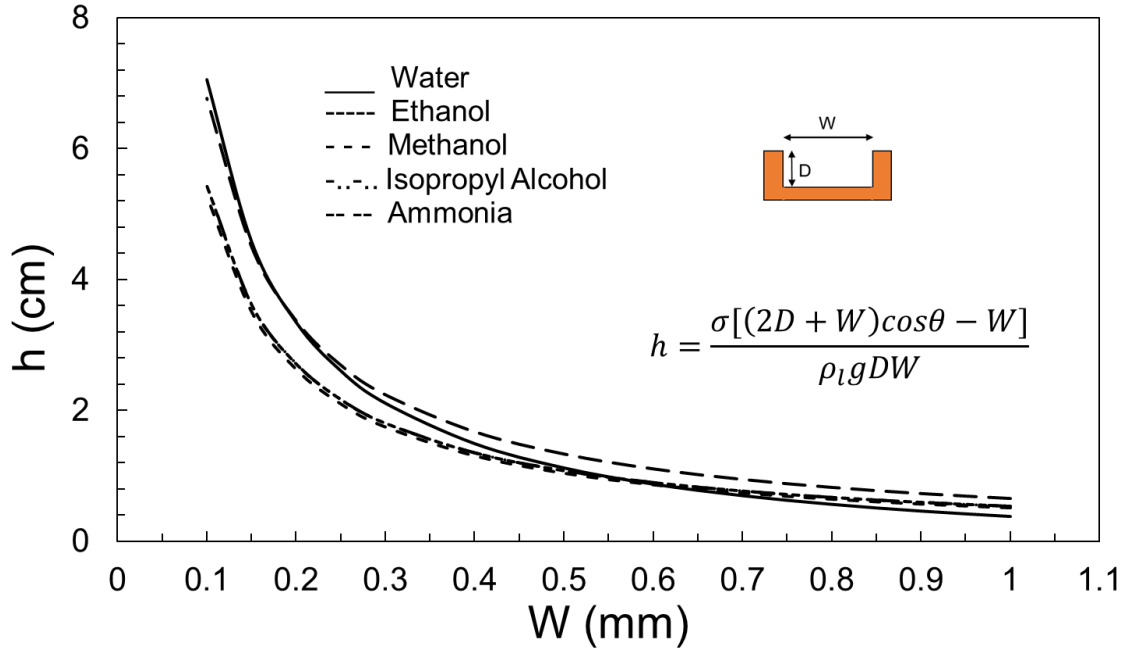


Figure 22. The effect of surface tension of different media on the capillary rise in a rectangular cross-section with $D=1$ mm

The unified non-dimensional capillary rise is given as Eq. 9. Before plotting a general form of this equation, it is interesting to compare the proposed model with experimental data from the literature. Here, two sets of data from [47] and [50] are chosen to see how Eq. 9 can capture the experimental capillary rise in a non-dimensional form. Figure 23 and Figure 24 compare the predicted h^* for a rectangular and triangular cross-section groove, respectively, with those from the literature. It is seen that the non-dimensional form of h falls within 10% of the experimental data, therefore, it can be used as a general and unified equation. The reported deviation of experimental data from the model's values is typical and expected, given many factors that affect a capillary rise experiment. Possible sources of this deviation are surface roughness, contact angle variation, and geometry inconsistency [47].

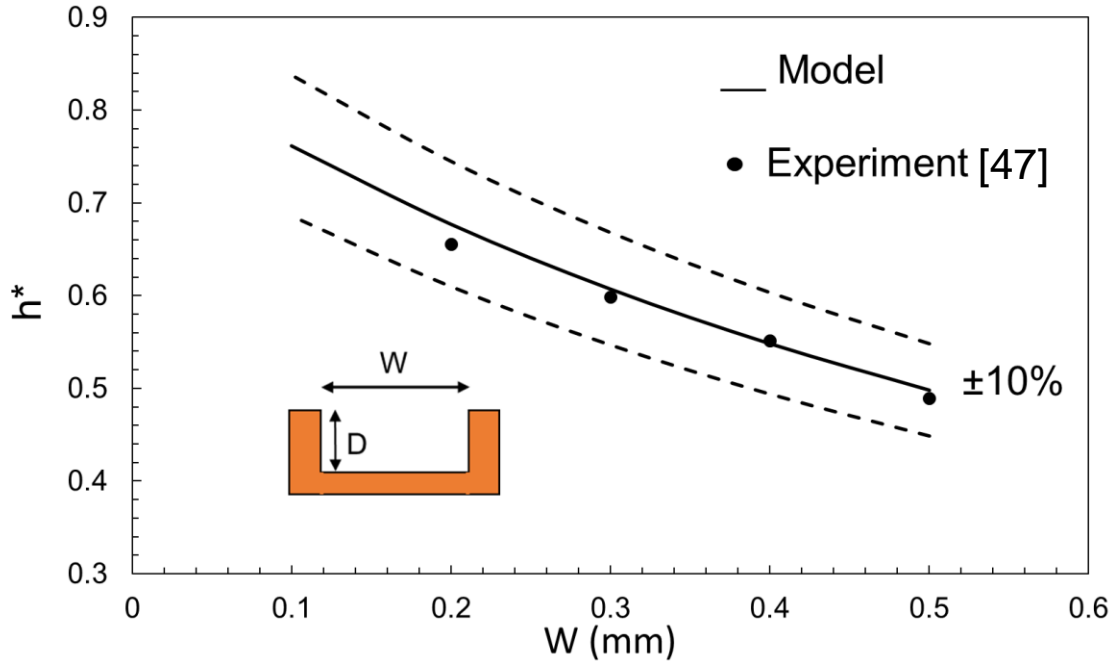


Figure 23. A comparison of capillary rise (Eq. 9) with data extracted from [47]

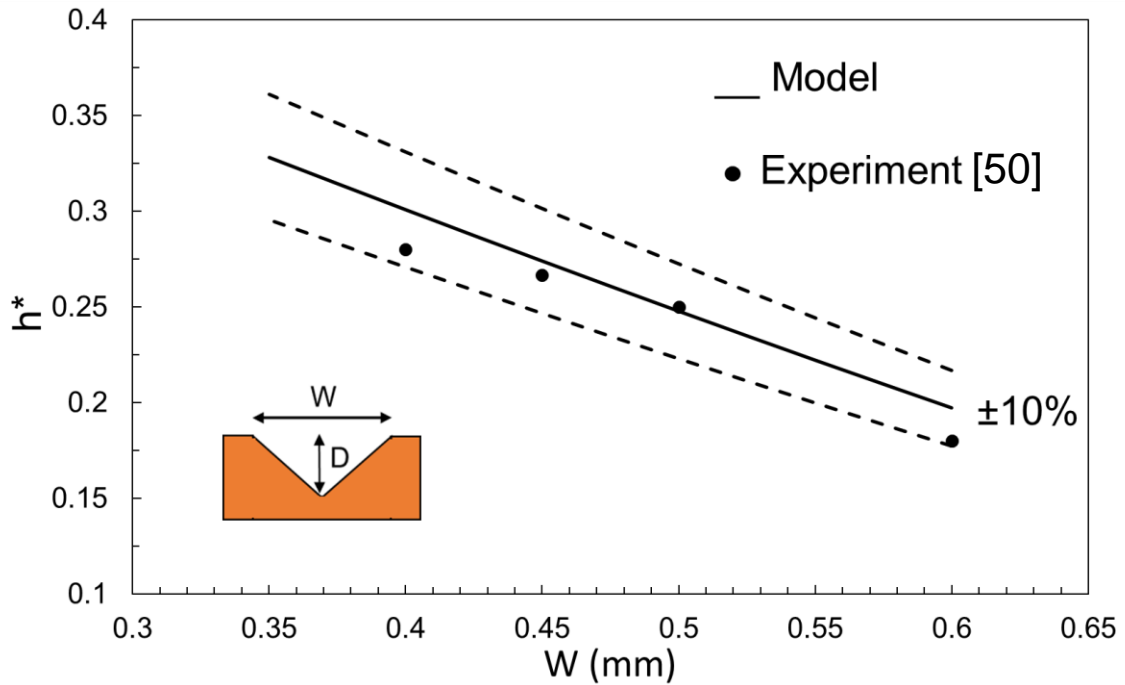


Figure 24. A comparison of capillary rise (Eq. 9) with data extracted from [50]

Figure 25 plots the final unified non-dimensional form of capillary rise as a function of L , characteristic length scale. It is seen that for each value of the contact angle, h^* is a line that intercepts the x-axis at some point. Returning to the first assumption in section 2, the maximum allowable characteristic length scale depends on the contact angle value, i.e., there exists a maximum L , for each contact angle value, above which the capillary action would not happen for that contact angle. In other words, for capillary to happen ($h^* > 0$), the characteristic length scale should be smaller than a certain value. This value depends on the contact angle, i.e., with a given contact angle, there exists a maximum characteristic length scale (hence, a maximum width), above which h^* would be zero. As an example, if contact angle is 70° , the maximum possible characteristic length scale (W/Pw) is ~ 0.34 (Figure 25). Therefore, by having the Pw of the channel, we can find a maximum width for capillary to happen.

It is also seen that surfaces with a smaller contact angle (more hydrophilic) would have a higher h^* . Finally, it is concluded that the difference between two sets of h^* lines increases significantly as the contact angle increases; i.e. The h^* lines for 0° and 10° contact angles are a lot closer to each other than the lines for 50° and 60° , even though they both have a 10° difference in contact angle. Figure 25 also includes experimental data from Ref. [47], [50], [52], and [53] and numerical data from [54] for reference.

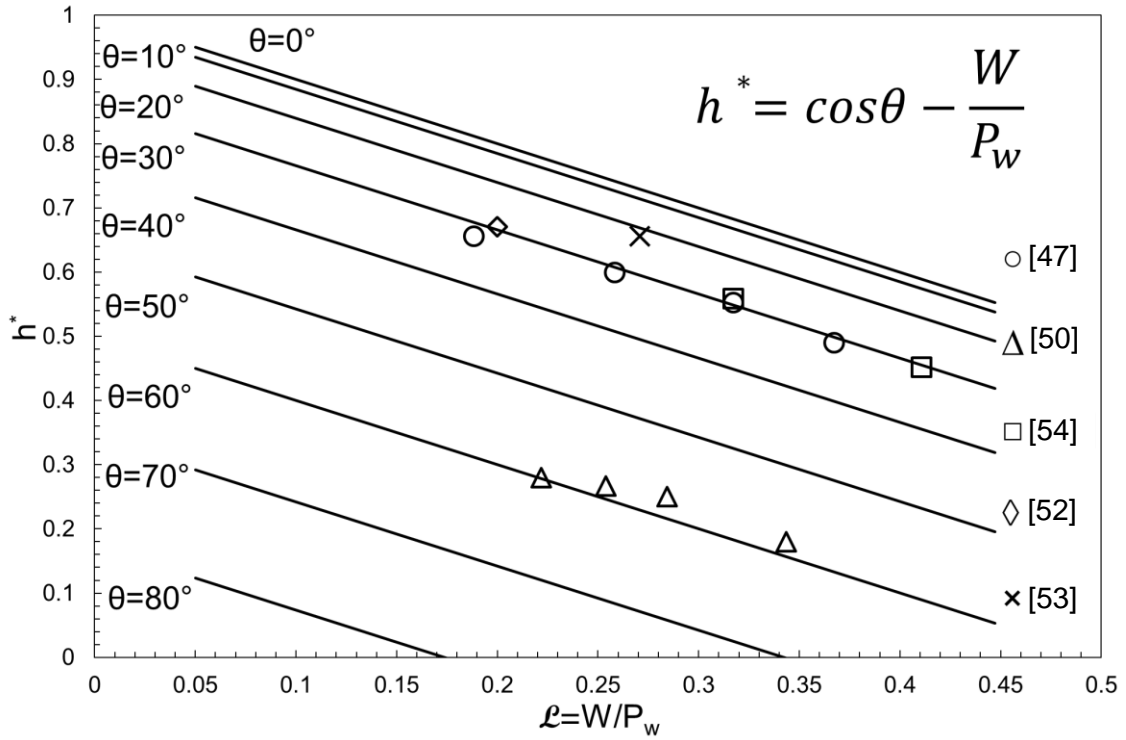


Figure 25. The unified non-dimensional form of capillary rise as a function of characteristic length scale and contact angle. Data from (\circ [47], Δ [50], \square [54], \diamond [52], \times [53])

2.5. Conclusion to the chapter

In this chapter, a unified non-dimensional closed-form analytical solution was proposed that can accurately predict the capillary rise for any given geometry, and only depends on two parameters: contact angle and a characteristic length scale, defined as the ratio of the liquid-vapor to solid-liquid interface. The effect of a groove's width, height, wetting perimeter, contact angle, and surface tension were studied using Eq. 6. It was seen that the unified non-dimensional form of h falls within 10% of the experimental data, therefore, it can be used as a general equation.

The following conclusions are made based on the unified closed-form model of capillary rise and can be used to increase the thin film evaporation heat transfer area, consequently, increasing the heat removal capacity of CALPE:

- The change in width of the groove had a greater effect on capillary height than the change in depth,
- The capillary rise in a triangular groove was considerably higher than for other cross-sections,
- A triangular cross-section fin has up to 83% higher wetted area as compared to a rectangular fin.
- The contact angle had a great effect on the overall capillarity in micro-grooves. The more hydrophilic the surface, the higher the capillary rise, and the higher the wetted area,
- Smaller inclination angles led to a longer liquid travel path,
- A 75% decrease in fin spacing can lead to up to a 300% increase in the wetted area of a rectangular fin.

It was seen that the unified non-dimensional form of h falls within 6% of the experimental data, therefore, it can be used as a general equation. It was also observed that:

- Using the proposed model, Eq. 9, a maximum characteristic length scale, \mathcal{L} , for applicability of capillary action can be found for a given contact angle,
- Surfaces with smaller contact angle (more hydrophilic) would have a higher h^* , and
- The difference between two sets of h^* lines increases significantly as the contact angle increases.

This general approach can be used as a unifying tool for designing various engineering solutions that involves any micro-groove.

Chapter 3.

The effect of surface roughness on capillary rise in micro-grooves

As discussed in Chapter 2, to have a CALPE that is compact, efficient, and with potential for commercialization, it needs to have a large active heat transfer area (wet area) on the fin side. Chapter 2 provided a unified non-dimensional model for capillary rise that can accurately predict the capillary rise for any given groove geometry and condition and only depends on two parameters: contact angle and characteristic length scale, defined as the ratio of the liquid-vapor to the solid-liquid interface. In this chapter, the unifying capillary rise model of chapter 2 is extended to include the effect of surface roughness. A new characteristic length scale is proposed that includes salient geometrical parameters, such as micro-grooves height, width, and surface roughness. Furthermore, it is shown that by using the proposed characteristic length scale, it can be determined whether the capillary action would occur in each micro-groove and liquid. Various metallic and polymeric surfaces with a wide range of surface roughness are fabricated from aluminum, stainless-steel, natural graphite sheet, and 3D-printed stainless-steel and a polymer. However, aluminum may not be a suitable material due to the corrosion from the salt in the sorption composite and the outgassing because of corrosion. A profilometer and sessile drop method are used to measure surface roughness and the contact angles, respectively. The present unifying model is compared against our measured data, and it is shown that it can predict the capillary rise in rough micro-grooves with less than a 10% relative difference. It is observed that the capillary height can be increased for a wetting surface by introducing surface roughness and by using optimal micro-groove cross-sections that are triangular as opposed to rectangular. The proposed compact, unifying model can be used to predict the capillary rise for any given micro-groove cross-section, and as a design tool for numerous industrial and biomedical applications, such as heat pipes, power electronic cooling solutions, sorption systems, medicine delivery devices, and microfluidics that utilize capillary micro-grooves.

3.1. Introduction

In chapter 2, a new unifying analytical model was proposed to predict the capillary rise in smooth micro-grooves with a wide range of cross-section geometries as a function of: i) contact angle, and ii) a novel characteristic length scale of the micro-grooves, defined as the ratio of the liquid-vapor to the solid-liquid interface. In this chapter, the effect of surface roughness and its impact on contact angle is investigated and added to our unifying model and experimentally validated. Surface roughness exists in all real and engineered surfaces, especially 3D printed and etched substrates.

The capillary action has long been the focus of much research. Leonardo da Vinci might have recorded the first observation of the capillary phenomenon [55]. Years later, Robert Boyle performed experiments by inserting a capillary tube in red wine and observing the independence of the liquid column from the pressure on top of the column [56]. The capillary action was successfully quantified in 1805 by Thomas Young and Pierre-Simon Laplace; i.e., the well-known Young–Laplace equation for capillary action [44]. Albert Einstein published his first paper on capillarity [57].

Recently, researchers have investigated capillary rise under numerous conditions, including zero gravity, tilted tubes, non-circular conduits, tubes with rough surfaces, and porous media [58–62]. Wang et al. [47] studied the capillarity rise in micro-grooves with rectangular cross-sections analytically and experimentally. They used a Helmholtz free energy method to model the capillary rise in a vertical open micro-groove and experimented with micro-grooves made by photolithography. They reported the effect of the micro-grooves' width on the capillary rise. Chen [34] studied the flow of a wetting fluid in metallic micro-grooves with various depths. They concluded that the flow in micro-grooves was proportional to the square root of time. Khumpuang et al. [63] modeled the capillary rise in a quadruplets-microneedle made by x-ray lithography for blood extraction. They compared their modeling results with experimental data and reported a good agreement. Yang et al. [49] studied the dynamic flow of capillary phenomenon by using a water and water-glycol mixture in hydrophilic micro-grooves. They reported that the capillary rise was faster in a micro-groove with a smaller width, regardless of its geometrical cross-section. Extrand [62] studied the forces, pressures, energies and kinetics of capillary rise in chemically homogeneous tubes and tubes with chemical gradients. Focusing on heat pipes, Wu et al. [64] explored the potential of increasing the

capillary force in grooved wicks by utilizing a novel skew-grooved structure when compared with a rectangle-grooved wick. They reported an improvement in capillary force by using a new structure as opposed to a rectangular micro-groove.

Contact angle depends on the specific solid-liquid interaction, environmental conditions, such as temperature and humidity, and surface features such as roughness. Therefore, many researchers attempted to quantify this interaction by experimental means. Smith et al. [65] studied the wettability of a fluid-solid interface with an application in oscillating heat pipes. They used two techniques to measure the contact angle: i) the sessile drop method, and ii) capillary rise. Reported contact angles included the interaction between copper, aluminum, and Teflon with liquid water, acetone, R-134a, and HFO-1234yf. Schwartz [66] provided a molecular interpretation of contact angle and studied an intrinsic contact angle, defined as variations not related to surface roughness, heterogeneity, or penetrability of the solid surface. Tadmor and Yadav [67] showed that the as-placed contact angle of a droplet decreased with the droplet size since its hydrostatic pressure increased. Khandekar et al. [68] studied the contact angle in pulsating heat pipes made from real engineering surfaces, as well as ideal smooth surfaces. Diaz et al. [69] hypothesized that the adsorption of liquid film in the droplet vicinity was the reason for intrinsic hysteresis during the sessile drop measurement of static contact angles. Butt et al. [70] defined the boundary conditions of Young's equation and then showed the effect of evaporation for macroscopic droplets to be negligible. Rodríguez-Valverde et al. [71] proposed a model for predicting the Young contact angle of rough solid surfaces based on the contact angle hysteresis measurements. Tadmor [72] reported the line energy to the contact angle resulted from the surface imperfections. Tadmor's proposed relationship was a function of the droplet volume, the interfacial energies, and the measured contact angle. Lamour et al. [73] proposed a simplified experimental setup to measure the contact angle as opposed to commercial goniometers and argued that their setup was precise enough for most applications, easier to construct, and affordable. Bernardin et al. [74] showed the temperature dependence of water-aluminum's contact angle, experimentally. They reported that for temperatures below 120°C, the contact angle remained unaffected. Others have studied the contact angle theoretically, and experimentally [75–77].

Wenzel [78] first proposed that the wetting properties of a solid surface should be directly related to surface roughness. He concluded that the increase in the surface area

of fibrous materials plays a large role in the hydrophobicity of the tested samples. Later, Cassie and Baxter [79] extended Wenzel's relationship between roughness and contact angle and applied it to porous surfaces. They contributed some naturally occurring hydrophobicity, such as in duck feathers to its unique structure. Tamai and Aratani [80] studied the effect of surface roughness on the contact angle for a silica glass-mercury interface using a sessile drop method. They concluded that Wenzel's model holds for their experiments, showing the variation in contact angle of silica glass samples with various roughness ratios. Ryan and Poduska [81] developed an experimental method to show the effects of surface roughness on contact angle on solid surfaces. They showed that the change in surface energy due to surface roughening was responsible for the change in the contact angle. Berim and Ruckenstein [82] calculated the microscopic contact angle of a liquid droplet on a rough surface. They recognized two limiting cases: i) Wenzel, and ii) Cassie-Baxter regime. Li et al. [83] studied samples with various surface roughness and used phase-field interface tracking to simulate the wetting phenomenon. They concluded that when the roughness increased, the contact angle of a hydrophilic surface would decrease.

Although the capillary phenomenon and the parameters affecting it are studied, a comprehensive capillary rise model that includes the surface roughness effect has not been proposed. In this study, a new closed-form and unifying capillary rise model is proposed that includes the effect of surface roughness. The proposed model is compared with our experimental data in micro-grooves with rectangular and triangular cross-sections. The effects of the micro-grooves' height, width, contact angle, and surface roughness are experimentally investigated and reported.

3.2. Model development and the effect of surface roughness

We start with a micro-groove with a rectangular cross-section, see Figure 26. When a micro-groove is placed in a liquid as shown in Figure 26, the liquid rises along the micro-groove due to capillary forces. The governing equations, main assumptions, and the solution approach to predict the effect of surface roughness on capillary rise are listed in this section. Similar steps can be taken for any other cross-section. The present model assumptions are as follows:

- The open micro-grooves' width is small enough for the capillary action to occur ($10\text{ nm} < \text{length scale} < 1\text{ cm}$) [43],
- The surface roughness has a Gaussian (random) distribution, which is created in our surfaces using an abrasive polishing method,
- The surface is wetting, or hydrophilic,
- The micro-grooves are filled with the liquid,
- The micro-groove is placed with a slanted angle, alpha, and that its bottom end always touches a fluid reservoir,
- The physical properties are constant,
- The vapor-liquid interface is homogenous, and
- Heat transfer is negligible since the capillary action is a fast, almost instantaneous process.

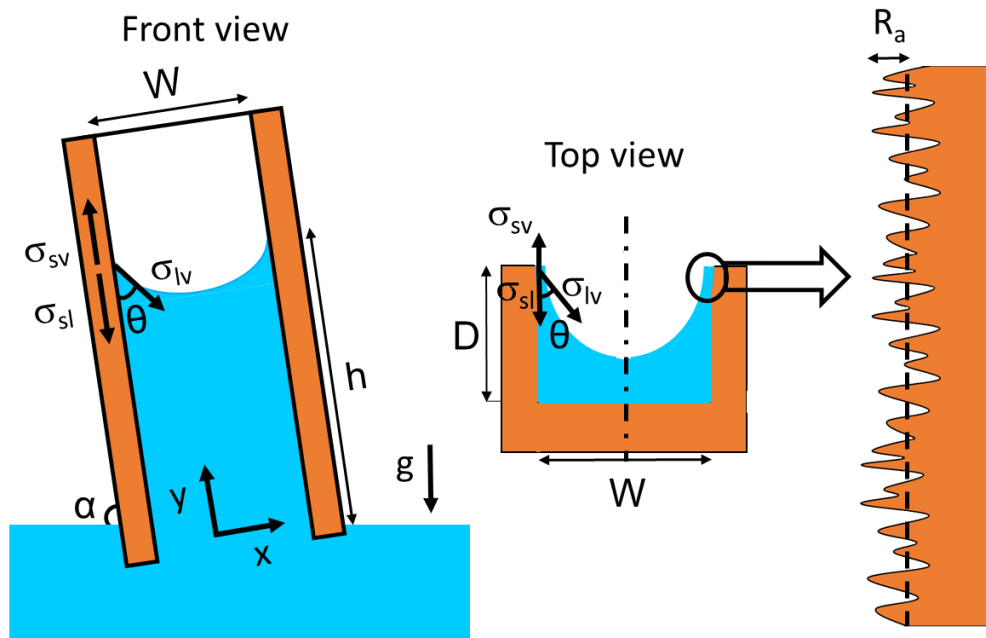


Figure 26. Top and front view of capillary rise, h , in a rough micro-groove with width of W and depth of D . Our previous model [84] is extended to include the effects of surface roughness. Dash line shows the mean surface line. α denotes an inclination angle of the capillary channel.

Considering the above-mentioned assumptions and Figure 27, Young's equation can be written as [44,46]:

$$\sigma_{sv} = \sigma_{sl} + \sigma_{lv} \cos\theta \quad (10)$$

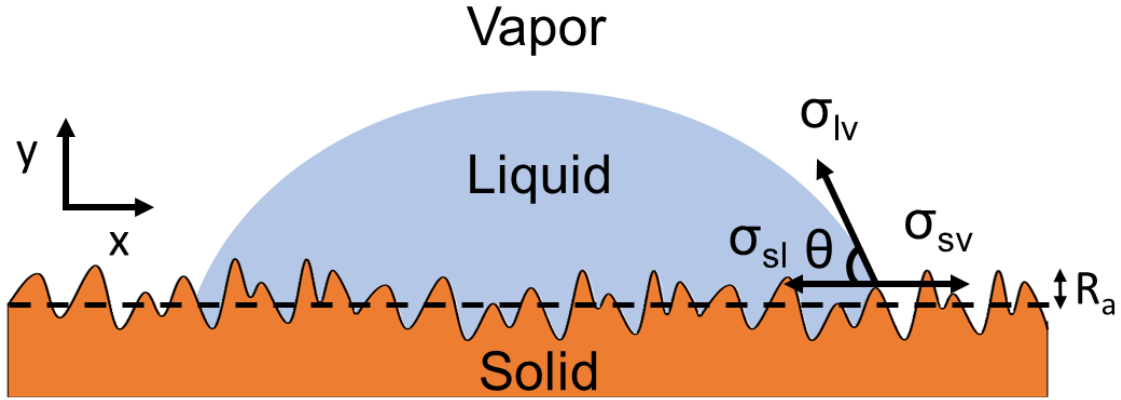


Figure 27. A schematic of a droplet on a flat surface showing three forces of surface tension leading to Young's equation under static equilibrium on a rough surface.

where, σ and θ are surface tension [N/m] and contact angle [°], respectively. The contact angle in Eq. 10 is the ideal contact angle on a smooth surface where there is no roughness. To incorporate the effect of surface roughness, Eq. 10 should be modified. Wenzel [78] proposed a relationship defined by the ratio of the actual surface area of a solid surface to the geometric surface area, or roughness factor, affecting the contact angle:

$$r = \frac{\text{actual surface area}}{\text{geometric surface area}} \quad (11)$$

Using Eq. 11, the apparent contact angle of a rough surface, θ^* , with a roughness factor of r , can be related to the contact angle of a smooth surface, θ , as follows:

$$\cos \theta^* = r \cos \theta \quad (12)$$

Assuming the droplet size is sufficiently larger than the scale of surface roughness ($V_{\text{droplet}} > 0.01$ mL), and using Eq. 12, introducing surface roughness leads to a decrease in contact angle on a wetting surface. Eq. 10 is then modified to Eq. 13:

$$\sigma_{sv} = \sigma_{sl} + r \sigma_{lv} \cos\theta \quad (13)$$

The change in the interface area [m^2] between the liquid-vapor and solid-liquid are:

$$dA_{lv} = (W + 2R_a)dy \quad (14)$$

$$dA_{sl} = r(2D + W)dy \quad (15)$$

where, W is the micro-groove width [m], D is the micro-groove depth [m], r is the roughness factor, and R_a is the average deviation of the surface roughness profile from the mean line [μm]. dy is the infinitesimal change in the capillary height in y -direction, see Figure 26.

The Helmholtz free energy between three interfaces can be written as [48]:

$$dE = \sigma_{sv} dA_{sv} + \sigma_{sl} dA_{sl} + \sigma_{lv} dA_{lv} \quad (16)$$

Substituting Eq. 10 in Eq. 16 results in the following:

$$dE = \sigma_{lv}(dA_{lv} - r dA_{sl} \cos\theta) \quad (17)$$

Since the capillary force is dE/dy and with substituting Eqs. 14 and 15 in Eq. 17, the capillary force can be found as:

$$F_c = \sigma_{lv}[r^2 \cos\theta (2D + W) - W - 2R_a] \quad (18)$$

The subscript “ lv ” is omitted henceforth for simplicity. The capillary force balances the gravity force:

$$F_g = \rho g r (D W h) \sin\alpha \quad (19)$$

where, ρ is the fluid density [kg/m^3], g is gravitational acceleration [m/s^2], and h is the equilibrium capillary height [m]. α denotes an inclination angle of the capillary channel [$^\circ$], e.g., 90° for a vertical micro-groove. Equating Eq. 18 and Eq. 19:

$$h = \frac{\sigma[r^2 \cos\theta (2D+W) - W - 2R_a]}{\rho g r D W \sin\alpha} \quad (20)$$

$$P_{w,i} = 2D + W, \quad P_w = r(2D + W)$$

$$A_{c,i} = D \times W \quad A_c = r \times D \times W$$

The ideal wetting perimeter and cross-sectional area for a smooth micro-groove are defined as $P_{w,i} = 2D+W$, and $A_{c,i} = D \times W$, respectively. The actual wetting perimeter and cross-sectional area are given by $P_w = r(2D+W)$, and $A_c = r \times D \times W$, respectively. Non-dimensionalizing Eq. 20, one can conclude:

$$h^* = \frac{\rho g h \sin \alpha}{\sigma} \times \frac{A_c}{P_w} = r \cos \theta - \frac{W+2R_a}{rP_{w,i}} = r \cos \theta - \mathcal{L} \quad (21)$$

where, h^* is defined as the non-dimensional capillary height, $r \cos \theta$ is the actual contact angle on a rough surface, and

$$\mathcal{L} = \frac{W+2R_a}{rP_{w,i}} \quad (22)$$

where, \mathcal{L} is a new characteristic length scale defined in this study to include the surface roughness of micro-grooves. The subscript “ i ” is dropped henceforth.

From Eq. 21, a criterion for capillary action to occur can be concluded by setting $h^* = 0$:

$$h^* = 0 \rightarrow r \cos \theta = \frac{W+2R_a}{rP_w} \quad \text{or} \quad r \cos \theta = \mathcal{L} \quad (23)$$

Therefore, for capillary action to occur, $h^* > 0$, the following should be true:

$$W < r^2 P_w \cos \theta - 2R_a \quad \text{or} \quad \mathcal{L} < r \cos \theta \quad (24)$$

Therefore, there is a threshold based on a micro-groove’s width, or characteristic length scale, as defined above, above which capillary action would not occur.

Surface roughness can be defined by various parameters and measured by different means. Here, surface roughness is defined based on EN ISO 4287 standard [85], characterized by R_a and R_{Lo} [86], and measured by a surface profilometer [87]. R_a is the average deviation of the surface roughness profile from the mean surface line, and R_{Lo} is the developed length of the surface roughness profile in percentage, as shown schematically in Figure 28. The unit for R_a is [μm] (micro-meters). R_{Lo} is non-dimensional.

To determine the roughness factor in Wenzel's equation, Eq. 12, from surface roughness data, the following is used [88]:

$$r = 1 + R_{Lo} \quad (25)$$

Hence, Eq. 21 can be rewritten as:

$$h^* = \cos\theta [1 + R_{Lo}] - \frac{W + 2R_a}{P_w [1 + R_{Lo}]} \quad (26)$$

where, $\cos\theta$ is the ideal contact angle, P_w is the ideal wetted perimeter (liquid-solid interface length), W is the ideal micro-groove width (liquid-vapor interface length), and R_a and R_{Lo} are surface roughness parameters as defined above.

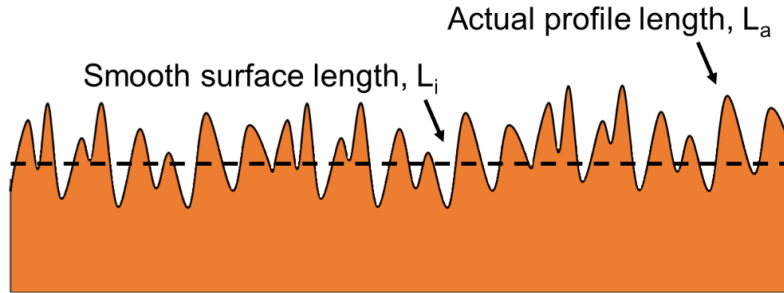


Figure 28. The actual surface roughness profile length vs the ideal smooth surface length. R_{Lo} is the percentage increase in the profile length.

3.3. Experimental study

The surface roughness of a solid surface can be determined by various means, including optical methods, such as laser reflectivity and scanning electron microscopy, and contact methods, such as contact stylus tracing, or a profilometer. Here, a Mitutoyo SJ-400 profilometer was used to measure the surface roughness. The tip of the stylus moves in a line across the surface and measures the peaks and valleys of the solid surface. The stylus height changes vertically over the peaks and valleys. These changes are interpreted internally in the device and a profile is created. This roughness profile is then used to calculate roughness parameters.

The contact angle was measured using the sessile drop method. A droplet of water was placed on a flat solid surface. A Dinolite digital microscope was used for taking images. Image processing was performed with the microscope's accompanying software. The solid surfaces used were stainless-steel, aluminum, natural graphite sheets, 3D-printed polymer, and 3D-printed stainless-steel. The liquid used in the experiments was water. Measurements were repeated at least five times and an averaged value is reported for the contact angle. The schematic of the test rig used for sessile drop measurements is shown in Figure 29. Low-power LED lights were used for illumination so that no heat is emitted to the water droplet from the light source. Tests were performed under identical conditions, at room temperature, relative humidity, and pressure. Higher pressures than room pressure potentially decreases the contact angle. Water droplets were placed on the solid surface gently using a syringe and needle. An approximately 0.05 mL water droplet was used in each measurement, following studies conducted in Ref. [65].

To experimentally show the capillary rise of water in micro-grooves, various micro-grooves were fabricated. The micro-grooves were created using various methods. Direct Metal Laser Sintering (DMLS) was used for 3D-printed micro-grooves with stainless-steel. Stereolithography (SLA) was used for micro-grooves made with polymers. Figure 30 shows an example of a micro-groove made by stereolithography used for our capillary rise measurements. The inset in Figure 30 shows a micro-groove thickness of 500 μm , and a micro-groove width of 400 μm , where the micro-groove depth is 1 mm. The micro-grooves were vertically inserted in a container with a pool of liquid water such that a small portion of the micro-grooves were in touch with the liquid. For ease of identifying the capillary height in the images, a 1% by-volume solution of water and food coloring was used. The micro-grooves were left in the pool until the capillary height was steady and the maximum height was achieved. After achieving an equilibrium state, the height of the liquid columns was measured and reported.

Due to the manufacturing defects and variation in surface roughness, the capillary rise in each micro-groove would not be uniform. Therefore, averaged values across the micro-grooves are reported for the capillary height for each sample. Images were taken using a Dinolite digital microscope at room temperature and pressure. Image processing was performed with the microscope's accompanying software to measure the capillary height. The microscope and the images were calibrated using a target ruler, provided by the manufacturer.

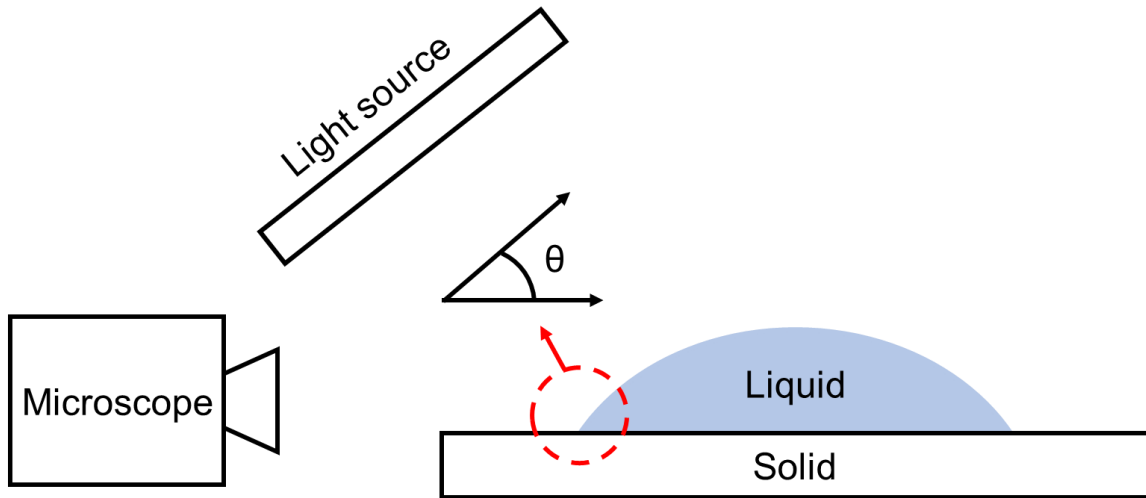


Figure 29. A schematic of the contact angle measurement using the sessile drop method. The contact angle is formed between the liquid-solid-vapor interface.



Figure 30. Micro-grooves made by stereolithography (SLA1.03) were used for the capillary rise measurement. The inset shows a micro-groove thickness of 500 μm and a micro-groove width of 400 μm . Micro-groove depth is 1 mm. Table 4 lists the sample details.

3.4. Sample preparation

The solid surfaces used for the roughness measurement were made of stainless-steel, aluminum, 3D-printed stainless-steel, 3D-printed polymer, and natural graphite sheets, with no coatings. Fine-finished stainless-steel and aluminum sheets were purchased and then roughened with abrasive polishing. Micro-grooves with various micro-groove depth and spacing were fabricated to make a comprehensive study. It was shown in our previous study [84] that as the micro-groove spacing, or micro-groove width, reduces, the capillary height increases. The micro-groove depth has little effect on the capillary height. Figure 31 shows the cross-section of various micro-grooves used for capillary height measurements in the present study. The micro-groove width range is between 100 to 500 μm with a micro-groove depth of 1 mm. The micro-groove thickness does not directly affect the capillary rise but its variation between 200 to 500 μm is studied as a limiting parameter in the fabrication process, and in compactness. As seen in Figure 32 and Figure 33, aside from variations in micro-groove dimensions, two main cross-sectional geometries were considered, rectangular and triangular micro-grooves. The triangular cross-section is expected to have a higher capillary height as compared to rectangular one, as per our model predication [84].

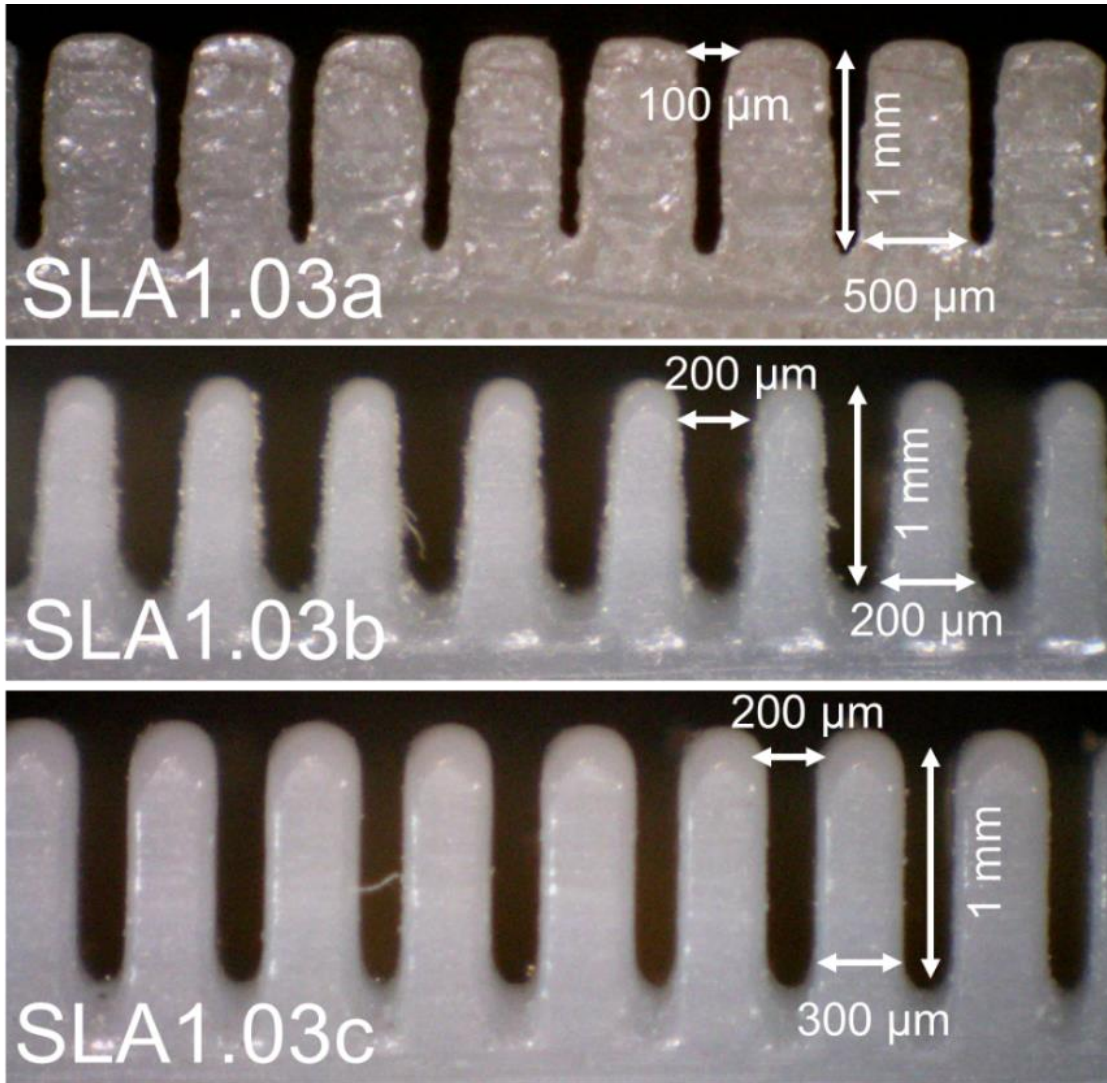


Figure 31. SLA (stereolithography) micro-grooves with various thicknesses and spacing fabricated to measure the capillary height. The micro-groove width range is between 100 to 500 μm . Micro-groove depth is 1 mm and their thickness ranges between 200 to 500 μm . Table 4 lists the sample details.

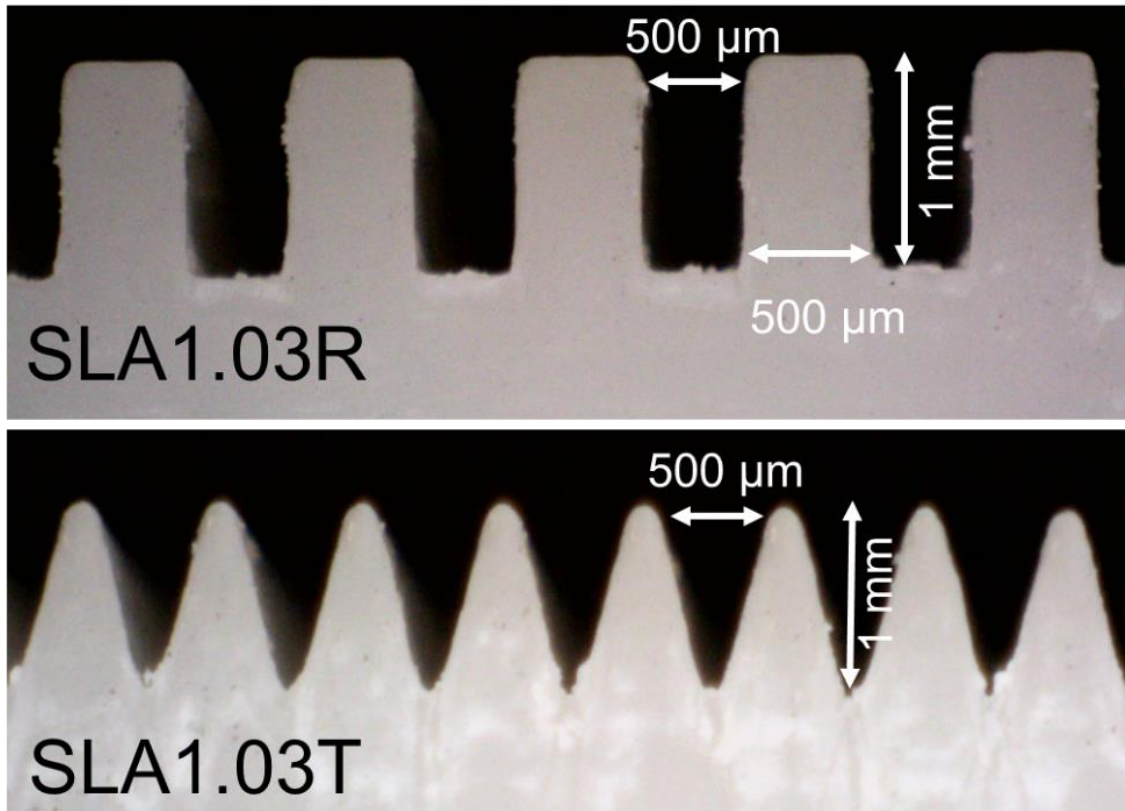


Figure 32. Two cross-sectional micro-groove geometries considered, rectangular (SLA1.03R) and triangular (SLA1.03T) cross-sections, made with stereolithography (SLA). The triangular cross-section has a higher capillary height as compared to the rectangular one. Table 4 lists the sample details.

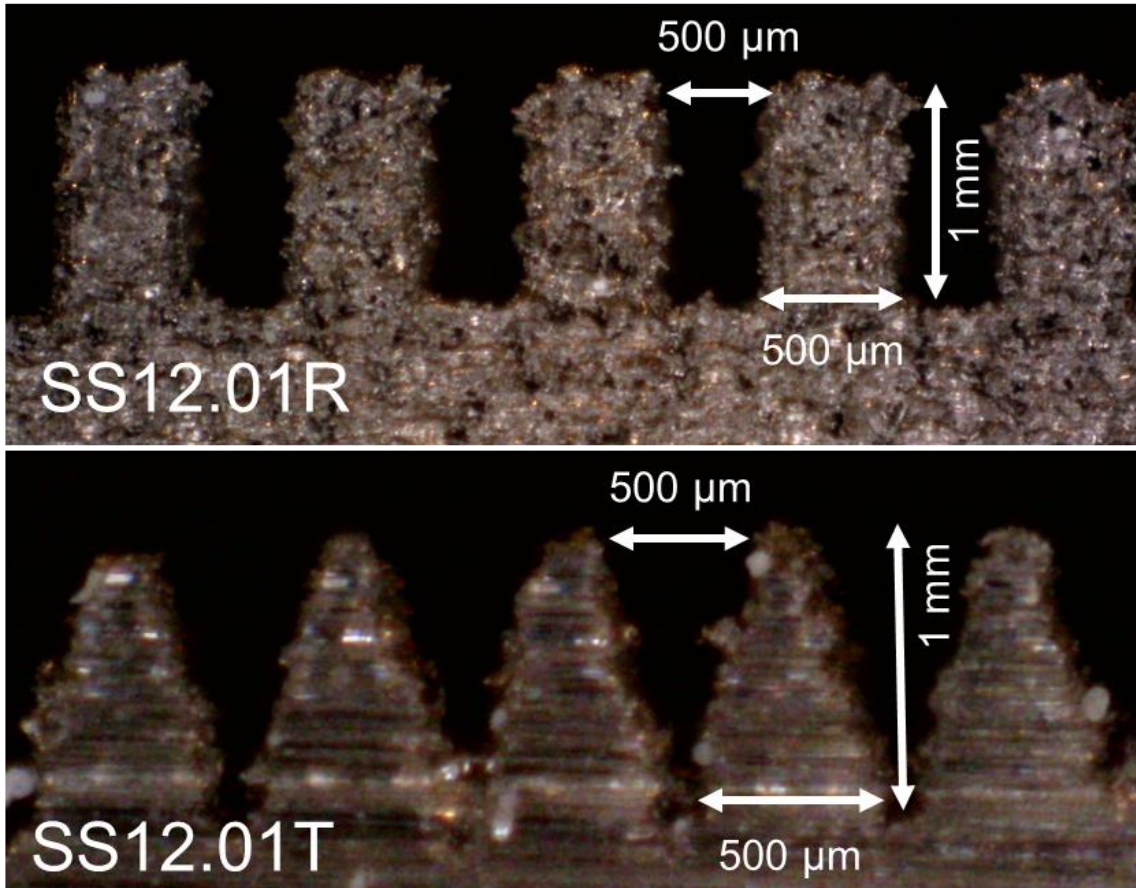


Figure 33. Two micro-grooves considered, rectangular (SS12.01R) and triangular (SS12.01T) cross-sections made with direct metal laser sintering (DMLS). The triangular cross-section has a higher capillary height as compared to the rectangular one, see the results. Table 4 lists the sample details.

3.5. Uncertainty analysis

The accuracy of the roughness measurements was $0.001 \mu\text{m}$. The contact angle accuracy was 0.01° . The microscope used for measuring the capillary height was accurate to $0.1 \mu\text{m}$. Considering the uncertainty in geometry dimensions, measured contact angle, measured capillary height, and standard deviation of data, the uncertainty of our capillary height measurement is estimated to be 8%, based on the method proposed by Moffat [89].

3.6. Results and discussion

Table 4 summarizes the surface roughness measurement results for our samples. Measurements were repeated at least five times and averaged values were reported. It was observed that with sandblasting, the aluminum sample surface roughness, R_a , was increased from 0.24 to $4.43 \mu\text{m}$ while its R_{Lo} increased from 0.5 to 1.77. Similarly, the stainless-steel sample surface roughness, R_a , was increased from 0.45 to $1.64 \mu\text{m}$ with its R_{Lo} increasing from 0.2 to 0.45. Since stainless-steel has shown a higher hardness than aluminum, the increase in its surface roughness was less than that of the aluminum sample. The polymer sample was 3D-printed by stereolithography (SLA). The measured surface roughness for the 3D-printed polymer sample was an R_a of $1.03 \mu\text{m}$ and an R_{Lo} of 1.21. The roughest sample was the 3D-printed stainless-steel with an R_a of $12.01 \mu\text{m}$ and an R_{Lo} of 1.12. The metal 3D-printing process, direct metal laser sintering (DMLS), uses powdered metals where a laser heat source melts and fuses the powders to create samples. The measured surface roughness of the natural graphite sheet, with density of 0.23 g/cm^3 , was an R_a of $4.45 \mu\text{m}$ and an R_{Lo} of 0.84.

Table 4. A summary of surface roughness values for each sample, measured by the SJ-400 profilometer. Contact angles were measured using a sessile drop method.

Sample	Material	R_a (μm)	R_{Lo}	Contact angle ($^\circ$)
SS1.64	Stainless-steel	1.64	0.45	58.8
SS0.45	Stainless-steel	0.45	0.20	67.4
Al4.43	Aluminum	4.43	1.77	42.1
Al0.24	Aluminum	0.24	0.50	65.2
SS12.01	3D-printed direct metal laser sintered (DMLS) stainless- steel	12.01	1.12	45.0
SLA1.03	3D-printed stereolithography (SLA) polymer	1.03	1.21	48.2
NGS4.45	Natural graphite sheet (NGS) – 0.23 g/cm ³	4.45	0.84	50.7

Figure 34 shows the static contact angle of water on various solid surfaces. Each solid surface was thoroughly cleaned with ethanol and left to dry before performing sessile drop tests. The natural graphite sheets that were supplied commercially were made by pressing graphite flakes and forming them into sheets. For metallic surfaces, flat sheets were used. As shown in Figure 34, the water droplet on the smoother aluminum surface made a 65.2° contact angle, which was close to that of a smoother stainless-steel surface, with a 67.4° contact angle. The rougher aluminum surface showed a contact angle of 42.1°, while the rougher stainless-steel made a contact angle of 58.8°. The 3D-printed polymer surface had a contact angle of 48.2° whereas the 3D-printed stainless-steel made a 45.0-degree contact angle. The natural graphite sheet with a density of 0.23 g/cm³ had a contact angle of 50.7°. The decrease in the contact angle of the stainless-steel surface was less than that of the aluminum sample. This can be explained by the fact that the increase in roughness of the stainless-steel sample was less than that of the aluminum sample during the sandblasting process, as listed in Table 4. Table 4 also lists the measured contact angle values for each sample. The experimental contact angles are compared to the present model, Eq. 25, and shown in Figure 35.

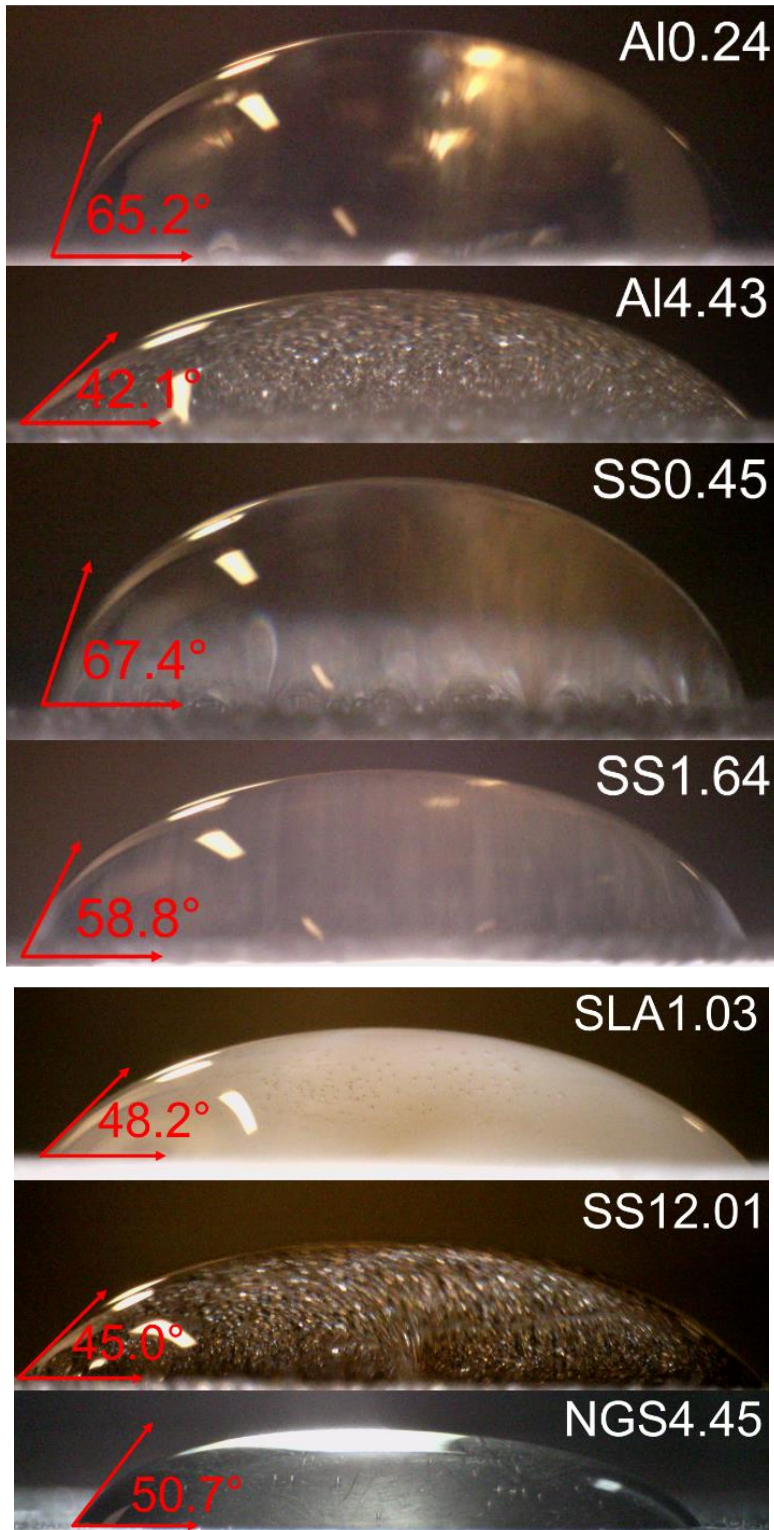


Figure 34. The contact angle measurement using the sessile drop method. Images show the static contact angle formed for water on aluminum, stainless-steel, 3D-printed polymer, 3D-printed stainless-steel, and natural graphite sheet surfaces. Table 4 lists the sample details.

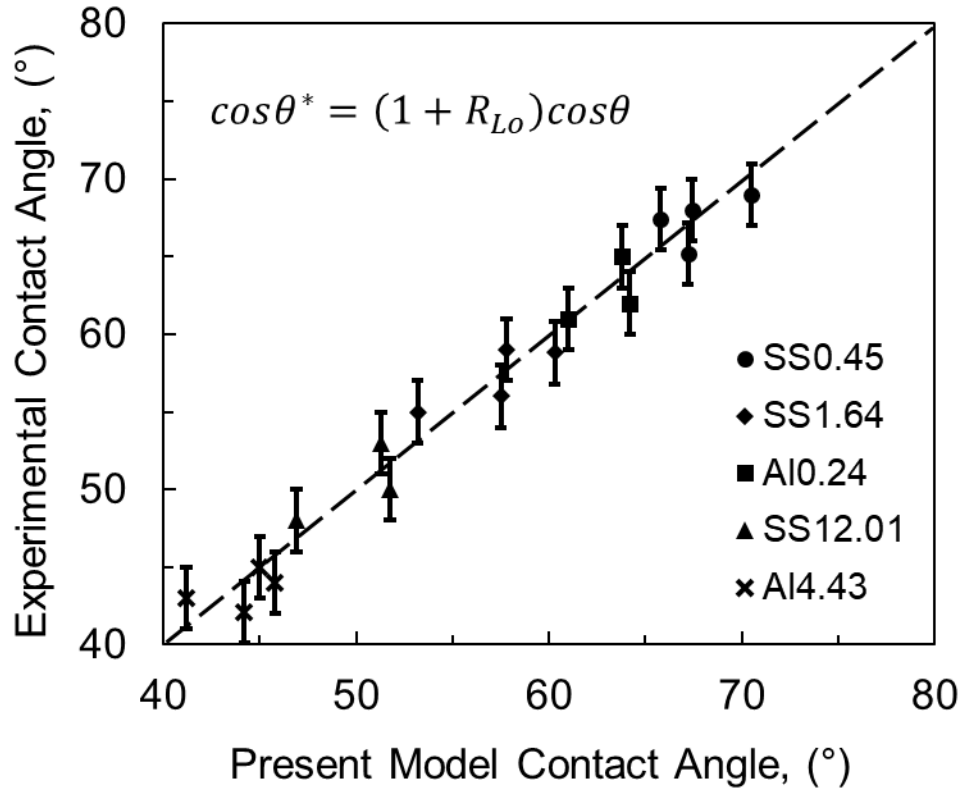


Figure 35. A comparison of experimental contact angles, measured in this study, with the present model, Eq. 25. Error bars show the uncertainty of the experimental data, approximately 10%.

As shown in Figure 36, when a liquid meets a micro-groove, a capillary meniscus is formed between the two adjacent walls due to the disjoining pressure. The capillary meniscus can change based on surface roughness, contact angle, and surface tension. Water properties such as surface tension and density can be found in the literature [90]; at a room temperature of 25 °C; surface tension is 7.28×10^{-2} N/m, and density is 999 kg/m³.

Figure 37 shows the capillary height measurement on two capillary micro-grooves with rectangular and triangular cross-sections. Images were taken by a digital microscope and were analyzed to measure the maximum equilibrium capillary height. The capillary height is not uniform in all micro-grooves due to manufacturing imperfections, variation in dimension, and surface roughness. As an example, the SLA1.03 with a 200-micron micro-groove had an average width of 192 microns, a standard deviation of 0.017, and coefficient of variation of 8%. Therefore, averaged values are reported for capillary height. These

groove dimensions were designed based on the analytical model developed in Chapter 2 to ensure performance and to validate the proposed model.

Figure 38 shows the predicted capillary height in micro-grooves, using the present model, Eq. 20, versus the measured values for the samples in this study. It can be observed that the capillary height increases rather non-linearly when reducing the micro-grooves' width. This figure also shows a capillary rise comparison between rectangular and triangular micro-grooves. The experimental results show a good agreement with the present analytical model, Eq. 20, and that discrepancy is within the experimental uncertainties. As previously mentioned, sources of uncertainties include variations in surface roughness, surface oxidization for metallic samples, geometry variations and meniscus corner effects [47].

The present unifying model in a non-dimensional form for capillary height is shown in Eq. 26. Figure 39 shows the non-dimensional capillary height, h^* , as a function of a new characteristic length scale, \mathcal{L} . For each value of $r\cos\theta$, the h^* is a line that intercepts the x-axis at some point, which is the maximum allowable characteristic length scale for the capillary action to occur. There exists a maximum \mathcal{L} , for each $r\cos\theta$ value, above which the capillary action would not occur for that $r\cos\theta$. In other words, for capillary action to occur ($h^* > 0$), the characteristic length scale, \mathcal{L} , should be smaller than a certain value. This value depends on the micro-groove's dimensions, contact angle and surface roughness, and equals $r \cos\theta$.

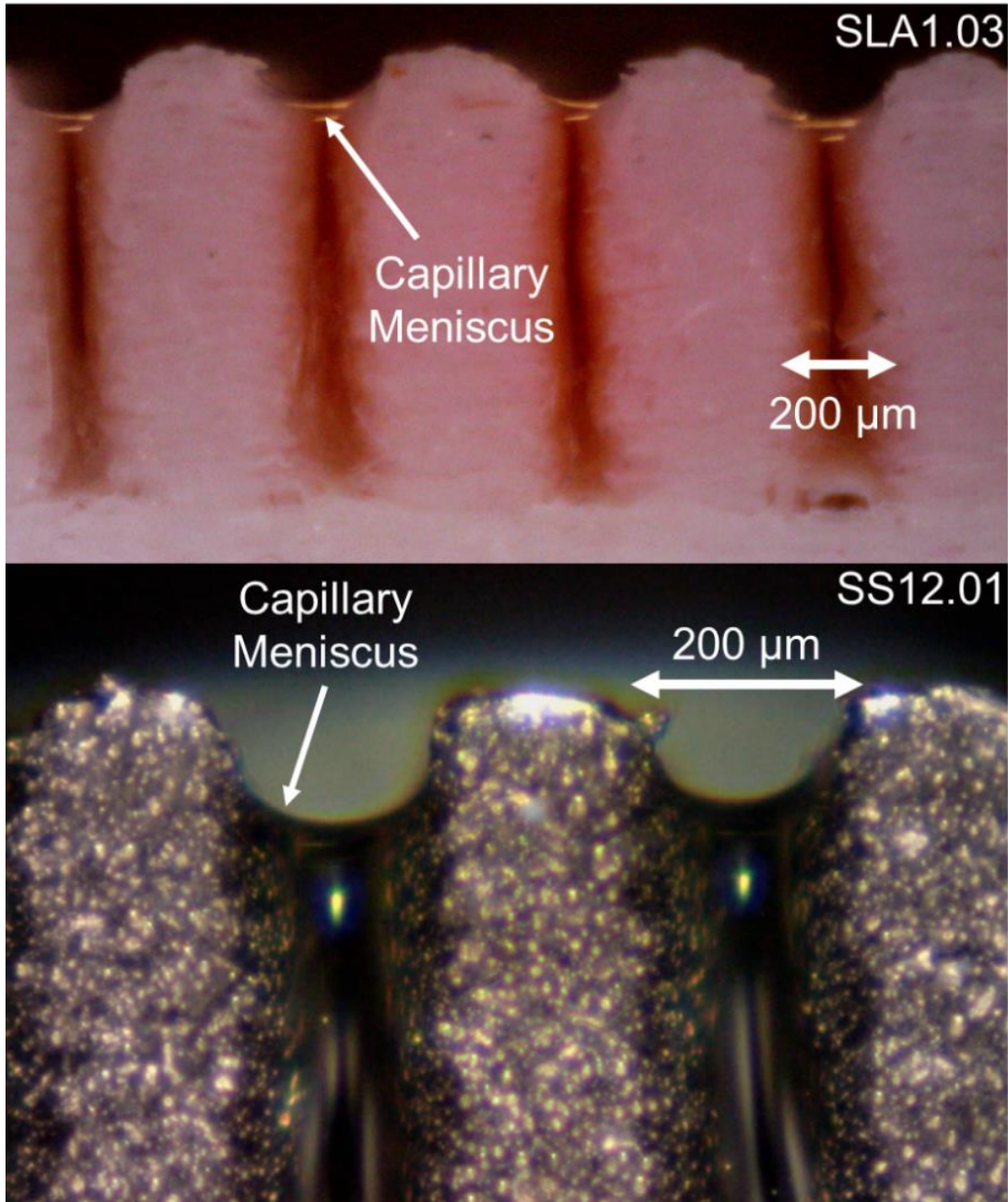


Figure 36. A capillary meniscus is formed between two adjacent micro-grooves due to the disjoining pressure. Top: SLA1.03, Bottom: SS12.01. A 1% solution of water and food coloring is used for better image contrast in the polymer sample. Table 4 lists the sample details.

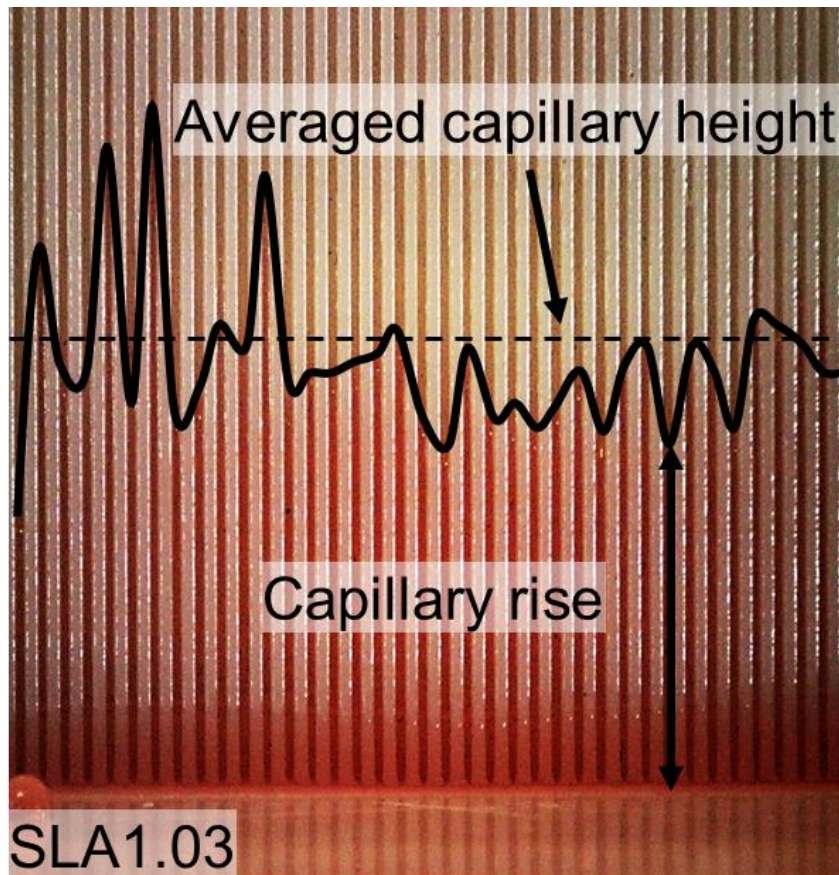
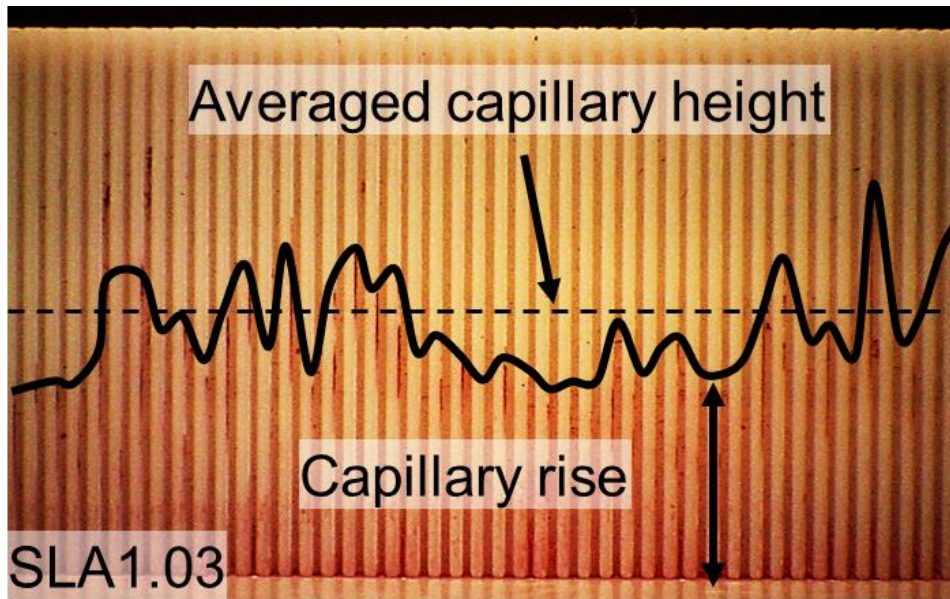


Figure 37. A comparison between the capillary height of SLA1.03 micro-grooves with different micro-groove geometry. Top: rectangular, bottom: triangular micro-grooves. Dashed lines are an average height. Table 4 lists the sample details.

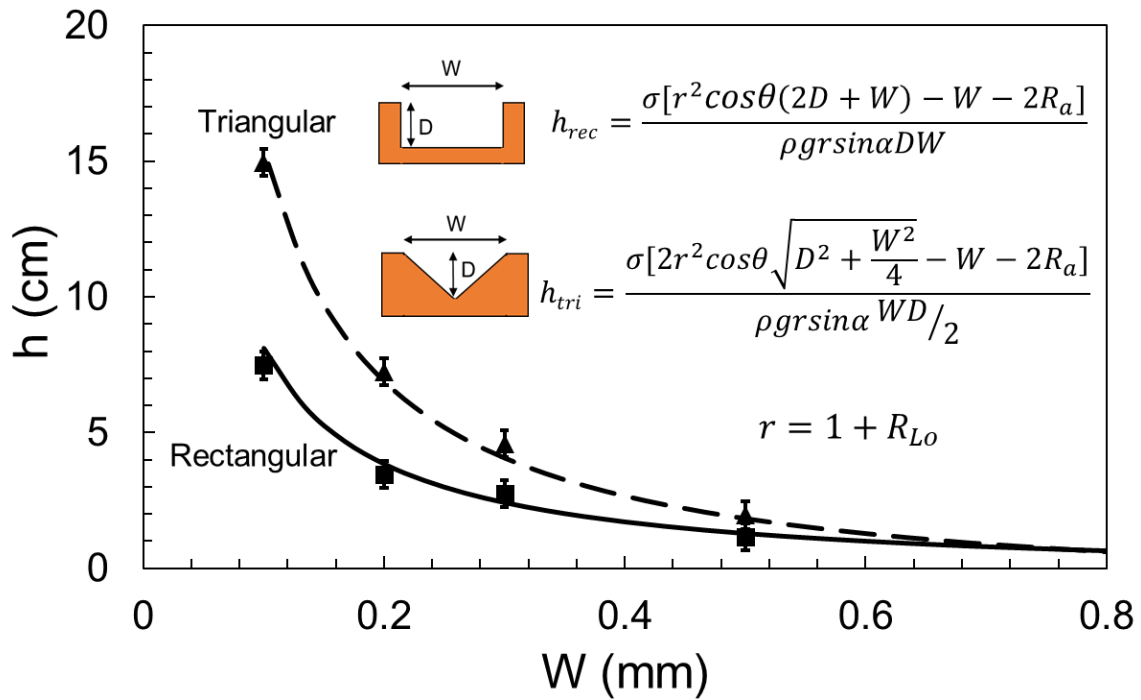


Figure 38. A comparison between capillary height in micro-grooves vs the micro-grooves' width. Two cross-sections are considered, rectangular and triangular, and experimental results are compared against the present model, Eq. 20.

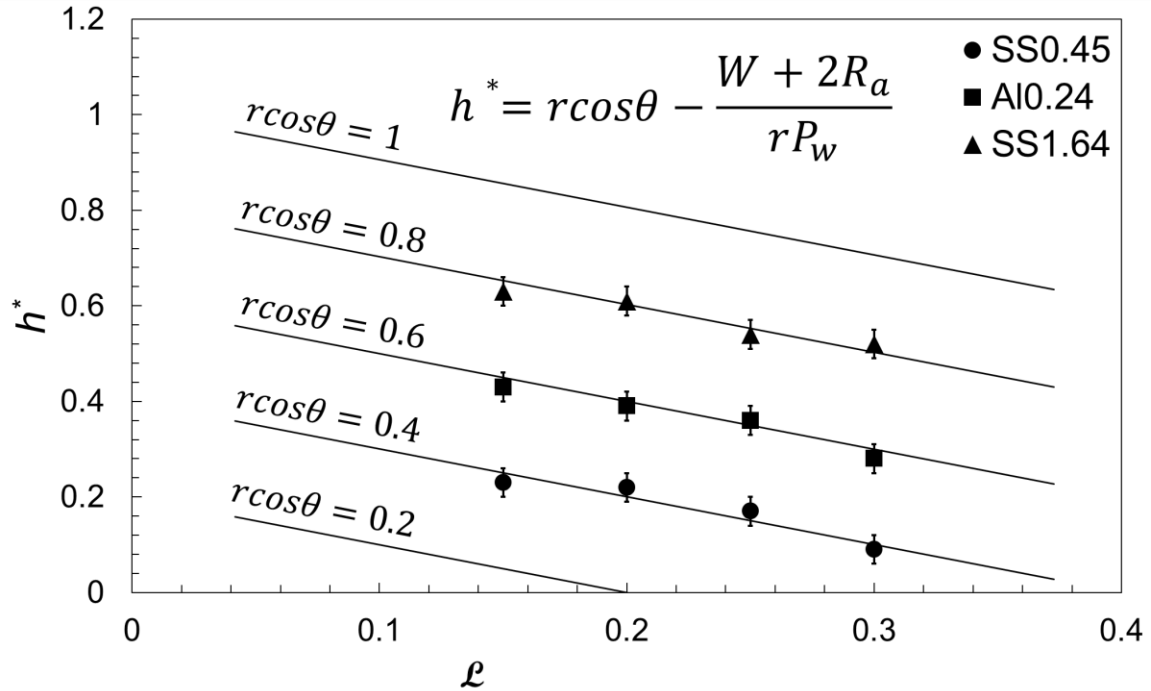


Figure 39. The unifying non-dimensional form of capillary height, Eq. 26, as a function of the characteristic length scale, contact angle, and surface roughness, as compared to our experimental data.

3.7. Hydrophilicity and hydrophobicity

Contact angle of a liquid on a solid surface, the angle that forms when a drop of liquid is placed on a solid surface, can be between 0 and 180 degrees. The contact angle characterizes the wettability of a surface by a liquid. The smaller the contact angle, the higher the wettability, and consequently, the higher the capillary rise. The contact angle is defined as the angle a drop of liquid makes when introduced on a solid surface. The contact angle discussed here is the equilibrium contact angle of water on a solid surface. When the contact angle is below 90 degrees, the liquid-solid interaction is said to be hydrophilic or wetting. Superhydrophilic interaction is where water makes almost no contact angle on the solid surface. Liquid-solid interactions that make contact angle over 90 degrees are called non-wetting, or hydrophobic. A superhydrophobic surface has an almost 180 degrees contact angle and is perfectly non-wetting. These definitions are summarized in Figure 40.

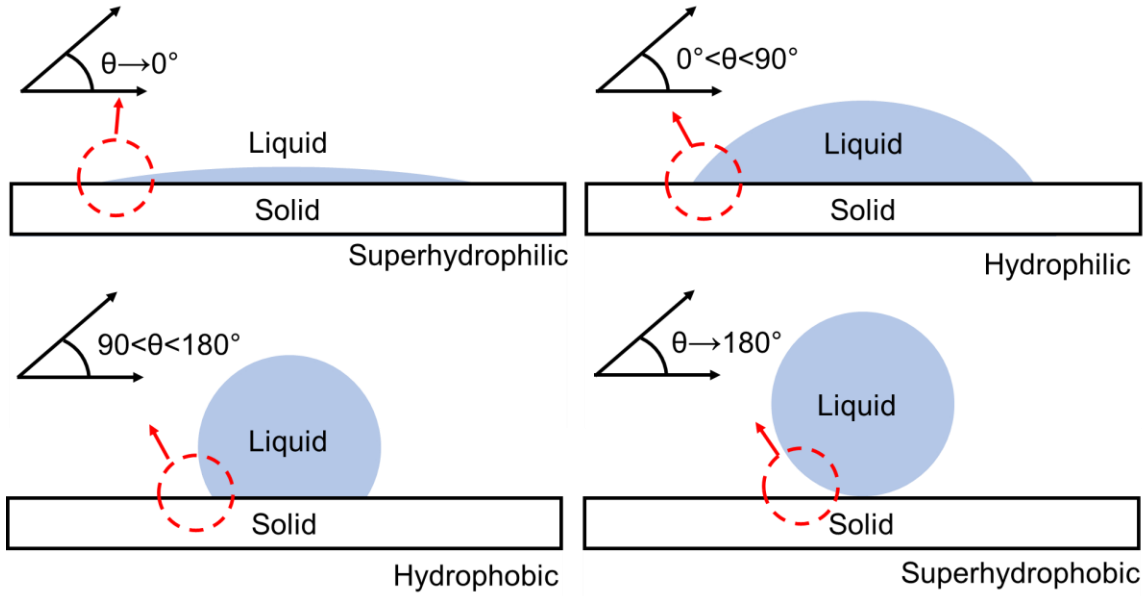


Figure 40. Contact angle definition for different wetting properties. Contact angle below 90 degrees: hydrophilic/wetting, almost no contact angle: superhydrophilic/perfectly wetting, contact angle over 90 degrees: hydrophobic/non-wetting, an almost 180 degrees contact angle: superhydrophobic/perfectly non-wetting.

3.8. Profilometer and sandblasting

Surface roughness is the degree of how uneven a solid surface is. Roughness can be defined by various parameters, and measured by different means, such as R_a and R_z , and measured by a profilometer. R_a is the arithmetic average deviation of the roughness profile from the mean line, and R_z is the arithmetic average of peak to valley heights of the profile. The unit for both roughness parameters is μm (micro-meters). A profilometer uses the following relationships to determine the roughness parameters [86]:

$$R_a = \frac{1}{l} \int_0^l |z(x)| dx \quad (27)$$

$$R_z = \frac{\sum_{i=1}^n \max z(x) + |\min z(x)|}{n} \quad (28)$$

Where l is the sampling length, n is the number of peaks or valleys, x is the coordinate along which the profilometer moves, and z is the coordinate perpendicular to x .

A contact profilometer measures the peaks and valleys of the solid surface by moving a tracing stylus, usually made of diamond or sapphire. Here, a Mitutoyo SJ-400 profilometer was used to measure the surface roughness. The tip of the stylus moves in a line across the surface. Figure 41 shows the surface roughness measurement using Mitutoyo SJ-400 profilometer.

The stainless steel and aluminum sheets were purchased as “smooth” sheets with a fine finish. They were then sandblasted and roughened. Figure 42 shows the metallic surfaces used for roughness measurement. The samples include sandblasted rough aluminum, smooth aluminum, sandblasted rough stainless steel, and smooth stainless steel. The inset takes a closer look at the surface of each sheet. Figure 43 shows the 3D-printed grooved samples used for roughness measurement. The samples include 3D-printed stainless steel, and 3D-printed SLA polymer. The opposite flat side of each sample was used for roughness and contact angle measurement. The rationale is that both sides would have the same surface roughness.

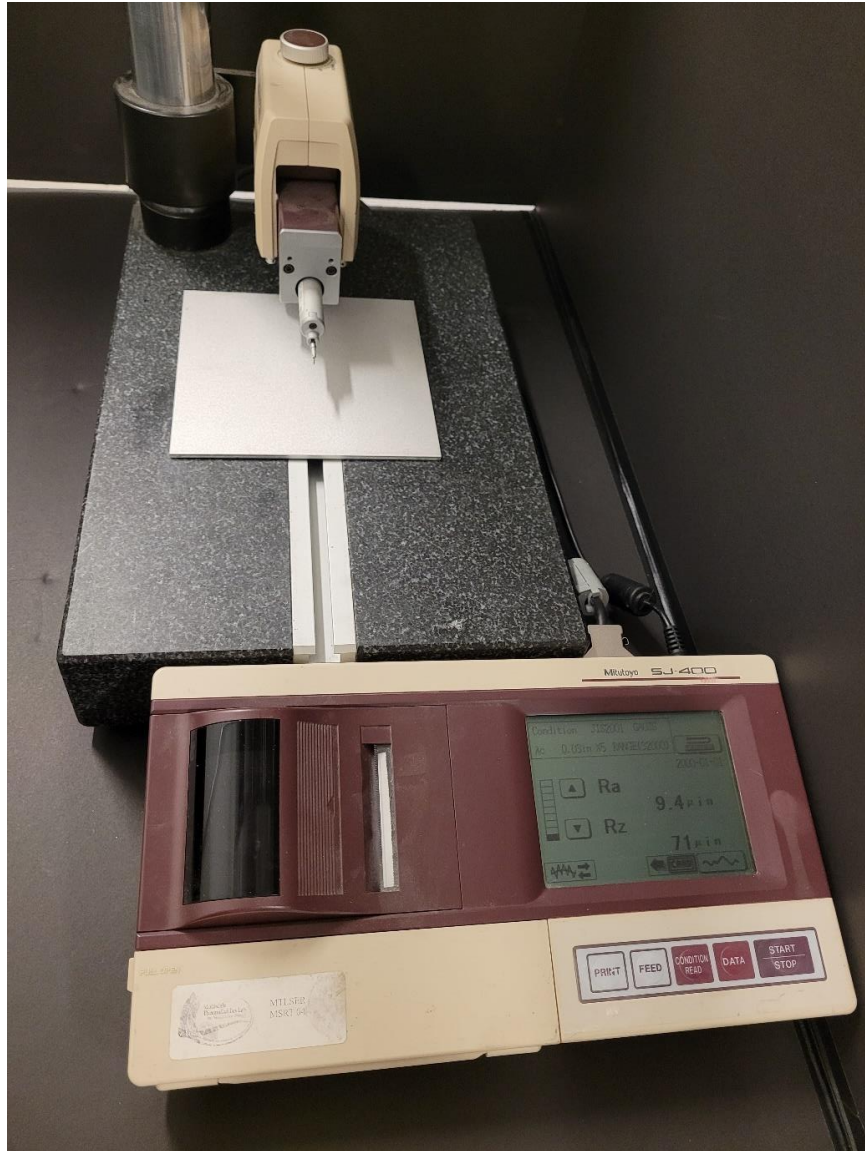


Figure 41. Surface roughness measurement using Mitutoyo SJ-400 profilometer.

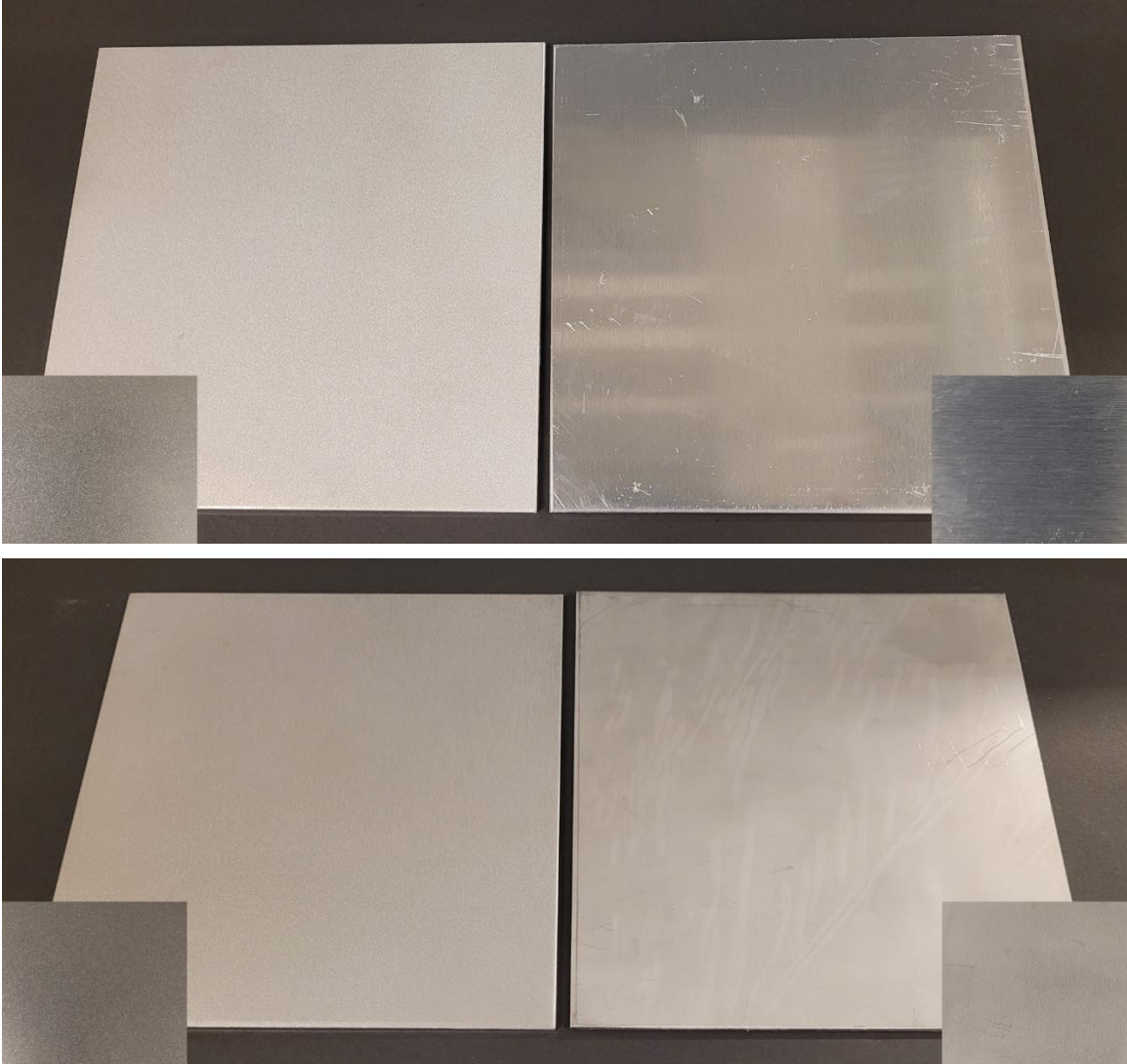


Figure 42. Smooth and rough metallic surfaces used for roughness and contact angle measurement. Top left: sandblasted rough aluminum, Top right: smooth aluminum, Bottom left: sandblasted rough stainless steel, Bottom right: smooth stainless steel. The inset takes a closer look at the surface of each sheet.

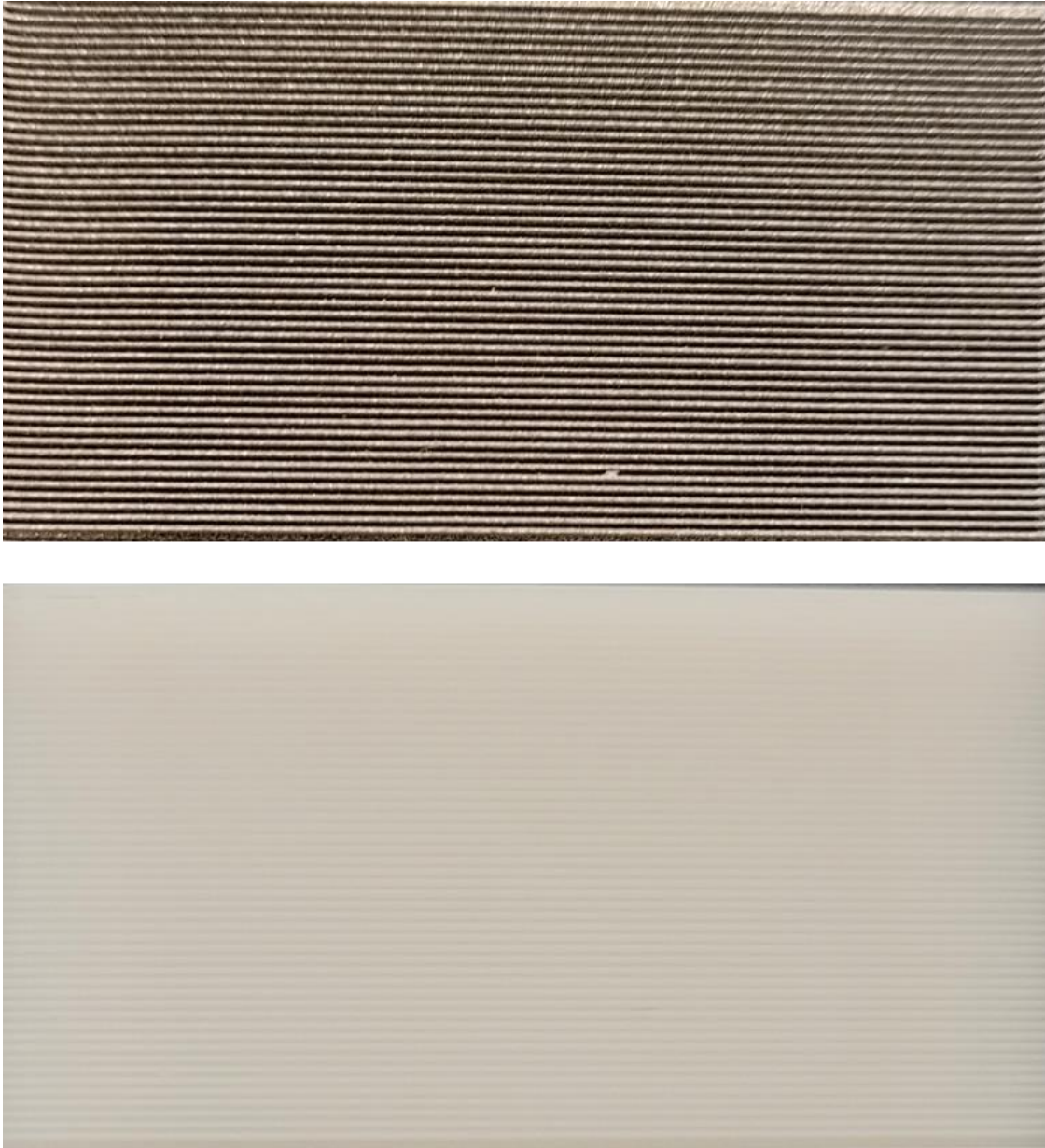


Figure 43. 3D-printed grooved samples used for roughness and contact angle measurement. Top: 3D-printed stainless steel, Bottom: 3D-printed SLA polymer. The opposite side of each sample was used for roughness and contact angle measurement.

3.9. Conclusion to the chapter

A previously proposed unifying, non-dimensional model for capillary rise in micro-grooves was extended to include the effect of surface roughness and was experimentally validated. A new characteristic length scale was proposed that includes all the key geometrical parameters, i.e., micro-grooves height, width, and surface roughness. Furthermore, it was shown that there exists a characteristic length scale, for each modified contact angle value, above which the capillary action would not occur ($\mathcal{L} > r \cos\theta$). The proposed unifying model can be used for any given micro-groove geometry and condition for designing heat pipes, vapor chambers, and capillary-assisted evaporators as well as biomedical devices.

Various metallic and polymer surfaces were fabricated and prepared, including aluminum, stainless-steel, natural graphite sheet, and 3D-printed stainless-steel and polymer. Experimental validation was performed using a profilometer and sessile drop to measure samples surface roughness and the contact angles, respectively. Results showed that there was a less than a 10% relative difference between the new unifying model and our experimental data. It was observed that a triangular cross-section micro-groove, as opposed to a rectangular one, offers a higher wetted area (and capillary height). Wenzel's model held true for most experimental data. It was concluded that to increase the capillary height in a micro-groove, the wettability of a solid surface can be increased by decreasing its contact angle by roughening the substrate. This is especially advantageous in applications, where compactness and miniaturization are key.

Chapter 4.

Heat transfer mechanisms of CALPE and governing equations

As discussed in chapter 2, and shown experimentally in chapter 3, alternative geometries increase the wetted area, and the active heat transfer area, in a CALPE. To assess the heat removal capacity of a CALPE, it is imperative to understand its heat transfer phenomenon on a fundamental level. Evaporation in a CALPE is a complex hydrodynamic and heat transfer mechanism. In this chapter, a detailed study of heat transfer in CALPE is conducted and governing equations for thin film evaporation, natural conduction, and two-dimensional conduction heat transfer are presented. Analytical models are first given for rectangular cross-sections, for its provability, and then extended to alternative geometries. Experimental and analytical studies have been carried out for different geometries. Jiao et al. [91] considered a trapezoidal groove in heat pipes. They developed a model that considers the effects of groove geometry, thin film evaporation, and contact angle. Their results show a strong dependence of thin film evaporation on groove geometry. They verified their findings with an experimental approach on a grooved heat pipe. Xu and Carey [92] presented an analytical model for thin film evaporation in a triangular capillary microgroove. Their correlation relates the Nusselt number to the fluid properties, groove geometry, and the disjoining pressure. They also reported experimental data for the evaporative in a microgroove. Their data suggests a strong relationship between the disjoining pressure and evaporation in a microgroove. Khrustalev and Faghri [93] published a model to describe the heat transfer in thin liquid films of the heat pipes with curved capillary grooves. Their model includes the interfacial thermal resistance, disjoining pressure, and surface roughness. They compared their numerical results to existing experimental data and reported that the surface roughness and interfacial thermal resistance are important to model the heat transfer coefficient in a capillary groove. Hanlon and Ma [94] developed a two-dimensional model for the overall heat transfer in a sintered wick structure. Their results show that thin film evaporation, which only takes place at the top of the meniscus, is the enhancement mechanism of evaporation and depends on the particle size, the porosity, and the wick structure thickness. They verified their analytical models with an experimental approach. Consequently, the thin film evaporation in a capillary groove has been the center of attention in many research due to its high heat

flux. Potash and Wayner [95] studied the heat transfer process in an evaporating two-dimensional meniscus with an adsorbed non-evaporating thin film. They presented their result for the meniscus profile, and heat flux. Wayner et al. [96] calculated the evaporation heat transfer coefficient of a thin film. Schonberg and Wayner [97] studied the thin film evaporation analytically and concluded that the film thickness is a function of film position. They presented analytical results for the film profile. Schonberg et al. [98] modeled the evaporation in a microchannel meniscus using the augmented Young-Laplace equation. They concluded that the heat flux is a function of the van der Waals force. Ma et al. [99] presented an analytical model for fluid flow and heat transfer in the thin film region of a meniscus. Their approach includes the inertial force, disjoining pressure, surface tension, and curvature. They used an order analysis to simplify their model. They concluded that the effect of the inertial force is negligible. They also reported that for a given superheat degree, a maximum heat flux exists in an extended meniscus. Xia et al. [22] provided an analytical solution to evaporation heat transfer in an inclined circumferential micro groove with rectangular cross sections. Their model considers natural convection, heat transfer in the intrinsic meniscus, and evaporation in thin film region. They also reported experimental data for enhanced tubes with circumferential rectangular micro grooves and demonstrated the influence of the tubes' geometries and operating parameters on the evaporation heat transfer [21]. Cheng et al. [100] presented an analytical model for the thin film evaporation and conductive heat transfer in the bulk region of a capillary meniscus. Their model considers the effect of contact angle and wall superheat on evaporation heat transfer. They concluded that the conductive heat transfer in the bulk region can be neglected for small superheat degrees. It is evident from this literature review that although common geometries have been studied, and their heat transfer models are published, the optimal geometry to maximize the heat removal capacity of a capillary groove has not been identified.

4.1. Fundamental definitions

Figure 44 shows a schematic of a rectangular groove on a finned wall. Capillary force pulls the water along the channel height against gravity. Surface tension inside the groove causes the liquid/vapor interface to form a meniscus, leading to a pressure difference across the interface. The following equation is used to determine this pressure difference [101]:

$$P_l = P_v - \frac{A}{6\pi\delta^3} - \sigma\kappa \quad (29)$$

where σ is the surface tension, κ meniscus curvature, and P_l and P_v the liquid and vapor pressure, respectively. A is a constant number (the Hamaker constant). δ is the film thickness.

Figure 45 demonstrates the thin film evaporation site in a rectangular groove. In a CALPE, evaporation occurs at the liquid/vapor interface and the presence of this thin film means that most of the heat transfers through this small region as it has the lowest thermal resistance [95]. The thin film evaporation region is surrounded by two other regions. As the film thickness decreases, the disjoining pressure, $\frac{A}{6\pi\delta^3}$, becomes dominant, no evaporation occurs, and the superheated liquid is adsorbed to the solid surface [22]. When the film thickness increases, the liquid exists in bulk in the meniscus. The mechanism in this region is a two-dimensional conductive heat transfer. The heat transfer in the thin film region is orders of magnitude larger than that in the bulk region [100].

The film thickness in the non-evaporating region can be calculated by [101]:

$$\delta_0 = \left(\frac{AT_v}{6\pi\rho h_{fg}(T_w - T_v)} \right)^{1/3} \quad (30)$$

where T_v and T_w are the vapor and wall temperature, respectively, and h_{fg} is the heat of evaporation. The meniscus curvature can be found using the following equation [101]:

$$\kappa = \frac{\frac{d^2\delta}{dx^2}}{\left[1 + \left(\frac{d\delta}{dx} \right)^2 \right]^{3/2}} \quad (31)$$

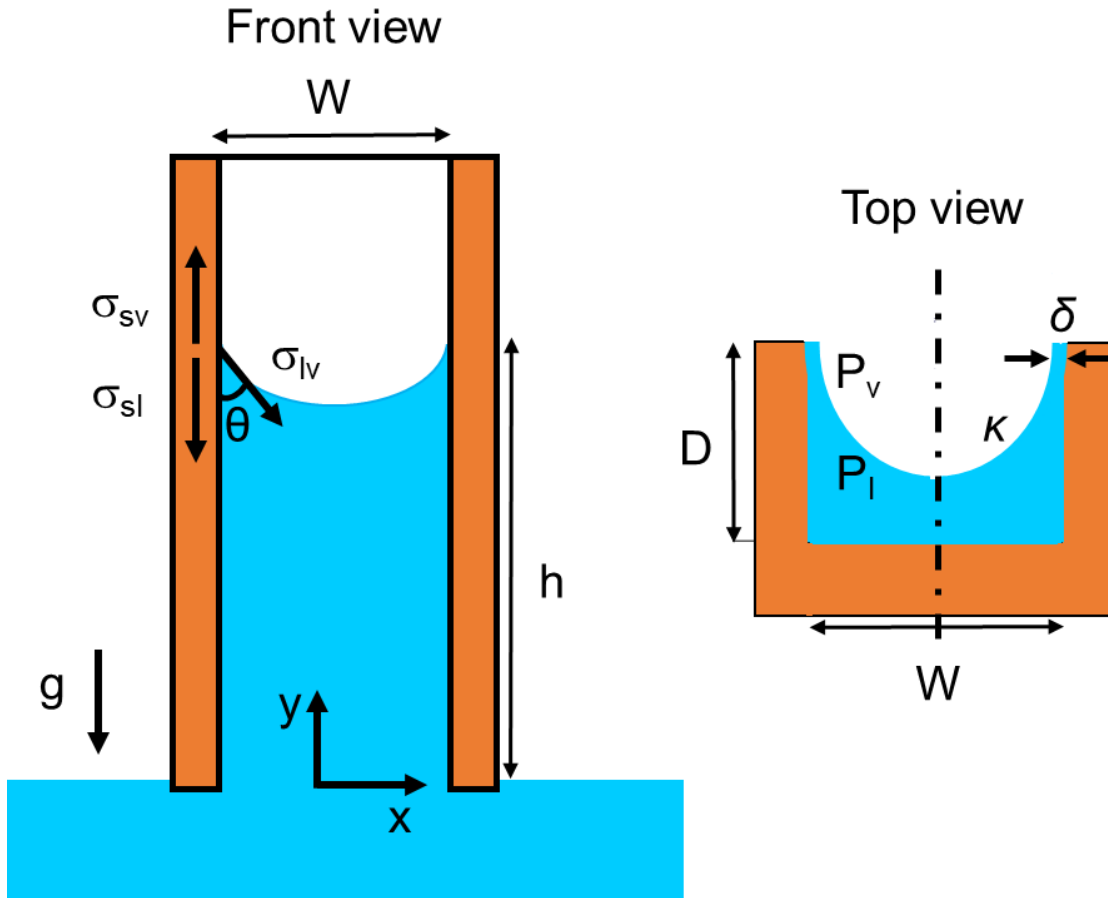


Figure 44. Schematic of a rectangular groove on a finned wall. θ is contact angle, σ surface tension, κ meniscus curvature, P_l and P_v the liquid and vapor pressure, respectively. W , D , and h are groove width, depth, and height respectively.

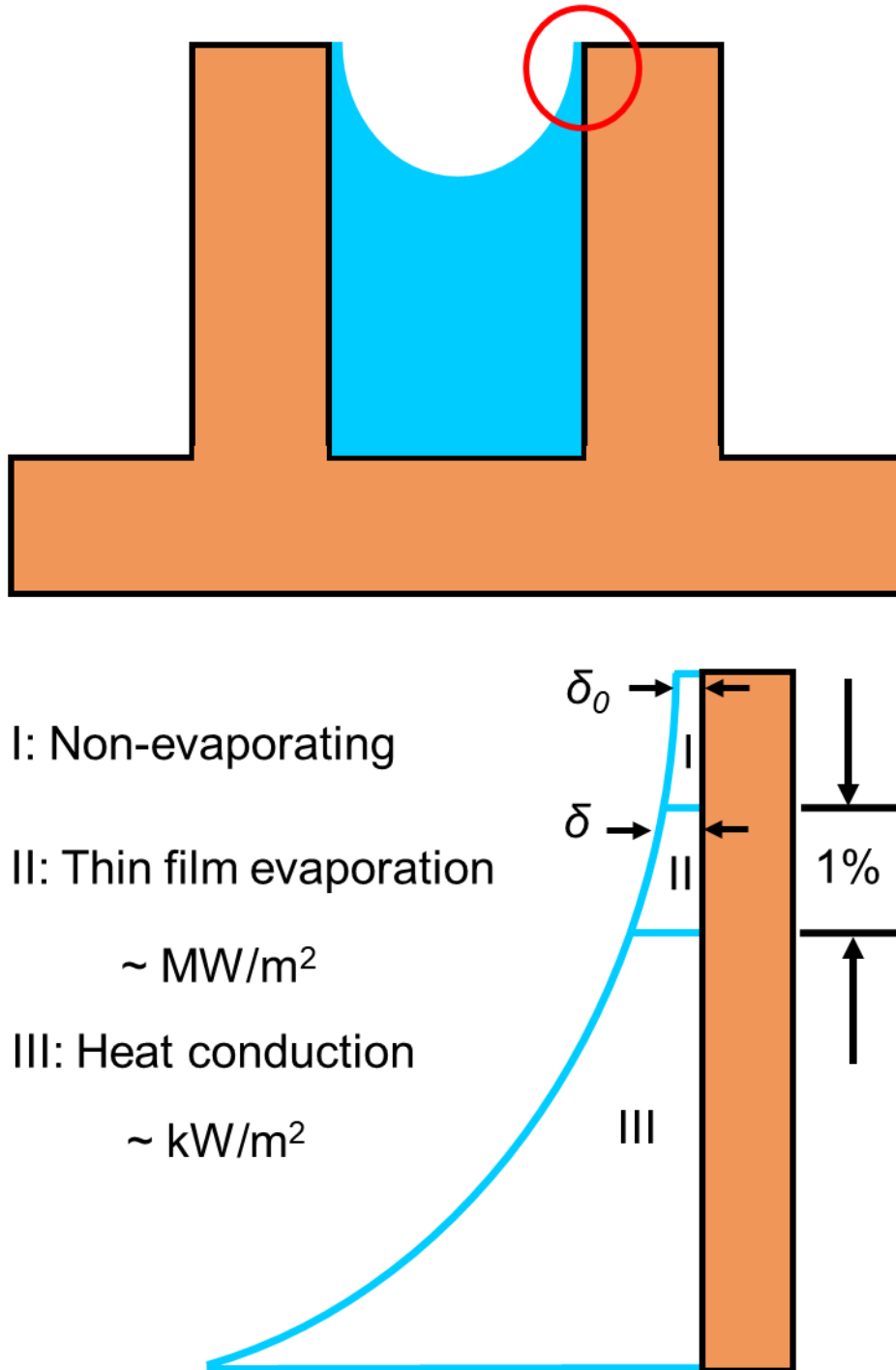


Figure 45. Schematic of thin film evaporation site in a rectangular groove. The thin film evaporation heat transfer is orders of magnitude larger than the conductive heat transfer.

4.2. Assumptions

The following assumptions are made in the heat transfer modelling of CALPE, based on the previous definitions:

- Constant thermophysical properties;
- Constant vapor pressure (P_v);
- Uniform and constant wall temperature (T_w);
- Constant, meniscus curvature, κ , in the bulk region;
- No evaporation in non-evaporating region;
- Steady state heat transfer;
- Saturation condition at the liquid-vapor interface;
- Convection heat transfer neglected within the meniscus.

4.3. Natural convection in liquid pool

Figure 46 shows a schematic of a finned wall partially submerged in a pool of water. Consequently, natural convection occurs due to the temperature difference between the pool of water and the finned wall. Due to the low pressure and low temperature difference between the finned wall and the pool, nucleate boiling is not present. Natural convection can be described by the Grashof number, Gr [102]:

$$Gr = \frac{g\beta(T_w - T_{sat})h^3}{\nu^2} \quad (32)$$

where g is gravitational acceleration, β is the coefficient of thermal expansion, T_w is the average wall temperature, T_{sat} is the saturation temperature (liquid pool), h is the capillary height, and ν is the kinematic viscosity. The Nusselt number, Nu can be found by [90]:

$$Nu = 0.48(Gr Pr)^{1/4} \quad (33)$$

Prandtl number, Pr , is defined as:

$$Pr = \frac{\mu c_p}{k} \quad (34)$$

and the natural convection heat transfer coefficient, h_{nc} , can be calculated by:

$$h_{nc} = \frac{Nu c_p}{k} \quad (35)$$

The heat transfer due to the natural convection can be calculated by having the heat transfer coefficient, h_{nc} , and heat transfer area, A_{nc} [102]:

$$Q_{nc} = h_{nc} A_{nc} (T_w - T_{sat}) \quad (36)$$

Both natural convection and two-dimensional conductive heat transfer heat transfer are orders of magnitude smaller than the thin film heat transfer.

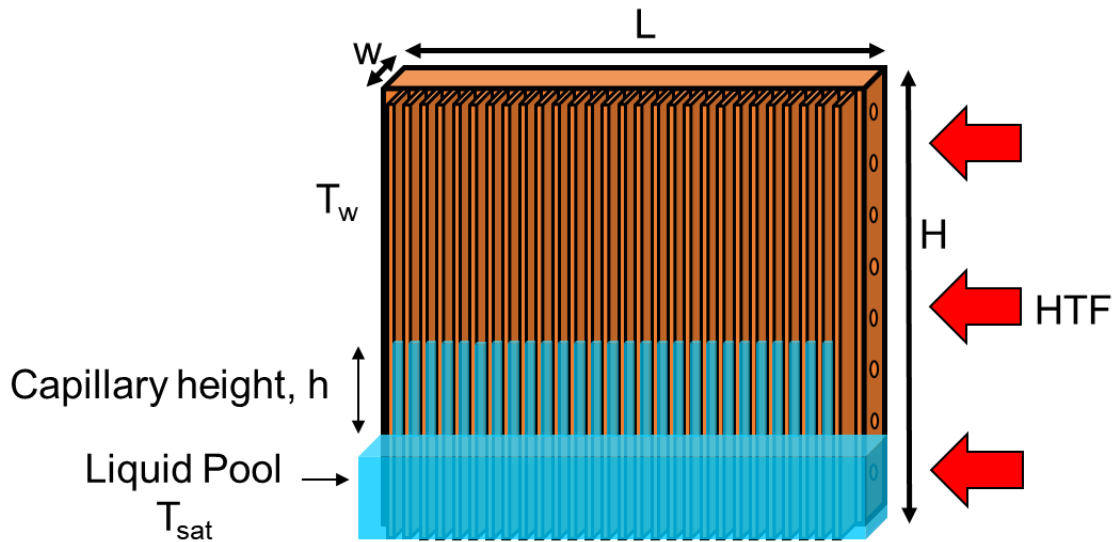


Figure 46. Schematic of a finned wall partially submerged in a liquid pool. Natural convection occurs between the wall and the liquid pool due to the temperature difference of $T_w - T_{sat}$

4.4. Two-dimensional conductive heat transfer in the bulk region

In this section, the relative importance of the two-dimensional conductive heat transfer in the bulk region of CALPE meniscus is investigated. An analytical solution to the two-dimensional conductive heat transfer is given. The assumptions mentioned before are used in the solution, along with additional assumptions of:

- i) the conductive heat transfer is considered two-dimensional, with isothermal assumption along the capillary channel, and
- ii) the interface temperature is considered constant and uniform.

Figure 47 depicts the solution domain for two-dimensional conductive heat transfer in CALPE meniscus with both dimensional and non-dimensional parameters. The surface tension leads to the curved shape of the liquid/vapor interface. The convective heat transfer is negligible in this region, therefore, the heat transfer through the bulk region is assumed to be only conductive. The liquid temperature distribution in the bulk region can be found the two-dimensional, steady-state conduction equation [100].

The governing conduction equation is given as Eq. 37:

$$\frac{\partial^2 T}{\partial x^2} + \frac{\partial^2 T}{\partial y^2} = 0 \quad (37)$$

Eq. 22 is subjected to the following boundary conditions:

$$\begin{cases} T = T_w, & \text{at } x = \pm W \\ T = T_w, & \text{at } y = 0 \\ T = T_{lv}, & \text{at } y = H^* \end{cases} \quad (38)$$

The height of the meniscus with respect to the bottom of the fin can be calculated by:

$$H^* = D - r(\cos \alpha - \cos \theta) \quad (39)$$

where α and θ are defined as:

$$\begin{cases} \alpha = \arcsin\left(\frac{x}{r}\right) \\ \theta = \arcsin\left(\frac{W}{r}\right) \end{cases} \quad (40)$$

Eq. 37 can be non-dimensionalized using the following non-dimensional parameters:

$$\begin{cases} \eta = \frac{x}{W} \\ \xi = \frac{y}{D} \\ K = \frac{W}{D} \end{cases} \quad (41)$$

where W is the width and D is the depth of the groove. The non-dimensional temperature is defined as [100]:

$$\phi(\eta, \xi) = \frac{T_w - T(\eta, \xi)}{T_w - T_{lv}} \quad (42)$$

where T_{wall} is the wall temperature, and T_{lv} is the liquid/vapor interface temperature. Eq.37 can be rewritten with non-dimensional parameters as Eq. 43:

$$\frac{\partial^2 \phi}{\partial \eta^2} + K^2 \frac{\partial^2 \phi}{\partial \xi^2} = 0 \quad (43)$$

The non-dimensional boundary conditions are given as:

$$\begin{aligned} \phi &= 0, \text{ at } \xi = 0, \eta = \pm 1 \\ \phi &= 1, \text{ at } \xi = \xi^* \end{aligned} \quad (44)$$

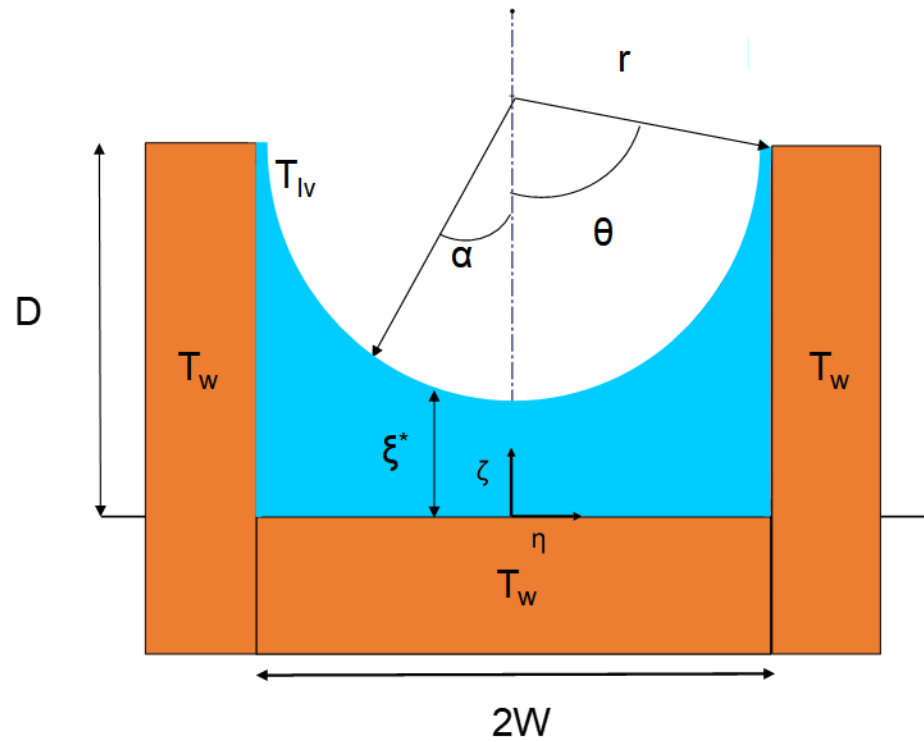
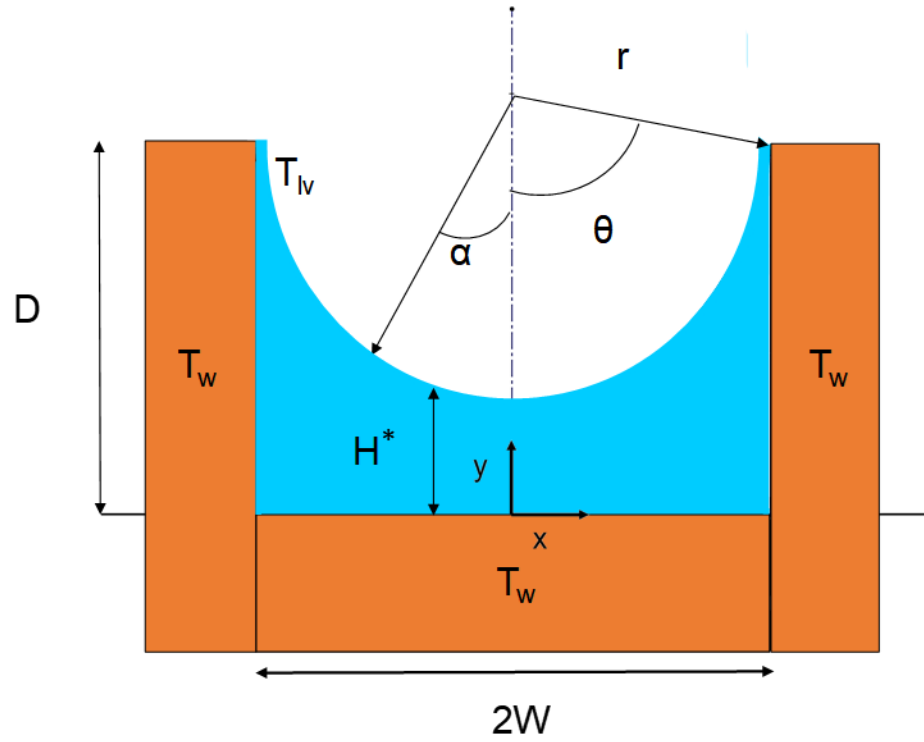


Figure 47. Schematic of two-dimensional conductive heat transfer solution domain in CALPE meniscus with top: dimensional, and bottom: non-dimensional parameters.

4.4.1. Analytical solution to the two-dimensional conductive heat transfer

Using the separation of variables, the non-dimensional temperature, ϕ , can be expressed as [100], [22]:

$$\phi(\eta, \xi) = \sum_{n=1}^{\infty} C_n \cos\left(\frac{2n-1}{2} \pi \eta\right) \sinh\left(\frac{2n-1}{2K} \pi \xi\right) \quad (45)$$

To solve Eq. 45, the meniscus is divided into $i \times j$ nodes where the coordinate of each node is (η_i, ξ_j) . The meniscus height, and the coefficient $C_{n,i}$, are calculated for each η_i . The height of the meniscus ξ_i^* is given by:

$$\xi_i^* = 1 - \frac{1}{K} (\cos(\text{asin}(\eta_i WK)) - \cos(\text{asin}(WK))) \quad (46)$$

The non-dimensional heat flux is given as:

$$q_{sides}^* = -\frac{Wq''_{sides}}{k(T_{wall}-T_{lv})} = \frac{\partial \phi}{\partial \eta}, \eta = \pm 1 \Rightarrow -\sum_{n=1}^{\infty} \frac{2n-1}{2} \pi C_n \sin\left(\pm \frac{2n-1}{2} \pi\right) \sinh\left(\frac{2n-1}{2K} \pi \xi\right) \quad (47)$$

$$q_{bottom}^* = -\frac{Dq''_{bottom}}{k(T_{wall}-T_{lv})} = \frac{\partial \phi}{\partial \xi}, \xi = 0 \Rightarrow \sum_{n=1}^{\infty} \frac{2n-1}{2K} \pi C_n \cos\left(\frac{2n-1}{2} \pi \eta\right) \quad (48)$$

The total conductive heat transfer is the sum of $2 \times |q_{sides}^*| + q_{bottom}^*$ since the conductive heat transfer occurs on both sides of the groove, as well as its bottom.

For demonstration, the model above is solved for a given operating condition, fin geometry, and physical properties. The material of the fins is copper. Water is chosen as the liquid. The results are for a saturation temperature of $T_{sat}=9$ °C, and wall temperature of $T_{wall}=10$ °C. Four sample results are given. A comparison is made between the conductive heat transfer rate to the bottom of the meniscus vs that to the side walls. Temperature contour is given showing the meniscus and the temperature evolution from wall temperature to saturation temperature. Table 5 summarizes the properties of water used in the model demonstration.

Table 5. Thermo-physical properties of water at 283 K

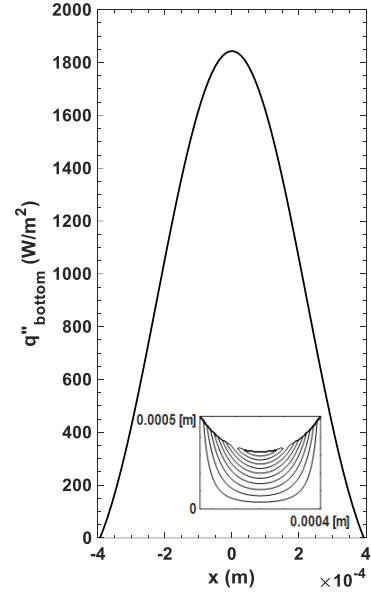
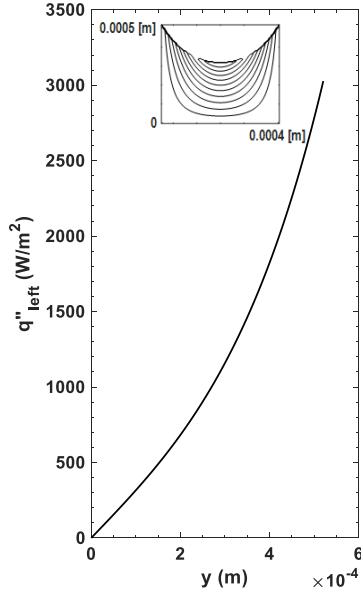
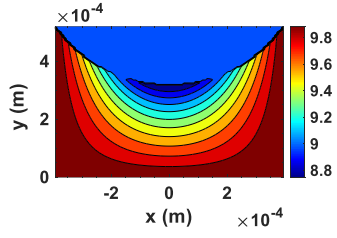
Property	Value
Thermal conductivity, (W/mK)	0.596
Heat of evaporation, (J/kg)	2477.2
Dynamic viscosity, (Pa.s)	$(-3.8 \times 10^{-5} \times T_{sat}) + 0.0121$
Kinematic viscosity, (m ² /s)	$(-3.94 \times 10^{-8} \times T_{sat}) + (1.26 \times 10^{-5})$
Specific heat, (J/kgK)	4186
Liquid Density, (kg/m ³)	999.8
Vapor Density, (kg/m ³)	0.0094

Figure 48 shows the temperature distribution for four different aspect ratios: a fin height of 0.5 mm and fin spacing of 0.4 mm, a fin height of 0.7 mm and fin spacing of 0.11 mm, a fin height of 1.2 mm and fin spacing of 0.224 mm, and a fin height of 2 mm and fin spacing of 1 mm, leading to aspect ratios of 0.8, 0.157, 0.186, and 0.5, respectively.

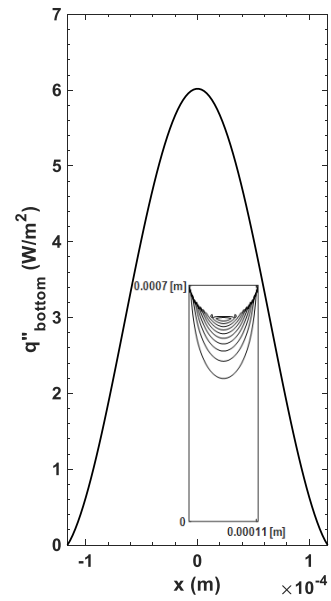
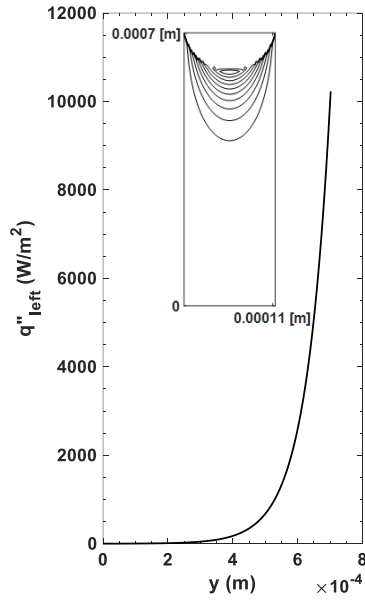
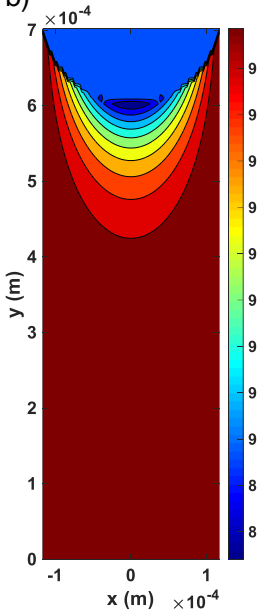
It is seen from Figure 48 that the temperature is close to the wall temperature of 10 °C in most of the meniscus. Contours of temperature and isotherms are shown near the liquid/vapor interface. The heat flux to the bottom and the side walls are also shown in Figure 48. Only one side wall is shown. The opposite side wall's heat flux is identical. The side wall heat flux starts from zero at $y=0$ and gradually increases toward the top of the meniscus. It reaches a maximum at the liquid/vapor interface. Figure 48 also shows the heat flux to the bottom. The heat flux to the bottom is negligible when the aspect ratio is small. It becomes meaningful when the aspect ratio approaches 1, as seen in Figure 48 (a). The heat flux to the bottom starts from zero at $x=0$, reaches a maximum at the center line, and gradually decreases to reach zero again at the opposite side.

Two conclusions are made based on these results. First, the conductive heat transfer is orders of magnitude smaller than thin film evaporation in CALPE. A comparison between the natural convection, conductive heat transfer, and thin film evaporation is given later, for comparison. Second, the heat flux to the sidewalls is greater than that to the bottom wall, unless the aspect ratio approaches 1.

a)



b)



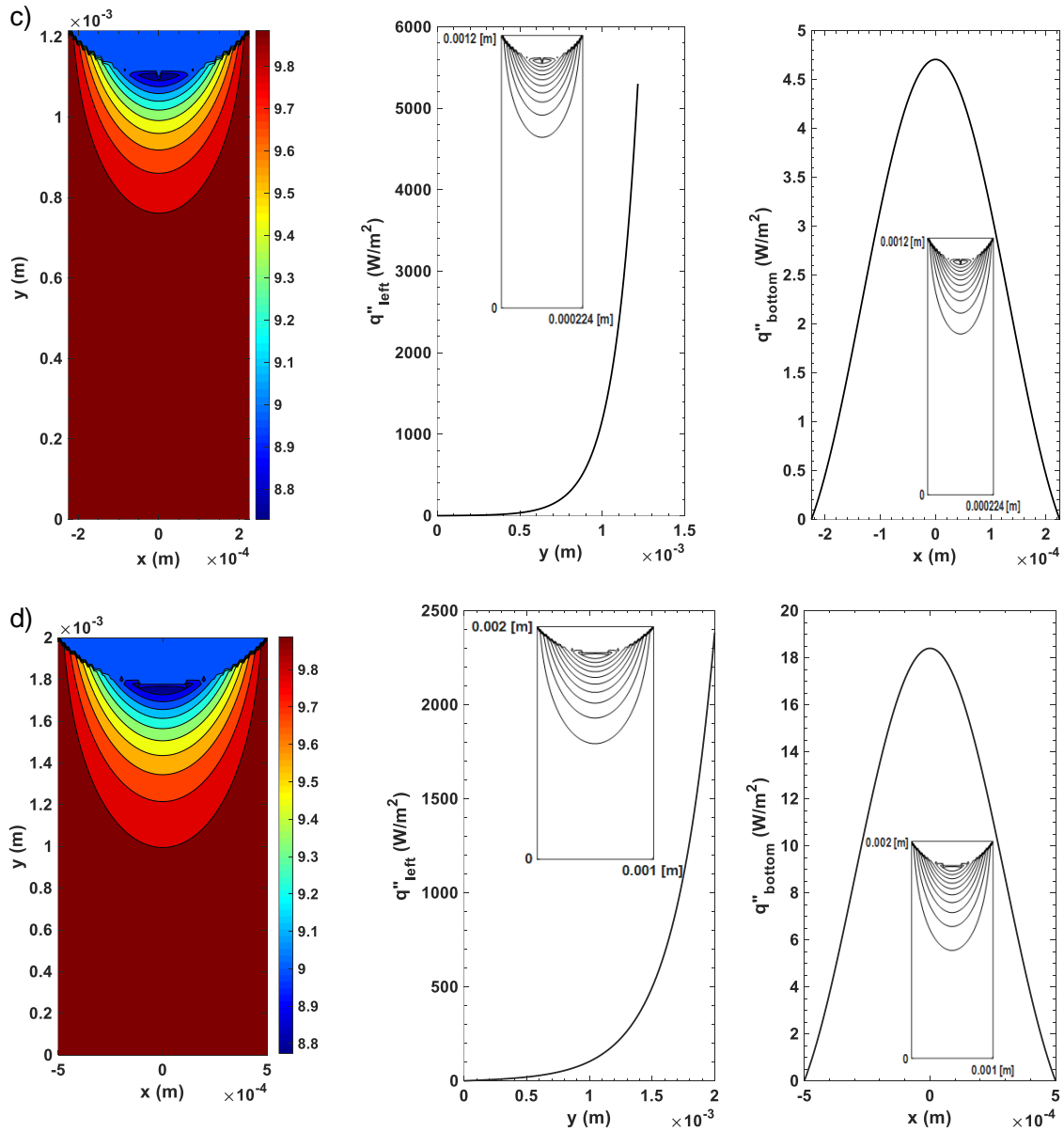


Figure 48. Temperature distribution, sides, and bottom heat flux for two-dimensional conductive heat transfer in a capillary meniscus, $T_{sat}=9$ °C and $T_{wall}=10$ °C. a) fin height 0.5 mm, fin spacing 0.4 mm, b) fin height 0.7 mm, fin spacing 0.11 mm, c) fin height 1.2 mm, fin spacing 0.224 mm, d) fin height 2 mm, fin spacing 1 mm.

4.5. Multi-objective genetic algorithm optimization

As seen in the previous section, the groove geometry affects the heat transfer in a way that an optimization scheme can be incorporated to maximize heat transfer. In this section a genetic algorithm (GA) code is used to optimize the multi-objective functions governing the two-dimensional conductive heat transfer, with constraints. It is not necessary to apply such optimization for natural convection since it has a positive direct relationship with the parameters affecting it, namely, h_{nc} , A_{nc} , $T_w - T_{sat}$. Optimization is also given for thin film evaporation, later.

In a genetic algorithm optimization scheme, a natural selection process that mimics biological evolution is used. A population of potential solutions is randomly generated and iteratively evolved toward better solutions. By increasing the population size, the accuracy enhances, and the number of iterations decreases. The crossover rate was close to the default value (0.8), and the effect of mutation functions were negligible.

The set of functions for optimization are given below. The total heat transfer and heat transfer coefficient are to be maximized:

$$\begin{aligned} \min_{x_i} F(x_i) &= [\text{objective1}(x_i); \text{objective2}(x_i)] \\ \text{where, } \text{objective1}(x_i) &= - Q_{total}, \text{ and} \\ \text{objective2}(x_i) &= - h_{total} \end{aligned} \tag{49}$$

Where Q_{total} and h_{total} are total conductive heat transfer and heat transfer coefficient. The following three variables were considered:

x_1 : fin thickness, $0.0001(\text{m}) < x_1 < 0.001(\text{m})$

x_2 : fin height, $0.0001(\text{m}) < x_2 < 0.002(\text{m})$ (50)

x_3 : fin spacing, $0.0001(\text{m}) < x_3 < 0.001(\text{m})$

More details of the genetic algorithm optimization along with a set of potential optimized solutions are given in Appendix VII.

4.6. Thin film evaporation

The thin film evaporation takes place in a relatively small portion of the top of the meniscus. Assuming constant and uniform wall temperature distribution on the fin, constant vapor temperature, and a known meniscus radius, Figure 49 demonstrates a schematic of a rectangular groove and where the thin film evaporation occurs. First, the general governing equations for heat transfer are written based on the Navier-Stokes formulation, then, they are simplified through scale analysis to achieve their final form. Figure 50 provides a detailed view of the extended meniscus. It is seen that the capillary meniscus can be divided into three regions; I: non-evaporating, II: thin film evaporation, and III: bulk region. The non-evaporating region has a small film thickness, in a way that the liquid adsorbs into the solid wall and evaporation does not occur. The liquid temperature is the same as the wall temperature and, therefore, is superheated. The thin film evaporation is where most of the heat transfer occurs. In this relatively small area, high heat flux is present due to the small film thickness and low thermal resistance. The bulk region has a larger film thickness and a higher thermal resistance, therefore, the heat transfer mechanism in this region is described by conduction, as presented earlier [101].

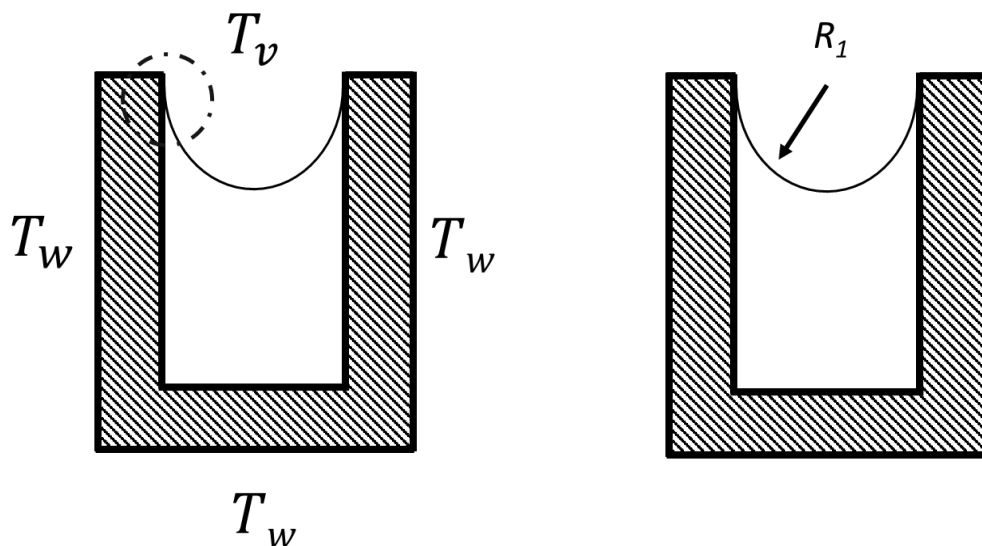


Figure 49. A schematic of a rectangular groove, temperature boundary conditions, and thin film evaporation location

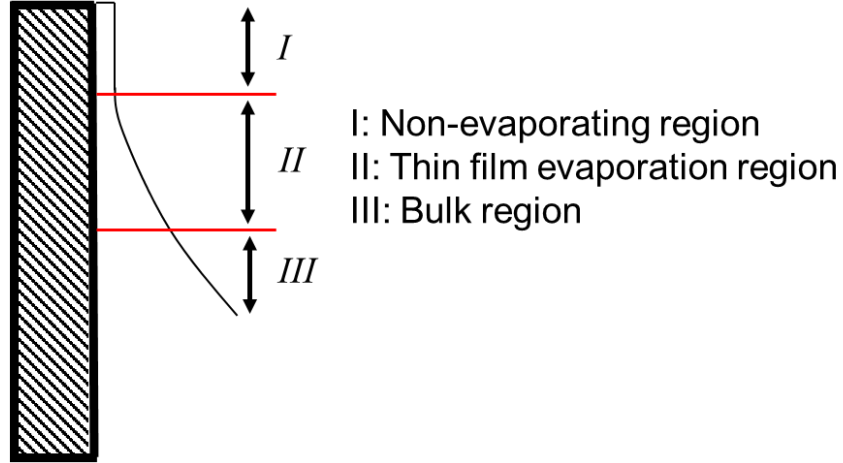


Figure 50. Detailed view of the extended meniscus in a rectangular groove and its division into I: non-evaporating, II: thin film evaporation, and III: bulk region

Let us consider a control volume as shown in Figure 51, selected from the thin film evaporation region shown in Figure 50. Pressures (P), forces ($P\delta$, τdx , g), film thickness (δ) and the evaporation mass flux (\dot{m}) are shown in Figure 51. The curvature of the meniscus where evaporation occurs is described by κ . Due to evaporation, the mass flux entering the control volume is equal to the summation of the mass flux exiting it through evaporation and, through the top of the control volume. A momentum conservation method is used to define the heat transfer and fluid flow in the control volume. The following equations of conservation of mass, x-momentum, and energy equation holds for the selected control volume [99]:

$$\frac{\partial u}{\partial x} + \frac{\partial v}{\partial y} = 0 \quad (51)$$

$$\rho_l u \frac{\partial u}{\partial x} + \rho_l v \frac{\partial u}{\partial y} = -\frac{A}{2\pi\delta^4} \frac{\partial \delta}{\partial x} + \sigma \frac{\partial \kappa}{\partial x} + \mu_l \frac{\partial^2 u}{\partial x^2} + \mu_l \frac{\partial^2 u}{\partial y^2} \quad (52)$$

$$u \frac{\partial T}{\partial x} + v \frac{\partial T}{\partial y} = \alpha \left[\frac{\partial^2 T}{\partial x^2} + \frac{\partial^2 T}{\partial y^2} \right] \quad (53)$$

where u and v are velocity in x and y direction, respectively. Appendix VIII provides the details of the conservation momentum model. After applying an order of magnitude analysis, Eqs. 52 and 53 can be rewritten as:

$$\rho_l u \frac{\partial u}{\partial x} + \rho_l v \frac{\partial u}{\partial y} = -\frac{A}{2\pi\delta^4} \frac{\partial \delta}{\partial x} + \sigma \frac{\partial \kappa}{\partial x} + \mu_l \frac{\partial^2 u}{\partial y^2} \quad (54)$$

$$u \frac{\partial T}{\partial x} + v \frac{\partial T}{\partial y} = \alpha \frac{\partial^2 T}{\partial y^2} \quad (55)$$

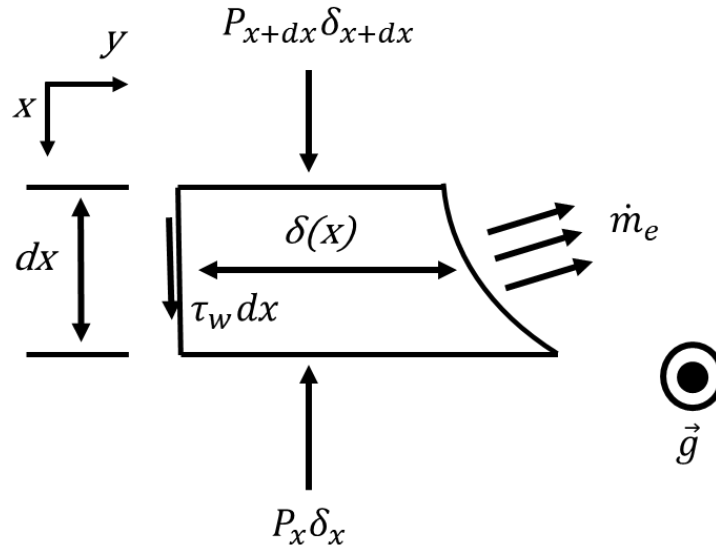


Figure 51. A control volume selected in the thin film region showing the forces, film thickness and the evaporation mass flux – rectangular groove

Eqs. 51, 54, and 55 are subjected to the following boundary conditions, using Figure 52 and appendix VIII as a reference:

$$\begin{cases} y = 0 \Rightarrow u, v = 0 \\ y = \delta \Rightarrow \frac{\partial u}{\partial y} = 0 \\ x = 0 \Rightarrow u, v = 0 \end{cases} \quad (56)$$

$$\begin{cases} y = 0 \Rightarrow T = T_w \\ y = \delta \Rightarrow T = T_v \\ x = 0 \Rightarrow T = T_w \end{cases} \quad (57)$$

$$\frac{d}{dx} \int_0^\delta \rho u \left(1 - \frac{c_p T}{h_{fg}} \right) dy - \frac{k}{h_{fg}} \frac{\partial T}{\partial y} \Big|_{y=0} = 0 \quad (58)$$

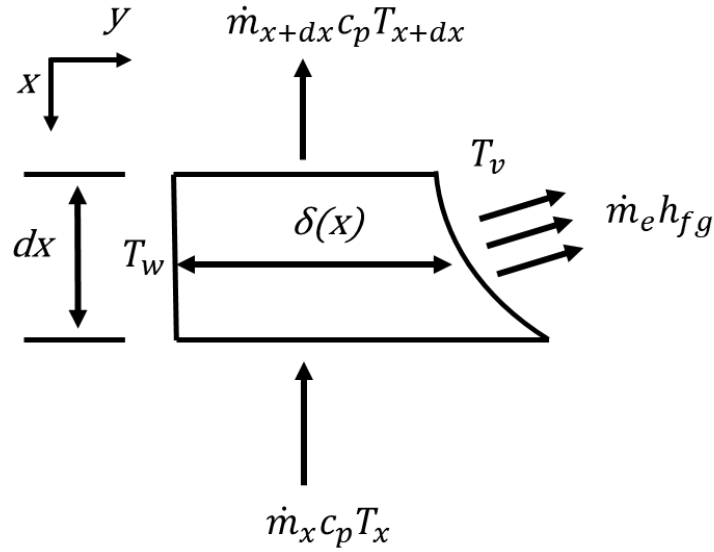


Figure 52. Schematic of the selected control volume in the thin film region; boundary conditions

The following non-dimensional parameters are used to non-dimensionalize Eqs. 54, 55, and 58:

$$\begin{cases} \eta = \frac{y}{\delta} \\ \zeta = \frac{x}{\delta} \\ u^* = \frac{u}{u_\delta} \\ v^* = \frac{v}{u_\delta} \\ \theta = \frac{T - T_v}{T_w - T_v} \end{cases} \quad (59)$$

where $u(x, \delta) = u_\delta(x)$. The non-dimensionalization process is given in appendix VIII along with an integral method to solve the above equations. The governing equations and their boundary conditions in their non-dimensional form is presented as the following:

$$b \left[\frac{u^*}{u_\delta} \frac{\partial u_\delta}{\partial \zeta} + \frac{\partial u^*}{\partial \zeta} \right] - \eta \frac{\partial \delta}{\partial \zeta} \frac{\partial u^*}{\partial \eta} + \frac{\partial v^*}{\partial \eta} = 0 \quad (60)$$

$$\rho_l u^* \left[-\eta \frac{\partial \delta}{\partial \zeta} \frac{\partial u^*}{\partial \eta} + b \left(\frac{\partial u^*}{\partial \zeta} + \frac{u^*}{u_\delta} \frac{\partial u_\delta}{\partial \zeta} \right) \right] + \rho_l v^* \frac{\partial u^*}{\partial \eta} = \frac{b}{u_\delta^2} \left(\sigma \frac{\partial \kappa}{\partial \zeta} - \frac{A}{2\pi\delta^4} \frac{\partial \delta}{\partial \zeta} \right) + \frac{\mu_l}{\delta u_\delta} \frac{\partial^2 u^*}{\partial \eta^2} \quad (61)$$

$$\left(v^* - \eta u^* \frac{\partial \delta}{\partial \zeta}\right) \frac{\partial \theta}{\partial \eta} + b u^* \frac{\partial \theta}{\partial \zeta} = \frac{\alpha}{\delta u_\delta} \frac{\partial^2 \theta}{\partial \eta^2} \quad (62)$$

where $b = \left(1 - \zeta \frac{\partial \delta}{\partial \zeta}\right)$. The non-dimensional boundary conditions are as follows:

$$\begin{cases} \eta = 0 \Rightarrow u^*, v^* = 0 \\ \eta = 1 \Rightarrow \frac{\partial u^*}{\partial \eta} = 0 \\ \zeta = 0 \Rightarrow u^*, v^* = 0 \end{cases} \quad (63)$$

$$\begin{cases} \eta = 0 \Rightarrow \theta = 1 \\ \eta = 1 \Rightarrow \theta = 0 \\ \zeta = 0 \Rightarrow \theta = 1 \end{cases} \quad (64)$$

$$\frac{d}{d\zeta} \int_0^1 b \rho \delta u^* u_\delta \left(1 - \frac{c_p}{h_{fg}} (\Delta T \theta + T_v)\right) d\eta - \frac{k \Delta T}{h_{fg}} \frac{\partial \theta}{\partial \eta} \Big|_{\eta=0} = 0 \quad (65)$$

After applying the integral method, given in appendix VIII, the following equations are to be solved to calculate the evaporative heat flux in a capillary meniscus:

$$\left(\frac{b}{2u'_\delta \mu_l} \left(\sigma \delta \kappa' - \frac{A \delta'}{2\pi \delta^3}\right) + \frac{\zeta}{2}\right) \delta' - 1 = 0 \quad (66)$$

$$b g' + \left(\frac{\zeta \delta' u'_\delta}{2u_\delta} - \frac{2\alpha}{\delta u_\delta} + b\right) g - \frac{\zeta \delta' u'_\delta}{2u_\delta} = 0 \quad (67)$$

$$0.1 \rho b \delta u_\delta c_p g' + \frac{k \Delta T}{h_{fg}} (g + 1) = 0 \quad (68)$$

where $\theta = 1 - \eta(g + 1 - g\eta)$, and g to be determined.

Similar approach was taken for a triangular groove, as shown in Figure 53 and Figure 54, with a selected control volume given in Figure 55.

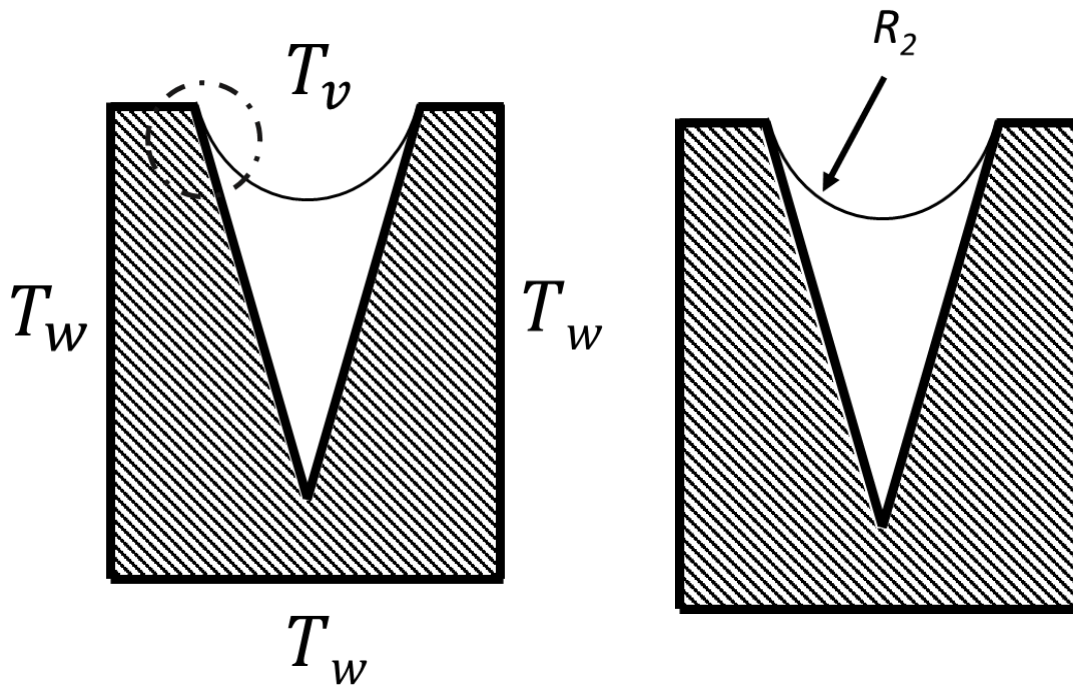


Figure 53. A schematic of a triangular groove, temperature boundary conditions, and thin film evaporation location

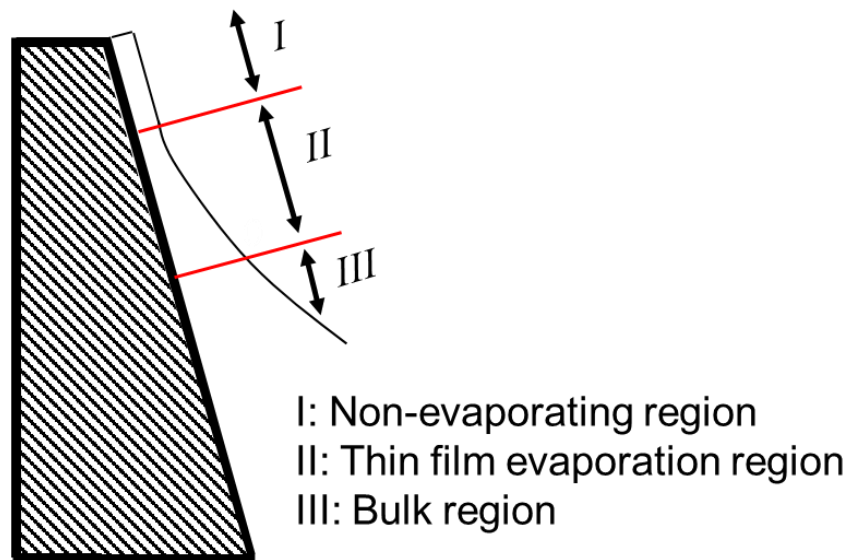


Figure 54. Detailed view of the extended meniscus in a triangular groove and its division into I: non-evaporating, II: thin film evaporation, and III: bulk region

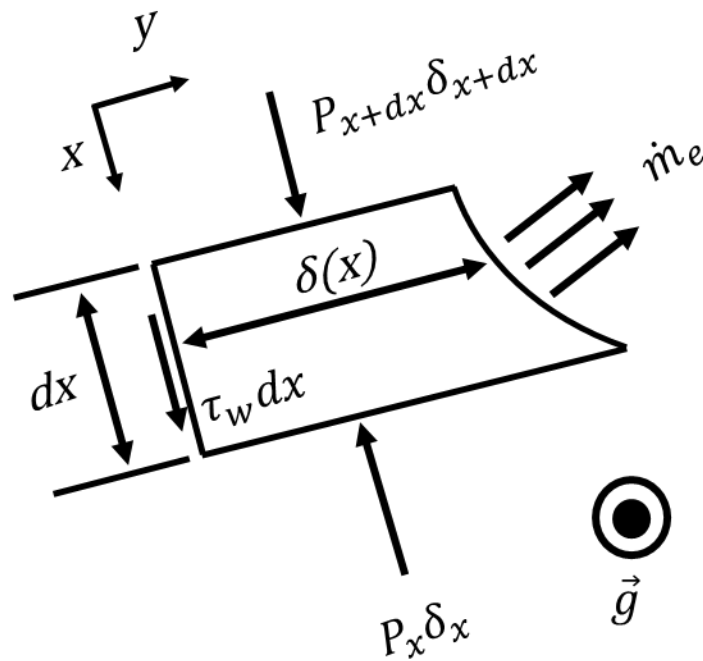


Figure 55. A control volume selected in the thin film region showing the forces, film thickness and the evaporation mass flux – triangular groove

By solving the equations above, it is possible to plot the key parameters of heat and fluid flow in an extended meniscus. Figure 56 plots the average velocity in x direction versus the x position in an extended meniscus shown in Figure 51, rectangular groove. It is seen in Figure 56 that the average velocity starts from zero at the non evaporating region, $x=0$, and ends with zero again in the bulk region where there was assumed to be no evaporation. The average velocity increases rapidly from the bulk region, peaks at a point in the thin film region, and declines rapidly nearing the non-evaporating region. Similarly, Figure 56 also plots the average velocity for the extended meniscus shown in Figure 55, triangular groove. It is seen that the thin film region is extended further to the right for the triangular groove with the position of the maximum average velocity shifted. Similar trends are seen for both geometries.

Figure 57 shows the evaporation mass flux versus the x position in an extended meniscus and compares them for a rectangular and triangular groove. It is seen that there exists no evaporating mass flux near the non-evaporating and bulk region, with a maximum mass flux occurring at a point in the thin film region. Evaporation mass flux declines rapidly on both sides of this maximum position. Similar trends are seen for both

rectangular and triangular grooves, while the triangular groove shows the meniscus extended further to the right and evaporation occurring on a longer span of the thin film region.

Figure 58 plots the evaporation heat flux versus the x position in an extended meniscus, comparing the rectangular and triangular groove geometries. Like the evaporation mass flux plot, heat flux starts from zero at non-evaporating region, reaches a maximum, and rapidly declines near the bulk region, for both rectangular and triangular grooves. To calculate the heat transfer rate in the thin film region, Figure 58 is integrated with respect to x , or in other words, the area under each heat flux curve is calculated. Using unit length for width, the heat transfer rate is acquired. The heat transfer rate is plotted for a typical 10 by 15 cm finned wall with 1000 fins versus the superheat degree (wall and vapor temperature difference) in Figure 59. Each fins have two thin film evaporation sides. Figure 59 also compares the heat transfer rate between rectangular and triangular grooves. It is seen that the triangular groove can increase the heat transfer rate by up to 140 % due to a higher capillary height, and an extended thin film region. Dividing the heat transfer rate by the total finned wall surface area gives the heat removal capacity. Figure 60 plots the heat removal capacity versus superheat degree and compares it for rectangular and triangular grooves. Figure 61 plots the heat removal capacity of both rectangular and triangular grooves in terms of their wetted area. A 25% increase in heat removal capacity of triangular grooves in terms of wetted area is seen. Appendix IX provides more detailed results of thin film evaporation in an extended meniscus.

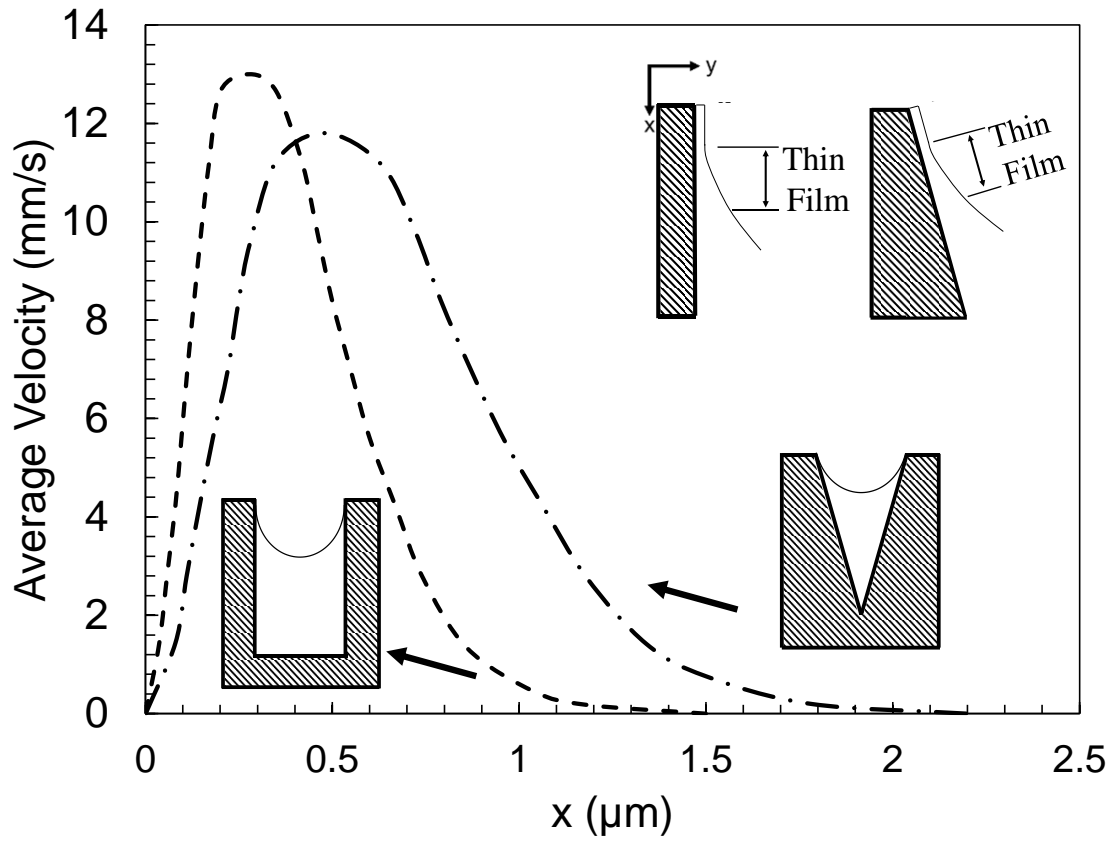


Figure 56. Average velocity in x direction versus the x position in an extended meniscus; comparison between rectangular and triangular groove

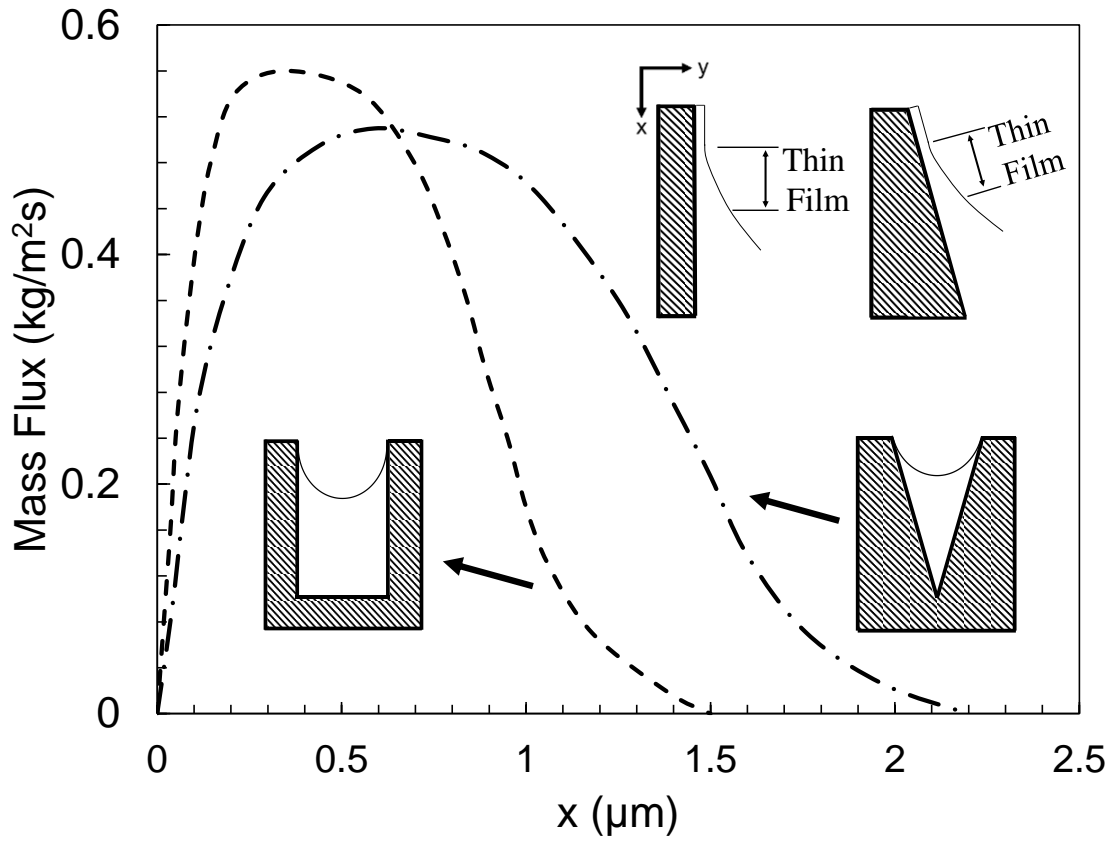


Figure 57. Evaporation mass flux versus the x position in an extended meniscus; comparison between rectangular and triangular groove

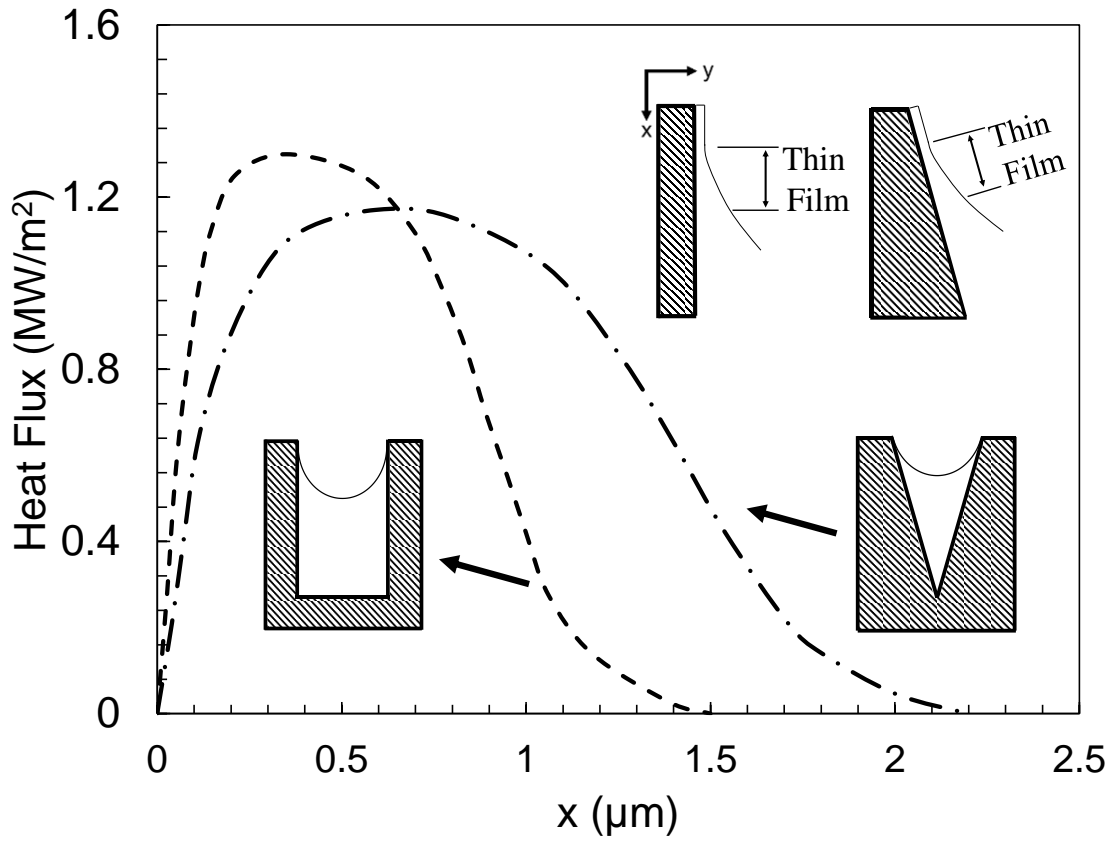


Figure 58. Evaporation heat flux versus the x position in an extended meniscus; comparison between rectangular and triangular groove

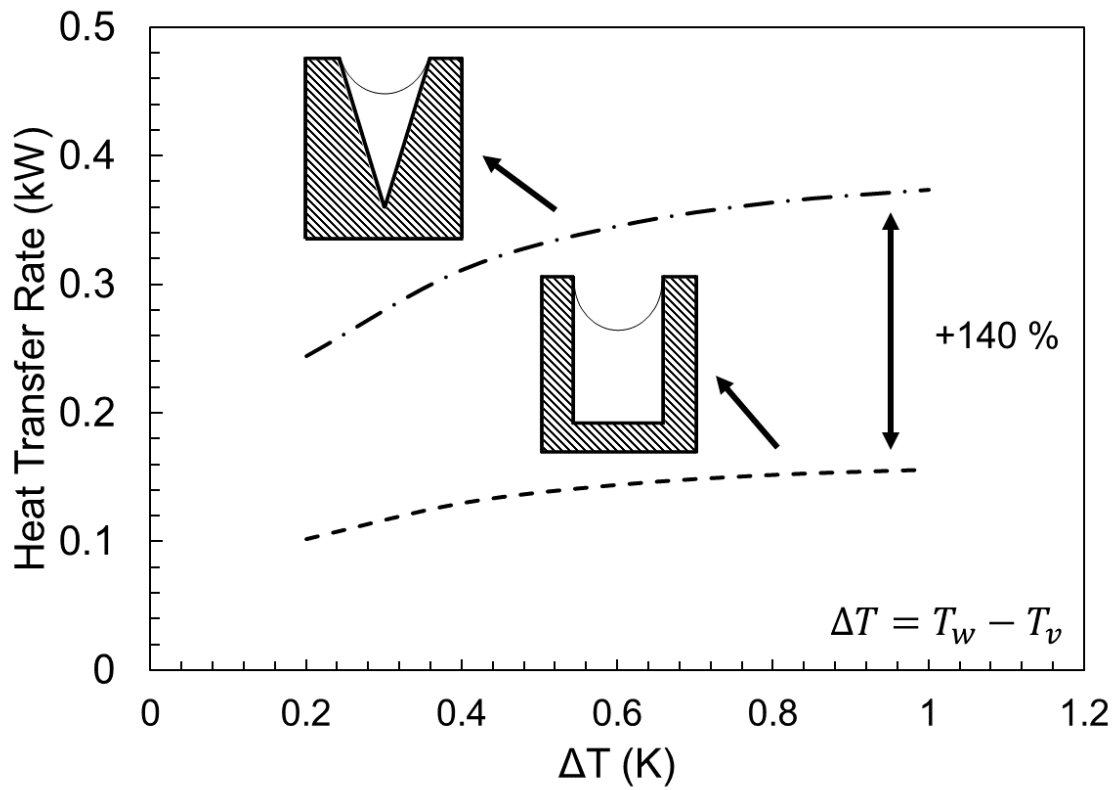


Figure 59. Heat transfer rate for a 10 by 15 cm finned wall with 1000 fins versus superheat degree; comparison between rectangular and triangular grooves

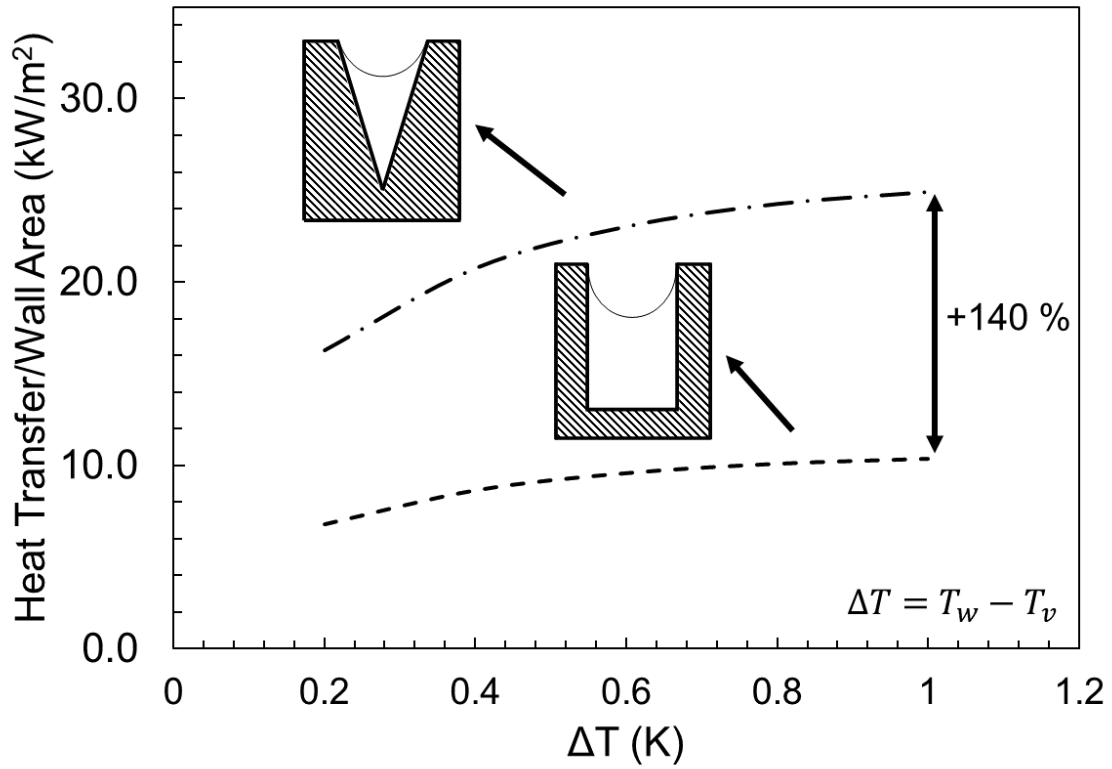


Figure 60. Heat removal capacity for a 10 by 15 cm finned wall with 1000 fins versus superheat degree; comparison between rectangular and triangular grooves

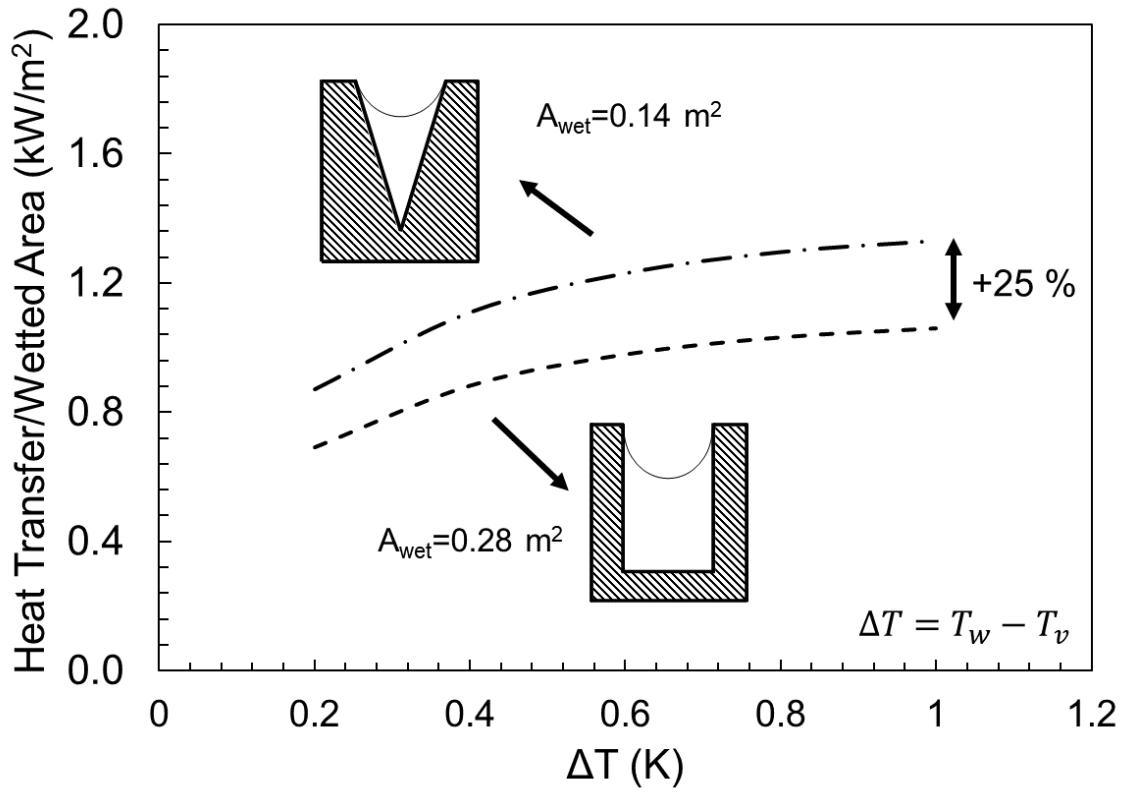


Figure 61. Heat removal capacity in terms of wetted area for a 10 by 15 cm finned wall with 1000 fins versus superheat degree; comparison between rectangular and triangular grooves

4.7. Comparison of natural convection, thin film evaporation, and bulk conductive heat transfer in CALPE

As mentioned previously, it is necessary to compare three heat transfer mechanisms in a CALPE to provide a perspective. While all three mechanisms help the heat removal occur in a finned wall, they have different orders of magnitude and depending on the operating conditions, one or two of them can be neglected for ease of calculation. Based on previously presented results, Figure 62 compares natural convection, two-dimensional conductive heat transfer, and thin film evaporation for a 10 by 15 cm finned wall with 1000 fins for a superheat degree of 1 K. It also compares each heat transfer mechanism for rectangular and triangular grooves. It is seen that for small superheat degrees, the thin film evaporation is the dominant heat transfer mechanism, with up to 93% of total heat transfer rate. Similar comparison is reported in [100].

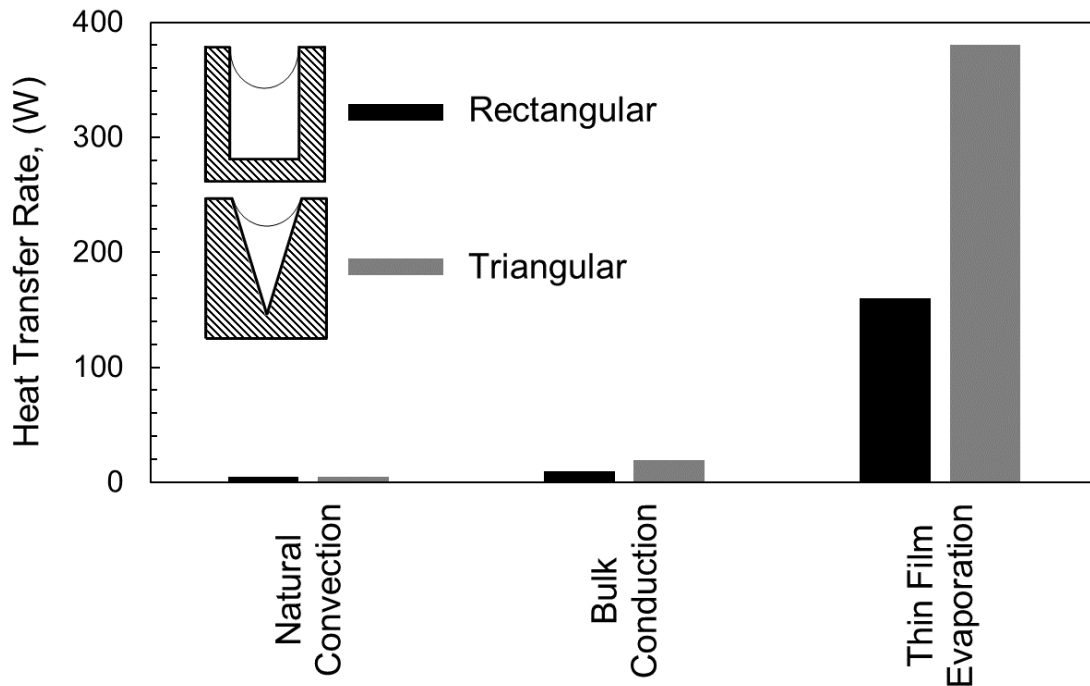


Figure 62. Comparison of natural convection, two-dimensional conductive heat transfer, and thin film evaporation for a 10 by 15 cm finned wall with 1000 fins for a superheat degree of 1 K; comparison between rectangular and triangular grooves

4.8. Bulk material conductive thermal resistance model

In chapter 1, and in Figure 9, thermal resistances of CALPE were introduced. To have a compact CALPE, three thermal resistances should be minimized. As shown in Figure 63, the external grooves should be designed so that they bring the maximum amount of liquid water to the evaporation site, the heat transfer fluid should be able to provide the necessary heat for evaporation, and the fins should be designed in a manner that have the least resistance between the heat transfer fluid and the evaporation site. These thermal resistances are called external convection, internal convection, and bulk material conduction thermal resistance. When off-the-shelf evaporator tubes are used as a CALPE, the internal convection thermal resistance accounts for up to 91% of total thermal resistance. However, when micro-grooves are used, the conduction and external convection resistances make up a more meaningful percentage of the total thermal resistance [12], [4]. Therefore, it is important to reduce these resistances to increase the total heat removal capacity of CALPE. The external thermal resistance was discussed in previous sub-chapters and can be reduced by designing the fins so that they improve the thin film evaporation. The internal thermal resistance research is abundant in the literature and not the major bottleneck in micro-groove design. The bulk material conductive thermal resistance, however, can be optimized based on the material and design choice.

The way these three thermal resistances are linked together is better explained with a solution flowchart. Looking at Figure 64, to analytically solve the overall heat transfer for a capillary groove analytically, first the thin film evaporation is calculated based on two temperatures; vapor temperature, which is the saturation temperature at a given pressure, and wall temperature at the evaporation site. The wall temperature at the heat transfer fluid site is then calculated based on heat conduction through the fin. Having the heat transfer fluid inlet temperature, the heat transfer from the heat transfer fluid is compared with the heat transfer calculated in previous steps. This might result in an imbalance; therefore, the wall temperature should be adjusted until the balance is restored between the two heat transfer values. This flowchart is shown in Figure 65. In the following, the focus will be given to the conductive thermal resistance, and more specifically, the effect of fin geometry on it.

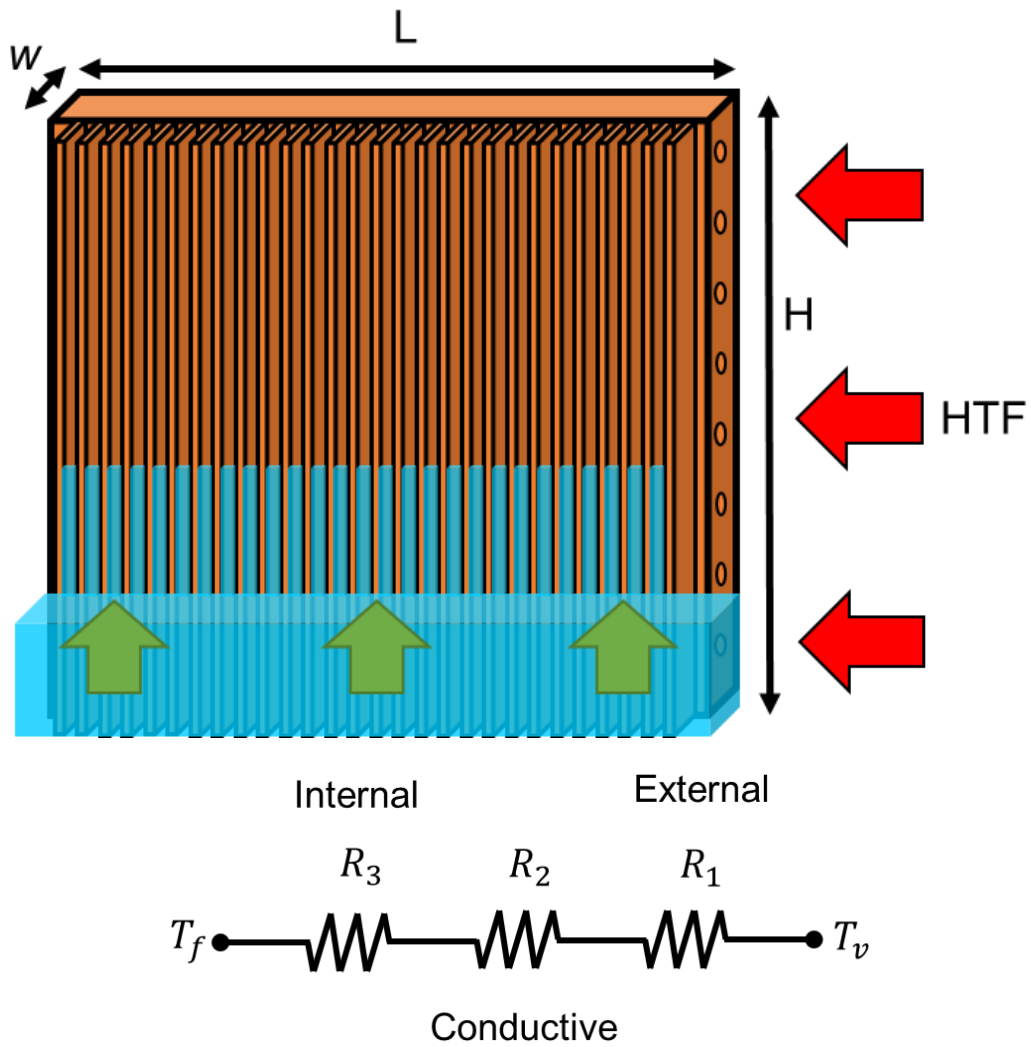


Figure 63. Thermal resistance of CALPE include the external convection, the internal convection, and the conductive bulk material thermal resistances.

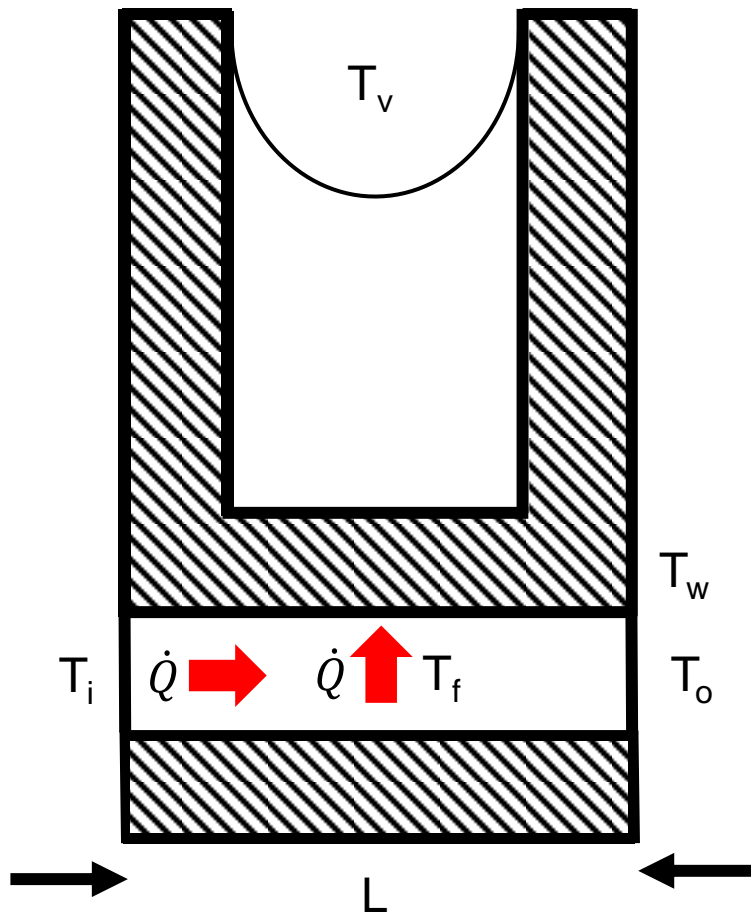


Figure 64. A schematic of CALPE showing the heat transfer fluid, bulk material, and fin side, along with the heat flow direction and important temperatures

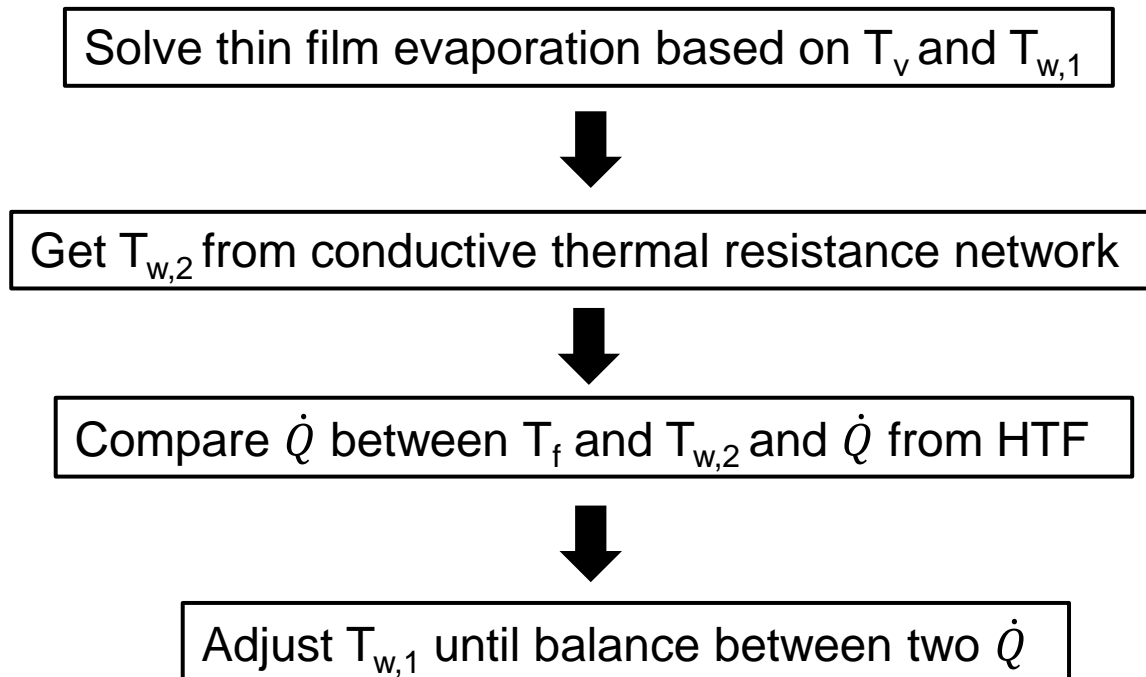


Figure 65. CALPE heat transfer solution flowchart; an analytical model follows the solution flowchart until there is a balance between heat transfers of CALPE

Figure 66 shows the fin geometries considered in this section. In each case, only a half of a cross-section is used in the modeling. Rectangular cross-section is the most popular, simply due to its manufacturability. Triangular cross-section has shown to have the best capillary rise performance. Between these two cross-sections, there are curved, circular, and the general hyperellipse cross-sections. Figure 67 shows the geometries overlaid and depicts the progression from a rectangular to a triangular cross-section.

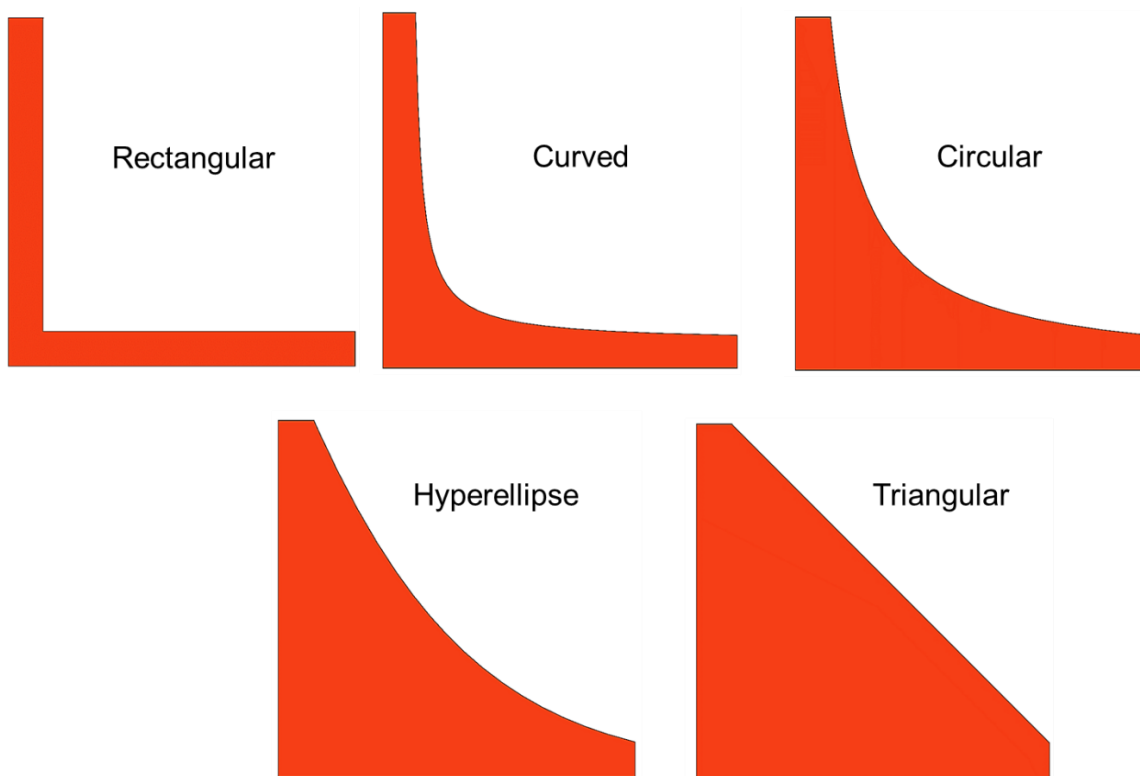


Figure 66. Various cross sections considered in modeling of effect of fin geometry on bulk material conduction thermal resistance

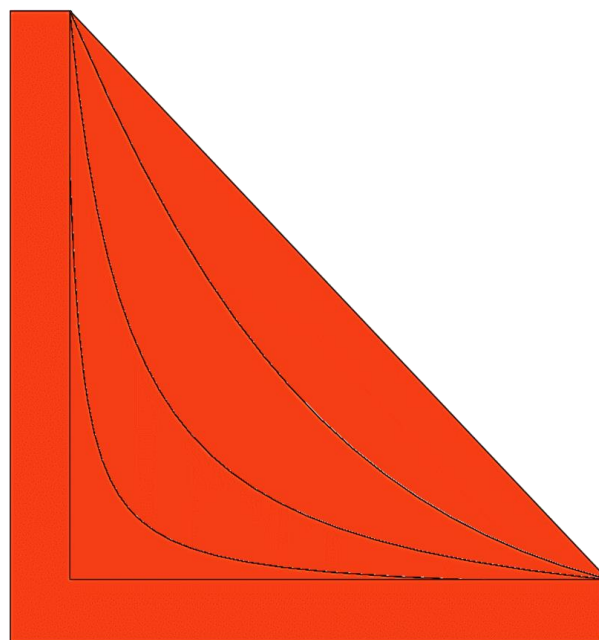


Figure 67. Various cross sections considered in modeling of effect of fin geometry on bulk material conduction thermal resistance; overlaid view

Figure 68 depicts the problem description. Here, thin film evaporation, Q_{eva} , occurring on the evaporation site, is given by the analytical solutions mentioned earlier. A wall temperature, T_w , is given from the heat transfer fluid side. The dimensions are denoted by $2t_f$ for fin thickness [m], and $2w$ for fin width [m]. D is the fin depth [m], and t_b is the fin base thickness [m]. Only half of the cross section is solved due to symmetry, as shown in Figure 69.

The assumptions and boundary conditions are listed below. An average heat flux is assumed at the tip of the fin. An average wall temperature is assumed at the base.

- Equal fin depth, and fin spacing for all geometries
- Constant wall temperature at the fin base
- Constant heat flux at the fin tip
- Constant thermal conductivity

A performance metric that considers the change in the mass or the volume of the fins as the cross-section changes needs to be defined. Here, R^* , the volumetric thermal resistance, is the product of thermal resistance and the volume. This is chosen so that higher volumes are associated with higher R^* .

$$R^* = R \times v \tag{69}$$

where R^* is the volumetric thermal resistance, [$K.m^3/W$], R is the thermal resistance, [K/W], and v is volume [m^3].

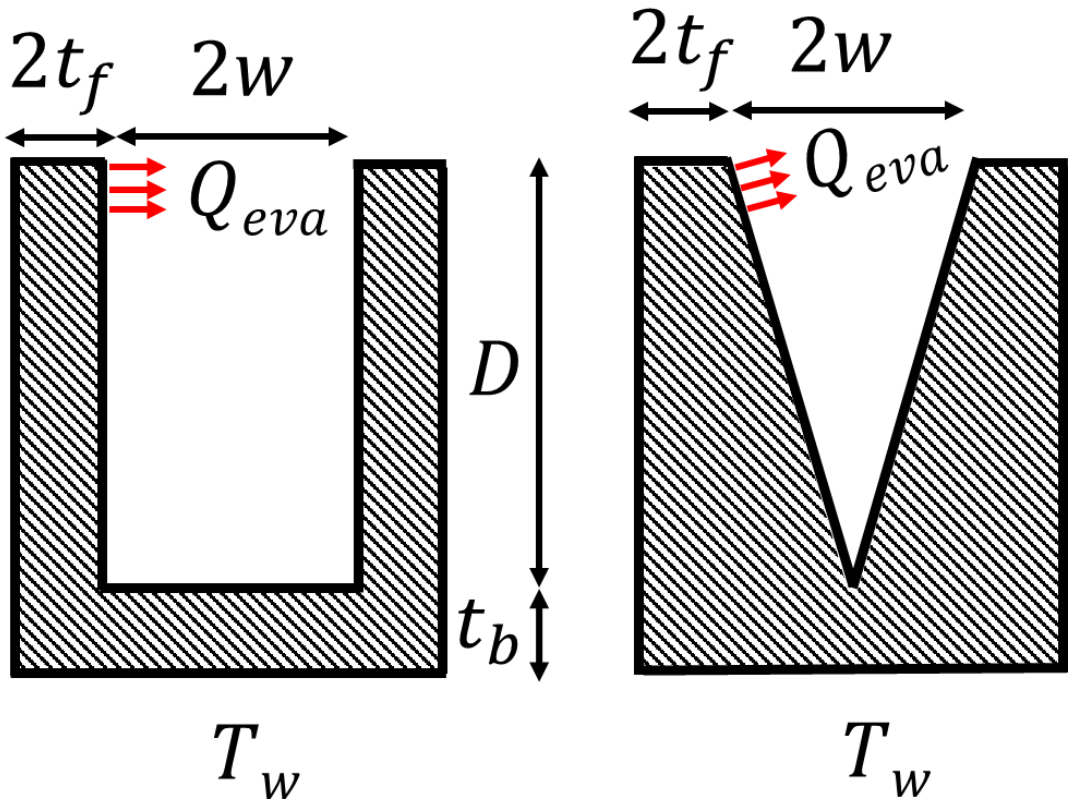


Figure 68. Geometrical parameters of a rectangular and a triangular cross-section considered in solving the bulk material conduction thermal resistance

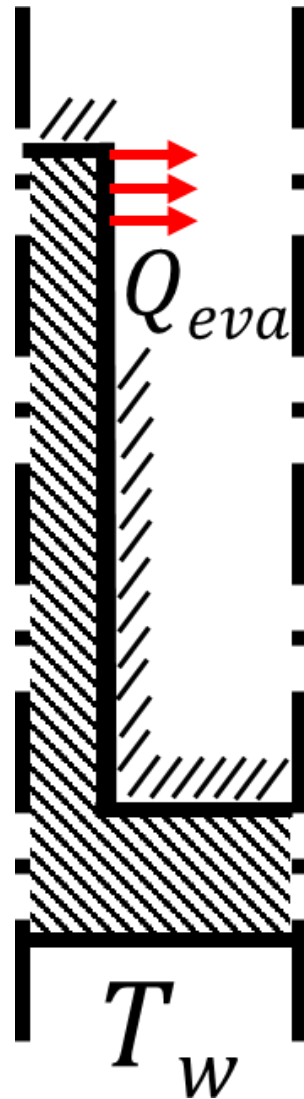


Figure 69. Half the symmetrical geometry of a rectangular cross-section considered in solving the bulk material conduction thermal resistance

Using Ansys Fluent software, the temperature distribution for a rectangular cross-section fin is calculated using the boundary conditions and assumptions mentioned before, seen in Figure 70. The wall temperature and the evaporation heat transfer are 15 °C and 1 [MW/m²], respectively. The fin depth and width are 1 [mm]. The fin and fin base thickness are 0.1 [mm]. Based on the temperature difference and the heat transfer, a thermal resistance can be calculated between the evaporation site and the bottom wall. R^* , or the volumetric thermal resistance is 0.017 [K.m³/W] for this specific scenario. The same analysis can be done for the remaining cross sections. Figure 71 shows the results for a curved cross-section. The evaporation heat transfer and R^* change with changing the geometry. R^* is 0.02 [K.m³/W] for a curved cross-section. Figure 72-75 show the results for the remaining cross-sections. Although the temperature variation across the cross section is small, it is the prerequisite for heat transfer to occur inside the fin.

The trend seen from the results indicates that the volumetric thermal resistance increases by increasing the amount of mass and volume between the tip and base of the fin. Figure 75 plots this progression. R^* increases from 0.017 to 0.024 [K.m³/W] when the fin geometry changes from rectangular to triangular cross-section.

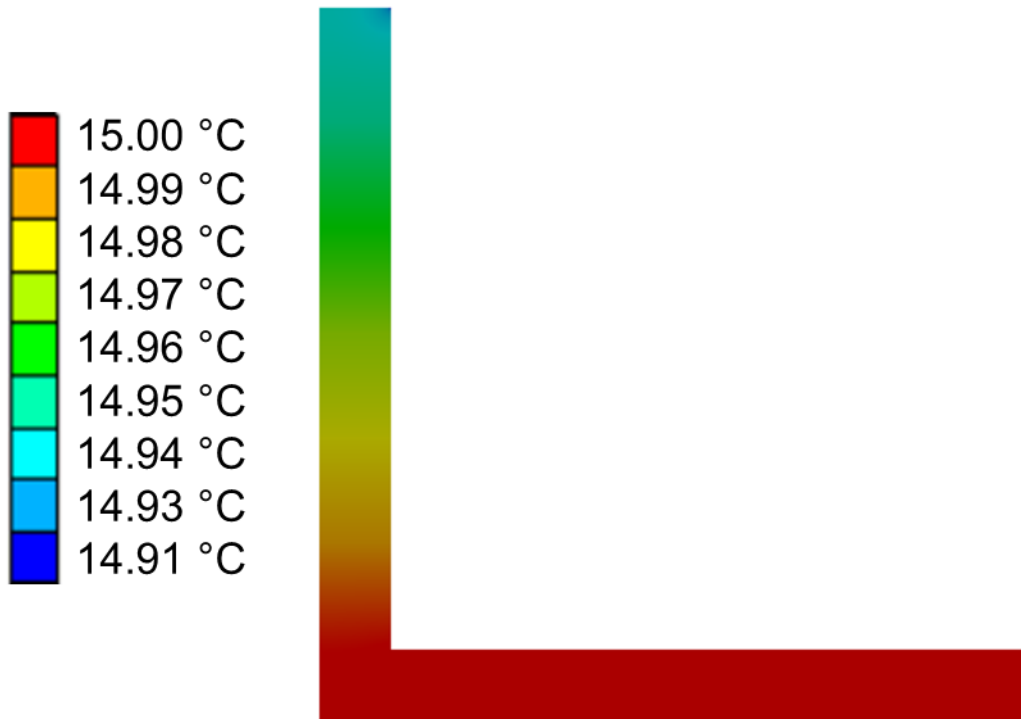


Figure 70. The temperature distribution for a rectangular cross-section fin with D and w of 1 mm, and t_f and t_b of 0.1 mm. Bottom wall temperature is 15 °C.

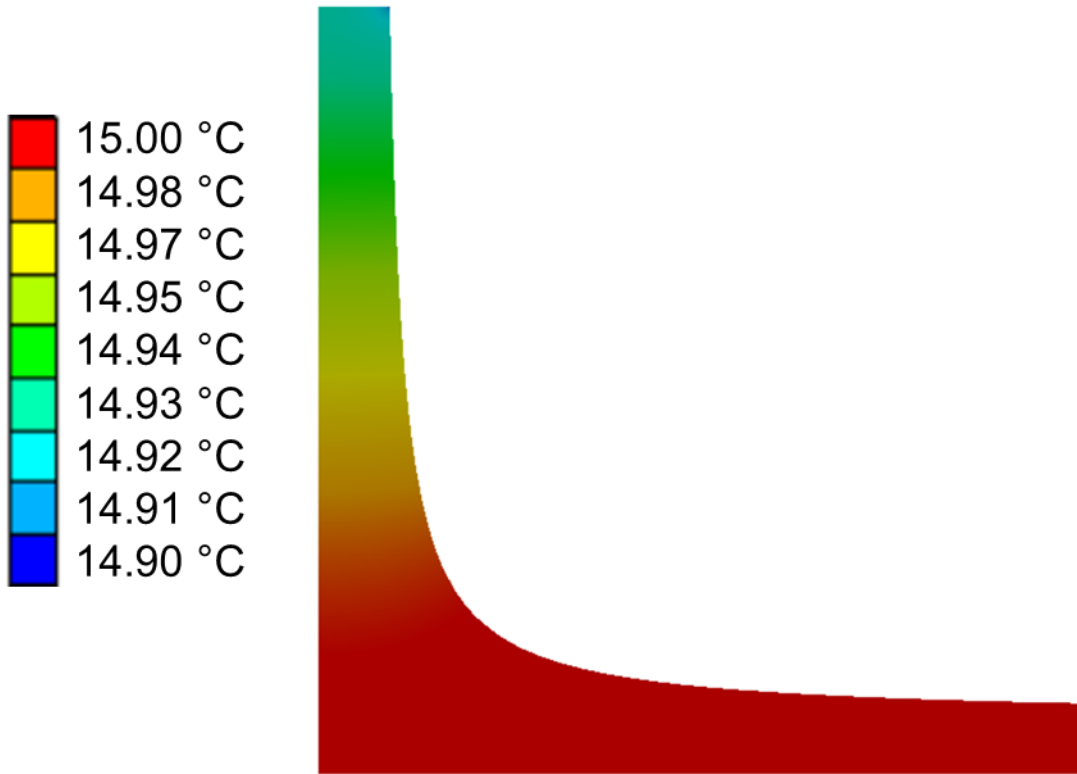


Figure 71. The temperature distribution for a curved cross-section fin with D and w of 1 mm, and t_f and t_b of 0.1 mm. Bottom wall temperature is 15 °C.

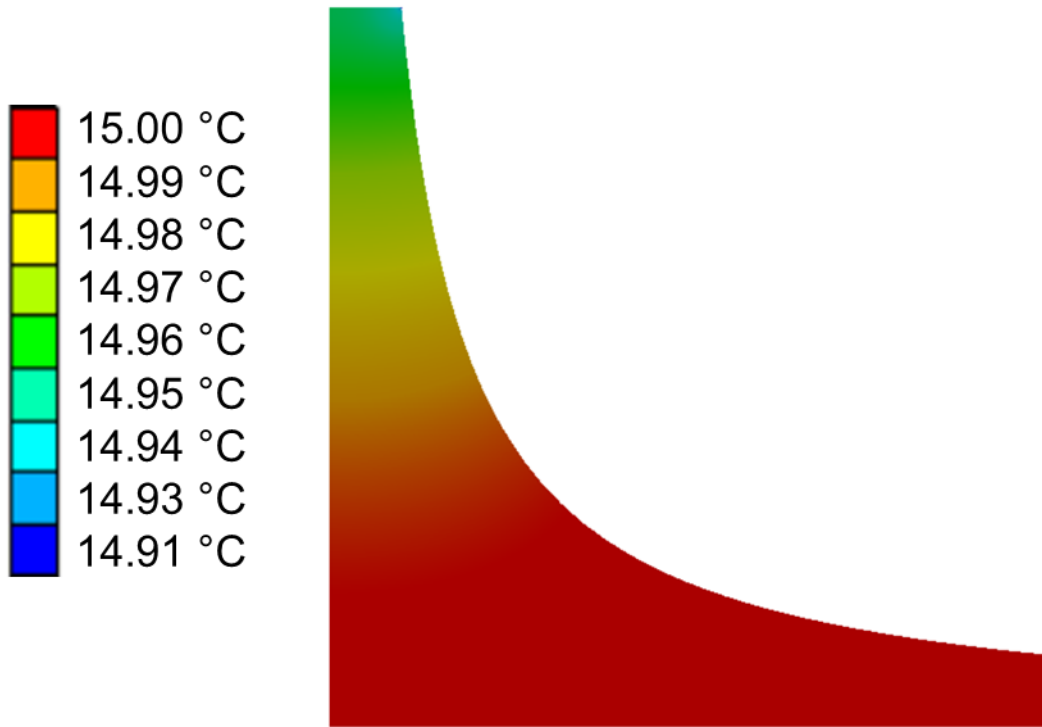


Figure 72. The temperature distribution for a circular cross-section fin with D and w of 1 mm, and t_f and t_b of 0.1 mm. Bottom wall temperature is 15 °C.

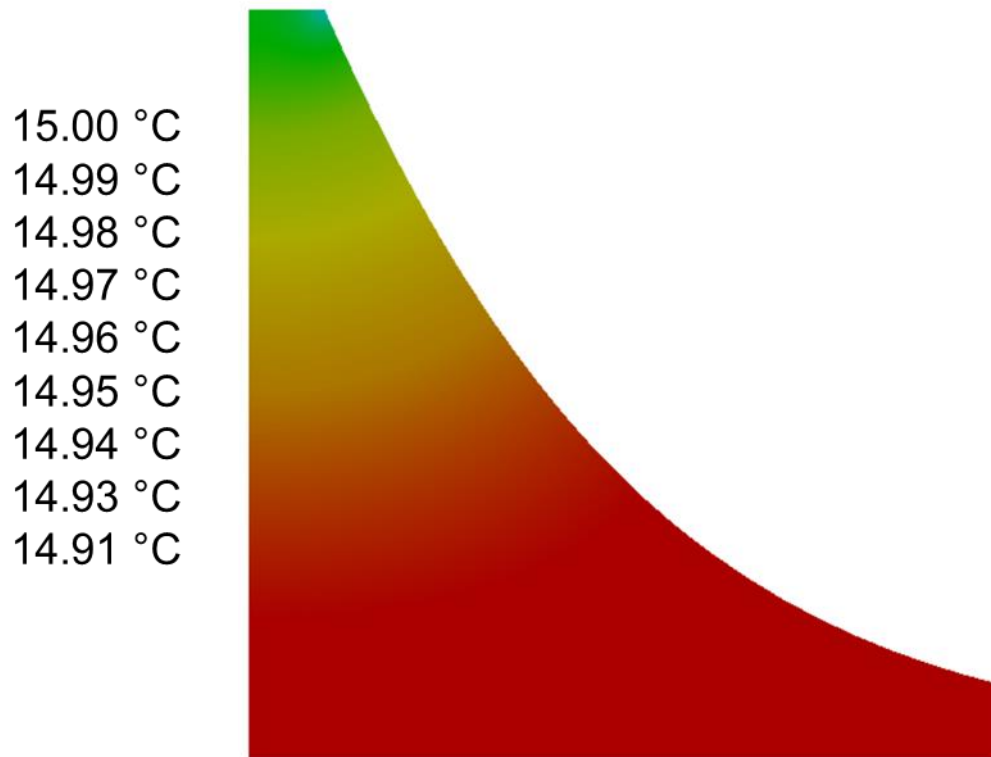


Figure 73. The temperature distribution for a hyperellipse cross-section fin with D and w of 1 mm, and t_f and t_b of 0.1 mm. Bottom wall temperature is 15 °C.

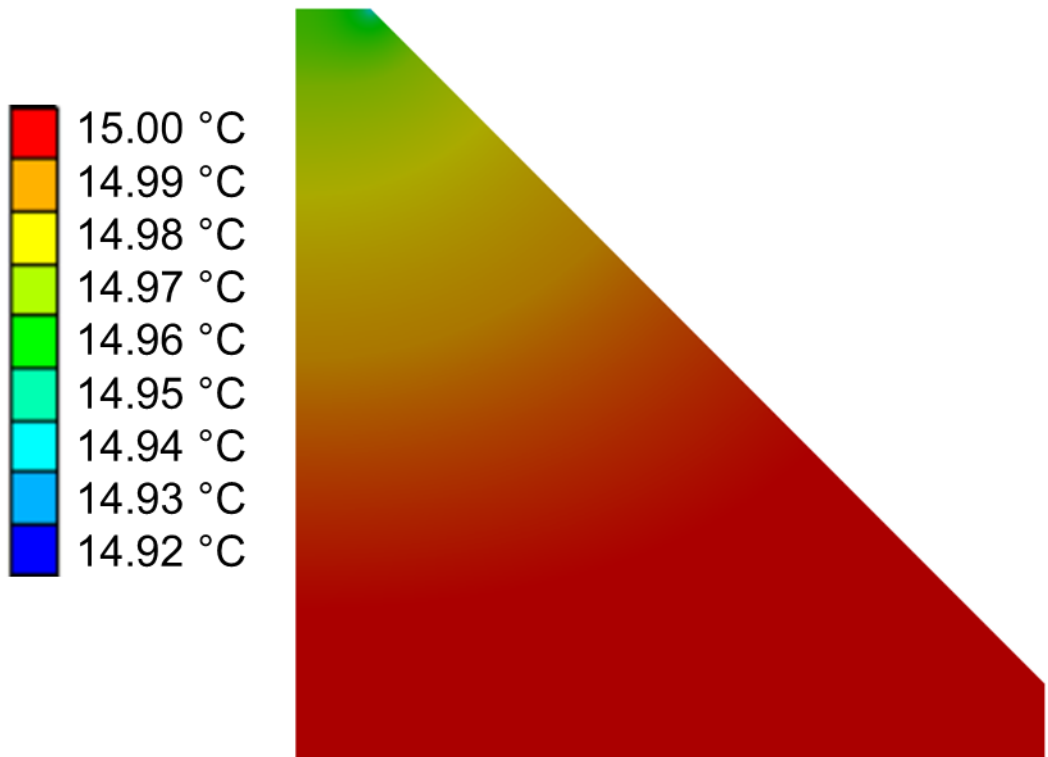


Figure 74. The temperature distribution for a triangular cross-section fin with D and w of 1 mm, and t_f and t_b of 0.1 mm. Bottom wall temperature is 15 °C.

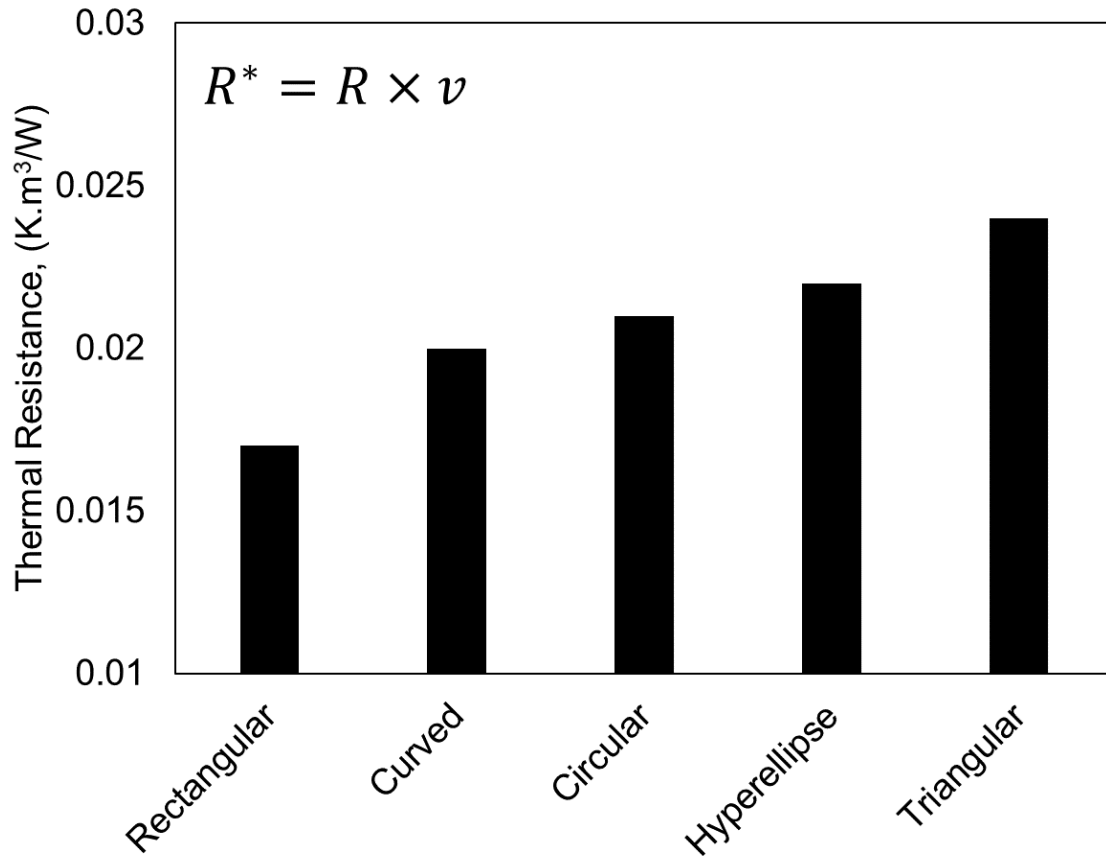


Figure 75. Comparison of the volumetric thermal resistance, R^* , for various cross-sections considered

4.9. Conclusion to the chapter

This chapter assessed the heat removal capacity of a CALPE through understanding its heat transfer phenomenon on a fundamental level. A detailed study of heat transfer in CALPE was conducted and governing equations for thin film evaporation, natural conduction, and two-dimensional conduction heat transfer were presented. Analytical models were given for rectangular cross-sections, and then extended to alternative geometries. The models consider the effects of groove geometry, thin film evaporation, and contact angle. The results show a strong dependence of thin film evaporation on groove geometry. It also suggests a strong relationship between the disjoining pressure and evaporation in a microgroove. An order of magnitude analysis was used to simplify the models. The effect of the inertial force, though negligible, was included. It was shown that for a given superheat degree, a maximum heat flux exists in an extended meniscus. Thin film evaporation, which only takes place at the top of the meniscus, is the enhancement mechanism of evaporation. Consequently, the thin film evaporation in a capillary groove was deemed the dominant factor when compared to other mechanism of heat transfer. It was also concluded that the conductive heat transfer in the bulk region can be neglected for small superheat degrees. A review of common geometries and their heat transfer models showed an optimal fin geometry to maximize the heat removal capacity of a capillary groove had not been identified. Guidelines to optimize heat removal capacity through alternative geometries, and a genetic algorithm was presented and discussed.

Chapter 5.

Experimental validation of heat removal capacity of CALPE

From chapter 2, it is concluded that fin spacing, contact angle, and groove cross-sectional area have a great effect on the capillary height of CALPE. Consequently, they influence its heat removal capacity, immensely. Chapter 3 was dedicated to experimental validation of closed form models presented in chapter 2 regarding the capillary height in micro grooves. This chapter provides an experimental study of CALPE and presents results for experimental heat removal capacity. It also compares these results with analytical models presented in chapter 4. Experimental data is collected at the Laboratory for Alternative Energy Conversion. The model captures the experimental results with less than 10% relative difference. This section mainly deals with rectangular and triangular cross sections due to triangular cross section's highest capillary rise among the studied geometries. The rectangular cross-section is chosen for comparison since it is widely used in the literature and the industry. An experimental study, such as presented in this chapter, is imperative to demonstrate the potential of analytical models to predict CALPE's heat removal capacity, and to showcase the effect of alternative geometries, such as triangular arrangement, in increasing the heat removal capacity. The effect of the grooves' width, and cross-sectional area is investigated and reported. Different operating conditions, such as saturation pressure, are considered to make a comprehensive conclusion.

Multiple stainless-steel 3D-printed CALPEs were built and tested. 3D-printing was chosen since traditional manufacturing methods do not offer feature sizes that were needed for these CALPEs. These CALPEs feature small microchannels on the heat transfer fluid side (1 mm) and small fin spacing on the vapor side (100, 200, and 500 μm). Rectangular and triangular fins were manufactured. The design is based on the result of analytical modeling, presented in previous sections, and an optimization scheme that aims to increase the total heat transfer area. The reason triangular grooves smaller than 500 μm were not tested in this study was the fabrication limitations that did not allow making 100 and 200 μm samples.

A test bed was made specifically for experimenting on performance of CALPEs. Tests were performed with water as a refrigerant, vapor pressure of 0.87 – 3.17 kPa, and a 5-25 °C heat transfer fluid inlet temperature. Results for heat removal capacity are presented and compared to the state-of-the-art CALPE from the literature, as well as results from the models. Pressure drop was measured and reported for each tested CALPE. An experimental comparison is made between CALPEs with rectangular cross section fins, and those with triangular cross-section.

5.1. 3D-printed CALPE

A set of novel CALPEs are fabricated to maximize both capillary height and heat removal capacity for various operating conditions, as seen in Figure 76. Commercially available enhanced finned tubes are limited in their design as they do not offer a small enough heat transfer fluid channel diameter, which is necessary to remove the heat from the fin side. They are also limited in the range of fin per inch (FPI) values; high fin densities are not widely manufactured [4]. Therefore, most commercial solutions are not compact nor are they efficient. A small internal diameter is desirable to decrease the internal heat transfer resistance, as discussed at length in [24]. A high fin density helps promote higher capillary rise and increases total heat transfer area. Moreover, alternative geometries, such as triangular cross section, are not commercially available.

3D-printing is a flexible manufacturing method that allows for customized geometries to be built. Recent advances in 3D-printing means that various materials such as polymers and metals are available for printing. It also means that geometries with fine features are now printable. Figure 77 shows an example of a 3D-printed CALPE manufactured for this study, compared with a Canadian quarter. An AM 400 RENISHAW metal 3D-printer was used to print these CALPEs from 316 SST stainless steel. Metal powders are sintered with direct laser exposure (DLMS). Figure 77 also shows an example geometry; a height of 6 cm and length of 10 cm. The fins were 100 μm thick and 100 μm apart, with fin height of 1.5 mm. Roughly 1000 capillary channels were achieved with this design. On the heat transfer fluid side, it had 28 parallel 1-mm channels inside. The inlet and outlet of the evaporator were $\frac{1}{4}$ " (6.35 mm inner diameter) ports that acted as a header for the parallel microchannels. Table 6 summarizes the geometry specifications of the CALPEs manufactured for this study. Figure 78 provides microscopic top view of multiple 3D-printed CALPE with fin spacing and thickness of 100, 200, and 500 μm . Triangular

grooves with fin spacing smaller than 500 μm were not feasible to manufacture with this 3D-printing method.



Figure 76. A set of novel CALPEs fabricated with stainless steel 3D-printing to maximize capillary height and heat removal capacity.

Table 6. Geometry specifications of the CALPEs manufactured for this study

Parameter	Value
CALPE height, (mm)	60
CALPE width, (mm)	5
CALPE length, (mm)	100
Fin height, (mm)	1, 1.5
Fin spacing, (mm)	0.1, 0.2, 0.5
Fin thickness, (mm)	0.1, 0.2, 0.5
Fin per inch	250, 125, 50
HTF port diameter, (mm)	1
Cross section	Rectangular, Triangular

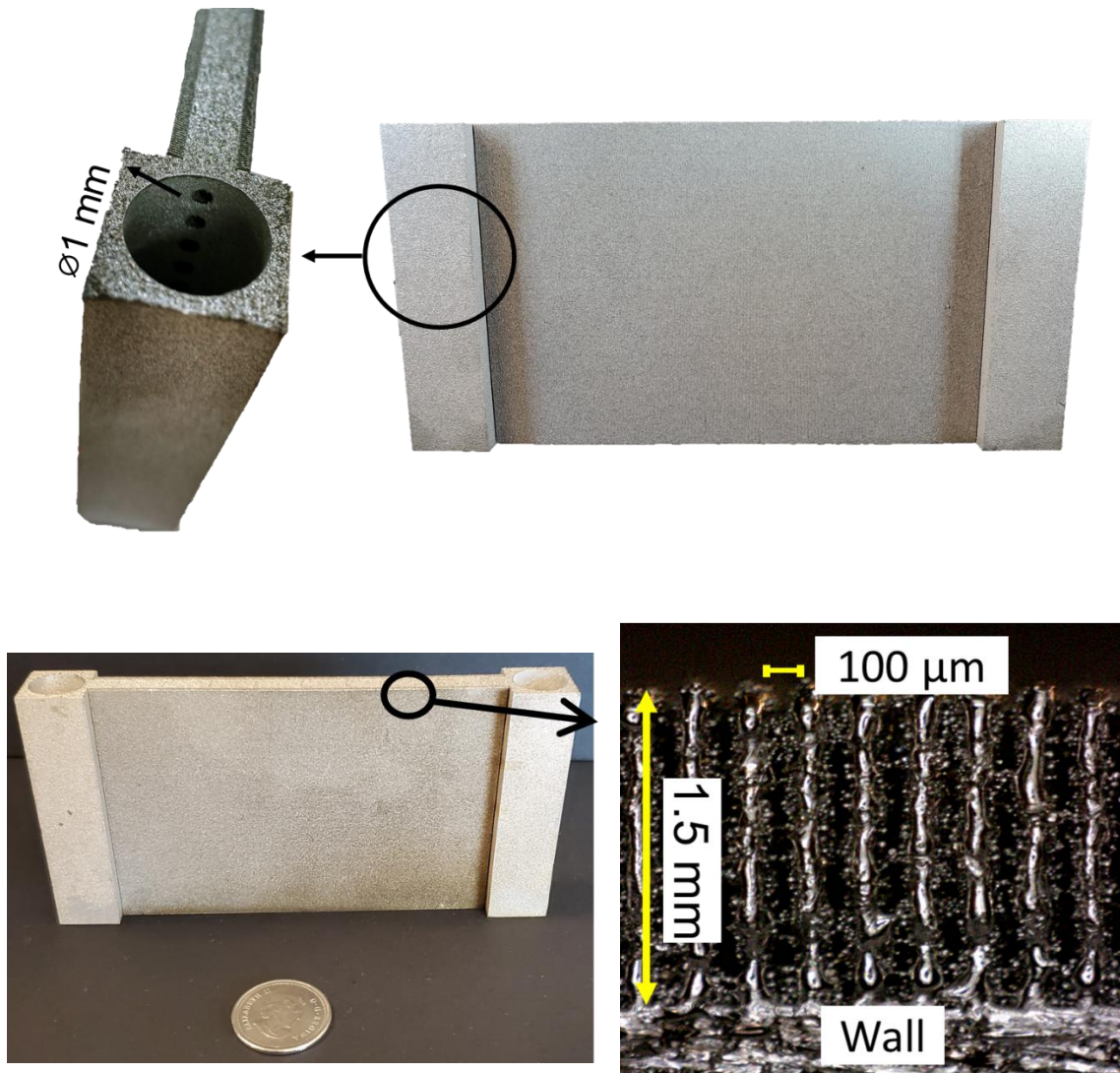


Figure 77. Front view and microscopic top view of an example 3D-printed CALPE compared with a Canadian quarter. Fin spacing and thickness: 100 μm , height: 6 cm, length: 10 cm. Detailed geometries are presented in Table 6. Tests were performed with a 5-25 $^{\circ}\text{C}$ heat transfer fluid (HTF) inlet temperature.

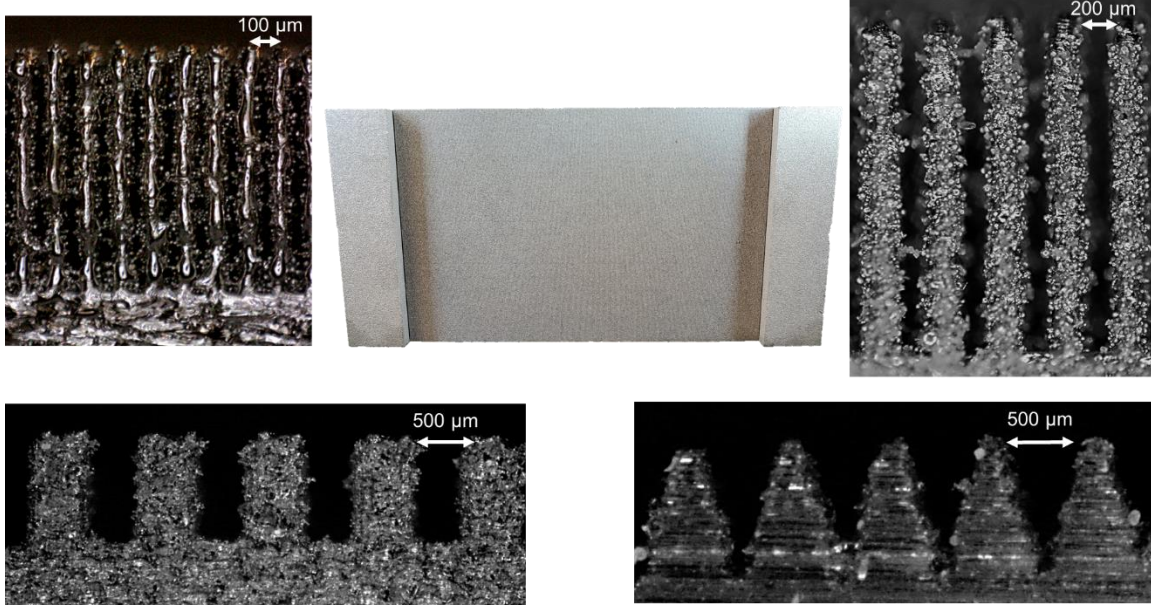


Figure 78. Microscopic top view of multiple 3D-printed CALPE with fin spacing and thickness of 100, 200, and 500 μm . CALPE height: 6 cm, length: 10 cm. Detailed geometries are presented in

5.2. Experimental setup

Non-capillary low-pressure evaporators are often flooded evaporators where the only heat transfer mechanism is natural convection. Natural convection has a direct relationship with the heat transfer area, or the area submerged in liquid pool. Therefore, in a non-capillary evaporator the heat removal capacity decreases with decreasing water height as the active heat transfer area decreases. However, in a CALPE, the dominant heat transfer mechanism is the thin film evaporation, as discussed in previous chapters. The capillary mechanism keeps the heat removal capacity constant even when the water height decreases [24]. This is true for cases where the heat transfer fluid has reached its maximum heat removal capacity, as well. Otherwise, as the liquid pool decreases, the thin film heat transfer area increases, and the total heat removal capacity increases, since the heat transfer fluid side can still remove more heat. Moreover, in a non-capillary low-pressure flooded evaporator, the saturation pressure difference between the surface of the liquid pool of water and its bottom leads to lowered heat removal capacity. This is since the added hydrostatic pressure at the bottom of the liquid pool increases the

saturation temperature. On the other hand, in a CALPE, it is possible to keep a lower liquid height and utilize the capillary action to keep the surface of the evaporator wet. This smaller volume of needed liquid in CALPEs decreases the total thermal inertia, as well.

Figure 79 presents a schematic diagram of the test bed purpose-built for heat removal capacity testing of CALPEs. Heat transfer fluid, water, was pumped through the evaporator by a Cole-Parmer Polystat thermal bath with controllable temperature and flowrate. The evaporator was placed inside a vacuum chamber which was connected to another vacuum chamber with a condenser (vapor collector) inside. Water vapor travels from the evaporator chamber to the vapor collector through flexible hoses and due to the pressure difference between the two chambers, because of saturation temperature difference. Experiments continued until the evaporator ran out of water. An identical thermal bath is used to control the temperature of the vapor collector. The two temperature control systems (Polystat thermal baths) provided a constant temperature heat transfer fluid (50%-50% water and ethylene glycol mixture). A solenoid valve is used between the two vacuum chambers for opening and closing the connection between the two vacuum chambers. The entire test bed was vacuumed for 6 hours using an Edwards rotary vane vacuum pump to create the initial vacuum, dry the surfaces, and remove any background gases.

The evaporator chamber was placed on a precision balance (ML4002E, Mettler Toledo) with an accuracy of 0.01 g to measure its weight. After placing the evaporator chamber on the scale, the scale was zeroed. The rate in decrease of overall weight was understood to be the evaporation rate. Before starting the experiments, it was confirmed that the scale would show the true weight change of the chamber, by using standard weight samples ranging from 1 to 100 grams. The effect of flexible hoses and wires were investigated, and it was shown that the scale shows the true weight change when standard weights were added or removed from the vacuum chamber. 200 ml of distilled water was used for this experiment, making an initial liquid pool height of 6.5 mm. The refrigerant water was de-aerated in a secondary chamber prior to the experiments and added to the evaporator chamber. Four T-type thermocouples with an accuracy of 0.5 °C were passed via a feedthrough into the vacuum chamber to measure the temperature of the evaporator's wall and the pool of water; two thermocouples were attached to the walls of the evaporator and two inside the pool of water. The pressure of the evaporator was measured using a 722B Baratron pressure transducer (MKS instruments) with an

accuracy of 0.5%. Figure 79 also shows an image of the test setup with the evaporator chamber, condenser (vapor collector), thermal bath, and data collection device. Tests were performed with water vapor pressure of 0.87 – 3.17 kPa, and a 5-25 °C heat transfer fluid inlet temperature.

It should be noted that the real sorption system operation is transient in which pressure difference between the evaporator and the sorber bed is changing with time. This transient process has also been studied and the results can be found in Appendix K. Considering that the variations in the pressure difference between the sorber bed and the evaporator chamber is relatively small over time, one can assume a quasi-steady-state process and use the results of steady-state process and integrate it over time.

5.3. Uncertainty analysis

T-type thermocouples, accurate to ± 0.5 °C, were used to monitor the evaporator and liquid pool temperature inside the chamber. The pressure sensor was calibrated and had an accuracy of 0.5%. The precision balance had an accuracy of 0.01 g. Therefore, and considering the standard deviation of data measurement and sensor accuracy, the maximum uncertainty of the heat removal capacity was 8% [103]. Appendix V provides the details of uncertainty analysis.

5.4. Data reduction

Temperatures, pressure, weight, and flowrate data were monitored and stored on a computer through an in-house LabView code. The following relationship is used to calculate the heat removal capacity [104]:

$$\dot{q} = \dot{m}h_{fg} \quad (70)$$

where \dot{q} [W] is the heat transfer rate, \dot{m} [kg/s] is the measured evaporation rate and h_{fg} [kJ/kg] is the heat of evaporation. The overall heat transfer coefficient, U [W/m²K], is:

$$U = \frac{\dot{q}}{\Delta T_{LMTD}} \quad (71)$$

The logarithmic mean temperature difference between the heat transfer fluid and the refrigerant water is calculated by:

$$\Delta T_{LMTD} = \frac{T_i - T_o}{\ln\left(\frac{T_i - T_{sat}}{T_o - T_{sat}}\right)} \quad (72)$$

T_{sat} is the saturation temperature inside the evaporator chamber.

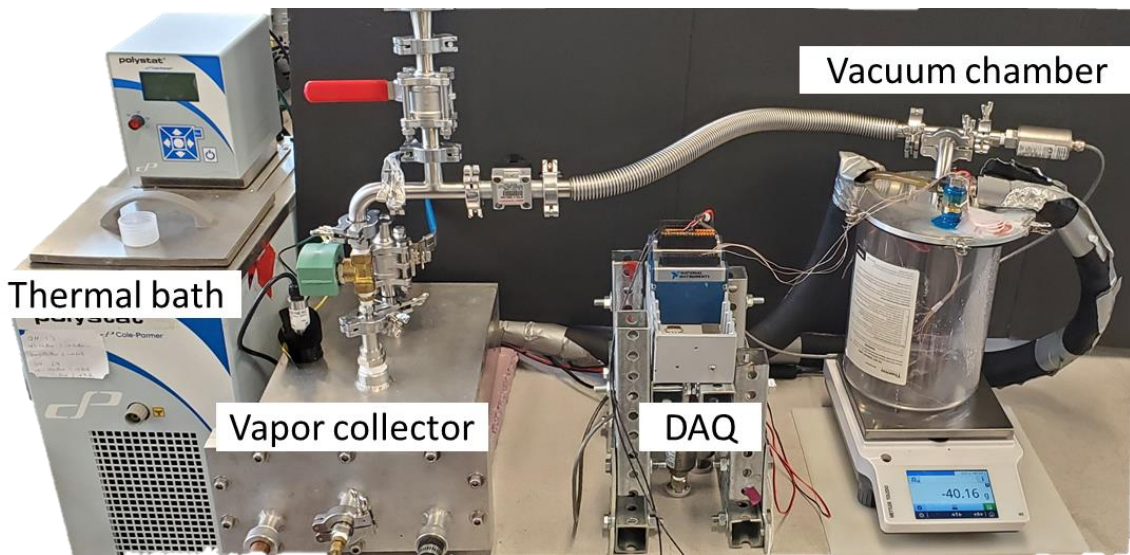
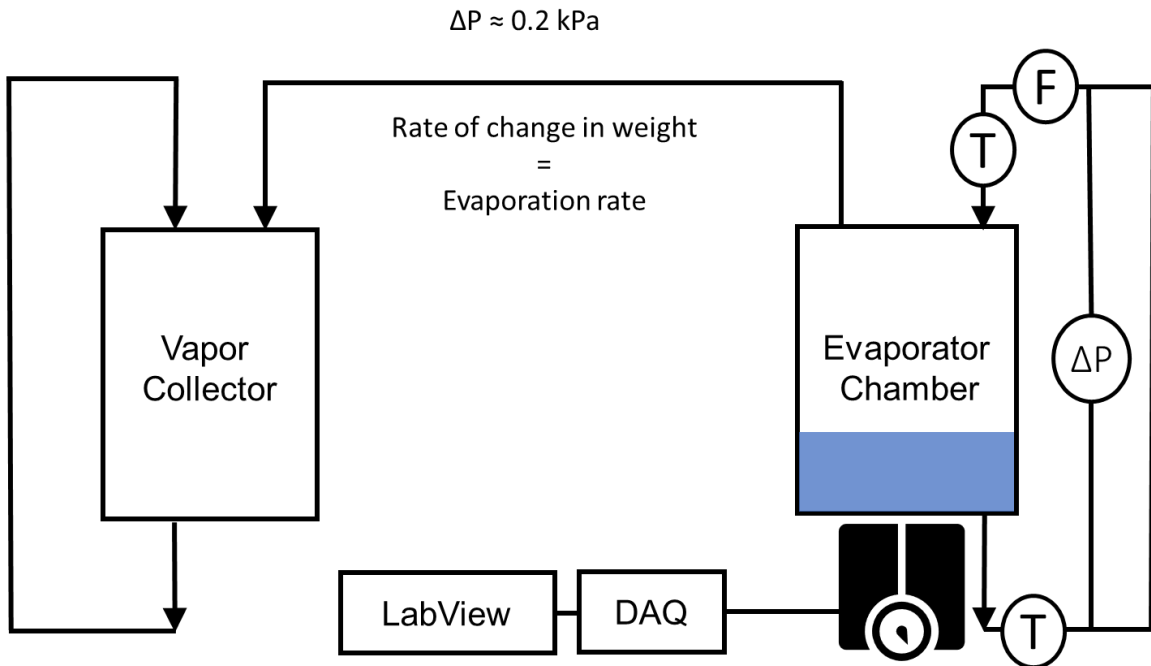


Figure 79. Top, a schematic diagram of the test bed purpose-built for heat removal capacity testing of CALPEs. Bottom, an image of the test setup showing the evaporator chamber, condenser (vapor collector), thermal bath, and data collection device.

5.5. Experimental results and comparison

Figure 80 shows the experimental results for the heat removal capacity of the 3D-printed CALPE vs the pressure difference between the evaporator and vapor collector chamber. As the driving force evaporation, the pressure difference between the two chambers, increases, so does the heat removal capacity of the evaporator. This is true for cases where the heat transfer fluid side of the evaporator is not limiting the heat transfer. A comparison is made between two of the CALPEs made with 100 and 200 μm groove spacing, and all the other parameters identical. A 100 μm groove spacing CALPE has a higher capillary height, and a higher active heat transfer area. It also has a higher number of fins in a given area, or fins per inch. Therefore, the 100 μm groove spacing CALPE outperforms the 200 μm CALPE. Experimental heat removal capacity values are compared with those obtained from the models discussed in previous chapters. It is seen that the models can capture the experimental data within 10 % difference. Figure 80 also provides the real-time experimental data showing the constant evaporator pressure and rate of weight change, during evaporation at 25 $^{\circ}\text{C}$, as an example. In this specific case, a 200- μm CALPE was used. A constant pressure of 2.65 kPa, and an evaporation rate of 2.1 g/min, associated with evaporation at 25 $^{\circ}\text{C}$, was observed. Data for other operating conditions and CALPEs are omitted for brevity, but their heat removal capacity is included in Figure 80, top.

Figure 81 makes a comparison between the experimental heat removal capacity of CALPEs with rectangular and triangular grooves. Data is presented in the same manner as Figure 80. Both CALPEs have identical dimensions and only differ in the fin cross section geometry. It is seen that an 85% increase in heat removal capacity is achieved when a triangular groove is used. This is since the triangular groove increases the capillary height and promotes thin film evaporation better than a rectangular groove, as discussed in previous chapters. A comparison with models is also included in Figure 81. The CALPEs made in this PhD program are compared to the CALPEs presented in Figure 11, from the literature. From Figure 82, it is evident that considerable improvement in heat removal capacity of CALPEs are achieved when off-the-shelf tubes are replaced with the present optimal design.

In terms of fabrication cost, it should be noted that the values shown in Figure 82 are expected to significantly reduce when the designed CALPE is mass produced, i.e., the

economy of scale. The minimum pressure difference between the evaporator chamber and the sorber bed that should exist to start the evaporation can be calculated based on the pressure drop of the piping between the two chambers, as it has been shown conceptually in Figure 80.

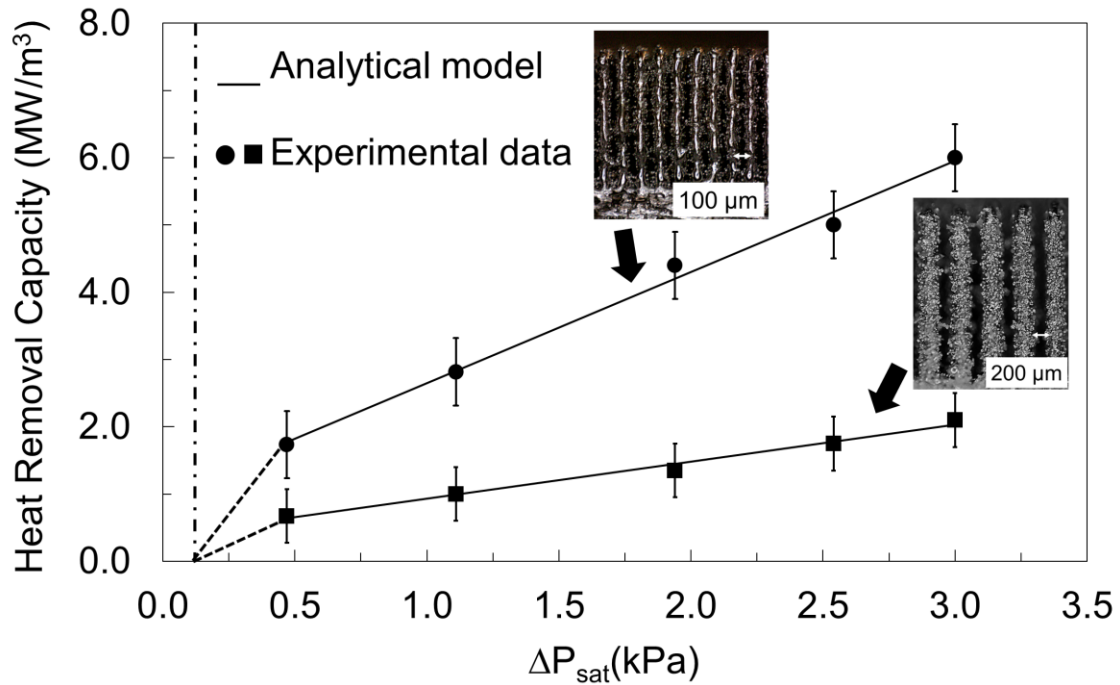


Figure 80. Experimental results for the heat removal capacity of the 3D-printed CALPE vs the pressure difference between the evaporator and vapor collector chamber

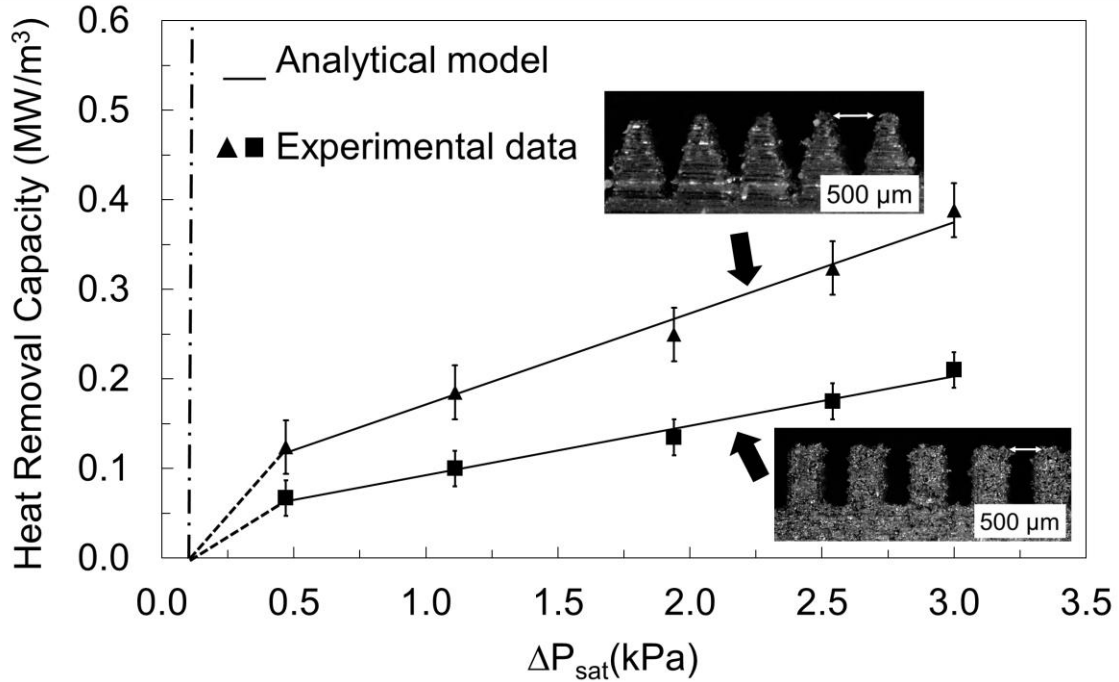


Figure 81. Experimental heat removal capacity of the 3D-printed CALPE vs the pressure difference between the evaporator and vapor collector chamber; comparison between rectangular and triangular grooves

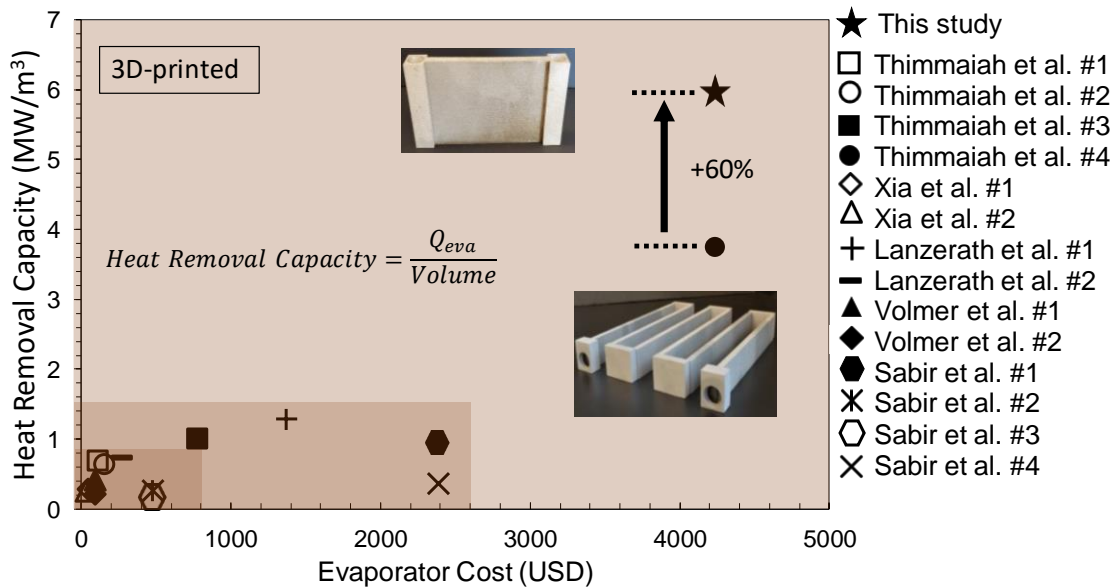


Figure 82. Comparison of experimental CALPEs – comparison between this study and state-of-the-art CALPEs, showing up to 60% improvement in heat removal capacity.

Utilizing microchannels in CALPEs increases the heat removal capacity significantly, but it also increases the pressure drop of the heat transfer fluid side. In most waste-heat recovery applications, this might not be an issue, since the low-grade waste-heat, which would otherwise be dumped in the atmosphere, is readily available, and the pressure drop increase might be justified. Nevertheless, a comparison of pressure drop for different CALPEs is performed. Figure 83 presents the pressure drop values for five different CALPEs. When off-the-shelf tubes are used, the pressure drop is very low, due to the large size of the tubes. Although, as shown previously, the large tube size also means lower heat transfer coefficient and lower heat removal capacity. 3D-printed CALPEs with microchannels have a significantly larger heat removal capacity. The increase in their pressure drop is shown in Figure 83. It is seen that the optimized design of this study decreases pressure drop up to 20 %, as compared to other 3D-printed designs. This is since the design of this study utilizes taller capillary channels and reduced the length of CALPE, lowering the pressure drop.

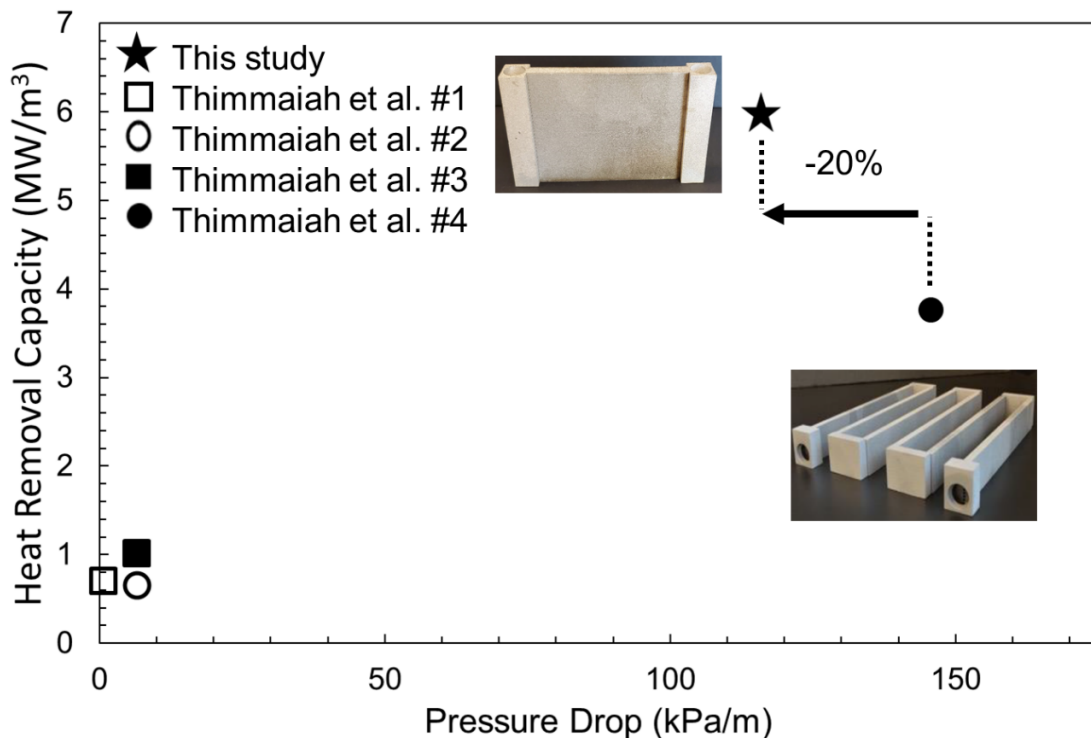


Figure 83. Comparison of experimental CALPEs – comparison between pressure drop of CALPE in this study and those made previously, showing up to 20% reduction

5.6. Conclusion to the chapter

A set novel CALPEs with different fin geometries and dimensions were designed and 3D-printed from stainless steel, aiming to increase their heat removal capacity compared to the off-the-shelf tubes currently used in sorption systems. The fine features of the manufactured CALPEs, namely the fin spacing and thickness of 100 μm , along with the small diameter of the microchannels of the heat transfer fluid side, led to a significant increase in surface-area-to-volume ratio. The 1-mm microchannels on the heat transfer fluid side decreased the internal thermal resistance considerably. Triangular grooves outperformed rectangular ones, due to higher capillary heights and active heat transfer area, leading to more thin film evaporation area. As a result, the presented 3D-printed CALPEs showed a notable per volume heat removal capacity improvement, compared to CALPEs in the literature, made predominantly from off-the-shelf tubes. The experimental data were compared with previously discussed analytical models and showed a good agreement with an average relative difference of 10%. Pressure drop values were reported for CALPEs with microchannels and those made from off-the-shelf tubes.

Chapter 6.

Summary, conclusions, and future work

6.1. Summary and general conclusions

In this PhD research major gaps in the literature regarding understanding of low-pressure evaporation were identified. A unified non-dimensional closed-form analytical solution was proposed that can accurately predict the capillary rise for any given geometry. This model depends on only two parameters: contact angle and a characteristic length scale. The effect of a groove's width, height, wetting perimeter, contact angle, and surface tension were studied. The unified non-dimensional form of capillary rise falls within 10% of the experimental data, therefore, it can be used as a general equation. Additionally, an experimental study of capillary rise was performed to demonstrate the potential of the closed-form model. The effect of variations in manufacturing processes, material choice, grooves' height, width, and contact angle were experimentally investigated and reported. Two parameters affecting the capillary height, characteristic length scale due to the geometry, and the contact angle due to surface roughness were examined. Therefore, the non-dimensional unified capillary rise model was validated with experimental data. The capillary rise in CALPE was experimentally visualized, in absence of heat transfer. A case was made to maximize the wetted area through the capillary action by using a triangular cross section as opposed to a rectangular one. Also, the relationship between contact angle and capillary rise and the effect of roughness on overall capillarity was studied. The contact angle values were measured for various metallic and polymer surfaces. Experimental samples made from metals, polymers, and 3D-printed metals and polymers were investigated. The contact angle was determined in-situ using a sessile drop method. The heat removal capacity of CALPEs were studied through understanding their heat transfer phenomenon on a fundamental level. A detailed study of heat transfer in CALPE was conducted and governing equations for thin film evaporation, natural conduction, and two-dimensional conduction heat transfer were presented. Analytical models were given for rectangular cross-sections, and then extended to alternative geometries. The models consider the effects of groove geometry, thin film evaporation, and contact angle. An order of magnitude analysis was used to simplify the models. The effect of the inertial force, though negligible, was included. A review of common geometries and their heat transfer

models showed an optimal fin geometry to maximize the heat removal capacity of a capillary groove had not been identified. Guidelines to optimize heat removal capacity through alternative geometries, and a genetic algorithm was presented and discussed. A set novel CALPEs with different fin geometries and dimensions were designed and 3D-printed from stainless steel, aiming to increase their heat removal capacity compared to the off-the-shelf tubes currently used in sorption systems. The 1-mm microchannels on the heat transfer fluid side decreased the internal thermal resistance considerably. The experimental data were compared with previously discussed analytical models and showed a good agreement with an average relative difference of 10%. Pressure drop values were reported for CALPEs with microchannels and those made from off-the-shelf tubes. At the end, it was shown that adding surface roughness and using alternative geometries are two methods with which performance of CALPEs can be improved.

6.2. Specific conclusions

The followings are the specific conclusions of this PhD research:

- The change in width of the groove had a greater effect on capillary height than the change in depth,
- The capillary rise in a triangular groove was considerably higher than for other cross-sections,
- A triangular cross-section fin has up to 83% higher wetted area as compared to a rectangular fin.
- The contact angle had a great effect on the overall capillarity in micro-grooves. The more hydrophilic the surface, the higher the capillary rise, and the higher the wetted area,
- Smaller inclination angles led to a longer liquid travel path,
- A 75% decrease in fin spacing can lead to up to a 300% increase in the wetted area of a rectangular fin.

- A maximum characteristic length scale for applicability of capillary action can be found for a given contact angle,
- Surfaces with smaller contact angle (more hydrophilic) would have a higher h^* , and
- The difference between two sets of h^* lines increases significantly as the contact angle increases.
- Wenzel's model holds true for most experimental data.
- In order to increase the capillary height in a groove, the wettability of a solid surface can be increased by decreasing its contact angle by roughening it.
- Smaller contact angle values in CALPEs lead to a higher capillary height and a larger heat transfer area.
- Alternative cross section geometries such as triangular grooves can be used in parallel with wetting surfaces to achieve maximum capillary height, and subsequently, maximum wetted area to be used for heat transfer.
- The results show a strong dependence of thin film evaporation on groove geometry.
- It also suggests a strong relationship between the disjoining pressure and evaporation in a microgroove.
- For a given superheat degree, a maximum heat flux exists in an extended meniscus.
- Thin film evaporation, which only takes place at the top of the meniscus, is the enhancement mechanism of evaporation.
- Thin film evaporation in a capillary groove was deemed the dominant factor when compared to other mechanism of heat transfer.
- The conductive heat transfer in the bulk region can be neglected for small superheat degrees.

- The fine features of the manufactured CALPEs, e.g., the fin spacing and thickness of 100 μm , along with the small diameter of the microchannels of the heat transfer fluid side, led to a significant increase in surface-area-to-volume ratio.
- The presented 3D-printed CALPEs showed a notable per volume heat removal capacity improvement, compared to CALPEs in the literature, made predominantly from off-the-shelf tubes.
- Triangular grooves outperformed rectangular ones, due to higher capillary heights and active heat transfer area, leading to more thin film evaporation area.

6.3. Future work

The following research directions can be considered as the continuation of this study:

- CALPE experiments can be performed with a constant water level height.
- CALPE experiments can be performed with a sorber bed instead of a condenser and can be compared with the results given in this thesis.
- Comparison of the CALPEs presented in this work with other low-pressure evaporation methods can be performed.
- Industrial scalability of the proposed CALPEs can be studied.
- The effect of vibration on CALPE, such as on a moving vehicle, can be studied.
- The capillary model can be extended to account for parameters not included, and by adding the effect of corner flows in capillary channels.
- Investigation of other capillary channel designs, such as pillars, can be performed by extending the methodology of this study.

- Nature-inspired designs can be investigated with designs inspired by trees.
- Design and manufacturing of CALPEs out of graphite or polymers instead of metals can be carried out to utilize their low heat capacity, low weight, and corrosion-resistance.
- Corrosion-resistant coatings can be applied to CALPEs.
- Plasma coating can be applied to make surfaces more hydrophilic.
- CALPEs can be tested for longevity, corrosion, and outgassing under vacuum.
- Consideration of the power consumption of the heat transfer fluid pumps and their pressure drop can be considered.
- Vacuum chambers can be specifically designed for a compact and light CALPE.
- A large-scale modeling and optimization of CALPE can be done to study the effect of scaling-up.
- Alternative manufacturing methods to reduce the cost of CALPEs should be explored.

References

- [1] U.S. Department of Energy. Buildings energy databook. Energy Effic Renew Energy Dep 2012:286.
- [2] Askalany AA, Salem M, Ismael IM, Ali AHH, Morsy MG, Saha BB. An overview on adsorption pairs for cooling. *Renew Sustain Energy Rev* 2013;19:565–72. <https://doi.org/10.1016/j.rser.2012.11.037>.
- [3] Pridasawas W. Solar-Driven Refrigeration Systems with Focus on the Ejector Cycle. 2006. <https://doi.org/10.1677/joe.0.1270351>.
- [4] Thimmaiah PC. Development Of Capillary - Assisted Low Pressure Evaporator For Adsorption Chillers. PhD Thesis 2016.
- [5] Bahrehmand H. Development of novel sorber bed heat exchangers for sorption cooling systems. PhD Thesis 2020.
- [6] BC Hydro. How inefficient A/C use is leaving British Columbians out of pocket in the cold 2020. <https://www.bchydro.com/>.
- [7] Lawrence Berkeley National Laboratory. Environmental Energy Technologies Division 2020. www.lbl.gov.
- [8] Farrington R, Rugh J. Impact of Vehicle Air-Conditioning on Fuel Economy, Tailpipe Emissions, and Electric Vehicle Range. *Earth Technol Forum* 2000:<http://www.nrel.gov/docs/fy00osti/28960.pdf>.
- [9] NRCan 2018. <https://www.nrcan.gc.ca/home>.
- [10] Statistics Canada 2020. www.statcan.gc.ca.
- [11] M. Bollwein, H. Bahrehmand, G. B. Abadi and MB. Integration of sorption cooling systems in PEM fuel cell buses. 5th IEA Expert. Meet., University of Ottawa: 2019.
- [12] Thimmaiah PC, Sharafian A, Rouhani M, Huttema W, Bahrami M. Evaluation of low-pressure flooded evaporator performance for adsorption chillers. *Energy* 2017;122:144–58. <https://doi.org/10.1016/j.energy.2017.01.085>.
- [13] Wang RZ, Oliveira RG. Adsorption refrigeration-An efficient way to make good use of waste heat and solar energy. *Prog Energy Combust Sci* 2006;32:424–58. <https://doi.org/10.1016/j.pecs.2006.01.002>.
- [14] Lemmon EW, Bell IH, Huber ML, McLinden MO. NIST Standard Reference Database 23: Reference Fluid Thermodynamic and Transport Properties-REFPROP, Version 9.0, National Institute of Standards and Technology 2018:135. <https://doi.org/http://dx.doi.org/10.18434/T4JS3C>.

- [15] Bu X, Ma W, Li H. Heat and mass transfer of ammonia-water in falling film evaporator. *Front Energy* 2011;5:358–66. <https://doi.org/10.1007/s11708-011-0161-y>.
- [16] Shahzad MW, Burhan M, Ng KC. Development of Falling Film Heat Transfer Coefficient for Industrial Chemical Processes Evaporator Design. *Stat Approaches With Emphas Des Exp Appl to Chem Process* 2018. <https://doi.org/10.5772/intechopen.69299>.
- [17] Shahzada MW, Ng KC, Thu K, Myat A, Gee CW. An improved film evaporation correlation for saline water at sub-atmospheric pressures. *AIP Conf Proc* 2012;1440:1085–91. <https://doi.org/10.1063/1.4704324>.
- [18] Huang K, Deng X, Chen M. Falling Film Evaporator for Desorption of Basic Aluminum Sulfate SO₂-Rich Solution and Enhancement of Heat and Mass Transfer. *Energy and Fuels* 2017;31:13871–82. <https://doi.org/10.1021/acs.energyfuels.7b02206>.
- [19] Sabir HM, ElHag YBM, Benhadj-Djilali R. Experimental study of capillary-assisted evaporators. *Energy Build* 2008;40:399–407. <https://doi.org/10.1016/j.enbuild.2007.02.036>.
- [20] Sabir HM, ElHag YBM. A study of capillary-assisted evaporators. *Appl Therm Eng* 2007;27:1555–64. <https://doi.org/10.1016/j.applthermaleng.2006.09.011>.
- [21] Xia ZZ, Yang GZ, Wang RZ. Experimental investigation of capillary-assisted evaporation on the outside surface of horizontal tubes. *Int J Heat Mass Transf* 2008;51:4047–54. <https://doi.org/10.1016/j.ijheatmasstransfer.2007.11.042>.
- [22] Xia ZZ, Yang GZ, Wang RZ. Capillary-assisted flow and evaporation inside circumferential rectangular micro groove. *Int J Heat Mass Transf* 2009;52:952–61. <https://doi.org/10.1016/j.ijheatmasstransfer.2008.05.041>.
- [23] Cheppudira Thimmaiah P, Sharafian A, Huttema W, Osterman C, Ismail A, Dhillon A, et al. Performance of finned tubes used in low-pressure capillary-assisted evaporator of adsorption cooling system. *Appl Therm Eng* 2016;106:371–80. <https://doi.org/10.1016/j.applthermaleng.2016.06.038>.
- [24] Cheppudira Thimmaiah P, Sharafian A, Huttema W, McCague C, Bahrami M. Effects of capillary-assisted tubes with different fin geometries on the performance of a low-operating pressure evaporator for adsorption cooling system applications. *Appl Energy* 2016;171:256–65. <https://doi.org/10.1016/j.apenergy.2016.03.070>.
- [25] Lanzerath F, Seiler J, Erdogan M, Schreiber H, Steinhilber M, Bardow A. The impact of filling level resolved: Capillary-assisted evaporation of water for adsorption heat pumps. *Appl Therm Eng* 2016;102:513–9. <https://doi.org/10.1016/j.applthermaleng.2016.03.052>.
- [26] Sabir HM, Bwalya AC. Experimental study of capillary-assisted water evaporators

- for vapour-absorption systems. *Appl Energy* 2002;71:45–57. [https://doi.org/10.1016/S0306-2619\(01\)00042-3](https://doi.org/10.1016/S0306-2619(01)00042-3).
- [27] Schnabel L, Witte K, Kowol J SP. Evaluation of different evaporator concepts for Thermally driven sorption Heat Pumps and Chiller., *Int Sorption Heat Pump Conf* 2011:525–43. doi:10.1081/E-EEE2-120046011.; n.d.
- [28] Cheng P, Dong J, Thompson SM, Ma HB. Heat transfer in bulk and thin-film fluid regions of rectangular microgroove. *J Thermophys Heat Transf* 2012;26:108–14. <https://doi.org/10.2514/1.T3684>.
- [29] Hopkins RC, Faghri A, Khrustalev D. Flat miniature heat pipes with micro capillary grooves. *Am Soc Mech Eng Heat Transf Div HTD* 1997;349:71–80.
- [30] Ma HB, Peterson GP. Experimental investigation of the maximum heat transport in triangular grooves. *J Heat Transfer* 1996;118:740–6. <https://doi.org/10.1115/1.2822694>.
- [31] Li X, Wang J, Hu Q, Bao L, Zhang H. Experimental and theoretical research on capillary limit of micro heat pipe with compound structure of sintered wick on trapezium-grooved substrate. *Heat Mass Transf Und Stoffuebertragung* 2013;49:381–9. <https://doi.org/10.1007/s00231-012-1090-y>.
- [32] Weibel JA, Garimella S V. Recent Advances in Vapor Chamber Transport Characterization for High-Heat-Flux Applications. vol. 45. 2013. <https://doi.org/10.1016/B978-0-12-407819-2.00004-9>.
- [33] Haake D, Klatt J, Grah A, Dreyer ME. Flow rate limitation of steady convective dominated open capillary channel flows through a groove. *Microgravity Sci Technol* 2010;22:129–38. <https://doi.org/10.1007/s12217-009-9164-2>.
- [34] Chen T. Capillary force-driven fluid flow in open grooves with different sizes. *J Thermophys Heat Transf* 2015;29:594–601. <https://doi.org/10.2514/1.T4313>.
- [35] Ayyaswamy PS, Catton I, Edwards DK. Capillary flow in triangular grooves. *J Appl Mech Trans ASME* 1974;41:332–6. <https://doi.org/10.1115/1.3423288>.
- [36] Raphaël E. Capillary rise of a wetting fluid in a semi-circular groove. *J Phys* 1989;50:485–91. <https://doi.org/10.1051/jphys:01989005004048500>.
- [37] Rye RR, Mann JA, Yost FG. The flow of liquids in surface grooves. *Langmuir* 1996;12:555–65. <https://doi.org/10.1021/la9500989>.
- [38] Romero LA, Yost FG. Flow in an open channel capillary. *J Fluid Mech* 1996;322:109–29. <https://doi.org/10.1017/S0022112096002728>.
- [39] Hartge KH, Bachmann J, Woche SK. Influence of the cross-section shape in the capillaries on the wetting properties demonstrated by the calculated wetting angles.

Int Agrophysics 2004;18:11–6.

- [40] Long L, Zhang B. The distribution of fluids in irregular capillary tubes: a new capillary model based on the single-corner capillary. *J Pet Explor Prod Technol* 2018;8:341–50. <https://doi.org/10.1007/s13202-017-0385-4>.
- [41] Kim J, Moon MW, Kim HY. Capillary rise in superhydrophilic rough channels. *Phys Fluids* 2020;32. <https://doi.org/10.1063/1.5133826>.
- [42] Abadi GB, Bahrami M. Combined evaporator and condenser for sorption cooling systems: A steady-state performance analysis. *Energy* 2020;209:118504. <https://doi.org/10.1016/j.energy.2020.118504>.
- [43] Honschoten JWV, Brunets N, Tas NR. Capillarity at the nanoscale. *Chem Soc Rev* 2010;39:1096–114. <https://doi.org/10.1039/b909101g>.
- [44] Young T. An essay on the cohesion of fluids. *Phil Trans R Soc* 1805;17:65–87. <https://doi.org/10.9772/jpspe1979.17.39>.
- [45] Whyman G, Bormashenko E, Stein T. The rigorous derivation of Young, Cassie-Baxter and Wenzel equations and the analysis of the contact angle hysteresis phenomenon. *Chem Phys Lett* 2008;450:355–9. <https://doi.org/10.1016/j.cplett.2007.11.033>.
- [46] Roura P, Fort J. Local thermodynamic derivation of Young's equation. *J Colloid Interface Sci* 2004;272:420–9. <https://doi.org/10.1016/j.jcis.2004.01.028>.
- [47] Wang HJ, Tsai HC, Chen HK, Shing TK. Capillarity of rectangular micro grooves and their application to heat pipes. *Tamkang J Sci Eng* 2005;8:249–55.
- [48] Carey VP. *Liquid-vapor phase-change phenomena: an introduction to the thermophysics of vaporization and condensation processes in heat transfer equipment* - Ghent University Library. Washington DC by Hemisphere; 1992.
- [49] Yang D, Krasowska M, Priest C, Popescu MN, Ralston J. Dynamics of capillary-driven flow in open microchannels. *J Phys Chem C* 2011;115:18761–9. <https://doi.org/10.1021/jp2065826>.
- [50] Deng D, Tang Y, Zeng J, Yang S, Shao H. Characterization of capillary rise dynamics in parallel micro V-grooves. *Int J Heat Mass Transf* 2014;77:311–20. <https://doi.org/10.1016/j.ijheatmasstransfer.2014.05.003>.
- [51] Bahrami M, Yovanovich MM, Culham JR. Pressure drop of fully-developed, laminar flow in microchannel of arbitrary cross-section. *J Fluids Eng Trans ASME* 2006;128:1036–44. <https://doi.org/10.1115/1.2234786>.
- [52] Fu R, Hu X, Zhang H, Yan Y, Zhou W, Wang J. Investigation of the influence of Fe₃O₄-water nanofluids on capillary performance in microgrooves wick. *Appl*

- [53] Deng D, Tang Y, Huang G, Lu L, Yuan D. Characterization of capillary performance of composite wicks for two-phase heat transfer devices. *Int J Heat Mass Transf* 2013;56:283–93. <https://doi.org/10.1016/j.ijheatmasstransfer.2012.09.002>.
- [54] Ouali FF, McHale G, Javed H, Trabi C, Shirtcliffe NJ, Newton MI. Wetting considerations in capillary rise and imbibition in closed square tubes and open rectangular cross-section channels. *Microfluid Nanofluidics* 2013;15:309–26. <https://doi.org/10.1007/s10404-013-1145-5>.
- [55] da Vinci L. Manuscripts of Léonardo de Vinci. Vol N, Folios 11, 67, 74 n.d.
- [56] Boyle R. New experiments physico-mechanicall, touching the spring of the air and its effects 1660.
- [57] Einstein A. Folgerungen aus den Capillaritätserscheinungen. *Ann Der Phys* 309 1901:513–523.
- [58] Marmur A. Line tension and the intrinsic contact angle in solid-liquid-fluid systems. *J Colloid Interface Sci* 1997;186:462–6. <https://doi.org/10.1006/jcis.1996.4666>.
- [59] Tsori Y. Discontinuous liquid rise in capillaries with varying cross-sections. *Langmuir* 2006;22:8860–3. <https://doi.org/10.1021/la061605x>.
- [60] Fries N, Dreyer M. An analytic solution of capillary rise restrained by gravity. *J Colloid Interface Sci* 2008;320:259–63. <https://doi.org/10.1016/j.jcis.2008.01.009>.
- [61] Ichikawa N, Satoda Y. Interface dynamics of capillary flow in a tube under negligible gravity condition. *J Colloid Interface Sci* 1994;162:350–5. <https://doi.org/10.1006/jcis.1994.1049>.
- [62] Extrand CW. Forces, pressures and energies associated with liquid rising in nonuniform capillary tubes. *J Colloid Interface Sci* 2015;450:135–40. <https://doi.org/10.1016/j.jcis.2015.03.007>.
- [63] Khumpuang S, Horade M, Fujioka K, Sugiyama S. Capillary Rise Modeling and Fabrication of Crown-shaped Microneedle Array for Blood Extraction. *Dep Microsyst Technol Grad Sch Sci Eng Ritsumeikan Univ* n.d.
- [64] Ju-hon W, Yong T, Long-sheng L. Capillary force of a novel skew-grooved wick structure for micro heat pipes. *J Cent South Univ Technol* 2011;18:2170–5.
- [65] Smith SM, Taft BS, Moulton J. Contact angle measurements for advanced thermal management technologies. *Front Heat Mass Transf* 2014;5. <https://doi.org/10.5098/hmt.5.6>.

- [66] Schwartz AM. Contact angle hysteresis: A molecular interpretation. *J Colloid Interface Sci* 1980;75:404–8. [https://doi.org/10.1016/0021-9797\(80\)90465-8](https://doi.org/10.1016/0021-9797(80)90465-8).
- [67] Tadmor R, Yadav PS. As-placed contact angles for sessile drops. *J Colloid Interface Sci* 2008;317:241–6. <https://doi.org/10.1016/j.jcis.2007.09.029>.
- [68] Khandekar S, Panigrahi PK, Lefèvre F, Bonjour J. LOCAL HYDRODYNAMICS OF FLOW IN A PULSATING HEAT PIPE: A REVIEW. *Front Heat Pipes* 2010;1:23003. <https://doi.org/10.5098/fhp.v1.2.3003>.
- [69] Diaz ME, Fuentes J, Cerro RL, Savage MD. Hysteresis during contact angles measurement. *J Colloid Interface Sci* 2010. <https://doi.org/10.1016/j.jcis.2009.11.055>.
- [70] Butt rgen, Golovko DS, Bonaccorso E. On the Derivation of Young’s Equation for Sessile Drops: Nonequilibrium Effects Due to Evaporation. *J Phys Chem B* 2007. <https://doi.org/10.1021/jp065348g>.
- [71] Rodríguez-Valverde MA, Montes Ruiz-Cabello FJ, Gea-Jódar PM, Kamusewitz H, Cabrerizo-Vílchez MA. A new model to estimate the Young contact angle from contact angle hysteresis measurements. *Colloids Surfaces A Physicochem Eng Asp* 2010;365:21–7. <https://doi.org/10.1016/j.colsurfa.2010.01.055>.
- [72] Tadmor R. Line Energy and the Relation between Advancing, Receding, and Young Contact Angles. *Langmuir* 2004, 2004. <https://doi.org/10.1021/la049410h>.
- [73] Lamour G, Hamraoui A, Buvailo A, Xing Y, Keuleyan S, Prakash V, et al. Contact Angle Measurements Using a Simplified Experimental Setup. *J Chem Educ* 2010. <https://doi.org/10.1021/ed100468u>.
- [74] Bernardin JI, Mudawar I, Christopher _F, Walshf B, Fransesi EI. Contact angle temperature dependence for water droplets on practical aluminum surfaces. *Inf J Heat Mass Trnsfr* 1997;40:1017–33.
- [75] Benner Jr RE, Scriven LE, Davis HT. Structure and Stress in the Gas-Liquid-Solid Contact Region 1981.
- [76] Zhang J, Li J, Han Y. Superhydrophobic PTFE surfaces by extension. *Macromol Rapid Commun* 2004;25:1105–8. <https://doi.org/10.1002/marc.200400065>.
- [77] Holmes-Farley SR, Reamey RH, Mccarthy TJ, Deutch J, Whitesides GM. Acid-Base Behavior of Carboxylic Acid Groups Covalently Attached at the Surface of Polyethylene: The Usefulness of Contact Angle in Following the Ionization of Surface Functionality1. *Langmuir* 1985;1:725–40.
- [78] WENZEL RN. RESISTANCE OF SOLID SURFACES TO WETTING BY WATER. *Ind Eng Chem* 1936;28:988.

- [79] Cassie ABD, Baxter S. WETTABILITY OF POROUS SURFACES. *Trans Faraday Soc* 1944;40:546.
- [80] Tamai Y, Aratani K. Experimental Study of the Relation between Contact Angle and Surface Roughness. *J Phys Chem* 1972;76.
- [81] Ryan BJ, Poduska KM. Roughness effects on contact angle measurements. *Am J Phys* 2008;76:1074. <https://doi.org/10.1119/1.2952446>.
- [82] Berim GO, Ruckenstein E. Microscopic Interpretation of the Dependence of the Contact Angle on Roughness. *Langmuir* 2005;21:7743. <https://doi.org/10.1021/la050676d>.
- [83] Li C, Zhang J, Han J, Yao B. A numerical solution to the effects of surface roughness on water-coal contact angle. *Sci Rep* 2021;11:459. <https://doi.org/10.1038/s41598-020-80729-9>.
- [84] Bamorovat Abadi G, Bahrami M. A general form of capillary rise equation in micro-grooves. *Sci Rep* 2020;10:19709. <https://doi.org/10.1038/s41598-020-76682-2>.
- [85] ASME. *Surface Texture*. The American Society of Mechanical Engineers; 2006.
- [86] Whitehouse D. *Surfaces and their Measurement*. Taylor Hobson Ltd 2002.
- [87] Mitutoyo. Mitutoyo America Corporation | Precision Metrology Solutions 2022. <https://www.mitutoyo.com>.
- [88] Kubiak KJ, Wilson MCT, Mathia TG, Carval P. Wettability versus roughness of engineering surfaces. *Wear* 2011;271:523–8. <https://doi.org/10.1016/j.wear.2010.03.029>.
- [89] Moffat RJ. Describing the uncertainties in experimental results. *Exp Therm Fluid Sci* 1988;1:3–17. [https://doi.org/https://doi.org/10.1016/0894-1777\(88\)90043-X](https://doi.org/https://doi.org/10.1016/0894-1777(88)90043-X).
- [90] Bergman T, Lavine A, Incropera F, DeWitt D. *Introduction to heat transfer*. John Wiley & Sons, Inc.; 2011.
- [91] Jiao AJ, Riegler AR, Ma AHB, Peterson AGP, Peterson GP, Nanofluid M. Thin film evaporation effect on heat transport capability in a grooved heat pipe. *Microfluid Nanofluid* 2005. <https://doi.org/10.1007/s10404-004-0015-6>.
- [92] Xu X, Carey VP. Film evaporation from a micro-grooved surface - An approximate heat transfer model and its comparison with experimental data. *Thermophysics* 2012;4:512–20. <https://doi.org/10.2514/3.215>.
- [93] Khrustalev D, Faghri A. Heat Transfer During Evaporation on Capillary-Grooved Structures of Heat Pipes. *Trans ASME* 1995.

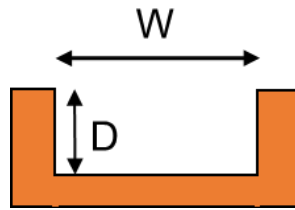
- [94] Hanlon MA, Ma HB. Evaporation Heat Transfer in Sintered Porous Media. *Trans ASME* 2003. <https://doi.org/10.1115/1.1560145>.
- [95] Potash M, Wayner PC. Evaporation from a two-dimensional extended meniscus. *Int J Heat Mass Transf* 1972;15:1851–63. [https://doi.org/10.1016/0017-9310\(72\)90058-0](https://doi.org/10.1016/0017-9310(72)90058-0).
- [96] Wayner PC, Kao YK, LaCroix L V. The interline heat-transfer coefficient of an evaporating wetting film. *Int J Heat Mass Transf* 1976;19:487–92. [https://doi.org/https://doi.org/10.1016/0017-9310\(76\)90161-7](https://doi.org/https://doi.org/10.1016/0017-9310(76)90161-7).
- [97] Schonberg JA, Wayner PC. Analytical solution for the integral contact line evaporative heat sink. *Thermophysics* 1992;6:128–34. <https://doi.org/10.2514/3.327>.
- [98] Schonberg JA, Dasgupta S, Wayner PC. An Augmented Young-Laplace Model of an Evaporating Meniscus in a Microchannel with High Heat Flux. *Exp Therm Fluid Sci* 1995.
- [99] Ma HB, Cheng AP, Borgmeyer AB, Wang AYX. Fluid flow and heat transfer in the evaporating thin film region. *Microfluid Nanofluid* 2008. <https://doi.org/10.1007/s10404-007-0172-5>.
- [100] Cheng P, Dong J, Thompson SM, Ma HB. Heat Transfer in Bulk and Thin-Film Fluid Regions of Rectangular Microgroove. *J Thermophys HEAT Transf* 2011. <https://doi.org/10.2514/1.T3684>.
- [101] Ma H. *Oscillating heat pipes*. Springer Science+Business Media New York; 2015. <https://doi.org/10.1007/978-1-4939-2504-9>.
- [102] Theodore L. Bergman, Frank P. Incropera, David P. DeWitt ASL. *Fundamentals of Heat and Mass Transfer*. John Wiley Sons 2011.
- [103] Moffat RJ. Describing the uncertainties in experimental results. *Exp Therm Fluid Sci* 1988;1:3–17.
- [104] J.P. H. *Heat Transfer*. 2008. <https://doi.org/10.1016/b978-1-933762-24-1.50019-x>.
- [105] Holman JP. *Experimental Methods for Engineers*. vol. s1-VIII. 1853. <https://doi.org/10.1093/nq/s1-VIII.193.43-b>.

Appendix A.

Capillary rise equation for different cross sections

In this Appendix, a step-by-step approach is given to attain the final capillary rise equation for different cross sections.

Rectangular cross-section:



$$\sigma_{sv} = \sigma_{sl} + \sigma_{lv} \cos \theta \quad (\text{A.1})$$

$$F_c = -dE/dy \quad (\text{A.2})$$

$$dE = \sigma_{sv} dA_{sv} + \sigma_{sl} dA_{sl} + \sigma_{lv} dA_{lv} \quad (\text{A.3})$$

$$E = \sigma_{lv} (A_{lv} - A_{sl} \cos \theta) \quad (\text{A.4})$$

$$dA_{lv} = W dy \quad (\text{A.5})$$

$$dA_{sl} = (2D + W) dy \quad (\text{A.6})$$

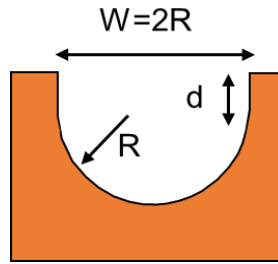
$$F_c = -dE/dy = \sigma_{lv} [(2D + W) \cos \theta - W] \quad (\text{A.7})$$

$$F_g = mg = \rho g (DWh) \quad (\text{A.8})$$

Since $F_c = F_g \sin \alpha$, it results:

$$h_{rec} = \frac{\sigma [(2D + W) \cos \theta - W]}{\rho g D W \sin \alpha} \quad (\text{A.9})$$

Cylindrical cross-section:



$$\sigma_{sv} = \sigma_{sl} + \sigma_{lv} \cos \theta \quad (\text{A.10})$$

$$F_c = -dE/dy \quad (\text{A.11})$$

$$dE = \sigma_{sv} dA_{sv} + \sigma_{sl} dA_{sl} + \sigma_{lv} dA_{lv} \quad (\text{A.12})$$

$$E = \sigma_{lv} (A_{lv} - A_{sl} \cos \theta) \quad (\text{A.13})$$

$$dA_{lv} = 2R dy \quad (\text{A.14})$$

$$dA_{sl} = (2d + \pi R) dy \quad (\text{A.15})$$

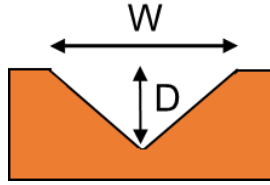
$$F_c = -dE/dy = \sigma_{lv} [-2R + (2d + \pi R) \cos \theta] \quad (\text{A.16})$$

$$F_g = mg = \rho g h [2dR + 0.5\pi R^2] \quad (\text{A.17})$$

Since $F_c = F_g \sin \alpha$, it results:

$$h_{cyl} = \frac{\sigma [(\pi R + 2d) \cos \theta - 2R]}{\rho g [2dR + \pi R^2 / 2]} \sin \alpha \quad (\text{A.18})$$

Triangular cross-section:



$$\sigma_{sv} = \sigma_{sl} + \sigma_{lv} \cos \theta \quad (\text{A.19})$$

$$F_c = -dE/dy \quad (\text{A.20})$$

$$dE = \sigma_{sv} dA_{sv} + \sigma_{sl} dA_{sl} + \sigma_{lv} dA_{lv} \quad (\text{A.21})$$

$$E = \sigma_{lv} (A_{lv} - A_{sl} \cos \theta) \quad (\text{A.22})$$

$$dA_{lv} = W dy \quad (\text{A.23})$$

$$dA_{sl} = 2 \sqrt{(D^2 + W^2/4)} dy \quad (\text{A.24})$$

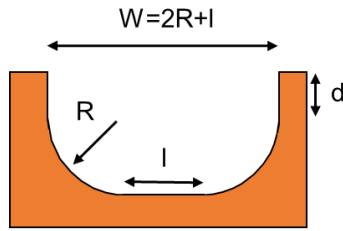
$$F_c = -dE/dy = \sigma_{lv} [(2 \cos \theta \sqrt{(D^2 + W^2/4)} - W)] \quad (\text{A.25})$$

$$F_g = mg = \rho g (DWh/2) \quad (\text{A.26})$$

Since $F_c = F_g \sin \alpha$, it results:

$$h_{tri} = \frac{\sigma [2 \cos \theta \sqrt{D^2 + \frac{W^2}{4}} - W]}{\rho g W D / 2 \sin \alpha} \quad (\text{A.27})$$

Curved cross-section:



$$\sigma_{sv} = \sigma_{sl} + \sigma_{lv} \cos \theta \quad (\text{A.28})$$

$$F_c = -dE/dy \quad (\text{A.29})$$

$$dE = \sigma_{sv} dA_{sv} + \sigma_{sl} dA_{sl} + \sigma_{lv} dA_{lv} \quad (\text{A.30})$$

$$E = \sigma_{lv} (A_{lv} - A_{sl} \cos \theta) \quad (\text{A.31})$$

$$dA_{lv} = (2R+l)dy \quad (\text{A.32})$$

$$dA_{sl} = (2d+l+\pi R)dy \quad (\text{A.33})$$

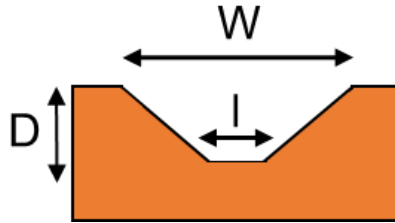
$$F_c = -dE/dy = \sigma_{lv} [-2R-l + (2d+l+\pi R)\cos \theta] \quad (\text{A.34})$$

$$F_g = mg = \rho g h [2dR + dl + Rl + 0.5\pi R^2] \quad (\text{A.35})$$

Since $F_c = F_g \sin \alpha$, it results:

$$h_{curv} = \frac{\sigma [(\pi R + 2d + l)\cos \theta - 2R - l]}{\rho g [2dR + dl + Rl + \pi R^2/2]} \sin \alpha \quad (\text{A.36})$$

Trapezoidal cross-section:



$$\sigma_{sv} = \sigma_{sl} + \sigma_{lv} \cos \theta \quad (A.37)$$

$$F_c = -dE/dy \quad (A.38)$$

$$dE = \sigma_{sv} dA_{sv} + \sigma_{sl} dA_{sl} + \sigma_{lv} dA_{lv} \quad (A.39)$$

$$E = \sigma_{lv} (A_{lv} - A_{sl} \cos \theta) \quad (A.40)$$

$$dA_{lv} = W dy \quad (A.41)$$

$$dA_{sl} = [1 + 2\sqrt{(D^2 + (W-l)^2/4)}] dy \quad (A.42)$$

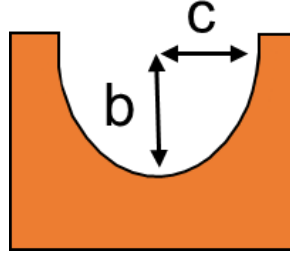
$$F_c = -dE/dy = \sigma_{lv} [\cos \theta (1 + 2\sqrt{(D^2 + (W-l)^2/4)}) - W] \quad (A.43)$$

$$F_g = mg = \rho g ((l+W)Dh/2) \quad (A.44)$$

Since $F_c = F_g \sin \alpha$, it results:

$$h_{trap} = \frac{\sigma [(1 + 2\sqrt{D^2 + \frac{(W-l)^2}{4}}) \cos \theta - W]}{\rho g (l+W)D/2 \sin \alpha} \quad (A.45)$$

Elliptical cross-section:



$$\sigma_{sv} = \sigma_{sl} + \sigma_{lv} \cos \theta \quad (\text{A.46})$$

$$F_c = -dE/dy \quad (\text{A.47})$$

$$dE = \sigma_{sv} dA_{sv} + \sigma_{sl} dA_{sl} + \sigma_{lv} dA_{lv} \quad (\text{A.48})$$

$$E = \sigma_{lv} (A_{lv} - A_{sl} \cos \theta) \quad (\text{A.49})$$

$$dA_{lv} = 2b\epsilon dy \quad (\text{A.50})$$

$$dA_{sl} = 2bE(\sqrt{1 - \epsilon^2}) dy \quad (\text{A.51})$$

$$F_c = -dE/dy = \sigma_{lv} [(2bE(\sqrt{1 - \epsilon^2})) \cos \theta - 2b\epsilon] \quad (\text{A.52})$$

$$F_g = mg \rho_l g (\pi b^2 \epsilon h / 2) \quad (\text{A.53})$$

Since $F_c = F_g \sin \alpha$, it results:

$$h_{ellip} = \frac{\sigma [(2bE(\sqrt{1 - \epsilon^2})) \cos \theta - 2b\epsilon]}{\rho g [\pi \epsilon b^2 / 2] \sin \alpha} \quad (\text{A.54})$$

An aspect ratio is defined for the elliptical micro-groove as:

$$0 \leq \epsilon \equiv \frac{c}{b} \leq 1 \quad (\text{A.55})$$

For an elliptical micro-groove, the cross-sectional area and the perimeter are:

$$\begin{cases} A = \pi bc \\ P = 4bE(\sqrt{1-\varepsilon^2}) \end{cases} \quad (\text{A.56})$$

Where, $E(x) = \int_0^{\pi/2} \sqrt{1-x^2 \sin^2 t} dt$ is the complete elliptic integral of the second kind.

Appendix B.

Non-dimensional capillary rise equation for different cross-sections

In this Appendix, a step-by-step approach is given to get the non-dimensional capillary rise equation for different cross-sections.

Rectangular cross-section:

$$h_{rec} = \frac{\sigma[(2D+W)\cos\theta - W]}{\rho g D W \sin\alpha} \quad (\text{B.1})$$

$$P_w = 2D+W \text{ and } A_c = DW$$

$$\frac{\rho g h \sin\alpha}{\sigma} = \frac{P_w \cos\theta - W}{A_c} = \frac{P_w \cos\theta}{A_c} - \frac{W}{A_c} \quad (\text{B.2})$$

$$h^* = \frac{\rho g h \sin\alpha}{\sigma} * \frac{A_c}{P_w} = \cos\theta - \frac{W}{P_w} \quad (\text{B.3})$$

Where, $\ell = \frac{W}{P_w}$ is a characteristic length scale.

Cylindrical cross-section:

$$h_{cyl} = \frac{\sigma[(\pi R + 2d)\cos\theta - 2R]}{\rho g [2dR + \pi R^2/2] \sin\alpha} \quad (\text{B.4})$$

$$P_w = \pi R + 2d \text{ and } A_c = 2dR + \pi R^2/2$$

$$\frac{\rho g h \sin\alpha}{\sigma} = \frac{P_w \cos\theta - W}{A_c} = \frac{P_w \cos\theta}{A_c} - \frac{W}{A_c} \quad (\text{B.5})$$

$$h^* = \frac{\rho g h \sin \alpha}{\sigma} * \frac{A_c}{P_w} = \cos \theta - \frac{W}{P_w} \quad (\text{B.6})$$

Where, $\ell = \frac{W}{P_w}$ is a characteristic length scale.

Triangular cross-section:

$$h_{tri} = \frac{\sigma [2 \cos \theta \sqrt{D^2 + \frac{W^2}{4}} - W]}{\rho g W D / 2 \sin \alpha} \quad (\text{B.7})$$

$$P_w = 2 \sqrt{D^2 + \frac{W^2}{4}} \text{ and } A_c = W D / 2$$

$$\frac{\rho g h \sin \alpha}{\sigma} = \frac{P_w \cos \theta - W}{A_c} = \frac{P_w \cos \theta}{A_c} - \frac{W}{A_c} \quad (\text{B.8})$$

$$h^* = \frac{\rho g h \sin \alpha}{\sigma} * \frac{A_c}{P_w} = \cos \theta - \frac{W}{P_w} \quad (\text{B.9})$$

Where, $\ell = \frac{W}{P_w}$ is a characteristic length scale.

Curved cross-section:

$$h_{curv} = \frac{\sigma [(\pi R + 2d + l) \cos \theta - 2R - l]}{\rho g [2dR + dl + Rl + \pi R^2 / 2] \sin \alpha} \quad (\text{B.10})$$

$$P_w = \pi R + 2d + l \text{ and } A_c = 2dR + l(d + R) + \pi R^2 / 2$$

$$\frac{\rho g h \sin \alpha}{\sigma} = \frac{P_w \cos \theta - W}{A_c} = \frac{P_w \cos \theta}{A_c} - \frac{W}{A_c} \quad (\text{B.11})$$

$$h^* = \frac{\rho g h \sin \alpha}{\sigma} * \frac{A_c}{P_w} = \cos \theta - \frac{W}{P_w} \quad (\text{B.12})$$

Where $\ell = \frac{W}{P_w}$ is a characteristic length scale.

Trapezoidal cross-section:

$$h_{trap} = \frac{\sigma[(l+2\sqrt{D^2+\frac{(W-l)^2}{4}})\cos\theta-W]}{\rho g(l+W)D/2 \sin \alpha} \quad (\text{B.13})$$

$$P_w = l + 2\sqrt{D^2 + \frac{(W-l)^2}{4}} \text{ and } A_c = (l+W)D/2$$

$$\frac{\rho g h \sin \alpha}{\sigma} = \frac{P_w \cos \theta - W}{A_c} = \frac{P_w \cos \theta}{A_c} - \frac{W}{A_c} \quad (\text{B.14})$$

$$h^* = \frac{\rho g h \sin \alpha}{\sigma} * \frac{A_c}{P_w} = \cos \theta - \frac{W}{P_w} \quad (\text{B.15})$$

Where, $\ell = \frac{W}{P_w}$ is a characteristic length scale.

Elliptical cross-section:

$$h_{cyl} = \frac{\sigma[(\pi R+2d)\cos\theta-2R]}{\rho g[2dR+\pi R^2/2]\sin \alpha} \quad (\text{B.16})$$

$$P_w = 2bE(\sqrt{1-\varepsilon^2}) \text{ and } A_c = \pi \varepsilon b^2/2$$

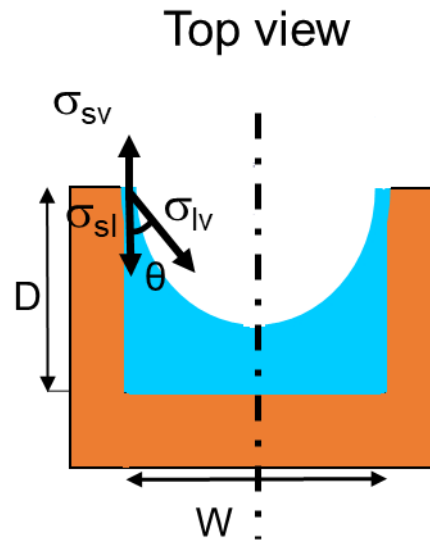
$$\frac{\rho g h \sin \alpha}{\sigma} = \frac{P_w \cos \theta - W}{A_c} = \frac{P_w \cos \theta}{A_c} - \frac{W}{A_c} \quad (\text{B.17})$$

$$h^* = \frac{\rho g h \sin \alpha}{\sigma} * \frac{A_c}{P_w} = \cos \theta - \frac{W}{P_w} \quad (\text{B.18})$$

Where, $\ell = \frac{W}{P_w}$ is a characteristic length scale.

Appendix C.

Force balance in a capillary groove



D: Fin height

W: Fin spacing

$$\sigma_{sv} = \sigma_{sl} + \sigma_{lv} \cos \theta \quad (\text{C.1})$$

$$2DF_c \cos \theta + P_{in} W dh = P_{out} W dh \quad (\text{C.2})$$

$$dF_c = \sigma_{lv} dh \quad (\text{C.3})$$

$$\cos \theta = \frac{\rho g W}{2\sigma} h \quad (\text{C.4})$$

Appendix D.

Fin resistance

The internal convective resistance is caused by the resistance of the heat transfer fluid inside the finned wall. To calculate it, the followings apply. Fins in a CALPE have rectangular cross-section. The CALPE's fin efficiency, located on the surface of the tube, is calculated by Eqs. (D.1-5). Considering a rectangular cross-section [102]:

$$\eta_f = C \left(\frac{K_1(mr_1)I_1(mr_{2c}) - I_1(mr_1)K_1(mr_{2c})}{I_0(mr_1)K_1(mr_{2c}) + K_0(mr_1)I_1(mr_{2c})} \right) \quad (D.1)$$

$$C = \frac{\left(\frac{2r_1}{m}\right)}{(r_{2c}^2 - r_1^2)} \quad (D.2)$$

$$m = \sqrt{\left(\frac{2h}{kt_f}\right)} \quad (D.3)$$

$$r_{2c} = r_2 + \left(\frac{t_f}{2}\right) \quad (D.4)$$

$$A_f = 2\pi(r_{2c}^2 - r_1^2) \quad (D.5)$$

Where r_1 is the distance between the center of the channel to the fin base and r_2 is the distance between the center of the channel to the fin tip. I_0 and K_0 in Eq. (D.1) are modified, zero-order Bessel functions of the first and second kinds, respectively. I_1 and K_1 in Eq. (D.2) are modified, first-order Bessel functions of the first and second kinds, respectively. Fin thickness is shown by t_f in Eq. (D.3) and the fin's heat transfer area is denoted by A_f in Eq. (D.5). To calculate the total external heat transfer surface area of the finned wall the following can be used:

$$A_t = N(A_f + A_b) \quad (D.6)$$

$$A_b = 2\pi r_1 t_b \quad (D.7)$$

Where N is the total number of fins, and A_b and t_b are the plain heat transfer surface area of the finned wall and the space between two fins, respectively. The overall efficiency of the finned wall is calculated by using Eqs. (D.1), (D.5), and (D.6), [102]:

$$\eta_{o,fin} = 1 - \frac{A_f}{A_f - A_b} (1 - \eta_f) \quad (D.8)$$

Therefore, the conductive heat transfer resistance due to the fins of the finned wall can be found by:

$$\eta_{o,fin} = 1 - \frac{A_f}{A_f - A_b} (1 - \eta_f) \quad (D.9)$$

Where the convection coefficient h_o can be calculated through experimental measurements. The finned wall's conductive resistance, under the fins, can be calculated by:

$$R_{wall} = \frac{\ln\left(\frac{r_1}{r_2}\right)}{2\pi kL} \quad (D.10)$$

where r_o and L are the internal radius and length of the finned wall, respectively. The two thermal resistances, R_{fin} and R_{wall} are in series. Consequently, the overall conductive resistance of the CALPE's finned wall is found by Eq. (D.11).

$$R_{o,finned\ tube} = R_{fin} + R_{wall} \quad (D.11)$$

Finally, the internal convective heat transfer resistance inside the finned wall is found by Eq. (D.12):

$$\frac{1}{h_i A_i} = \frac{1}{UA} - \left(\frac{1}{h_o A_o} + R_{o,finned\ tube} \right) \quad (D.12)$$

The capillary evaporation coefficient on the external side of the finned wall is calculated by the experimental measurements. Table D1 is needed to calculate the internal convective resistance. Table D1 is given for 20 °C chilled water inlet temperature.

Table D1. Detailed geometry of CALPE

Parameter	Value
CALPE height, (mm)	60
CALPE width, (mm)	5
CALPE length, (mm)	100
Fin height, (mm)	1.5
Fin spacing, (mm)	0.1
Fin thickness, (mm)	0.1
Fin per inch, (mm)	250
HTF port diameter, (mm)	1

Appendix E.

Uncertainty analysis

The systematic uncertainty [105] of heat transfer rate in a CALPE is calculated by:

$$\left(\frac{\delta \dot{q}_e}{\dot{q}_e}\right)_{systematic} = \sqrt{\left(\frac{\delta \dot{m}_{in}}{\dot{m}_{in}}\right)^2 + \left(\frac{\delta(T_i - T_o)}{T_i - T_o}\right)^2} \quad (E.1)$$

where,

$$\frac{\delta(T_i - T_o)}{T_i - T_o} = \sqrt{\left(\frac{\delta T_i}{T_i}\right)^2 + \left(\frac{\delta T_o}{T_o}\right)^2} \quad (E.2)$$

Therefore, in the calculation of evaporator heat transfer rate, the maximum systematic uncertainty can be found by:

$$systematic\ uncertainty_{max} = \left(\frac{\delta \dot{q}_e}{\dot{q}_e}\right)_{systematic} \times 100 \quad (E.3)$$

Additionally, the standard deviation in measurement of \dot{q}_e , due to the random uncertainty, can be calculated by the measured data during the experiments. The systematic uncertainty for the overall heat transfer coefficient is given by:

$$\left(\frac{\delta U}{U}\right)_{systematic} = \sqrt{\left(\frac{\delta \dot{Q}_e}{\dot{Q}_e}\right)_{systematic}^2 + \left(\frac{\delta \Delta T_{LMTD}}{\Delta T_{LMTD}}\right)^2} \quad (E.4)$$

The maximum uncertainty of overall heat transfer coefficient can be found by having the random uncertainty in data measurement of U_{evap} , over time. The systematic uncertainty of the external heat transfer coefficient is given by:

$$\left(\frac{\delta h_o}{h_o}\right)_{systematic} = \sqrt{\left(\frac{\delta \dot{Q}_e}{\dot{Q}_e}\right)_{systematic}^2 + \left(\frac{\delta \Delta T}{\Delta T}\right)^2} \quad (E.5)$$

Appendix F.

Data analysis

T_{in} and T_{out} , and \dot{m}_{in} were measured to determine the chilled water inlet and outlet temperatures, and the mass flow rate. The following is used to calculate the heat transfer rate:

$$\dot{q}_e = \dot{m}_{in} c_p (T_{in} - T_{out}) \quad (F.1)$$

The average specific heat capacity of chilled water at constant pressure is used. The total evaporation rate, \dot{Q}_e , is the time-average of the heat flow rate:

$$\dot{Q}_e = \frac{\int_{t_1}^{t_2} \dot{q}_e dt}{t_2 - t_1} \quad (F.2)$$

t_1 and t_2 are the beginning and the end time temperatures when the evaporator is at steady state. The average overall heat transfer conductance, UA , of the evaporator is:

$$\overline{UA} = \frac{\dot{Q}_e}{\Delta \bar{T}_{LMTD}} \quad (F.3)$$

where A is the nominal surface area of the tubes and $\Delta \bar{T}_{LMTD}$ is the logarithmic mean temperature difference between the chilled water inside and the liquid water outside the channels:

$$\Delta T_{LMTD} = \frac{T_{in} - T_{out}}{\ln \left(\frac{T_{in} - T_{sat}}{T_{out} - T_{sat}} \right)} \quad (F.4)$$

$$\Delta \bar{T}_{LMTD} = \frac{\int_{t_1}^{t_2} \Delta T_{LMTD} dt}{t_2 - t_1} \quad (F.5)$$

where T_{sat} is the refrigerant saturation temperature.

The overall heat transfer conductance, UA, is expressed by [102]:

$$\frac{1}{UA} = \left(\frac{1}{h_i A_i} + \frac{1}{h_o A_o} + R_{o,finned\ wall} \right) \quad (F.6)$$

The first term of the right-hand side, $\frac{1}{h_i A_i}$, is the internal convective thermal resistance caused by the single-phase flow inside the channel. The second term, $\frac{1}{h_o A_o}$, is the external convective thermal resistance caused by the evaporation on the fin side of the channel. The last term is the conductive thermal resistance of the finned wall. The internal convective resistance, h_i , can be calculated separately. The chilled water flowing inside the channel can be expressed by the non-dimensional parameter Reynolds number, Re_i :

$$Re_i = \frac{\rho V D_{i,tube}}{\mu} \quad (F.7)$$

with V being the chilled water velocity. If the Reynolds number is higher than 2300 ($2300 < Re_i < 5 \times 10^6$) the Gnielinski correlation [102] is valid for the Nusselt number:

$$Nu_i = \frac{\left(\frac{f}{2}\right) (Re_i - 1000) Pr_i}{1 + 12.7 \left(\frac{f}{2}\right)^2 \left(Pr_i^{\frac{2}{3}} - 1\right)} \quad (F.8)$$

where,

$$f = 0.078 Re_i^{-\frac{1}{4}} \quad (F.9)$$

Using Eq.s (F.8) and (F.9), the internal heat transfer coefficient, h_i , can be found:

$$h_i = \frac{Nu_i k_{water}}{D_{i,tube}} \quad (F.10)$$

To calculate the conductive thermal resistance of the finned wall, Appendix IV is used. Eq. (A.106) is given to obtain the external heat transfer coefficient, h_o , of the finned wall:

$$h_o = \frac{1}{\left(\frac{1}{UA} - \frac{1}{h_i A_i} - R_{o, \text{finned tube}}\right) A_o} \quad (\text{F. 11})$$

The finned wall resistance, $R_{o, \text{finned tube}}$, is not given explicitly, as it depends on the external heat transfer coefficient. Therefore, an iterative process should be used to calculate h_o .

Appendix G.

Genetic algorithm optimization

The set of functions for optimization are given below. The total heat transfer and heat transfer coefficient are to be maximized:

$$\min F(x_i) = [\text{objective1}(x_i); \text{objective2}(x_i)]$$
$$x_i \tag{G.1}$$

where, $\text{objective1}(x_i) = - Q_{\text{total}}$, and

$$\text{objective2}(x_i) = - h_{\text{total}}$$

Where Q_{total} and h_{total} are total conductive heat transfer and heat transfer coefficient. The following three variables were considered:

$$\begin{aligned} x_1: \text{fin thickness, } 0.0001(\text{m}) < x_1 < 0.001(\text{m}) \\ x_2: \text{fin height, } 0.0001(\text{m}) < x_2 < 0.002(\text{m}) \\ x_3: \text{fin spacing, } 0.0001(\text{m}) < x_3 < 0.001(\text{m}) \end{aligned} \tag{G.2}$$

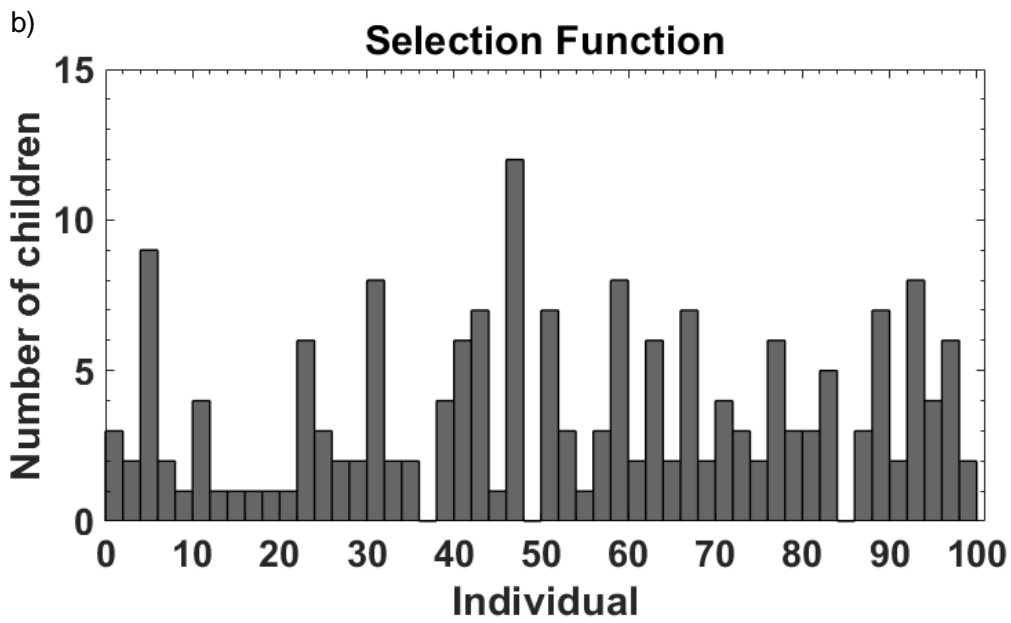
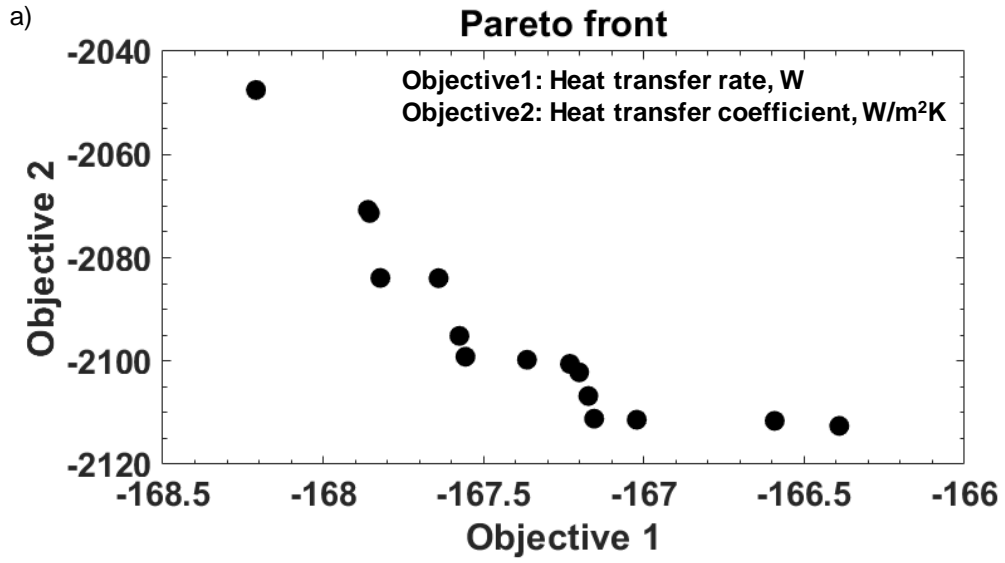
A Pareto frontier is given for a set of solutions. Table G1 gives the options used for GA. The genetic algorithm code ran for 179 generations and had a total of 17,900 function calls. The average Pareto distance was 0.0029 and Pareto spread was 0.28. The first and second objectives are maximizing Q_{total} and h_{total} , respectively, by varying three variables: Fin height, spacing, and thickness. A set of optimal solutions is given in Table G2.

Table G1. Genetic algorithm options used for optimization of two-dimensional conductive heat transfer

Option	Value
Pareto function	0.35
Constraint tolerance	0.001
Crossover fraction	0.8
Function tolerance	0.0001
Max generations	$200 \times N_{\text{variables}} = 600$
Max stall generations	100
Population size	100
Population type	Double vector

Table G2. A set of optimal solutions based on genetic algorithm optimization of two-dimensional conductive heat transfer in a capillary meniscus

Fin height, $\times 10^2$ (m)	Fin spacing, $\times 10^3$ (m)	Fin thickness, $\times 10^3$ (m)	Heat transfer rate, $(W) \times 10^{-3}$	Heat transfer coefficient, $(W/m^2K) \times 10^{-3}$
0.1001	0.1017	0.1056	-0.1664	-2.1126
0.1003	0.1017	0.1054	-0.1666	-2.1116
0.1026	0.1016	0.1043	-0.1676	-2.0951
0.1012	0.1018	0.1047	-0.1672	-2.1068
0.1077	0.1010	0.1041	-0.1682	-2.0475
0.1018	0.1016	0.1047	-0.1672	-2.1006
0.1038	0.1015	0.1041	-0.1678	-2.0839
0.1016	0.1015	0.1048	-0.1672	-2.1022
0.1019	0.1014	0.1048	-0.1674	-2.0998
0.1007	0.1016	0.1049	-0.1672	-2.1112
0.1021	0.1016	0.1043	-0.1676	-2.0992
0.1051	0.1010	0.1045	-0.1679	-2.0707
0.1037	0.1013	0.1046	-0.1676	-2.0840
0.1006	0.1014	0.1052	-0.1670	-2.1114
0.1051	0.1013	0.1043	-0.1679	-2.0713



a) Pareto front and b) selection function data for optimization of total conductive heat transfer in a capillary meniscus

Appendix H.

Momentum conservation model

Conservation of mass can be written as:

$$\frac{\partial u}{\partial x} + \frac{\partial v}{\partial y} = 0 \quad (\text{H. 1})$$

The momentum equation along the x axis is given by (Figure H1):

$$\rho_l u \frac{\partial u}{\partial x} + \rho_l v \frac{\partial u}{\partial y} = -\frac{A}{2\pi\delta^4} \frac{\partial \delta}{\partial x} + \sigma \frac{\partial \kappa}{\partial x} + \mu_l \frac{\partial^2 u}{\partial x^2} + \mu_l \frac{\partial^2 u}{\partial y^2} \quad (\text{H. 2})$$

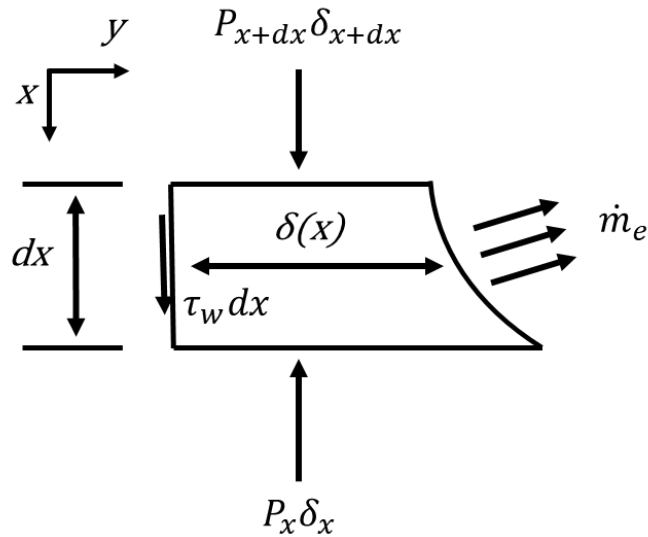


Figure H1. Schematic of the selected control volume in the thin film region for conservation of momentum equation

The energy equation is given as below (Figure H2):

$$u \frac{\partial T}{\partial x} + v \frac{\partial T}{\partial y} = \alpha \left[\frac{\partial^2 T}{\partial x^2} + \frac{\partial^2 T}{\partial y^2} \right] \quad (\text{H. 3})$$

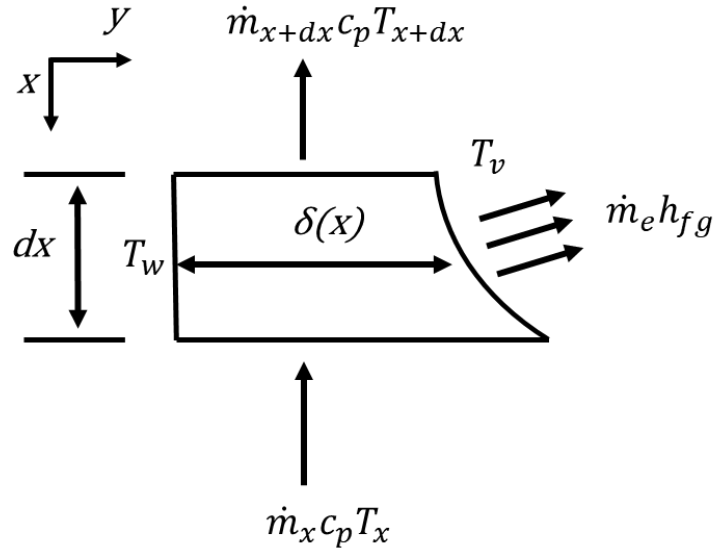


Figure H2. Schematic of the selected control volume in the thin film region for energy equation

Due to evaporation at the boundary, the following can be written for the mass flux (Figure H3):

$$(\dot{m}c_pT)_{in} - (\dot{m}c_pT)_{out} + q''_w dx - \dot{m}''_e h_{fg} dx = 0 \quad (\text{H. 4})$$

$$-\frac{d}{dx} \int_0^\delta \rho u c_p T dy - k \left. \frac{\partial T}{\partial y} \right|_{y=0} = \dot{m}''_e h_{fg} \quad (\text{H. 5})$$

$$\dot{m}_{in} - \dot{m}_{out} - \dot{m}''_e dx = 0 \quad (\text{H. 6})$$

$$-\frac{d}{dx} \int_0^\delta \rho u dy = \dot{m}''_e \quad (\text{H. 7})$$

$$\Rightarrow \frac{d}{dx} \int_0^\delta \rho u \left(1 - \frac{c_p T}{h_{fg}}\right) dy - \frac{k}{h_{fg}} \left. \frac{\partial T}{\partial y} \right|_{y=0} = 0 \quad (\text{H. 8})$$

An order of magnitude analysis can be performed to simplify Eqs. (H.2) and (H.3).

Since $\frac{\partial^2}{\partial x^2} \sim \frac{1}{L^2}$ and $\frac{\partial^2}{\partial y^2} \sim \frac{1}{\delta^2}$ (Figure H4), it follows:

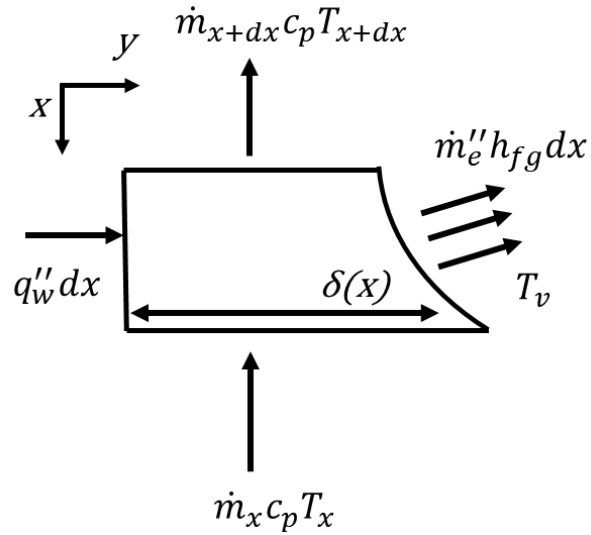


Figure H3. Schematic of the selected control volume in the thin film region for evaporation at the boundary

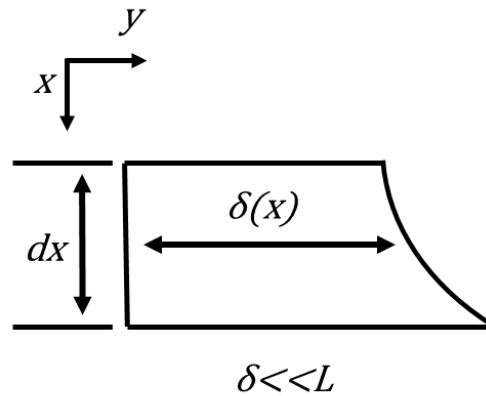


Figure H4. Order of magnitude analysis for the selected control volume in the thin film region. L : Thin film evaporation region length, δ : film thickness

$$\rho_l u \frac{\partial u}{\partial x} + \rho_l v \frac{\partial u}{\partial y} = -\frac{A}{2\pi\delta^4} \frac{\partial \delta}{\partial x} + \sigma \frac{\partial \kappa}{\partial x} + \mu_l \frac{\partial^2 u}{\partial y^2} \quad (\text{H. 9})$$

$$u \frac{\partial T}{\partial x} + v \frac{\partial T}{\partial y} = \alpha \frac{\partial^2 T}{\partial y^2} \quad (\text{H. 10})$$

Subjected to the following boundary conditions:

$$\begin{cases} y = 0 \Rightarrow u, v = 0 \\ y = \delta \Rightarrow \frac{\partial u}{\partial y} = 0 \\ x = 0 \Rightarrow u, v = 0 \end{cases} \quad (\text{H. 11})$$

$$\begin{cases} y = 0 \Rightarrow T = T_w \\ y = \delta \Rightarrow T = T_v \\ x = 0 \Rightarrow T = T_w \end{cases} \quad (\text{H. 12})$$

$$\frac{d}{dx} \int_0^\delta \rho u \left(1 - \frac{c_p T}{h_{fg}} \right) dy - \frac{k}{h_{fg}} \frac{\partial T}{\partial y} \Big|_{y=0} = 0 \quad (\text{H. 13})$$

Using the following relations, the above the governing equations can be non dimensionalized (Figure H5):

$$\begin{cases} \eta = \frac{y}{\delta} \\ \zeta = \frac{x}{\delta} \\ u^* = \frac{u}{u_\delta} \\ v^* = \frac{v}{u_\delta} \\ \theta = \frac{T - T_v}{T_w - T_v} \end{cases} \quad (\text{H. 14})$$

where $u(x, \delta) = u_\delta(x)$.

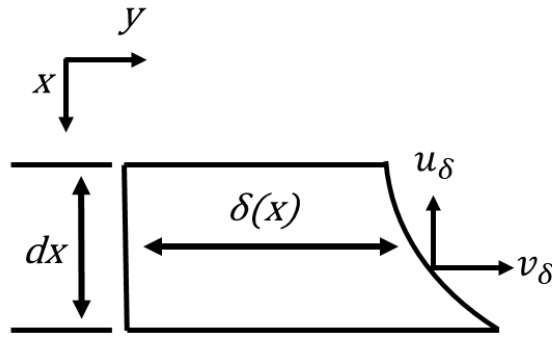


Figure H5. Definition of u_δ and v_δ on the boundary of the meniscus

Eqs. H.1, H.9, and H.10 can be written in their non-dimensional form as:

$$b \left[\frac{u^*}{u_\delta} \frac{\partial u_\delta}{\partial \zeta} + \frac{\partial u^*}{\partial \zeta} \right] - \eta \frac{\partial \delta}{\partial \zeta} \frac{\partial u^*}{\partial \eta} + \frac{\partial v^*}{\partial \eta} = 0 \quad (\text{H. 15})$$

$$\rho_l u^* \left[-\eta \frac{\partial \delta}{\partial \zeta} \frac{\partial u^*}{\partial \eta} + b \left(\frac{\partial u^*}{\partial \zeta} + \frac{u^*}{u_\delta} \frac{\partial u_\delta}{\partial \zeta} \right) \right] + \rho_l v^* \frac{\partial u^*}{\partial \eta} = \frac{b}{u_\delta^2} \left(\sigma \frac{\partial \kappa}{\partial \zeta} - \frac{A}{2\pi\delta^4} \frac{\partial \delta}{\partial \zeta} \right) + \frac{\mu_l}{\delta u_\delta} \frac{\partial^2 u^*}{\partial \eta^2} \quad (\text{H. 16})$$

$$\left(v^* - \eta u^* \frac{\partial \delta}{\partial \zeta} \right) \frac{\partial \theta}{\partial \eta} + b u^* \frac{\partial \theta}{\partial \zeta} = \frac{\alpha}{\delta u_\delta} \frac{\partial^2 \theta}{\partial \eta^2} \quad (\text{H. 17})$$

where $b = \left(1 - \zeta \frac{\partial \delta}{\partial \zeta} \right)$. The non-dimensional boundary conditions are as follows:

$$\begin{cases} \eta = 0 \Rightarrow u^*, v^* = 0 \\ \eta = 1 \Rightarrow \frac{\partial u^*}{\partial \eta} = 0 \\ \zeta = 0 \Rightarrow u^*, v^* = 0 \end{cases} \quad (\text{H. 18})$$

$$\begin{cases} \eta = 0 \Rightarrow \theta = 1 \\ \eta = 1 \Rightarrow \theta = 0 \\ \zeta = 0 \Rightarrow \theta = 1 \end{cases} \quad (\text{H. 19})$$

$$\frac{d}{d\zeta} \int_0^1 b \rho \delta u^* u_\delta \left(1 - \frac{c_p}{h_{fg}} (\Delta T \theta + T_v) \right) d\eta - \frac{k \Delta T}{h_{fg}} \frac{\partial \theta}{\partial \eta} \Big|_{\eta=0} = 0 \quad (\text{H. 20})$$

An integral method is used to solve equations H.15 – H.20. Assuming $u^* = a_0 + a_1 \eta + a_2 \eta^2$ and applying the boundary conditions,

$$\text{Assume } u^* = a_0 + a_1 \eta + a_2 \eta^2 \quad (\text{H. 21})$$

$$\eta = 0 \Rightarrow u^* = 0 \Rightarrow a_0 = 0 \quad (\text{H. 22})$$

$$\eta = 1 \Rightarrow \frac{\partial u^*}{\partial \eta} = 0 \Rightarrow a_1 = -2a_2 \quad (\text{H. 23})$$

$$\eta = 1 \Rightarrow u^* = 1 \Rightarrow a_2 = -1 \quad (\text{H. 24})$$

$$u^* = 2\eta - \eta^2 \quad (\text{H. 25})$$

Therefore, Eq. H.15 becomes:

$$c - bc \left(\frac{u'_\delta}{\delta' u_\delta} \right) + \frac{\partial v^*}{\partial \eta} = 0 \quad (\text{H. 26})$$

$$\eta = 0 \Rightarrow v^* = 0 \quad (\text{H. 27})$$

$$v^* = -2\zeta\eta^2\delta' \left(\frac{u'_\delta}{u_\delta}\right) \left(\frac{\eta}{3} - \frac{1}{2}\right) \quad (\text{H. 28})$$

where $c = 2\eta\delta'(\eta - 1)$. Eq. H.16 becomes:

$$-\rho_l\eta(\eta - 2)(c - bcd) + 2cd\rho_l\zeta\eta\delta' \left(\frac{\eta}{3} - \frac{1}{2}\right) = \frac{b}{u_\delta^2} \left(\sigma\kappa' - \frac{A\delta'}{2\pi\delta^4}\right) - 2\frac{\mu_l}{\delta u_\delta} \quad (\text{H. 29})$$

Since $\delta(\zeta)$ and $u_\delta(\zeta)$ are not a function of η , at $\eta = 0$:

$$\frac{b}{u_\delta^2} \left(\sigma\kappa' - \frac{A\delta'}{2\pi\delta^4}\right) - 2\frac{\mu_l}{\delta u_\delta} = 0 \quad (\text{H. 30})$$

It follows that:

$$u_\delta = \frac{b}{2\mu_l} \left(\sigma\delta\kappa' - \frac{A\delta'}{2\pi\delta^3}\right) \quad (\text{H. 31})$$

where $d = \frac{u'_\delta}{\delta' u_\delta}$. By having u^* , v^* and u_δ , the momentum equation can be simplified

as:

$$\frac{\delta' u_\delta}{u'_\delta} + \frac{\zeta\delta'}{2} - 1 = 0 \quad (\text{H. 32})$$

or,

$$\left(\frac{b}{2u'_\delta\mu_l} \left(\sigma\delta\kappa' - \frac{A\delta'}{2\pi\delta^3}\right) + \frac{\zeta}{2}\right) \delta' - 1 = 0 \quad (\text{H. 33})$$

Similarly, an integral method is used for energy equation:

$$\text{Assume } \theta = g_0 + g_1\eta + g_2\eta^2 \quad (\text{H. 34})$$

$$\eta = 0 \Rightarrow \theta = 1 \Rightarrow g_0 = 1 \quad (\text{H. 35})$$

$$\eta = 1 \Rightarrow \theta = 0 \Rightarrow g_1 = -g_2 - 1 = -g - 1 \quad (\text{H. 36})$$

Therefore, Eq. H.17 becomes:

$$bg' + \left(\frac{\zeta\delta'u'_\delta}{2u_\delta} - \frac{2\alpha}{\delta u_\delta} + b\right)g - \frac{\zeta\delta'u'_\delta}{2u_\delta} = 0 \quad (\text{H. 37})$$

And Eq. H.20 becomes:

$$0.1\rho b\delta u_{\delta}c_p g' + \frac{k\Delta T}{h_{fg}}(g + 1) = 0 \quad (\text{H. 38})$$

Eqs. H.33, H.37, and H.38 are solved together to calculate the heat flux in the thin film region of the meniscus. Derivative of the meniscus curvature is calculated as:

$$\frac{d\kappa}{dx} = \frac{1}{\left[1 + \left(\frac{d\delta}{dx}\right)^2\right]^{\frac{3}{2}}} \left(\frac{d^3\delta}{dx^3} - 3 \frac{d\delta}{dx} \left(\frac{d^2\delta}{dx^2}\right)^2 \right) \quad (\text{H. 39})$$

The initial film thickness, or the non-evaporating region film thickness, is given as:

$$\delta(0) = \delta_0 = \left(\frac{AT_v}{6\pi\rho h_{fg}(T_w - T_v)} \right)^{1/3} \quad (\text{H. 40})$$

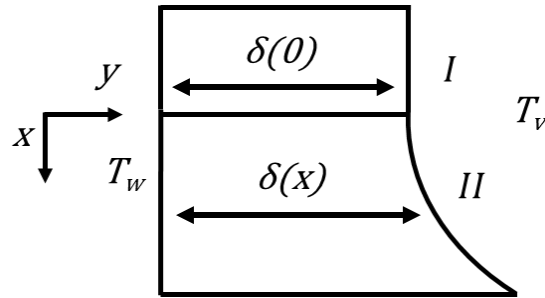


Figure H6. Definition of film thickness at the non-evaporating region

Appendix I.

Results for thin film evaporation in an extended meniscus

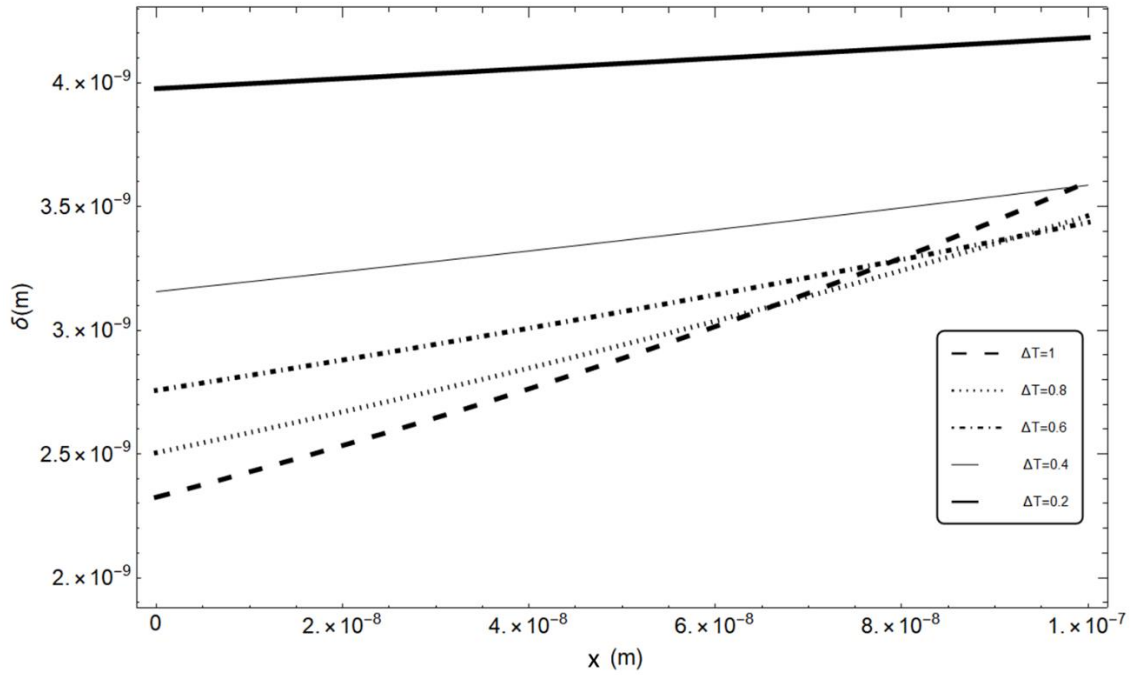


Figure I1. Film thickness as a function of location for various superheat degrees

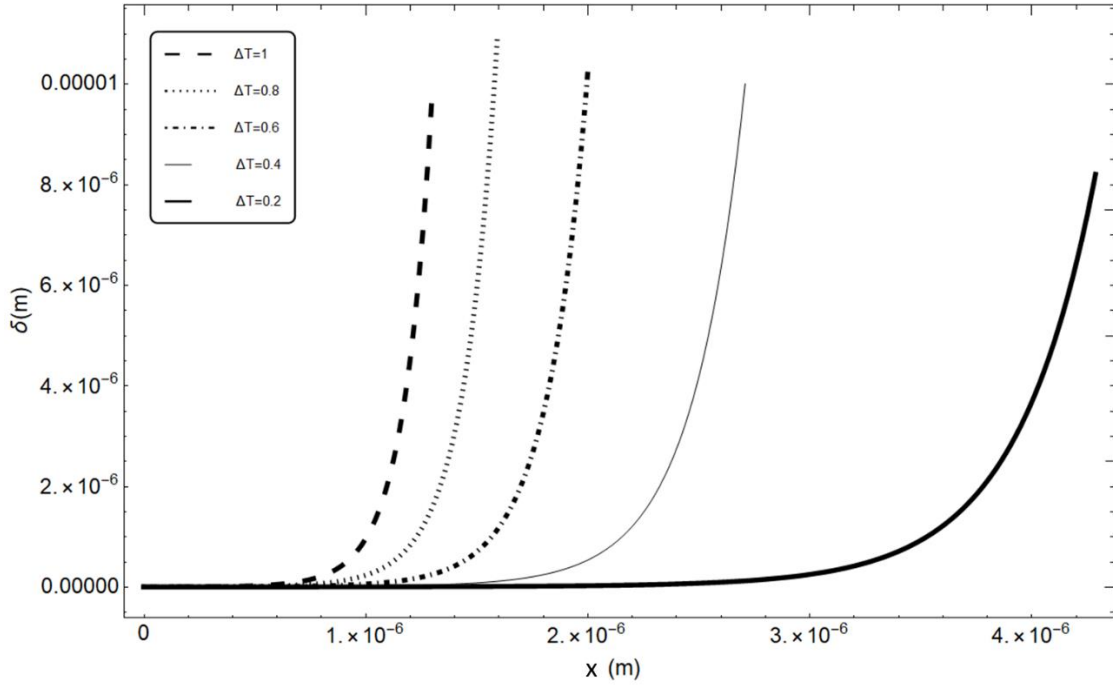


Figure I2. Film thickness as a function of location for various superheat degrees

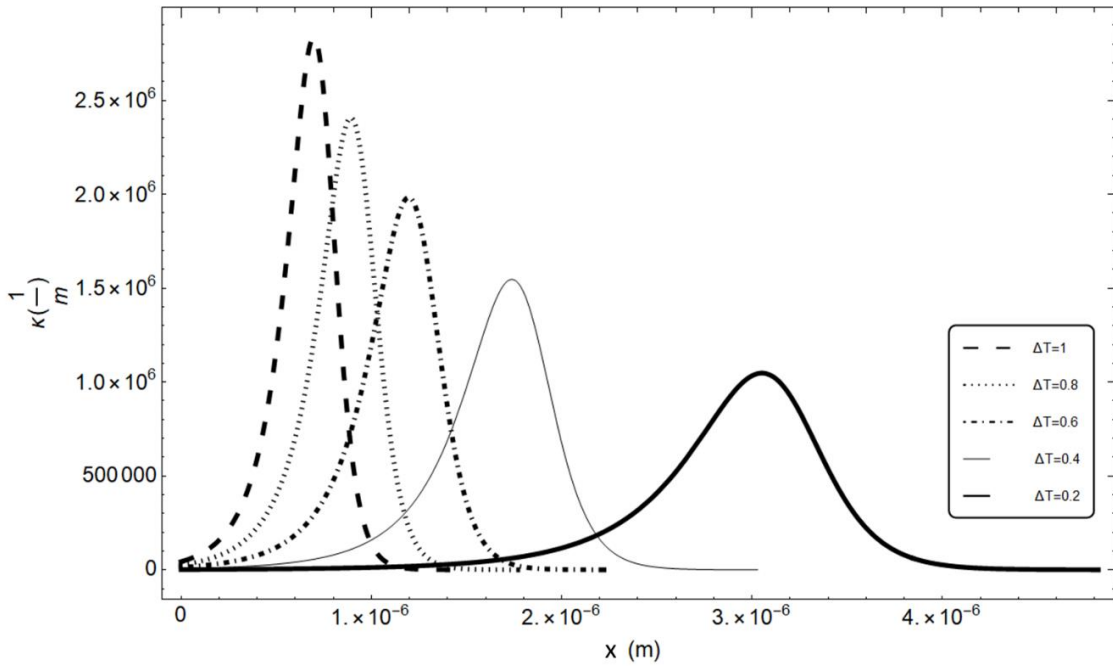


Figure I3. Local curvature as a function of location for various superheat degrees

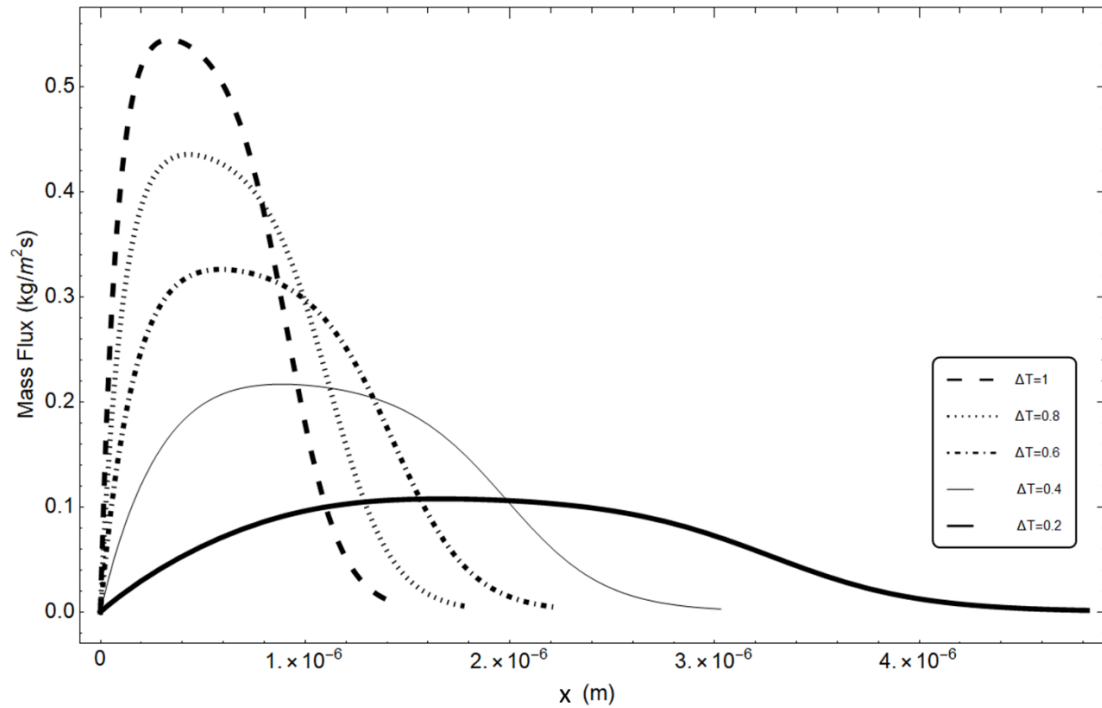


Figure 14. Local mass flux as a function of location for various superheat degrees

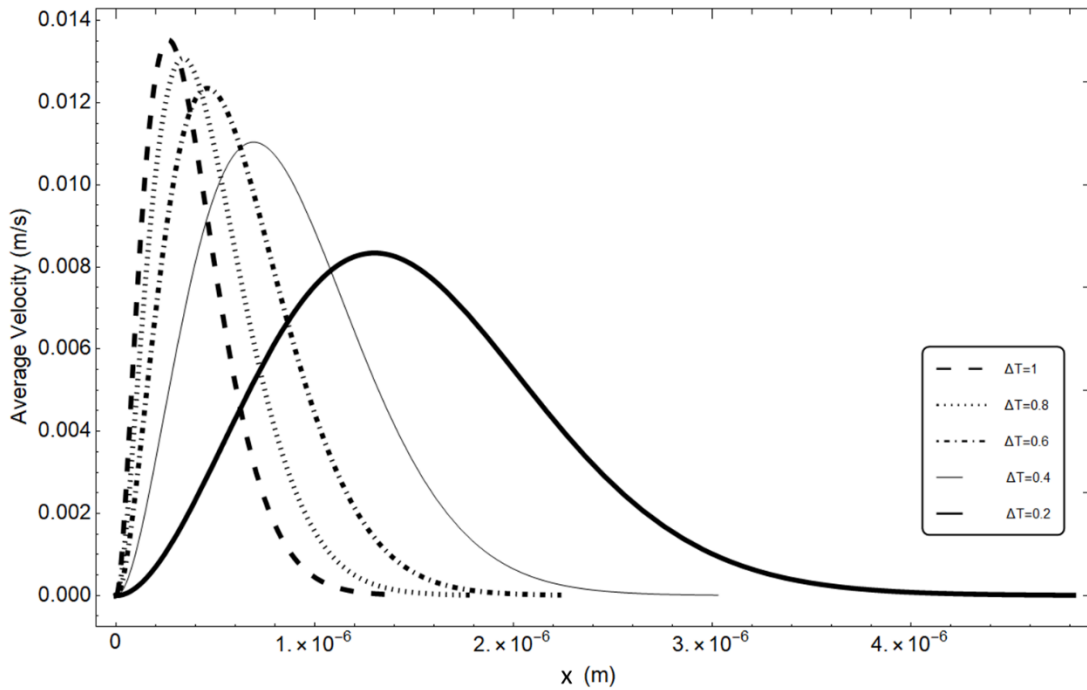


Figure 15. Average velocity as a function of location for various superheat degrees

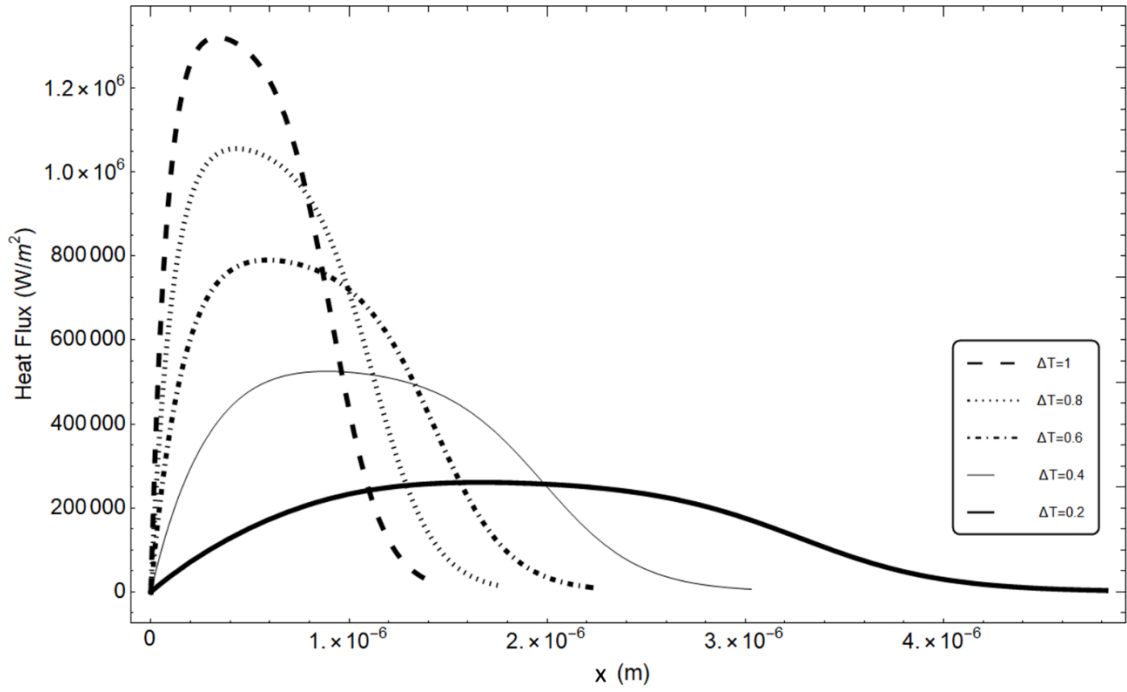


Figure I6. Local heat flux as a function of location for various superheat degrees

Appendix J.

P&ID and equipment list

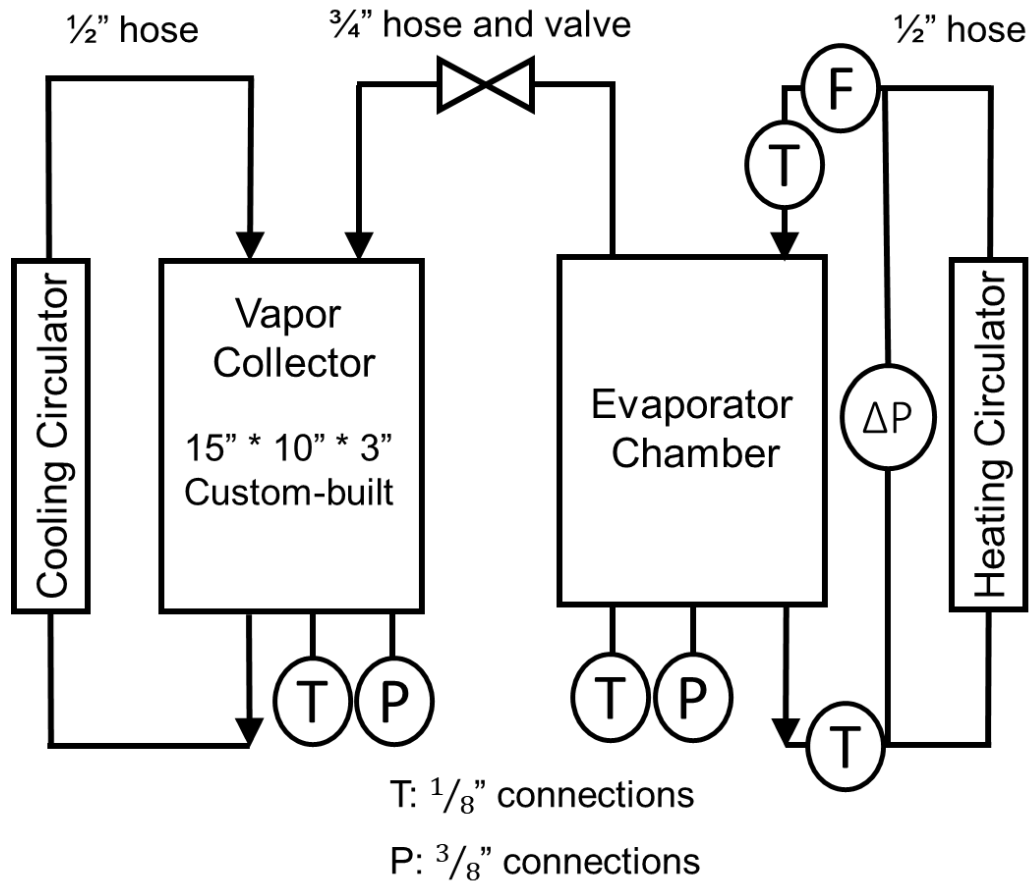


Figure J1. P&ID diagram of experimental setup

Circulators: Cole-Parmer Polystat RK12122

Flowmeter: Kobold DUK

Pressure sensors: Omega 0-5 PSIA

Pressure difference sensor: Omega 0-100 PSID

Temperature sensors: Omega T-type thermocouples

Valve: LDS vacuum solenoid valve, 3/4"

Vacuum chamber: ThermoFisher Nalgene 12L

Scale: Mettler Toledo ME5002TE

Appendix K.

CALPE experiment transient data

The following is the transient performance data of CALPE measured in custom-built setup, described in chapter 5.

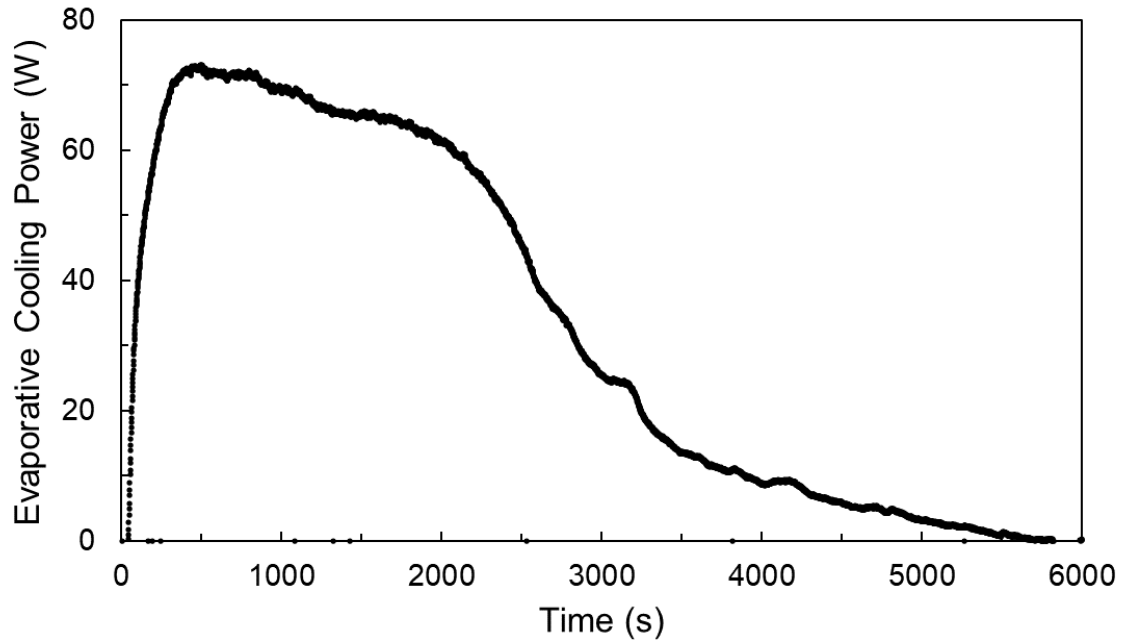


Figure K1. Transient performance data of CALPE with rectangular micro-grooves

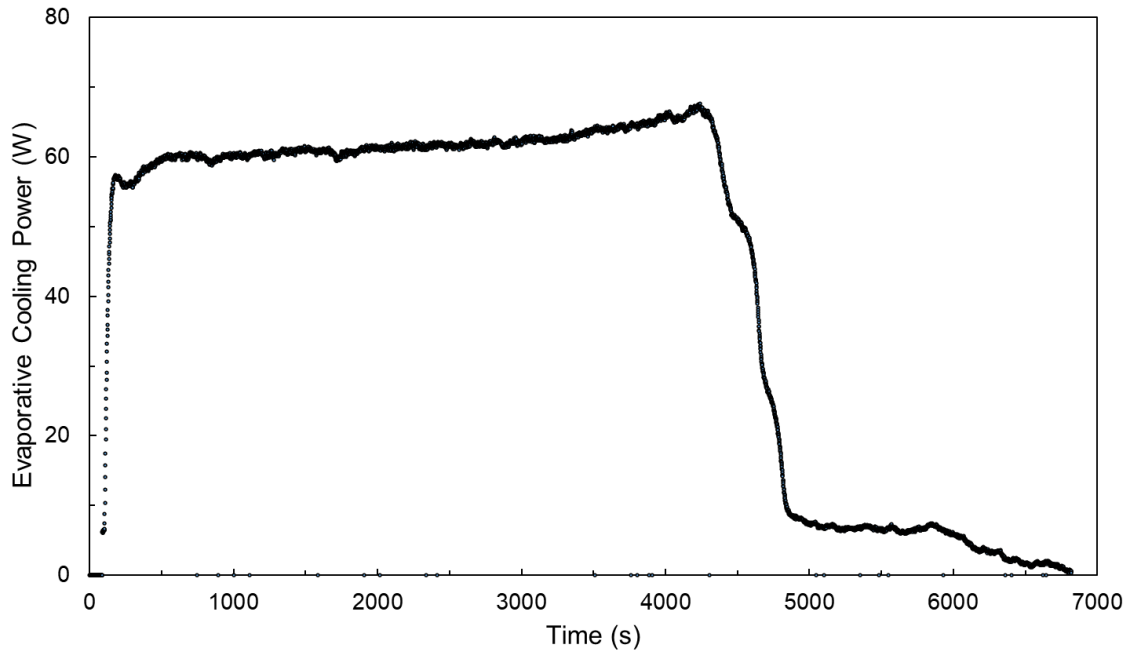


Figure K2. Transient performance data of CALPE with triangular micro-grooves